UNIVERSIDADE ESTADUAL DE CAMPINAS
FACULDADE DE ENGENHARIA MECÂNICA

JÉSSICA LEONEL GONÇALVES

NUMERICAL AND EXPERIMENTAL INVESTIGATION OF SLUG FLOW THROUGH STEEL LAZY WAVE RISER

INVESTIGAÇÃO NUMÉRICA E EXPERIMENTAL DO ESCOAMENTO INTERMITENTE EM RISERS DO TIPO LAZY WAVE

CAMPINAS

2024

JÉSSICA LEONEL GONÇALVES

NUMERICAL AND EXPERIMENTAL INVESTIGATION OF SLUG FLOW THROUGH STEEL LAZY WAVE RISER

INVESTIGAÇÃO NUMÉRICA E EXPERIMENTAL DO ESCOAMENTO INTERMITENTE EM RISERS DO TIPO LAZY WAVE

Thesis presented to the Mechanical Engineering Faculty of the Universidade Estadual de Campinas in partial fulfillment of the requirements for the degree of Doctor in Mechanical Engineering in the area of Thermal and Fluids.

Tese de Doutorado apresentada à Faculdade de Engenharia Mecânica da Universidade Estadual de Campinas como parte dos requisitos exigidos para obtenção do título de Doutora em Engenharia Mecânica, na Área de Térmica e Fluidos.

Orientador: Prof. Dr. Ricardo Augusto Mazza

Este exemplar corresponde à versão final da Tese defendida pela aluna Jéssica Leonel Gonçalves e orientada pelo Prof. Dr. Ricardo Augusto Mazza.

CAMPINAS

2024

Ficha catalográfica
Universidade Estadual de Campinas (UNICAMP)
Biblioteca da Área de Engenharia e Arquitetura
Rose Meire da Silva - CRB 8/5974

G586n

Gonçalves, Jessica Leonel, 1991-
Numerical and experimental investigation of slug flow through steel lazy wave riser / Jéssica Leonel Gonçalves. – Campinas, SP : [s.n.], 2024.

Orientador: Ricardo Augusto Mazza.
Tese (doutorado) – Universidade Estadual de Campinas (UNICAMP), Faculdade de Engenharia Mecânica.

1. Escoamento bifásico. 2. Escoamento intermitente. 3. Seguimentos de pistões. 4. Óleo e gás. I. Mazza, Ricardo Augusto, 1969-. II. Universidade Estadual de Campinas (UNICAMP). Faculdade de Engenharia Mecânica. III. Título.

Informações Complementares

Título em outro idioma: Investigação numérica e experimental do escoamento intermitente em risers do tipo lazy wave
Palavras-chave em inglês:
Two-phase flow
Slug flow
Slug tracking
Oil and Gas
Área de concentração: Térmica e Fluídos
Titulação: Doutora em Engenharia Mecânica
Banca examinadora:
Ricardo Augusto Mazza [Orientador]
Valdir Estevam
Ivanilto Andreolli
Jorge Luis Baliño
Hendy Tisserant Rodrigues
Data de defesa: 10-07-2024
Programa de Pós-Graduação: Engenharia Mecânica

Identificação e informações acadêmicas do(a) aluno(a)
- ORCID do autor: https://orcid.org/0000-0002-6711-8869
- Currículo Lattes do autor: https://lattes.cnpq.br/7316726337268469

UNIVERSIDADE ESTADUAL DE CAMPINAS

FACULDADE DE ENGENHARIA MECÂNICA

TESE DE DOUTORADO ACADÊMICO

NUMERICAL AND EXPERIMENTAL INVESTIGATION OF SLUG FLOW THROUGH STEEL LAZY WAVE RISER

INVESTIGAÇÃO NUMÉRICA E EXPERIMENTAL DO ESCOAMENTO INTERMITENTE EM RISERS DO TIPO LAZY WAVE

Autora: Jéssica Leonel Gonçalves
Orientador: Prof. Dr. Ricardo Augusto Mazza

A Banca Examinadora composta pelos membros abaixo aprovou esta Tese:

Prof. Dr. Ricardo Augusto Mazza, Presidente
DE/FEM/UNICAMP

Prof. Dr. Valdir Estevam
CEPETRO/FEM/UNICAMP

Prof. Dr. Ivanilto Andreolli
Petróleo Brasileiro SA

Prof. Dr. Jorge Luis Baliño
Departamento de Engenharia Mecânica/POLI-USP

Prof. Dr. Hendy Tisserant Rodrigues
BP, British Petroleum

A Ata da defesa com as respectivas assinaturas dos membros encontra-se no SIGA/Sistema de Fluxo de Dissertação/Tese e na Secretaria do Programa da Unidade.

Campinas, 10 de julho de 2024

AGRADECIMENTOS

Objetivos são alcançados através de uma trajetória de muito esforço, disciplina e dedicação, mas a presença de uma rede de apoio ao nosso redor torna esse caminho muito mais leve e feliz. Por esse motivo, não posso deixar de agradecer.

Agradeço imensamente a minha família. Aos meus pais, Maria Inês e Joracy, por enfrentarem todos os obstáculos para fornecer as ferramentas necessárias para a construção dos meus sonhos. E por terem me ensinado que dedicação e resiliência são a base para alcançar qualquer objetivo. A eles e à minha irmã, Gabrielle, por serem símbolo de amor, carinho e suporte em todos as fases da minha vida. Ao meu marido, Lucas, por todo o apoio e incentivo desde o início desse processo. E também pelo companheirismo ao longo das muitas horas de trabalho, pelo esforço de fazer os momentos livres mais felizes e por toda a ajuda dispendida para que isso se tornasse real.

Agradeço também ao meu orientador, Prof. Dr. Ricardo Mazza. Durante esses quase 9 anos de trabalho conjunto, nossa troca contribuiu muito para o meu desenvolvimento técnico, profissional e pessoal. Obrigada pela confiança e pelas oportunidades no mestrado, nos projetos de pesquisa e no doutorado. Serei eternamente grata e orgulhosa de ter feito parte da equipe do Flow&Rs Laboratory e por ter acompanhado o seu crescimento.

Aos meus colegas de laboratório, agradeço a troca de conhecimento, as discussões enriquecedoras e pelos momentos compartilhados. Em especial, gostaria de agradecer a Gabriela Toledo, Matheus Pasquini, Caio Araújo e José Rodrigues por todo apoio e disponibilidade ao longo da aquisição dos dados e das filmagens.

Por fim, agradeço à empresa Petrobras S.A pelo projeto de pesquisa que permitiu a construção da linha experimental e a realização de todo este trabalho.

RESUMO

Os campos de petróleo em águas profundas exigem sistemas de produção mais robustos para garantir sua segurança e vida útil. A condição ambiental extrema e o comportamento da produção intensificam os esforços exercidos sobre o sistema flowline-riser, podendo gerar acidentes com altos danos ambientais, econômicos e humanos. Steel Lazy Wave Riser é uma opção ao riser em catenária livre devido ao uso de módulos de flutuadores (curva em S) que minimizam tais esforços. Os dados de produção são influenciados pelo padrão do escoamento e suas propriedades. O escoamento intermitente é o padrão mais comum na produção de petróleo, e o que causa a maior influência em análises estruturais de riser devido a sua característica aleatória. Por outro lado, a geometria complexa do lazy wave riser também influencia os parâmetros do escoamento devido às suas mudanças de inclinação e direção (hilly terrain). Existem estudos prévios que analisam essa influência, porém eles utilizam geometrias mais simples e menores inclinações. Este estudo propõe uma investigação experimental e numérica do escoamento ao longo da curva em S. A seção de teste é um lazy wave riser em escala de laboratório, onde é realizado a aquisição de dados e visualização do escoamento. A linha contém 10 estações de medição, cada uma delas tem um sensor de pressão e dois sensores de impedância. As filmagens de alta frequência foram realizadas em seis posições da curva. A matriz de teste consiste em seis condições operacionais, que abrange duas velocidades de mistura e quatro razões entre velocidades superficiais de ar e da água. Os parâmetros de interesse são pressão, velocidades e comprimentos da bolha e do pistão e frequência de passagem de células. O comportamento do escoamento ao longo do hilly terrain é fortemente influenciado pela velocidade da mistura e razão ar e água. Adicionalmente, este estudo propõe algumas melhorias ao modelo de seguimento de pistões de Rosa et al. (2015) visando utilizá-lo em geometrias complexas e cenários de produção de óleo e gás. Essas melhorias englobam metodologias para capturar a influência do hilly terrain e da mudança da interface da bolha devido a inclinação da linha, e para definir as propriedades do petróleo e as condições de entrada e de contorno do modelo. A validação é feita com os dados experimentais. Além disso, baseado nos dados de Andreolli (2018), o software simula o escoamento em um riser real (lazy wave) utilizado em um campo de petróleo. As duas análises numéricas apresentam boa concordância.

Palavras-chave: escoamento intermitente, lazy wave riser, hilly terrain, slug tracking, produção de óleo e gás, análise dinâmica de riser

ABSTRACT

The deep offshore oil gas field requires a robust production system to ensure its security and to enhance its useful life. The extreme environmental condition and production behavior intensify the forces exerted in the flowline-riser, which can lead to accidents with high environmental, economic and human impacts. Steel Lazy Wave Riser is an alternative to the conventional Steel Catenary Riser due to the usage of a buoyancy section (S curve) that minimizes those effects. The production data is influenced by the flow pattern and properties. The slug flow is the most common pattern encountered in petroleum production systems and it highly influences the structural analysis due to its random feature. On the other hand, the complex lazy wave geometry also influences the flow parameters due to the pipe inclination and orientation change (hilly terrain). There are previous studies that analyzed that influence, but most of them employed simpler geometries and small inclination changes. This study proposes an experimental and numerical investigation of the flow behavior along the S curve. The test loop is a laboratory-scale lazy wave riser where the data acquisition and the flow visualization are conducted. The line has 10 measuring stations, and each of them contains a pressure transducer and two impedance sensors. The high-speed filming was recorded in six positions along the curve. The test grid contains six operation points that cover two mixture velocities and four superficial air and water velocities ratio. The desired parameters are the pressure, bubble and liquid slug lengths and velocities, as well as the cell frequency. The experimental images show that the flow behavior strongly depends on the mixture velocity and the superficial gas and liquid velocities ratio. In addition, this study improves Rosa et al.'s (2015) slug tracking model by targeting complex geometries and real-world oil and gas scenarios. Those upgrades cover the hilly terrain influence, the bubble interface transition due to the pipe inclination and the oil and gas thermodynamic properties. In addition, a new initial and boundary conditions are proposed. The updated model is validated against a dedicated experimental data. In addition, the software simulates an actual lazy wave riser employed in a petroleum field which was provided by Andreolli (2018). Both numerical analyses show good agreement.

Keywords: slug flow, lazy wave riser, hilly terrain, slug tracking, oil and gas production, dynamic riser analysis

LIST OF FIGURES

LIST OF TABLES

NOTATIONS

Latin Letters

U_S	Liquid slug velocity	[m/s]
U_M	Mixture velocity at liquid slug	[m/s]
U_b	Dispersed bubble velocity	[m/s]
U_T	Translation bubble velocity	[m/s]
U_G	Gas phase velocity	[m/s]
U_f	Liquid film velocity	[m/s]
V_S	Liquid slug front velocity	[m/s]
u_D, v_D	Drift velocity	[m/s]
J_L	Superficial liquid velocity	[m/s]
J_G	Superficial gas velocity	[m/s]
Q	Volumetric flow rate	[m^3/s]
P_G	Gas pressure at bubble	[kPa] or [kgf/cm^2]
R_S	Liquid holdup at slug	[-]
R_f	Liquid holdup at bubble region	[-]
h_f	Liquid film thickness	[m]
L_B	Bubble length	[m]
L_S	Liquid slug length	[m]
L	Unit cell length	[m]
f	Cell frequency	[Hz]
x	Front of liquid slug	[m]
y	Front of elongated bubble nose	[m]
C_f	Fanning factor	[-]
c_b, C_0	Distribution parameter	[-]

h	Wake function	[-]
g	Gravity	[m/s²]
D	Pipe inside diameter	[m]
A	Cross section area	[m²]
M	Molar mass	[g/mol]
L	Pipe length	[m]
H	Height	[m]
t	Time	[s]
S	Perimeter	[m]
s	Standard deviation	[-]
d_{D-U}	Distance between the downstream and upstream impedance sensor	[m]

Greek Letters

χ	Density or dynamic viscosity	[-]
ρ	Density	[kg/m³]
μ	Dynamic viscosity	[Pa.s]
σ	Surface tension	[N/m]
α_S	Void fraction at liquid slug	[-]
α_f	Void fraction at bubble	[-]
α_G	Cell void fraction	[-]
β	Intermittence factor	[-]
θ	Inclination angle	[-]
τ_S	Liquid slug wall shear	[N.m²]
ε	Pipe roughness	[m]
Δt	Time step	[s]

Δ	Interval	[-]
$\forall$	Volume	[m^3]

Superscript or subscript

L	Liquid phase
G	Gas phase
i	Interface gas-liquid
M	Mixture
N	New time
j	Number of cells
S	Liquid slug
f	Liquid film
U	Unit cell
B	Elongated bubble
b	Dispersed bubble
atm	Atmosphere condition
lam	Laminar flow element – gas flow rate data
O	Old time or Oil
SEP	Separator facilities
w	Water

Abbreviation

B_O	Volume factor formation
BSW	Basic Sediment and Water
CFD	Computational Fluid Dynamics
GOR	Gas-oil-rate

ID	Inside Diameter
RS	Solution gas-oil ratio
S	Station
SLWR	Steel Lazy Wave Riser (SLWR)
WOR	Water-oil-rate

CONTENTS

1 INTRODUCTION

The offshore oil and gas production has been increasing during the last decades. According to Wen et al. (2023), the offshore reservoirs represent 60% of the total oil and gas reserves discovered over the world during the last ten years. In addition, the authors stated that 62% of these reserves are encountered in deep and ultra-deep water. This kind of exploration requires the development of new technologies, equipment, procedures and modeling due to the extreme environment. This scenario also influences the production system. The determination of the riser configuration and the flow assurance analysis become even more important to avoid operational problems.

The riser is the pipe that transports the petroleum from the seabed to the production facilities. Some authors also named this pipeline as a flowline-riser system (Andreolli, 2018; Oliveira *et al.;* 2013; Pots *et al.*, 1987). The flowline is the horizontal or near-horizontal section, and the riser is the inclined and/or vertical section. Based on the subsea project design, the pipeline integrity, materials and cost, Bai and Bai (2005) described four potential configurations: free-hanging catenary riser, lazy wave, steep wave, and lazy-S. The most common configuration is the free-hanging catenary riser (Meneses et al., 2023; Pollio and Mossa, 2009; Zhu et al., 2021) due to its cost efficiency, simplicity and reliability (Kim and Kim, 2015). Nonetheless, recent researches mentioned that the Steel Lazy Wave Riser (SLWR) is more suitable for deep and ultra-deep water (Meneses et al., 2023; Ruan et al., 2024; Zhang et al., 2023). Its main geometric characteristic is the "S" curve that is created via buoyancy modules. Figure 1.1 illustrates that. This configuration aims to avoid or minimize the efforts exerted on the riser by the environment and production conditions.

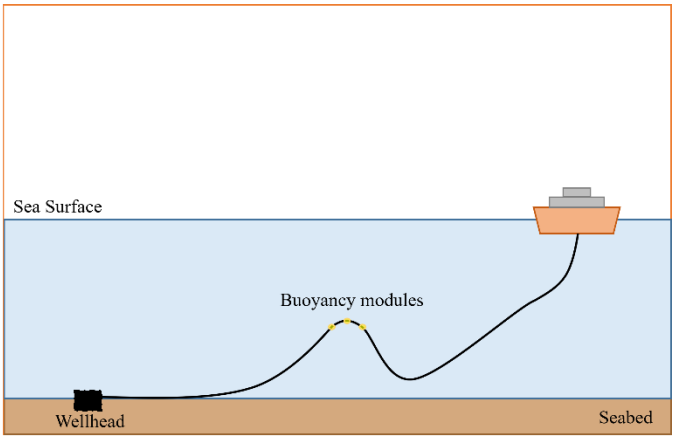

Figure 1.1. Schematic of Steel Lazy Wave Riser configuration.

On the other hand, the lazy wave riser configuration influences the parameters of the internal flow. The oil, gas natural and water mixture flows through hilly terrain pipeline over long distance, high-pressure gradient and temperature variation. These conditions are critical for the flow assurance issues. One of them is slugging, which covers hydrodynamic slug, terrain-induced slug, turn-up slugs, pigging slug and severe slug (Hussein, 2023; Makogon, 2019). This work comprehends the first and second one only. Hydrodynamic and terrain-induced slugging are phenomena described within the slug flow pattern. The main difference between them is their formation mechanism. The first one occurs due to instabilities over stratified interface (liquid-gas). The latter is formed by the liquid accumulation in hilly terrain pipelines, which can result in the slug flow formation or the severe slug occurrence.

In general, the slug flow is the most common pattern encountered in petroleum production systems (Grigoleto et al., 2021; Yu et al., 2024). Its main feature is the alternate passage of liquid slug and elongated bubbles with different lengths and void fractions. The coupling of both structures are named unit cell as proposed by Wallis (1969). Figure 1.2 shows the unit cell and highlights the bubble interfaces for horizontal and vertical pipelines. The liquid slug has dispersed bubbles, regardless of the orientation. In horizontal tubes, the bubble region seems to be a stratified pattern (plane interface), the bubble flows at the top of the pipe and the liquid film at the bottom (Shoham, 2005). In the vertical pipe, this region is similar to the annular pattern (concentric interface), where the bubble is at the center of the pipe and a thin liquid film is between the bubble and pipe wall (Taitel et al., 1980).

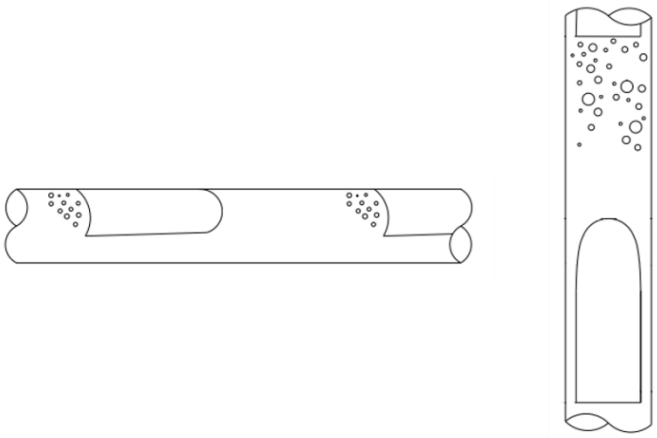

Figure 1.2. Schematic of slug flow pattern in horizontal and vertical pipeline orientation.

Studies about the slug flow influence on dynamic riser analysis have been increasing. Some authors named this phenomenon as internal slug flow-induced vibration (FIV). Zhu et al. (2021), (2019) stated that the internal flow is an important factor to

determine the system mass and can change the dynamic behavior of this structure. The slug flow pattern induces the highest structural vibration (Haile et al., 2022; Miwa et al., 2015; Porter et al., 2023). It occurs because of its random feature, which results in mixture fluid density, momentum and pressure fluctuations along the time and space. Ma and Srinil (2020) commented that this variability could affect the riser natural vibration and reduce its lifetime. The accurate assessment of vibration intensity is also crucial due to its impact on corrosion rate (Hadi and Jasim, 2018; Yakupov and Yakupov, 2018). It becomes even more critical in pre-salt scenarios where petroleum often contains high fractions of contaminants (i.e., H_2S and CO_2). But some authors have still highlighted the usage of simplified mathematical models to represent the slug flow modeling on dynamic risers analysis (Ortega Malca, 2015; Pollio and Mossa, 2009; Vásquez and Avila, 2021).

The slug flow modeling along the lazy wave riser becomes even more complex due to the hilly terrain. Experimental campaigns demonstrated that small inclination changes had strongly modified the bubble and liquid lengths, and consequently, the fluid mass in the pipe (Al-Safran et al., 2005; Scott and Kouba, 2004; Taitel and Barnea, 2000). Zheng et al., 1995 pointed out the hilly terrain increases the interaction between neighboring unit cells resulting in longer liquid slugs compared to horizontal pipes. Ragab et al. (2008) indicated that this geometry configuration increases or dissipates liquid slug. Other researchers describe the potential occurrence of severe slug in some operational conditions (Duan et al., 2017; Mokhatab, 2007; Park and Nydal, 2014; Zhu et al., 2021). Ersoy et al. (2011) cited operational problems caused by the lack of realistic slug flow modeling along the hilly terrain, such as flooding of separator facilities, corrosion/erosion and structural integrity of the pipeline, production loss and poor reservoir management.

Many of those researchers have studied the flow through simpler geometry configuration compared to lazy wave risers. Thus, the slug flow behavior over the S curve still suffers a lack of investigation. This research aims to improve the knowledge in this gap. Based on the experimental campaign, this work aims to describe the flow characteristics along the S curve and to identify the occurrence of phenomena previously mentioned in the literature or new ones. This work also proposed some improvements to Rosa et al.'s (2015) slug tracking model in order to employ it in actual oil and gas production lines. It covers hilly terrain submodels, transition of the bubble interface shape due to the pipe inclination, methodologies to treat the inlet and outlet boundary conditions and a Black-Oil model to determine the oil and

gas properties. The validation of those new approaches will be done via a dedicated experimental campaign. As an additional validation, Andreolli's (2018) data for an actual lazy wave riser is used to demonstrate the model performance to simulate oil and gas flow under high-pressure gradients over long distances and complex geometry pipelines. The numerical results obtained in this research are useful for production management and dynamic riser analysis. The specific objectives are:

- Visualize and analyze the flow images at critical section of the S curve.
- Identify potential pattern changes on the downward section.
- Assess the experimental data obtained for bubble and liquid slug lengths, the translational bubble and liquid slug front velocities, frequency, and pressure along the S curve.
- Update the inlet and outlet boundary condition used by Rosa et al. (2015) to further application in oil and gas production lines.
- Create and implement submodels to Rosa et al.'s (2015) slug tracking model to capture the geometry influence on slug flow parameters.
- Validate the numerical results with a dedicated experimental campaign.
- Apply the updated slug tracking to an actual real-word scenario (lazy wave riser used in the petroleum field).
- Provide the slug flow parameters required by dynamic riser analysis.

1.1 Research outline

This work is divided into two parts: experimental and numerical. Both subjects have their own description, but their results are complementary. The content is written in six chapters. The first one briefly introduces the thesis interest and presents its applicability and relevance to the oil and gas industry. As reported below, the following five chapters describe:

- Chapter 2 – Literature review: It presents an overview of slug flow modeling, mainly the previous studies that have discussed the hilly terrain influence. It also presents a review about the increasing number of studies that have covered the influence of slug flow behavior on the dynamic riser analysis.
- Chapter 3 – Experimental apparatus: It presents the experimental setup, with its equipment, instruments and air-water lines. This chapter also describes the programs employed to control the line and to perform the data processing. Lastly, it presents the testing procedure for images and data acquisition.

- Chapter 4 – Numerical model: It describes the mathematical formulation of the slug tracking model. This formulation covers the mass and momentum equations developed by Rosa et al., 2015 and new submodels employed to adapt their model for lazy-wave riser application. This chapter also presents the modification proposed in their numerical method, boundary conditions and the insertion of a Black-Oil model to predict the thermodynamic properties of oil and gas mixture.
- Chapter 5 – Results and discussion: This section is divided into two sections, which covers the experimental campaign and numerical analysis. The first one discusses the flow images recorded in six pipe sections. Based on the recorded movies, it is assessed the occurrence of phenomena previously mentioned in the literature or identified new ones. The experimental mean and distribution data are also analyzed. The last section focuses on the numerical results. The model validation is based on the current experimental data. In addition, the results obtained for an actual lazy wave riser are also presented.
- Chapter 6 – Conclusion: It contains the conclusion of this work as well as suggestions for future studies.

2 LITERATURE REVIEW

This chapter contains two sections. Section 2.1 reviews the studies about the slug flow through hilly terrain pipelines. It covers experimental and numerical studies. Section 2.2 discusses the models used to predict the slug flow parameters for dynamic riser analysis, focusing on the desired parameters and the modeling assumptions.

2.1 Slug flow modeling: hilly terrain

According to Manfield (2000), many models and experimental campaigns idealize the multiphase flow through offshore pipeline networks. They considered the pipe as perfectly horizontal or uniformly inclined. Nevertheless, the pipe inclination should change due to the uneven seabed. In flowline-riser systems, this characteristic is even more noticeable, since there are changes due to seabed and riser configurations. In the literature, hilly terrain is the name used to describe pipeline sections with inclination or flow direction changes.

Hill et al. (1996) pointed out that the flow analysis through hilly terrain is crucial to predict the properties at the production facilities as well as to ensure the correct prediction of the pressure gradient. The slug flow pattern has been extensively studied for horizontal, vertical and inclined orientations. Nonetheless, there still is a lack of studies about hilly terrain influence on the intermittent flow parameters. It is more evident for complex geometry like oil and gas production systems. As reported in Figure 1.1, the lazy wave riser is a hilly terrain pipeline due to the buoyancy modules. This region results in three different pipeline orientations: (i) horizontal, (ii) upward and (iii) downward inclined. The coupling of those sections creates two configurations previously described in the literature as “A” and “V” formats.

Figure 2.1 (a) illustrates the V format that has a downward followed by an upward inclined pipeline. Some studies have pointed out that the V format also describes the phenomena that occur at the transition from horizontal to upward inclined pipe. Figure 2.1 (b) shows the A format, where the flow passes from an uphill to a downhill section. Those geometries affect the flow parameters, which require independent modeling. When the slug flow travels through the hilly terrain, it might generate new unit cells or increase the liquid slug length at the low elbow (V format). On the other hand, it might reduce or dissipate the liquid slug at the top elbow (A format). In addition, the bubble length, the void fraction and the liquid slug holdup might also change.

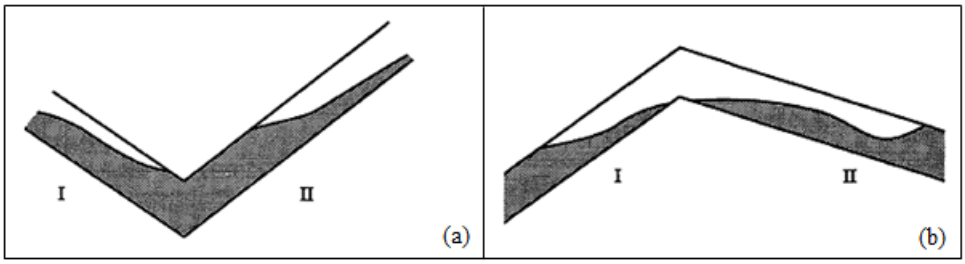

Figure 2.1. Schematic of the A and V hilly terrain formats - Zheng et al. 1993.

Research on hilly terrain has been developed since the end of the 20th century. Most of those studies cover the influence of small inclination changes on the flow parameters. The lazy wave riser is more complex, but the literature review is essential to understand the phenomenon that has been already identified in simpler geometry configurations.

The first experimental study developed in this area was proposed by Schmidt et al. (1980). The authors carried out their tests on a flowline-riser setup, where the pipe might have different inclinations (5, -2, 0 and 5°). Later, Taitel (1986), Pots et al. (1987), Taitel et al. (1990) and Fabre et al. (1990) proposed similar theoretical or experimental studies. Those authors focused on severe slugging description, modeling and mitigation. However, the occurrence of this phenomenon is out of this work scope. The following literature review covers the hilly terrain influence on stable flow.

Zheng et al. (1993) proposed the first mathematical model to predict the effects of hilly terrain in slug flow parameters. This study is based on experimental data obtained by Zheng (1991) and posteriorly published by Zheng et al. (1995). The authors described the phenomena using the sink and source concepts. Both of them act as a tool that removes and adds liquid to the low and top elbow. At the V format, there is a liquid accumulation (sink) at the low elbow. Then, the liquid release (source) occurs in two potential situations. The first condition results in the sudden increase of the approaching liquid slug. The second one forms a new unit cell. The author's criterion to the unit cell generation is the liquid slug size that must have at least the minimum stable length adapted to inclined lines. This hypothesis aimed to avoid the formation of short liquid slugs (pseudo-slugs) that will quickly disappear. At the A format, the authors pointed out the bubble void fraction increases while it is passing the top elbow. It occurs because the liquid film is drained to neighboring cells by gravity. Thus, the sink and source concepts are employed to avoid the void fraction bubble reduction. While the bubble is at the top elbow, there is a liquid addition (source). Then, the same liquid amount is subtracted (sink) from the approaching liquid slug. This liquid release reduces the slug length

or it causes its total dissipation. Zheng et al. (1993) validated the model with their own experimental campaign. The authors attested the good agreement. Nonetheless, they also affirmed the model requires an improvement of the slug flow model along the pipeline.

Zheng et al. (1994) proposed the first slug tracking model with hilly terrain treatment. However, the authors considered incompressible gas and constant film thickness. The liquid film velocity is an input data. They also validated the model with their own experimental campaign and attested that it is able to describe the hilly terrain phenomena accurately. In the following year, Zheng et al. (1995) published the experimental campaign used in their previous papers. The air-kerosene tests were conducted in a pipeline with 77.9 mm ID and 420 m long. The flow-loop has two horizontal sections that are upstream and downstream the main pipe. This pipe inclination varied from -1° to 5°. The superficial liquid and gas velocities ranges are not clear. Their main goal was to analyze the liquid slug length and void fraction through nine ring-capacitance sensors. Each horizontal line has two sensors, and the others are at the main inclined pipe. The slug flow pattern is presented in the upstream horizontal line for all tests. The authors had the following conclusions:

(a) There is slug flow along the hilly terrain, except for some tests with downward inclined pipe (-1°). In those cases, the flow transitioned to a stratified pattern.
(b) Liquid slug length increases after the low elbow. That parameter presents lognormal distribution on the horizontal and uphill section.
(c) The small liquid slug formed at the low elbow quickly disappears on the uphill section, as modeled by Zheng et al. (1993).
(d) At the low elbow, the liquid slug traps small bubbles. Thus, the liquid slug holdup is lower on the uphill section. The inclination of the main pipe influences the holdup value.
(e) The liquid film also changes from horizontal to uphill sections.
(f) At the A format, the liquid slug length decreases in the downhill section. It mainly occurs for low gas flow rates.
(g) There is an intense bubble overtaking in the downhill section due to buoyancy.
(h) For high liquid flow rate, the unit cell frequency is constant. For low rate, the frequency changes along the hilly terrain.

Later, Taitel and Barnea (2000) added the hilly terrain treatment to Taitel and Barnea's (1998) slug tracking model. The updated model takes into account the gas

compressibility and the liquid slug holdup. They also analyzed the A and V formats (see Figure 2.1). At the A format, the authors pointed out the potential transition to stratified pattern as illustrated in Figure 2.2 (a). At the top elbow, the authors affirmed that the liquid film migrates to neighboring cells due to the gravity force, resulting in a dry region ($R_f = 0$). In addition, this phenomenon influences the liquid slug length reduction or the dissipation in the downward inclined section. This one might cause the flow pattern transition. At the V format, their comprehension is similar to Zheng et al. (1993), as presented in Figure 2.2 (b).

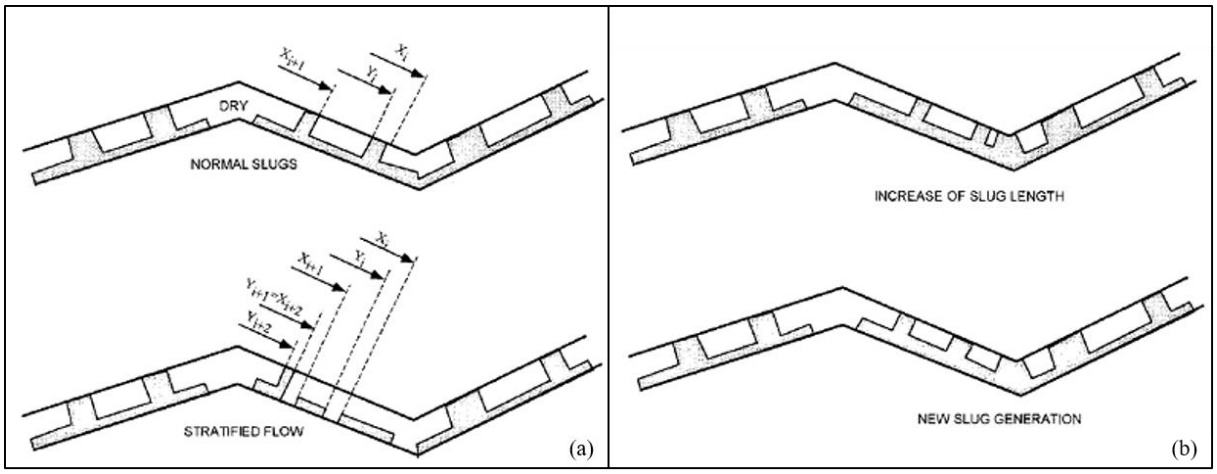

Figure 2.2. Schematic of the slug flow modification across the A (a) and V (b) format according to Taitel and Barnea (2000).

Taitel et al. (2000) delved their studies into the downhill section, aiming to describe some situations in which transition from slug flow to stratified pattern occurs. The authors developed an theoretical analysis based on the Taitel and Barnea's (1990) bubble model and liquid and mass balances. Their study considered the slug flow travels from an upward inclined to a downward inclined pipeline (- 1°). In the first case, they pointed out the transition occurs because the liquid film is faster than the liquid slug mixture. Thus, the slug loses liquid and gradually becomes shorter and dissipates. Due to this gradual process, the author affirmed that the transition occurs after some distance in the downward section. They named that distance as dissipation length. The second case follows the theory proposed by Taitel and Barnea (2000) related to the dry zone, as shown in Figure 2.2 (a). Taitel et al. (2000) also presented a discussion about the relation between superficial gas and liquid velocities and the dissipation length. They affirmed that the dissipation distance increases with the gas flow rate. The liquid flow rate has a strong effect on that only for low superficial gas velocities (until $J_G \approx 1.0$ m/s).

Yoshida et al. (2000) developed an extensive experimental campaign to describe the hilly terrain influence. The authors conducted 286 tests using two different pipeline lengths

and diameters, type of fluids (air, nitrogen, water and kerosene) and a wide range of superficial liquid and gas velocities. The test loop had four sections with the following orientations: horizontal-inclined-inclined-horizontal. The angle of inclined pipes varies from -10° to 10°. Their main goals were the analysis of liquid slug length and holdup, liquid film holdup as well as the development of new correlation for bubble translation velocity. The authors proposed a different formulation for each pipe orientation that was compared with Andreussi and Bendiksen's (1989) correlation. Their results presented a good agreement, except for the downward inclined pipe. Yoshida et al. (2000) also presented the following conclusions:

(a) Liquid slug length has a lognormal distribution in all pipe orientations.
(b) There is liquid accumulation before the upward inclined pipe (low elbow).
(c) For high liquid and gas flow rates, the downward inclined section does not affect the liquid slug length.

Sharma et al. (2002) proposed a slug tracking model based on Taitel and Barnea (1998) and Dukler and Hubbard (1975) models. In their model, the pressure gradient considered the shear stress and gravity force only. The velocities are calculated by mass balance. The authors did not propose any model for hilly terrain. Their results are validated using Yoshida et al.'s (2000) data and an actual oil and gas gathering system data. On the first validation, the authors employed the model for small inclination change (0, 1, 3 and 5°). On the second one, the pipe has 15 inches ID and 4.5 km, and its inclination is not clear. The authors affirmed that the model has good agreement for both cases.

Zhang et al. (2003) carried out an experimental campaign along a hilly terrain pipeline. In addition, they also validated Zhang et al.'s (2000) model. The test section had four pipeline sections: horizontal-inclined-inclined-horizontal. The angle of the inclined pipes was -2° and 2°. The authors positioned 11 capacitance sensors along the pipeline with three in each inclined section, one at the elbow and the others placed on the horizontal pipes. The fluids were air and mineral oil. The superficial liquid and gas velocities vary between 0.3 to 0.91 m/s and 1.07 to 3.05 m/s, respectively. Their main goal was the investigation of liquid slug dissipation and generation. The authors made it through the analyses of the liquid slug and unit cell lengths ratio and the unit cell frequency along the hilly terrain. Their conclusions were:

(a) According to the flow pattern map from Taitel and Dukler (1976), there is slug flow in the horizontal, upward and downward inclined sections. For some tests, the transition to stratified pattern occurs in the downward pipe.
(b) For the lowest superficial liquid and gas velocities (0.3 and 1.07 m/s), the liquid slug is totally dissipated in the downward section.
(c) For the highest gas superficial velocity (3.05 m/s), the flow has similar behavior in the downstream and upstream horizontal sections (low hilly terrain effect).
(d) For low gas superficial velocities (1.07 to 2.1 m/s), the liquid length decreases in the downward section and suddenly increases after the elbow.
(e) Zhang et al. (2000) model considered the liquid slug is constant, thus the unit cell frequency is a function of the bubble length only. This assumption reduces their model quality in the low gas superficial velocity tests, since there is a high hilly terrain influence.

Al-safran et al. (2004) proposed a slug tracking model similar to Taitel and Barnea (2000). The studied parameter was the liquid slug length (average, statistical distribution and standard deviation). The authors also presented an experimental campaign using the Zhang et al.'s (2003) test loop for two operation points: J_L = 0.305 m/s and J_G = 1.067 m/s (Case 1) and J_L = 0.61 m/s and J_G = 1.128 m/s (Case 2). For Case 1, they observed that the liquid slug dissipation happens in the downhill section. As the liquid slug is short, the bubble velocity increases and intensifies the bubble overtaking. According to the authors, the slug tracking model captured this phenomenon after they tuned the translational bubble velocity correlation (Talvy et al., 2000). For Case 2, there is a partial slug dissipation in the downhill section. The authors commented that the model captured the liquid slug length reduction in the downward section, but on the upward pipeline, it is more difficult. They explained that the modeling of slug initiation at the bottom elbow was complex and affected the results of the upstream section. In general, Al-safran et al. (2004) pointed out the results have a good agreement with experimental data, but the model was not able to capture the maximum liquid slug length at the pipe exit.

Al-Safran et al. (2005) extended their last experimental campaign. They investigated the flow behavior along the downhill section and at the bottom elbow using different superficial velocities. They used the same fluid work and test loop, but the pipe inclinations were ±0.915° and ±1.93°. The upward and downward pipelines had the same angle;

the hilly terrain pipe is symmetric. Based on those tests, the authors divided the phenomena in the following five categories:

(a) Category 1 – Complete slug dissipation with slug initiation: It occurs with low and moderate superficial liquid and gas velocities. The total dissipation in the downward section occurs due to the short and slow liquid slugs. When the gas superficial velocity increases, the gravity effect reduces, and that phenomenon did not occur. However, those effects increase again when J_G is high enough to increase the liquid slug aeration. For small pipe inclination, this phenomenon is less frequent due to gravity force reduction. Regarding the slug initiation, it occurs due to the high liquid level at the bottom elbow (liquid accumulation).

(b) Category 2 – No hilly terrain effects: It occurs with high J_G and J_L. The liquid slug dissipation, slug initiation or growth at the bottom elbow are not observed. Due to the high velocities, the unit cell frequency does not change in the downhill section, and there is not enough time for the liquid accumulation at the elbow.

(c) Category 3 – Partial slug dissipation with slug initiation and growth: It occurs with moderate J_L and J_G. The cell frequency reduces in the downward pipe, but there is not a pattern transition. Due to the liquid accumulation, slug generation or growth can occur.

(d) Category 4 – No slug dissipation with slug initiation and growth: This scenario is more observed for the lowest inclination angle with moderate J_L and moderate or high J_G. At higher angles, this phenomenon only occurs when the liquid slug quickly moves in the downhill section.

(e) Category 5 – No slug dissipation with slug growth: It occurs with moderate J_L for both angles. The liquid accumulation happens, but the upstream liquid slug picks up the liquid volume before the cell generation.

The authors also analyzed the mean, maximum and distribution data of the liquid slug length and unit cell frequency in the upstream and downstream sections of the hilly terrain. Their goal was to identify the flow parameters behavior for each category. The authors also commented about two types of initiation mechanisms. The first one is based on the Kelvin-Helmholtz (K-H) instability. The liquid accumulation reduces the gas flowing area. The gas acceleration consequently results in a wave that blocks the whole cross-section area. The slug formation occurs at the bottom elbow. The second mechanism is described as the coalescence

of small waves to create a new cell. According to the authors, the unit cells are created on the uphill section and have the same characteristics of the pseudo-slugs described by Zheng et al. (1994).

Al-Safran et al. (2006) developed a statistical analysis to determine which distribution is more appropriate for the liquid slug length at bottom elbow. Their study is based on Al-Safran et al.'s (2005) data for Category 1. The authors reported that the lognormal distribution is the best fit. They also presented a new slug generation criterion based on the liquid film thickness, but they assumed there is a stratified flow pattern in the downward section which is not a general condition in hilly terrain pipelines.

Conte et al. (2011) proposed the addition of new methodologies to Rodrigues's (2009) slug tracking model. The authors added methods to predict the pipe inclination change, the increase of liquid slug length or unit cell generation at the low elbow. They employed the Taitel and Dukler's (1976) criterion to model the transition from stratified to slug flow patterns at the bottom elbow. They also carried out an experimental campaign using water and air. The test loop has a horizontal section followed by an upward inclined one (3°, 5° and 7°). The average and distribution of bubble and liquid slug lengths and bubble nose velocities are the desired parameters. According to the authors, the numerical model presented good agreement with the experimental data.

Yang et al. (2017) investigated the unit cell generation at the low elbow using CFD simulation through the commercial software ANSYS Fluent. Volume of fluid (VOF) and k-ε turbulence models are employed to track the gas and liquid interface along the hilly terrain pipeline. The test loop was symmetric and had a downward pipe followed by an upward one. In the simulation, there is an amount of stagnant water in the low elbow and the gas methane was flowing in the line. They investigated the flow behavior for different diameters, pipeline inclinations and superficial gas velocities and liquid heights. The authors concluded that the internal diameter had a tiny influence on the liquid slug formation, while the pipe inclination is crucial to the occurrence of this phenomenon. The increase of superficial gas velocity and liquid height caused a faster liquid slug generation. This phenomenon is a result of interface instability. The stagnant liquid reduces the flow area at the bottom elbow, thus the gas velocity increases, and its pressure reduces. This mechanism destroys the stability of the gas-liquid interface. If this liquid level uplifts to the top of the pipe, it will generate a liquid slug.

Yin et al. (2018) proposed an experimental and numerical study to describe the slug initiation in hilly terrain pipeline for low liquid velocity. Their test loop had three sections with 40 mm ID: horizontal, upward and downward. The inclined pipes were symmetric with inclination equal to ±10°. The working fluids were air and water. The superficial gas and liquid velocities ranges were 1.2 to 30 m/s and 0.002 to 0.1 m/s, respectively. A VOF and k-ε turbulence models were employed to simulate the same pipeline and operational condition. Based on their flow images, the authors described three types of slug formations: (a) Kelvin-Helmotz instability, (b) wave coalescence and (c) collision between the flowing liquid in the flow direction and the falling liquid from the upward line. The first two mechanisms are also described by Al-Safran et al. (2005). Nonetheless, Yin et al. (2018) affirmed that the (a) and (c) methods are more common when the superficial liquid velocity is less than 5.03 m/s. When the superficial gas velocity is higher than 5.1 m/s, the (b) method becomes dominant. The authors pointed out their numerical simulation presented a reliable prediction of the flow characteristics.

Alves et al. (2019) performed an experimental campaign to visualize and identify the flow behavior along a horizontal pipeline section followed by a downward inclined one. These sections are 5.76 m and 3.38 m long, respectively. The inner diameter is 0.026 m ID. The pipe inclination angle can be set as -3º, -5° and – 7°. Their test grid has 45 operation points in which the superficial gas and liquid velocities vary from 0.25 to 3.25 m/s and from 0.50 to 2.25 m/s. They affirmed that there is slug flow in the horizontal section for all tests, but some of them transitioned to a stratified pattern in the downhill section. Unlike Taitel and Barnea (2000), the authors did not observe the formation of dry zones in the top elbow. In concordance with Bendiksen et al. (1996) and Taitel et al. (2000), they concluded that the transition to stratified pattern occurs because the liquid film travels faster than the liquid slug.

Barros et al. (2022) conducted an experimental campaign similar to Alves et al.'s (2019) test loop, however their setup is longer. They also have a horizontal section followed by a downward inclined one, but their lengths are 15 m and 20.6 m. The inclination and diameter are equal to Alves et al. (2019). The ranges of superficial gas and liquid velocities are from 0.3 to 3.0 m/s and from 0.25 to 2.5 m/s. There is slug flow in the horizontal section in all operations points, but in some cases the transition to stratified pattern occurs. The authors described three phenomena in the top elbow and downhill section:

(a) After the elbow, the liquid film is accelerated by gravity. As the film flows faster than the bubble, the liquid slug occupies that film space and modifies

the bubble tail. It results in the slug acceleration as well, and its gradual dissipation along the section.

(b) The top elbow causes the formation of the dry zone for J_G = 0.7 m/s and J_L = 0.3 m/s at -5° and -7° pipe angles, as discussed by Taitel and Barnea (2000). However, the gas plugs quickly disappear in the downhill section.

(c) For cases in which the superficial liquid velocity is higher than the gas, the wave flooding mechanism is observed. They explained that the amount of liquid is higher, resulting in intense gravity effects. For this reason, the bubbles coalescence is interrupted by the entrance of the liquid film in the downstream liquid slug.

Tables 2.1 and 2.2 briefly summarize the experimental and numerical studies discussed in the current section. Table 2.1 shows that the experimental tests are conducted in a pipeline with small inclination changes, the highest one is ±10° (Yin et al., 2018; Yoshida et al., 2000). In oil and gas production flowline-risers with configurations as free-hanging catenary or lazy wave, the angle variation is significantly higher. Therefore, the experimental campaign conducted in this work aims to extend the knowledge to a more complex geometry. Similar to them, the desired parameters are the mean parameters of liquid (L_S) and bubble (L_B) lengths, pressure, bubble (U_T) and slug front velocities and frequency, as well as the statistical distribution of U_T, L_B and L_S.

Table 2.2 reveals the hypotheses considered in the numerical studies presented in the current section. Most of them employed the slug tracking methodology. The Lagrangian approach allows the cell tracking, facilitating the punctual treatment of the hilly terrain phenomena. By considering the slug tracking options, most of them assumed constant film thickness, except for Conte et al. (2011). The liquid slug aeration is considered for all, but some of them neglected the gas compressibility. In addition, it is noted that Zhang et al. (2000) and Sharma et al. (2002) are the only models employed to simulate oil and gas flow. However, both papers assumed constant thermodynamic properties.

For simulation of oil and gas production systems, thermodynamic properties and gas compressibility are essential due to the high pressure gradient. In addition, the flowline-riser normally reaches high pipeline inclination. That is the reason why the accurate modeling

of the bubble profile is very important. Since this work also aims to provide a numerical model to predict the flow through this type of application, the hilly terrain mechanisms are added to Rosa et al.'s (2015) slug tracking model. Their model has a more complete formulation, which is described in detail in Chapter 4. The next subsection will describe some models employed in oil and gas simulation. Their main goal is the usage of the slug flow parameters as input to the dynamic riser analysis.

Table 2.1. Summary of experimental literature review in hilly terrain.

Experimental studies			
Research	Main goals	Pipe angles	Pipeline configuration
Zheng et al. (1995)	(i) Liquid slug length and holdup (ii) Mixture velocity (iii) Flow pattern	-1° to 5°	(i) horizontal-inclined-horizontal (ii) 77.9 mm ID and 420.3 m long (iii) air-kerosene
Yoshida et al. (2000)	(i) Bubble nose velocity (ii) Slug length distribution (iii) Liquid slug and film holdup.	±10°	(i) horizontal-inclined-horizontal (ii) ID: 106 mm/ L: 500 m or ID: 54 mm/ L: 200 m (iii) air or nitrogen/water or kerosene
Zhang et al. (2003)	(i) Liquid slug and cell lengths ratio (ii) Unit cell frequency	±2°	(i) horizontal-inclined-horizontal (ii) 50.8 mm ID and 420 m long (iii) air-mineral oil
Al-safran et al. (2004)	(i) Liquid slug length: mean value, statistic distribution and standard deviation	±2°	Zhang et al.'s (2003) test loop.
Al-Safran et al. (°2005)	(i) Liquid slug: mean and maximum values and distribution data (ii) Unit cell frequency (iii) Slug initiation process	0.915° and 1.93°	Zhang et al.'s (2003) test loop.
Conte et al. (2011)	(i) Liquid slug: mean value and distribution. (ii) Bubble nose velocity and length	3°, 5° and 7°	(i) horizontal-upward inclined (ii) 25.4 mm ID and 4.4 m long (iii) air-water
Yin et al. (2018)	(i) Slug initiation and its influence on the pressure drop, liquid holdup and phase distribution	±10°	(i) horizontal-inclined-horizontal (ii) 40 mm ID and 16 m long (iii) air-water
Alves et al. (2019)	(i) The phenomena observed in the horizontal to downward incline section.	3°, 5° and 7°	(i) horizontal-downward inclined (ii) 26.0 mm ID and 9.14 m long (iii) air-water
Barros et al. (2022)	(i) The phenomena observed in the horizontal to downward incline section.	3°, 5° and 7°	(i) horizontal-downward inclined (ii) 26.0 mm ID and 35.6 m long (iii) air-water

Table 2.2. Summary of hypotheses employed in the numerical studies for hilly terrain.

Numerical studies		
Research	Method	Hypotheses
Zheng et al. (1993)	Mathematical model	(i) Air-water (ii) Unit cell constant in the hilly terrain vicinity (iii) R_S* obtained by Gregory et al.'s (1978) correlation
Zheng et al. (1994)	Slug tracking model	(i) Similar to Zheng et al. (1993) (ii) Film thickness is constant
Taitel and Barnea (2000)	Slug tracking model	(i) Air-water (ii) Film thickness is constant (iii) R_S obtained by Gregory et al.'s (1978) correlation (iv) Compressible Gas
Zhang et al. (2000)	Slug tracking model	(i) Oil-air with constant properties (ii) Liquid slug constant and equal to 30D (iii) R_S obtained by Gregory et al.'s (1978) correlation (iv) Gas incompressibility (v) Liquid film velocity and holdup are constant
Sharma et al. (2002)	Slug tracking model	(i) Nitrogen-water or oil-gas (constant properties) (ii) Film thickness is constant and has a plane interface shape (iii) Liquid slug is aerated (iv) Compressible Gas
Al-safran et al. (2004)	Slug tracking model	(i) Based on Taitel and Barnea's (2000) model
Conte et al. (2011)	Slug tracking model	(i) Air-water (ii) R_S obtained by Andreussi et al.'s (1993) correlation (iii) Bubble profile defined by Taitel and Barnea's (1990) model with plane interface
Yang et al. (2017)	CFD simulation	(i) Methane-water (ii) VOF and k-ε turbulence models (iii) Tests conducted for different diameters, inclination angles and stagnant liquid height
Yin et al. (2018)	CFD simulation	(i) Air-water (ii) VOF and k-ε turbulence models

*R_S is the liquid slug holdup.

2.2 Slug flow modeling: dynamic riser analysis

The prediction and comprehension of slug flow is extremely important to the determination of the parameters that reach the production facilities and the pressure gradient. The number of studies that extends that importance to dynamic riser analyses has been increasing. The slug flow pattern is intermittent in time and space, and this feature intensifies the influence of internal flow on the riser behavior. Patel and Seyed (1989) pointed out that the internal flow exerts three types of forces on the structure: (i) hydrostatic force induced by the fluid weight and the curvature of the pipe, (ii) forces due to the momentum variation and (iii) forces induced by the small Coriolis acceleration. The effects of the latter one are more

significant for high internal velocities (Porter et al., 2023; Vásquez and Avila, 2021; Wang et al., 2018). Ortega Malca (2015) explained that the effective riser tension is the sum of the axial stress (T_w), the external and internal fluid pressures and the liquid and gas momentum:

$$T = T_w - \Delta PA + \sum \dot{m}_k u_k \text{, where } \begin{cases} \Delta PA = P_e A_e - P_i A_i \\ \sum \dot{m}_k u_k = \dot{m}_L u_L + \dot{m}_G u_G \end{cases} . \quad (2.1)$$

Based on Eq. (2.1), the temporal and spatial evolution of the mixture velocity, pressure and fluid weight should be provided as input to structural analyses. Several authors proposed methodologies to determine the required internal flow parameters. Their focus is on the structural analysis; thus, they did not deeply discuss the results of the slug flow modeling. This current section will be limited to the slug flow point of view. There are different methodologies, from the simplest one to the most complex. The following authors presented some of them.

Patel and Seyed (1989), Pollio and Mossa (2009), Bordalo and Morooka (2018) and Vásquez and Avila (2019) employed a sine function to represent the gas and liquid density along the pipe. Patel and Seyed (1989) presented the simplest methodology in which all cells have the same properties along the pipe, regardless of its angle. Vásquez and Avila (2019) used Patel and Seyed's (1989) approach. Pollio and Mossa (2009) included the influence of pipe inclination on the liquid slug length, which is used in the density function. Bordalo and Morooka (2018) proposed that density is a function of the mixture velocity and unit cell frequency. Unlike the other authors, they considered that the mixture velocity is constant in time and uniform in space. Nonetheless, those papers neglected the random flow features and the interaction between neighboring cells. These simplifications directly affect the representativeness of the required parameters.

Ortega Malca (2015) combined a structural and flow modeling. The authors highlighted that both programs have a mutual relation. The internal flow influences the dynamic riser behavior, but the opposite is also true. The hybrid model developed by Kjølås (2007) is used to predict the slug flow parameters. It employed two-fluid and slug tracking models in the bubble and liquid slug regions (Kjeldby et al., 2011), respectively. The slug is non-aerated. To assess their dual program performance, the authors conducted a simulation in a catenary riser (450 m long and 360 mm ID) with mass flow rate of 300 kg/s for the water and 8 kg/s for the

air. It shows that the passage of bubble and liquid slug with different properties directly affects the structural results.

Chatjigeorgiou (2017) proposed a comparison between the structural analysis with and without the slug flow modeling in a catenary riser (2 km long and 0.385 m ID). The internal fluids are 48 °API oil and gas methane. The superficial liquid and gas velocities are 0.4 and 2.0 m/s, respectively. To determine the internal flow, the author combines Taitel and Barnea's (1990) model, mass balances and correlations to predict the following slug flow parameters: the bubble profile (plane interface), bubble translational, dispersed bubble, liquid film and slug velocities, as well as the liquid slug holdup. The cell length is an input data and remains constant along the pipe. In addition, the fluids are incompressible. He concluded that predicting the variation of spatial parameters had a greater influence on the structural analysis than simplified modeling did. For this reason, the author highlighted the importance of developing a slug flow model that also accurately predicts the temporal variation.

Wang et al. (2018) employed Zhang et al.'s (2003b) model to describe the slug flow properties along a horizontal pipe. Zhang et al. (2003b) predicted the flow parameters by applying the mass and momentum equation to the bubble region for the liquid and gas phases. They considered the slug flow is fully developed, the film thickness is constant and the liquid slug holdup and length are obtained by correlation. Wang et al.'s (2018) structural model requires as input data: the gas and liquid mass per unit length and the velocities of each phase. They obtained those data, but they neglected the flow interaction and its randomness.

Ma and Srinil (2020) proposed a study to analyze the influence of flow parameters on the structural analysis of a catenary riser. The cell properties are calculated based on the unit cell concept (Wallis, 1969). Taitel and Barnea's (1990) model is employed to determine the bubble profile and pressure gradient. Mass balances are used to obtain the gas and liquid velocities. Nonetheless, the authors assumed that the cell units are constant along the pipe (same pressure gradient and length), regardless of the pipe inclination. To assess the flow effects, the cells properties are defined considering different values for cell length (L_U), pipe inclination (θ) and bubble translational velocity (U_T). They modify one of those parameters and keep the other ones constant. Based on that analysis, the authors concluded:

(a) U_T has a strong influence on the bubble profile. They pointed out that the assumption of film thickness constant is not representative.

(b) The increase of U_T leads to a lower pressure gradient, and it consequently increases the bottom tension caused by the slug flow (Eq.(2.1)).
(c) If L_U increases with a constant void fraction, the pressure gradient also increases (longer liquid slugs). It reduces the bottom tension (Eq.(2.1)).
(d) The increase of θ leads to a smaller bubble length, and longer liquid slug and cell void fraction. It also reduces the bottom tension (Eq.(2.1)).

Vásquez and Avila (2021) extended their first modeling and employed a more robust methodology to predict the slug flow parameters. They used a slug tracking model based on Rodrigues's (2009) approach. In accordance with Ortega Malca's (2015) statement, the authors added a term to account the influence of riser movement on the internal flow. Their slug tracking model considers the liquid slug is non-aerated, the film thickness is constant along the pipe and equal to equilibrium thickness and the wake effect is null. They validate the structural and flow analysis through a water and air experimental campaign. The test loop is a catenary riser with 28.7 m long and 0.019 m ID. The authors affirmed that their new methodology presented a better agreement compared to Vásquez and Avila (2019). Nonetheless, they highlighted that their simplifications still affect the quality of results.

There also are some studies in the experimental field (Bordalo et al., 2008; Vieiro et al., 2019; Zhu et al., 2021, 2019). However, their goal is not to predict, demonstrate and analyze the flow features. This data is only the input to assess the influence of internal flow on the structural analysis. For this reason, they are not described in detail in this section.

Table 2.3 summarizes the slug flow models employed to define the required parameters used by dynamic riser analysis. Those papers aimed to predict the oil and gas flow, but most of them considered air and water as working fluid. Chatjigeorgiou (2017) and Ma and Srinil (2020) simulated oil and gas, but the thermodynamic properties remain constant. The assumptions of non-aerated liquid slug and constant film thickness are also dominant in those models. Zhu et al.'s (2019) experimental campaign shows the flow randomness is the main cause of the efforts generated by internal flow. However, the majority of them neglected it.

As discussed in Section 2.1, the hilly terrain pipeline modifies the bubble and liquid slug holdups and lengths. It consequently changes the internal fluid weight and the pressure gradient. Most of the papers presented in Table 2.3 employed their model in free-catenary risers, which have variation of pipe orientation (horizontal-upward inclined), and the hilly terrain

phenomena are already present. However, those models do not account for that. Their effects are even more noticeable in lazy wave configurations. The improvements added to Rosa et al.'s (2015) slug tracking model aims to fill those gaps. Therefore, this new approach could be a good alternative to provide the slug flow properties for the structural studies.

Table 2.3. Summary of the slug flow mechanisms considered in the dynamic riser analysis - adapted to Gonçalves and Mazza (2024).

	Slug flow mechanism						
Models	Random along the pipe	Bubble profile	Liquid slug aeration	Bubble wake effect	Oil & gas fluid properties	Pipeline inclination effect	Hilly terrain effects
Patel and Seyed (1989)	-	-	-	-	-	-	-
Pollio and Mossa (2009)	-	-	-	-	-	X	-
Ortega Malca (2015)	X	X	-	-	-	X	-
Chatjigeorgiou (2017)	-	X	X	-	X	X	-
Bordalo and Morooka (2018)	-	-	-	-	-	-	-
Wang et al. (2018)	-	-	X	-	-	X	-
Ma and Srinil (2020)	-	X	X	-	X	X	-
Vásquez and Avila (2019)	-	-	-	-	-	-	-
Vásquez and Avila (2021)	X	-	-	-	-	X	-

3 EXPERIMENTAL APPARATUS

This chapter covers all aspects related to the experimental campaign setup. Section 3.1 describes the setup equipment: water and gas injection lines and instruments. Section 3.2 presents the procedure of data post-processing and the uncertainty of the slug flow parameters obtained from that. In addition, Section 3.3 presents the pressure gradient analysis for the liquid flow to validate the experimental measurements. Finally, Sections 3.4 and 3.5 present the steps to obtain the flow parameters and images.

3.1 Description of experimental setup

The experimental setup is at Flow&Rs Lab (Flow and Research Laboratory) in Centro de Estudos de Energia e Petróleo (CEPETRO) located at Universidade Estadual de Campinas (UNICAMP). The building has a 40-meter tower (with 10 floors) where vertical flow studies are developed – see Figure 3.1.

Figure 3.1. Flow&Rs Lab building.

This study uses the vertical tower for water recirculation and water-air separation only. The focus is on predicting the flow parameters through the S curve of the Steel Lazy Wave Riser (SLWR). The installed riser represents an actual Pre-Salt riser in laboratory scale. Figure 3.2 (a) shows the two experimental setup pipelines: one in stainless steel and the other in Plexiglas. Both lines share the same mixer and length, 50 m long and 30 m high from the injector. The experimental test focuses on the S curve, which is 18 m long. The total length and height are essential for the numerical simulation since the model must consider the pressure at the end of the pipe. The air and water were injected through a Y-type mixer, as shown in Figure 3.2 (c). Figure 3.2 (b) shows the manifold used to choose between stainless and Plexiglas lines. Their inner diameters are 23.4 mm and 24 mm, respectively.

Both lines have an identical geometry and are fixed to the base structure. The horizontal distance from the flow mixer to the riser basis is 6.44 m (275D). The S curve has three different radius of curvature: 2.952 mm, 1.137 mm and 1.987 mm. This shape creates a test loop with three pipe orientations: horizontal, upward and downward inclined. The inclined section presents a gradual pipeline inclination change. The first upward, downward and second upward inclined sections reach approximately 55°, - 43° and 60°.

The experimental campaign covers both lines, but their applications are different. The acrylic pipe is employed to make a high-speed movie at some S curve positions, while the stainless steel pipe is used to measure the desired data. However, these lines share the same water and air injection, measurement and separation facilities. Figure 3.3 presents the facilities and measuring station position at the stainless-steel tube.

As shown in Figure 3.3, the stainless pipe has 10 measuring stations along the S curve. The first station is at the horizontal section (S1), and the second (S2) and third (S3) are at the upward-inclined section. The following three stations are in the A format line section: S4 and S6 are at the upward and downward part and S5 at the inflection point (top of the curve). The seventh (S7) station is at the downward inclined section, and the eighth (S8) is at the lower point of the curve (V format). The ninth (S9) and tenth (S10) stations are at the upward inclined section. The distance from air-water mixer to these stations are 6.44 m (275D), 7.56 m (323D), 9.25 m (395D), 10.94 m (467D), 11.81 m (505D), 12.69 m (542D), 13.79 m (589D), 14.90 m (637D), 16.00 m (684D), e 17.11 m (731D). All ten stations have pressure transducers

and two impedance sensors. The following subsections describe the instruments on the S curve and the water and air injections.

(a)

(b)

(c)

Figure 3.2. Experimental setup: (a) mainline view, (b) manifold and (c) flow mixer.

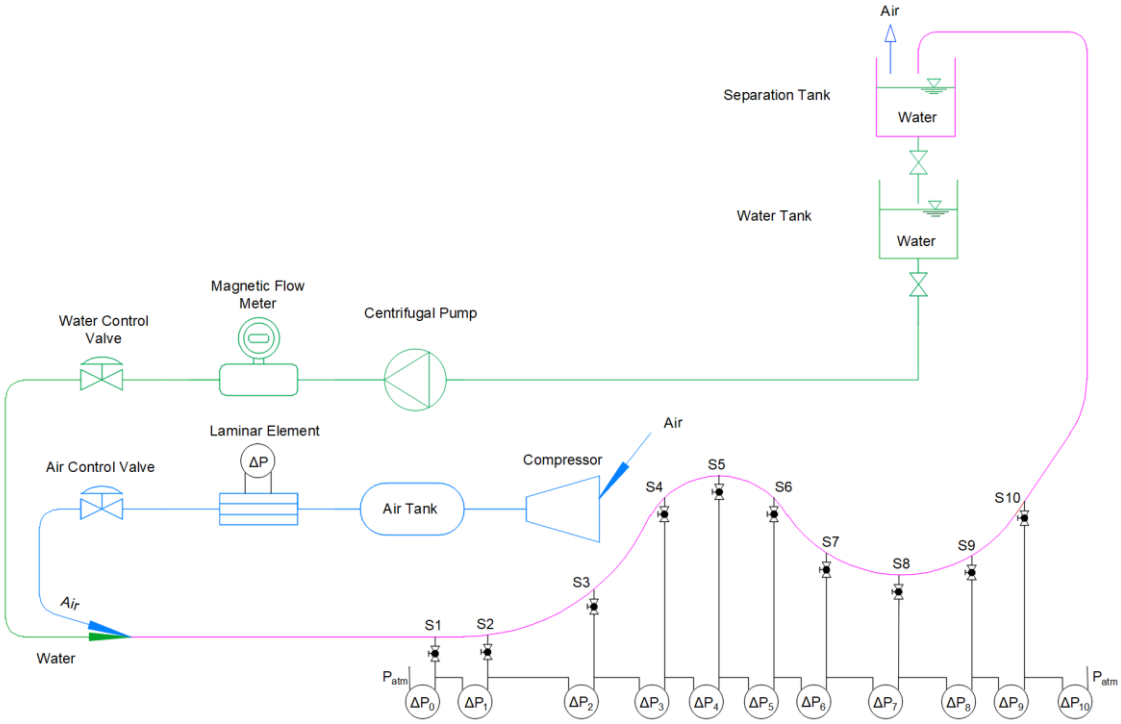

Figure 3.3. Schematic of experimental system: injection, measurement and separation facilities.

3.1.1 Instruments positioned on the S curve

Figure 3.4 shows the eleven pressure transducers employed at the lazy wave riser. The first and last stations are equipped with an absolute pressure transducer (P0 and P10), and nine differential sensors measure the pressure difference between two consecutive stations. Table 3.1 describes the sensors model and their location and accuracy.

Figure 3.4. Absolute and differential pressure transducers along the lazy wave riser.

As demonstrated in Figure 3.4, all pressure sensors are positioned on the same level. This strategy aims to facilitate the hydrostatic column determination between the pressure tap and the sensor inlet. These parameters must be disregarded in the post-processing of pressure data. Two methods are employed to determine them: (1) the differential pressure measured by the sensor when the pipeline is empty, and (2) the pressure by measuring the height between

the pressure tap and sensor inlet. The results of both methodologies are compared, as shown in Table 3.2.

Table 3.1. Range and accuracy of the pressure transducers.

Equipment	Location	Range [kPa]	Accuracy
Rosemount 2051-CD4	S1 e S11	0 a 600	0.065% of the span
Rosemount 2051-CD1	S2	-6 a 6	0.1% of the span
Rosemount 3051	S3, S4, S5, S6, S7, S8, S9 e S10	-62 e 62	0.04% of the span

As demonstrated in Table 3.2, both methods have similar results. The total uncertainty of the second methodology is the sum of the uncertainties on the determination of water density, gravity, height, and the radius of curvature (capillary effect). In addition, using a unique reference position for all sensors can also influence the results of Method 2. For this reason, the post-processing uses the results obtained by Method 1.

Table 3.2. Differential pressure [kPa] generated by the height difference between stations.

	Method 1*	Method 2*
ΔP_0	2.16 ± 0.39	1.89 ± 0.06
ΔP_1	-0.23 ±0.01	-0.23 ±0.01
ΔP_2	-7.07 ±0.05	-7.07 ±0.21
ΔP_3	-13.60 ±0.05	-13.59 ±0.41
ΔP_4	-3.09 ±0.05	-3.05 ±0.09
ΔP_5	2.86 ±0.05	2.91 ±0.09
ΔP_6	5.91 ±0.05	5.84 ±0.18
ΔP_7	3.70 ±0.05	4.08 ±0.12
ΔP_8	-1.71 ±0.05	-1.52 ±0.05
ΔP_9	-7.10 ±0.05	-6.91 ±0.21
ΔP_{10}	23.29 ±0.39	21.80 ±0.66

*Method 1: differential pressure measured by instruments, Table 3.1 shows their accuracy. Method 2: differential pressure calculated by height differences between stations with an uncertainty of 4%.

As illustrated in Figure 3.5, each station has two impedance sensors spaced 110.8 mm. Figure 3.5 also shows that the first sensor is positioned before the pressure tap and the second one after it. These sensors are in-house instruments described by Rosa et al. (2010) in detail. Briefly, the sensor has a vertical rod that captures the electrical properties of the flowing fluids. Based on the electrical conductivity of the fluid, the sensor transmits an analog signal with a 4-20 mA (current loop or digital enlace) to the acquisition or supervisory systems. Thus, the sensor is calibrated to detect the minor (air) and higher (water) fluid conductivity.

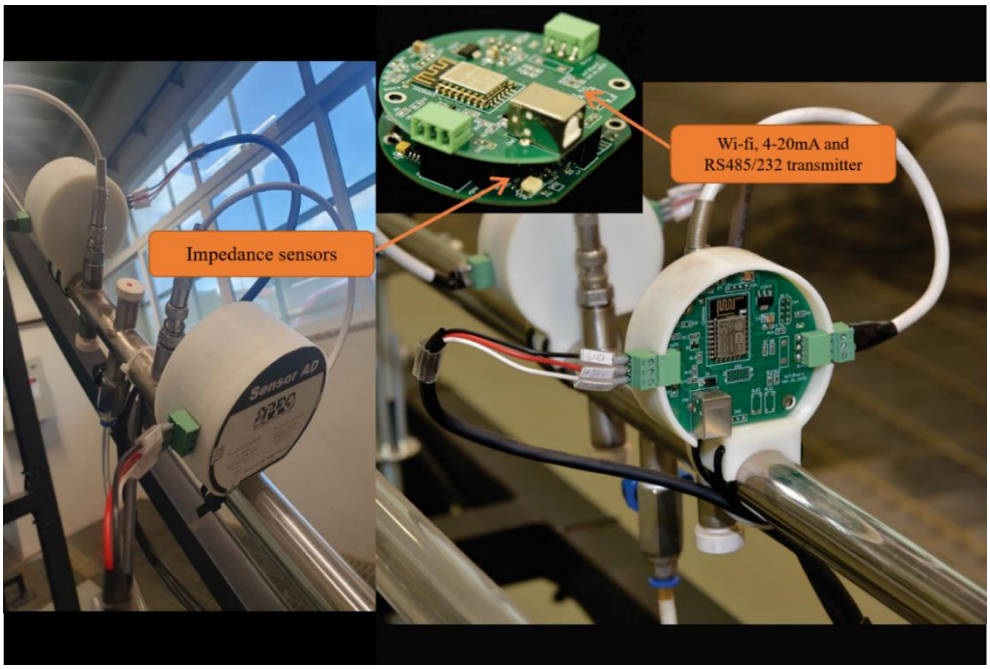

Figure 3.5. Impedance sensor axially spaced for 110.8 mm.

The analog signal does not have a linear relationship with the cross-section void fraction. Thus, it is not able to evaluate the bubble void fraction or the liquid film thickness. The main objective of this sensor is to detect the bubble and liquid slug front. Then, a post-processing procedure has to be applied to determine all the desired slug flow parameters:

a. Translational bubble velocity [U_T].
b. Liquid slug front velocity [dx^j/dy].
c. Bubble [L_B] and liquid slug [L_S] lengths.
d. Cell frequency [f].
e. Bubble overtaking rate.

All pressure and impedance data are sampled at 3 kHz using a data acquisition (DAQ) system from National Instruments (NI), model NI CDAQ-9188 and NI C9203, which has 16-bit resolution.

3.1.2 Water injection line

As illustrated in Figure 3.3, the water injection system is a closed circuit. The pump, flow meter and pneumatic valve are on the ground floor. The water supply tanks and separation are on the sixth and eighth floors. The cycle starts from the tank that supplies the water pump. This tank is connected to the suction of a centrifugal pump KSB MCPK-40-25-160 CC, demonstrated in Figure 3.6 (a). Its maximum pump head and flow rate are 50.8 m.w.c and 8.48 m^3/h.

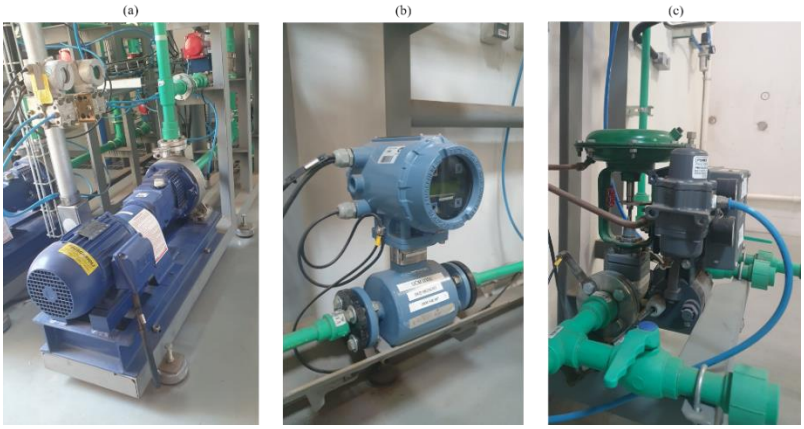

Figure 3.6. (a) Centrifugal pump, (b) water flow meter and (c) pneumatic globe valve.

In sequence, a magnetic flow meter and a pneumatic globe valve are used to measure the volumetric flow rate. Figure 3.6 (b) and (c) show both equipment and Table 3.3 describes them. After this valve, the water flows on the entire lazy wave line and is discharged into a gravity separator tank with 950 L of capacity. Then, the water returns to the storage tank, and the air vents into the atmosphere. The desired water volumetric flow rate is obtained through a frequency inverter and pneumatic globe valve opening.

Table 3.3. Range and accuracy of the water injection line equipment.

Equipment	Brand	Model	Range	Accuracy
Magnetic flow meter	Emerson	Rosemount® 8750W	$3x10^{-4}$ to $3.1x10^{-3}$ m^3/s	±0.5% of the flow rate
Pneumatic globe valve	Emerson	24000CVF	-	-

3.1.3 Air injection line

As shown in Figure 3.3, the gas injection line is supplied by a Chicago Pneumatic screw compressor. Its maximum pressure is 12.5 bar. Merian laminar flow element (LFE), model LFE 50MJ10-9, measures the air mass flow rate. To evaluate the air volumetric flow rate, the laminator element must be combined with other instruments, such as a differential

pressure transducer, a temperature transmitter, and a barometer. Figure 3.7 presents the Meriam LFE, and Table 3.4 describes all those instruments. The air mass flow rate is manually controlled using a JELPC mechanical air pressure regulator model BRF 4000 and a Swagelok needle valve.

Figure 3.7. Meriam Laminar Element.

Table 3.4. Range and accuracy of the air injection line instruments.

Equipment	Brand	Model	Range	Accuracy
Laminar Flow Element (LFE)	Meriam	50MJ10	2.25×10^{-4} to 1.59×10^{-3} m^3/s	±0.8% of the flow rate
Pressure transducer	Emerson	Rosemount 2051	0 to 1200 kPa	0.065% of the span
Temperature transmitter	Hart	Smar TT301	0 to 60 °C	±0.2 °C
Barometer	Zürich	Z.10	0 to 101.3 kPa	0.1% of the span

3.1.4 Supervisory system

A LabVIEW program was employed to collect the data obtained from the impedance sensors and pressure transducers, named "*Adquiri* Lazy Wave". This program has four main applications: (i) to visualize the measured signals and the flow information in real-time, (ii) to define the acquisition time and record desired parameters, (iii) to determine the range of pressure transducers (see Table 3.1) and (iv) to convert the electrical signal obtained by these instruments in pressure unit.

Figure 3.8 shows the initial program window, where activities (i) and (ii) are performed. On the left side, two other buttons to execute the activities are (iii) and (iv). The graphical interface presents the raw data (electric current) obtained by the NI system for impedance sensors. Pressure data is shown in the engineering unit on the right side. Based on the initial window, the user tracks real-time parameters such as superficial liquid velocity, superficial gas velocity at the laminator element and first station (S1) and the gas

thermodynamic properties. This program also records the atmosphere pressure, pressure and temperature at the laminator element, liquid volumetric flow rate and air mass flow rate. These data are sampled directly from a HiTecnologia PLC system.

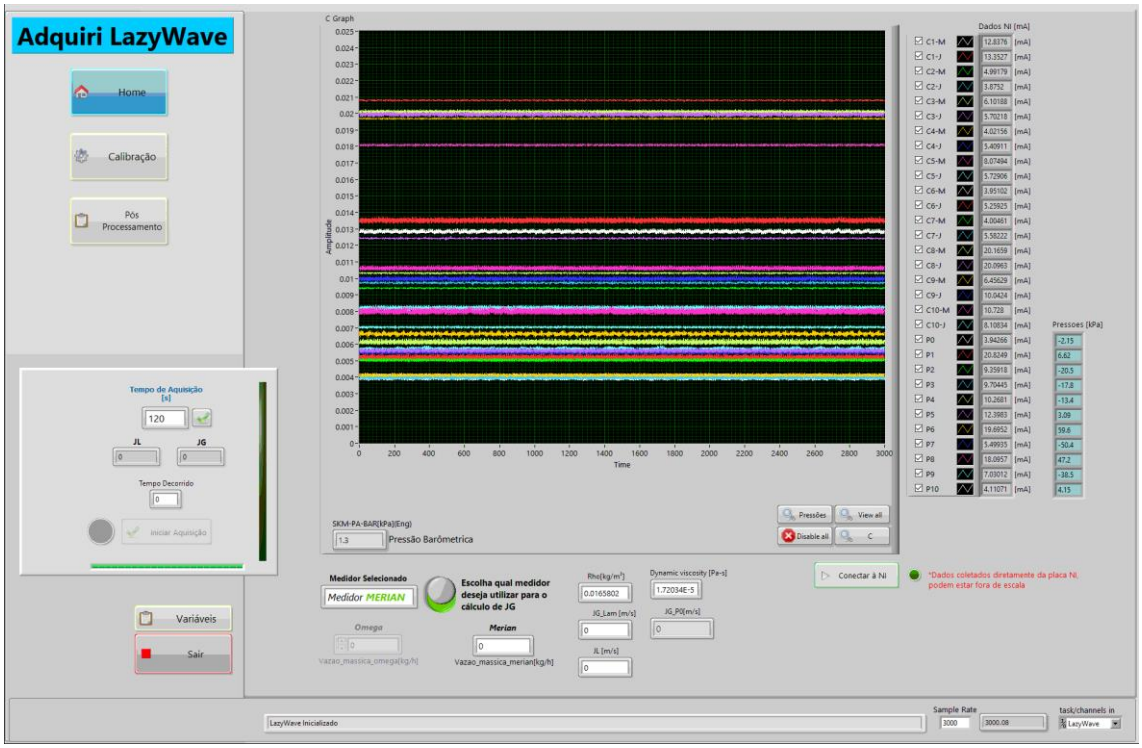

Figure 3.8. *Adquiri* Lazy Wave program.

As demonstrated in Figure 3.9, a LabVIEW supervisory system controls the experimental test loop (equipment and valves). This program determines the desired operation condition. On the upper side of the program window, two flags highlight the communication status between the supervisory and the CLP. Establishing that communication is the first step to initiating the line startup procedure.

Figure 3.9 also illustrates the equipment described in Sections 3.1.2 and 3.1.3 and the valves used to control the air-water flow. On the bottom side of the program window, the pump rotation and valve opening are changed to achieve the desired water flow condition. In the center of the window, there is the air pipeline. The mass flow rate is manually changed and tracked on the supervisory. Since the gas injection influences the system's operation, the needed changes are performed to achieve the superficial gas and liquid velocities expected on the first station (S1).

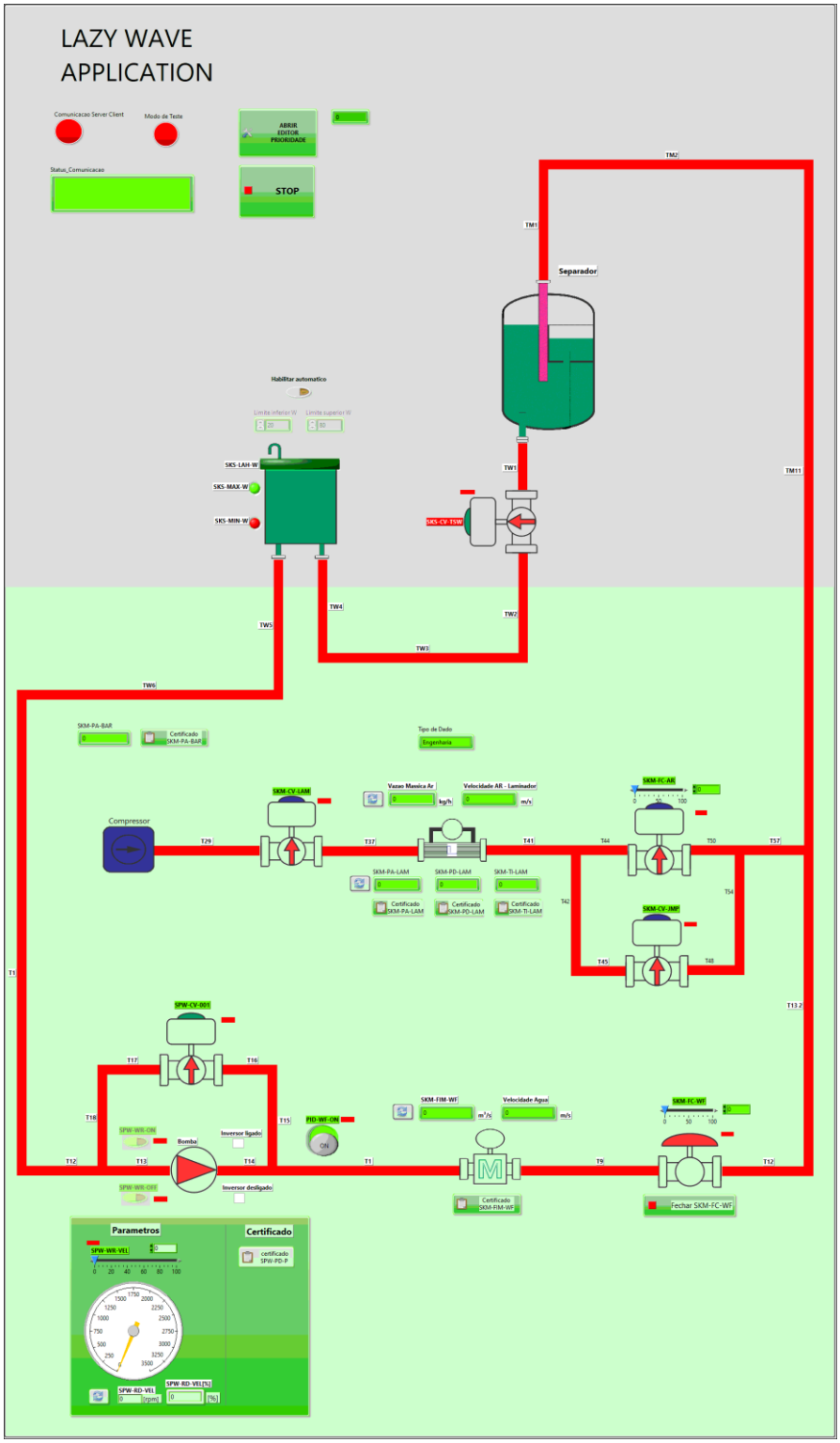

Figure 3.9. Supervisory controls equipment and valves used by the test loop.

3.2 Data processing and uncertainty

As reported above, the data from 11 pressure transducers and 20 impedance sensors are recorded. However, that data must be processed to allow the flow analysis along the lazy

wave riser. In addition, the pressure and temperature at the laminator element, air mass flow rate, liquid superficial velocity and atmosphere pressure are saved during the test.

The post-processing program has been developed in-house. It has already been utilized in many studies such as Duarte (2007), Bueno (2010), Bressani (2016), Dalla Maria (2016) and Maidana (2017). It had the limitation of four measuring stations, but it was adapted to the present study (with 10 stations) and rewritten in Python language. The data processing is divided into four steps: (i) to filter and binarize the data to identify the bubble and slug passage, (ii) to calculate the cell properties, (iii) to evaluate the pressure along the elongated bubble and (iv) to reconstitute the pressure in each station.

Steps (i), (ii) and (iii) depend on the data obtained for both impedance sensors in each station. As reported in Section 3.1.1, the raw data can span between 4-20mA. However, the signal can have a smaller span due to liquid or void fractions over the cross-sectional area. The data presents a substantial variability due to the randomness of the bubble and liquid slug parameters (liquid film thickness, liquid slug holdup and bubble and liquid slug length). For this reason, the new program version applies a low pass filter on the impedance sensor data. In addition, the program uses a function to calculate the cross-correlation between the two impedance sensors (Figueiredo, 2020).

The slug flow properties are evaluated based on the movement time of bubble and liquid slug fronts between both impedance sensors. Figure 3.10 illustrates the time based on the binary signal. The post-processing program applies filters to select unit cells that meet the requirements. Duarte (2007) discussed these filters in detail.

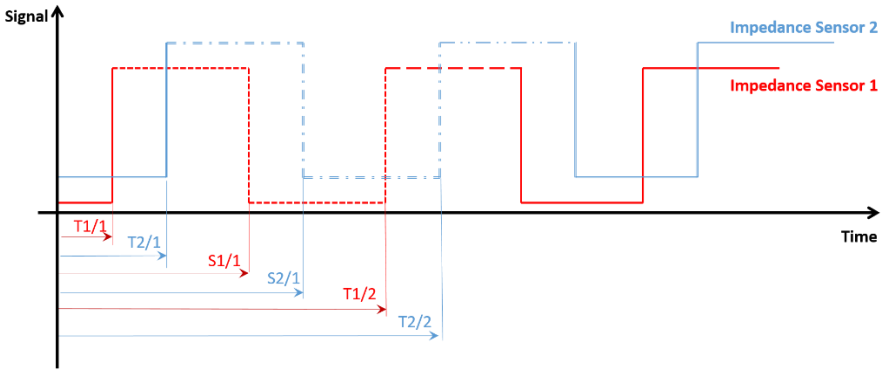

Figure 3.10. Schematic of the binary signal of the two impedance sensors, downstream (1) and upstream (2) of the pressure tap.

Based on the square wave presented in Figure 3.10, the traveling time of the bubble and liquid slug front between the impedance sensors are:

$$\Delta t_B = t_{S2/1} - t_{S1/1} \,, \tag{3.1}$$

$$\Delta t_S = t_{T2/1} - t_{T1/1} \,. \tag{3.2}$$

As sensors distance $\left(d_{D-U}\right)$ is known, the translational bubble and liquid slug front velocities are:

$$U_T = \frac{d_{D-U}}{\Delta t_B} \,, \tag{3.3}$$

$$\frac{dx^j}{dt} = V_S = \frac{d_{D-U}}{\Delta t_S} \,. \tag{3.4}$$

The bubble and liquid lengths depend on how long the flow structures travel through the sensor. Bressani (2016) mentioned that time is calculated based on the upstream sensor data. Thus, L_B and L_S are:

$$L_B = U_T \cdot t_b = U_T \cdot \left[t_{T2/2} - t_{S2/1}\right] \,, \tag{3.5}$$

$$L_S = V_S \cdot t_s = V_S \cdot \left[t_{S2/1} - t_{T2/1}\right] \,. \tag{3.6}$$

The cell frequency is:

$$f = \frac{1}{t_U} = \frac{1}{t_B + t_S} \,. \tag{3.7}$$

The passage time also influences the determination of the pressure in the bubble region. Since the pressure tap is equally distant from impedance sensors and U_T has already been calculated, the bubble pressure can be tracked during its passage through the sensor. Thus, the program estimates the average pressure for each elongated bubble.

Step (iv) aims to reconstitute the pressure based on the first absolute sensor and the subsequent differential pressure transducers. The hydrostatic pressure presented in Section 3.1.1 and Table 3.2 must be disregarded for each station, as demonstrated in Eq. (3.8). The last absolute pressure sensor can be used to validate this procedure.

$$
\begin{aligned}
P_0 &= \Delta P_{0-atm} + P_{atm} - \left[\Delta P_H\right]^{S_1}, \\
P_1 &= P_0 + \Delta P_{0-1} - \left[\Delta P_H\right]^{S_2}, \\
P_2 &= P_1 + \Delta P_{1-2} - \left[\Delta P_H\right]^{S_3}, \\
P_3 &= P_2 + \Delta P_{2-3} - \left[\Delta P_H\right]^{S_4}, \\
P_4 &= P_3 + \Delta P_{3-4} - \left[\Delta P_H\right]^{S_5}, \\
P_5 &= P_4 + \Delta P_{4-5} - \left[\Delta P_H\right]^{S_6}, \quad , \\
P_6 &= P_5 + \Delta P_{5-6} - \left[\Delta P_H\right]^{S_7}, \\
P_7 &= P_6 + \Delta P_{6-7} - \left[\Delta P_H\right]^{S_8}, \\
P_8 &= P_7 + \Delta P_{7-8} - \left[\Delta P_H\right]^{S_9}, \\
P_9 &= P_8 + \Delta P_{8-9} - \left[\Delta P_H\right]^{S_{10}}, \\
P_{10} &= \Delta P_{9-atm} + P_{atm} - \left[\Delta P_H\right]^{S_{10}}
\end{aligned}
\tag{3.8}
$$

where ΔP is the differential pressure measured by the transducer, ΔP_H the pressure calculated by Method 1 (see Table 3.2), P_{atm} is the atmospheric pressure. The subscripts refer to the measuring station number (see Figure 3.3)

Lastly, Table 3.5 shows the uncertainty of slug flow parameters calculated by the post-processing program. Table 3.5 demonstrates the propagation of uncertainty for pressure and superficial gas velocities. The pressure has a growing uncertainty profile because of the procedure described in Eq. (3.8). The superficial gas velocity is a function of pressure and has the same behavior. APPENDIX A presents the uncertainty analysis.

Table 3.5. Uncertainty of experimental properties.

Flow properties	Symbol	Uncertainty [%]
Translation bubble velocity	U_T	0.06
Liquid slug front velocity	V_S	0.06
Bubble length	L_B/D	0.22
Liquid slug length	L_S/D	0.22
Slug frequency	f	0.05
Superficial liquid velocity	J_L	0.39
Absolute pressure at S1	P_0	3.27
Pressure at S2	P_1	3.28
Pressure at S3	P_2	3.79

Pressure at S4	P_3	4.24
Pressure at S5	P_4	4.64
Pressure at S6	P_5	5.02
Pressure at S7	P_6	5.36
Pressure at S8	P_7	5.69
Pressure at S9	P_8	6.00
Pressure at S10	P_9	6.29
Absolute pressure at S10	P_{10}	3.27
Superficial gas velocity at S1	J_{G1}	3.38
Superficial gas velocity at S2	J_{G2}	3.39
Superficial gas velocity at S3	J_{G3}	3.88
Superficial gas velocity at S4	J_{G4}	4.32
Superficial gas velocity at S5	J_{G5}	4.72
Superficial gas velocity at S6	J_{G6}	5.09
Superficial gas velocity at S7	J_{G7}	5.43
Superficial gas velocity at S8	J_{G8}	5.75
Superficial gas velocity at S9	J_{G9}	6.06
Superficial gas velocity at S10	J_{G10}	6.35

3.3 Validation: liquid flow

The test loop commissioning was conducted by using a liquid monophase flow. The objective was the validation of the differential pressure measured by transducers. Gravitational and wall shear stress terms mainly cause the pressure drop (ΔP). The centrifugal force is neglected. However, similar to Eq.(3.8), the hydrostatic pressure must be disregarded as:

$$\Delta P_{sensor} = -\Delta P_{grav} - \Delta P_{wallshear} - \Delta P_{hydrostatic} \ . \tag{3.9}$$

For water flow, the gravitational term is equal to the hydrostatic column. Figure 3.11 illustrates this similarity since the density (ρ) and height (h) are the same for both lines. Thus, the measured pressure is given by the wall shear stress term only.

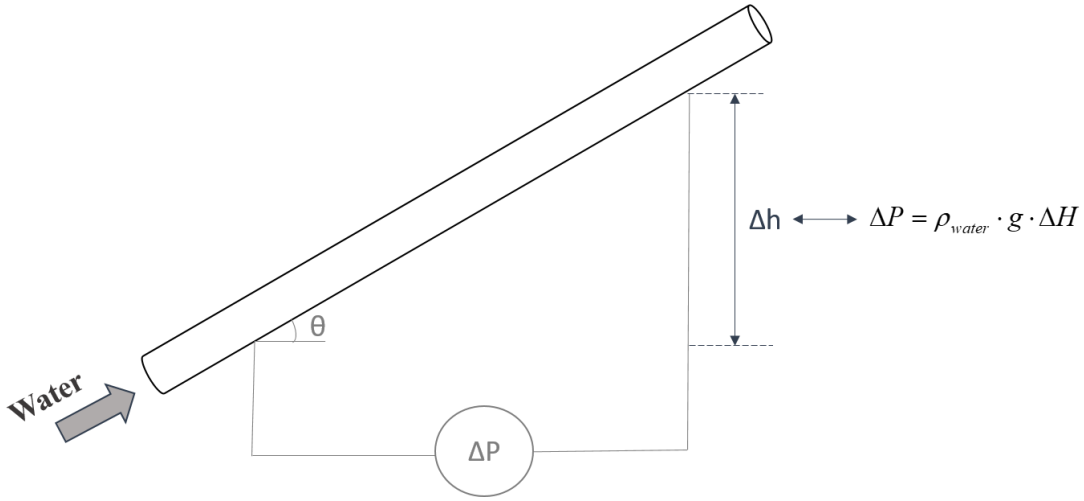

Figure 3.11. Schematic of the relation between hydrostatic column, gravitational effect and wall shear force on liquid flow.

Based on the above assumption, the experimental friction factor (C_f) can be calculated from each measured differential pressure (ΔP) as:

$$C_f = \frac{\Delta P 2D}{L \rho_L J_L^{\,2}} \ . \tag{3.10}$$

By comparing that parameter with the result of a renowned friction factor correlation, the representativeness of pressure measurement is guaranteed. This study applies Swamee and Jain's (1976) correlation:

$$C_f = \left[\left(\frac{64}{\mathrm{Re}} \right)^8 + 9{,}5 \cdot \left[\ln\left(\frac{\varepsilon/D}{3.7} + \frac{5.74}{\mathrm{Re}^{0.9}} \right) - \left(\frac{2500}{\mathrm{Re}} \right)^6 \right]^{-16} \right]^{\frac{1}{8}} , \tag{3.11}$$

where Re is the Reynolds number of the liquid phase.

Five single-phase tests were conducted with water as a working fluid. The superficial liquid velocities are 0.39, 0.95, 1.4, 2.0 and 2.7 m/s, respectively named Case 1, 2, 3, 4 and 5. For each test, the data acquisition takes 120 seconds and repeats twice. The acquisition frequency is 3 kHz. It considers the pipe roughness to be 0.07 mm. The maximum uncertainties of friction factor through experimental data and correlation are 12.8% and 18%, respectively.

Figure 3.12 compares the experimental (Eq.(3.10)) and theoretical (Eq.(3.11)) friction factors. The minimum relative error is 3% for Case 2. Cases 1, 3 and 4 have relative

errors lower than 10%. The last case has a relative error equal to 12.8%. Thus, all cases agree well with the Swamee and Jain's (1976) correlation.

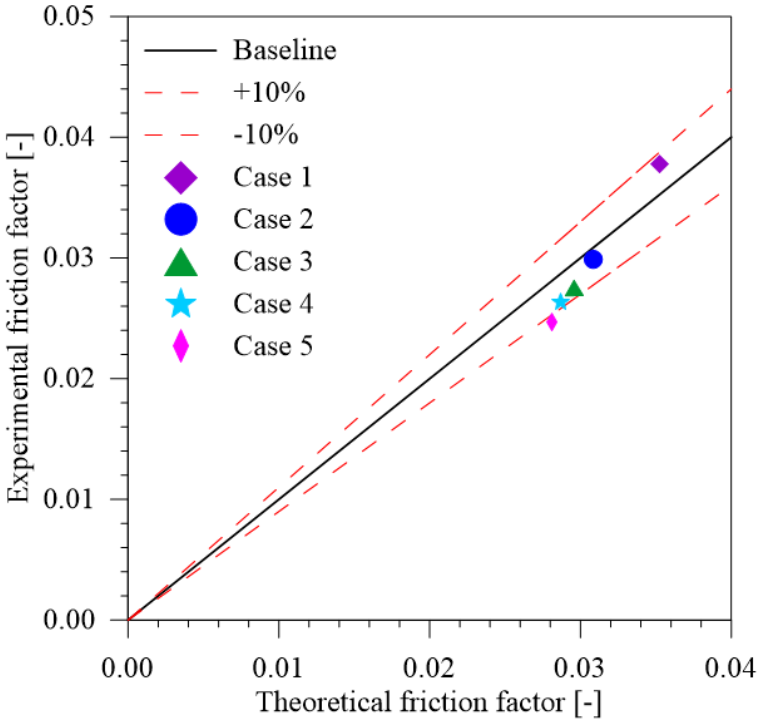

Figure 3.12. Comparison between the experimental and theoretical friction factor for water flow along the S curve.

In addition, a second analysis aims to validate the procedure of pressure reconstitution based on Eq. (3.8). Table 3.6 presents the pressure evolution along the SLWR riser based on the value measured by each differential transducer. The reconstituted pressure at S9 is compared with the last absolute pressure sensor. Figure 3.12 and Table 3.6 show that relative errors are proportional to the superficial liquid velocity. Nonetheless, all cases present a relative error of less than 5%. This error is smaller than the uncertainty of the pressure sensor at S9.

Table 3.6. Pressure reconstitution in each differential transducer for single-phase flow tests.

[kPa]	Case 1	Case 2	Case 3	Case 4	Case 5
P_0	439.81	448.36	471.95	517.57	583.13
P_1	439.45	447.46	470.35	514.65	578.27
P_2	432.17	439.45	461.42	503.97	565.06
P_3	418.37	424.92	445.96	486.76	545.39
P_4	415.28	421.82	442.87	483.67	542.30
P_5	418.14	424.68	445.72	486.53	545.15

P_6	424.05	430.59	451.64	492.44	551.07
P_7	427.75	434.29	455.34	496.14	554.77
P_8	426.04	432.58	453.63	494.43	553.06
P_9	418.94	425.49	446.53	487.33	545.96
P_{10}	418.45	422.20	439.71	473.78	522.59
Relative error [P_9-P_{10}]	0.12%	0.78%	1.55%	2.86%	4.47%

3.4 Experimental procedure: data acquisition

The experimental campaign performs six tests on the stainless steel pipe and three tests on the acrylic tube. Table 3.7 shows the test grid has two different mixture velocities (2 and 4 m/s). Different gas fractions are also proposed to verify their influence on the flow behavior along the riser.

Table 3.7. Experimental test grid.

	J_L [m/s]	J_G^{S1} [m/s]	U_M [m/s]	J_G/J_L [-]
Test 1	1.33	0.67	2.00	0.50
Test 2	1.20	0.80	2.00	0.67
Test 3	1.00	1.00	2.00	1.00
Test 4	0.80	1.20	2.00	1.50
Test 5	2.00	2.00	4.00	1.00
Test 6	1.60	2.40	4.00	1.50

The choice for those mixture velocities has two main goals: to cover proper velocities in the oil and gas industry and to encounter a slug flow regime in most parts of the S curve. The flow regime map was analyzed by the Drift-Flux model presented by Santim et al. (2020). This analysis expects the presence of a stratified pattern on the downward section for cases with a mixture velocity equal to 2 m/s.

The tests were carried out on the stainless steel pipe, and all instruments were applied, as presented in Section 3.1.1. The data acquisition takes 120 seconds and is repeated six times. The acquisition frequency is 3 kHz. The procedure has three steps: (i) determination of the operation point through the supervisory system (Section 3.1.4), (ii) waiting for the startup effects to fade away, and (iii) starting the data acquisition.

3.5 Experimental procedure: image acquisition

The acquisition of flow images is more complex due to the pipeline geometry and the positions of interest along the curve. Thus, the acquisition is limited to Tests 1, 4 and 5. This choice aims to cover two mixture velocities (2 and 4 m/s) and three different gas and liquid superficial velocities ratios (0.5, 1.0 and 1.5). To capture the influence of geometry on the flow parameters, this study captures the images in six pipe sections with approximately 28 cm extension. Each one is described in detail below:

i. The position coincides with the first station [S1], approximately 6.44 m from the mixer: horizontal section. These images aim to identify a slug flow pattern and verify the bubble and liquid slug features.
ii. The position coincides with the third station [S3], approximately 7.6 m from the mixer: an upward inclined section closes to 43°. These images aim to observe any change in the interface bubble region (plane or concentric).
iii. Position between the fourth and fifth stations [S4-S5], approximately 11.4 m from the mixer: Near the highest point of the S curve, the angle is about 18°. These images aim to identify phenomena that have been already described in the literature for hilly terrain – A format (Figure 2.1): (a) liquid slug dissipation and (b) decrease in liquid film thickness or generation of gas plugs ($R_f = 0$).
iv. Position between the sixth and seventh stations [S6-S7], approximately 13.2 m from the mixer: Downward inclined section, close to - 40°. These images aim to verify potential flow behavior changes, such as the transition for stratified flow or the alteration of the elongated bubble interface (plane or concentric).
v. Position coincides with the eighth station [E8], approximately 14.9 m from the mixer: The lowest point of the S curve. These images aim to identify phenomena that have already been described in the literature for hilly terrain – V format (Figure 2.1): (a) increase in liquid slug length or (b) unit cell generation. In addition, this section is essential to realize which flow pattern is present.
vi. Position coincides with the ninth station [E9], approximately 16 m from the mixer: An upward inclined section, close to 26°. These images aim to visualize the flow behavior after the hilly terrain (flow pattern and features).

The high-speed filming was made with a MotionXtra N3 camera. Its maximum resolution is 1280x1024, using 1000 frames per second. A Nikon AF NIKKOR 50 mm f/1.8D lens was also used. The camera configuration remained the same, regardless of the pipe position. The acquisition frequency is 2000 frames per second, with an aperture of f/4.0 and an exposure time of 70 µs. In addition, an LED panel with continuous lighting was employed.

The supervisory system adjusts the gas and liquid velocities (Section 3.1.4). The acrylic tube has a manometer pressure sensor to guarantee the repeatability of gas superficial velocity at S1 (Table 3.7). Its position coincides with the first station in the stainless steel pipe. Four recordings were carried out for each operational point and position. The post-processing was conducted using a program written in Wolfram Mathematica software. The short movies created through each recording and tests are available on the laboratory channel on YouTube (https://www.youtube.com/playlist?list=PL1MP4hf_uV1gJ8Eti12HEI9V4L-BFE0vE).

4 NUMERICAL MODEL

This chapter explains the numerical model employed in this work and the improvements added to it. First section briefly presents Rosa et al.'s (2015) slug tracking equations. In addition, it describes the closure laws and the numerical method. Due to the geometry complexity of a lazy wave riser, some modifications were done in the original model, such as: (i) insertion of submodels to predict the properties along the hilly terrain, (ii) modification of initial and boundary conditions, (iii) insertion of a Black-Oil model to determine the oil and gas properties. Sections 4.2, 4.3 and 4.4 describe the three approaches, respectively. Lastly, Section 4.5 presents the current program logic and the submodels interaction.

4.1 Slug tracking model

Slug tracking model is a Lagrangian methodology employed to track the unit cell, predicting their evolution and interactions with neighboring cells along the pipeline. Due to this feature, the model is able to predict the temporal and spatial variation of the slug flow parameters, as well as their mean values and statistical distributions. Barnea and Taitel (1993) developed the first model. Since then, many authors proposed new slug tracking models, which incorporate new mechanisms such as gas compressibility, liquid slug aeration, bubble profile, hilly terrain and wake effects. Besides the slug tracking models cited in Chapter 2, Grenier (1997), Franklin (2004), Rodrigues (2009), Rosa et al. (2015) and Padrino et al. (2023) are other examples.

As demonstrated in Table 2.3, the latest models aim to simulate the oil and gas production systems, but they still have some limitations related to the influence of the pipeline geometry on the flow parameters. This work aims to fill those gaps. For this purpose, new submodels are added to Rosa et al.'s (2015) slug tracking model. It has already considered all previously cited mechanisms, and it is applied to horizontal and inclined pipelines. An additional benefit is that their model considers the advection term in the liquid slug momentum and the phases momentum fluxes through the control volume boundaries. These terms capture the liquid slug acceleration, resulting in the bubble compression or expansion along the pipe (similar to the mass–dashpot–spring system).

Rosa et al. (2015) developed their model based on the mass and momentum equations applied to a control volume that encompasses the bubble and liquid slug (the j^{th} unit cell). Figure 4.1 illustrates it. This figure also shows the main properties correlated to the flow. The pipeline has length L, inner diameter D, inclination θ, cross section area A, and roughness ε. This line is filled with a succession of unit cells, exchanging mass and moment. Each cell has its own void fraction (α_U) and length (L_U). This length is the sum of the bubble (L_B) and liquid slug (L_S) lengths. At a particular moment, the elongated bubble parameters are the gas pressure (P_G), liquid holdup (R_f), void fraction (α_f), liquid film thickness (h_f) and the bubble nose (U_T), film (U_f) and gas (U_G) velocities. The liquid slug properties are the liquid holdup (R_S), void fraction (α_S) and the dispersed bubble (U_b) and liquid (U_S) velocities. In addition, the density and viscosity of gas and liquid are named ρ_G, ρ_L, μ_G and μ_L. The surface tension between the phases is defined by σ.

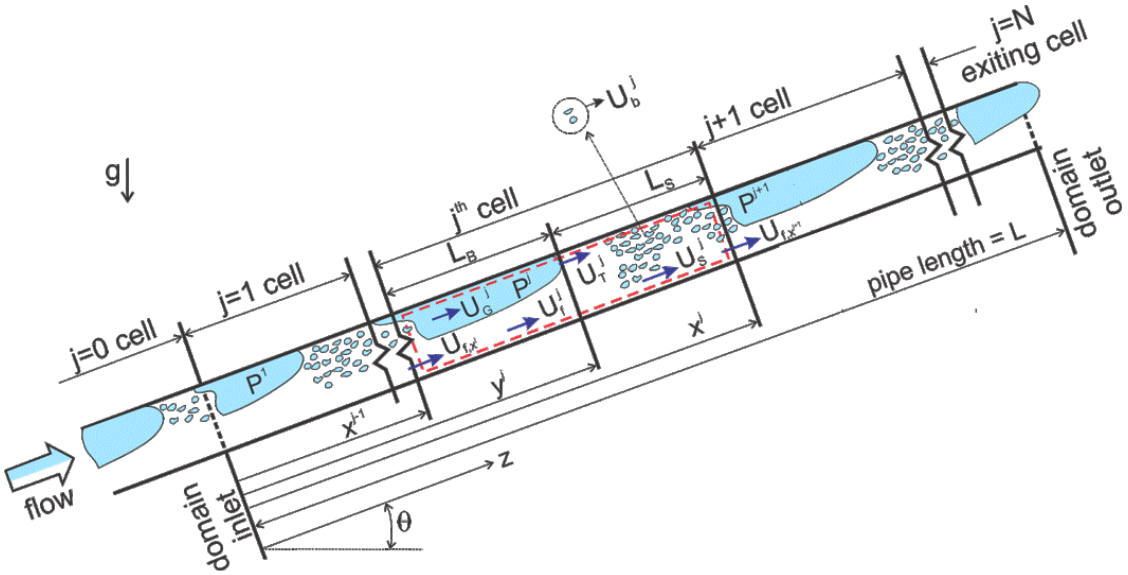

Figure 4.1. Schematic of the slug flow: cell properties and numbering, and pipeline configuration - Gonçalves and Mazza (2022) adapted.

Rosa et al. (2015) employed the following hypothesis in their model:

1. The flow is isothermal.
2. The liquid phase is incompressible.
3. The gas is compressible. The gas density is constant in each cell, but it can change along the pipe because of the pressure gradient.
4. The gas and liquid density ratio is much smaller than 1.0 $(\rho_G/\rho_L \ll 1.0)$.
5. The elongated bubble transports the gas present in this region.

6. The pressure is constant along the bubble, so the liquid and gas share the same pressure.

Based on those hypotheses, their model results in:

$$\frac{d\rho_G^j}{dt}K_1 = K_2 U_S^{j-1} - K_3 U_S^j + K_4 \ , \tag{4.1}$$

$$\frac{dU_S^j}{dt} = -\left(U_S^j\right)^2 Q_1 - U_S^j Q_2 + Q_3\left(P_G^j - P_G^{j+1}\right) - Q_4 \ . \tag{4.2}$$

Toledo (2023) and Gonçalves and Mazza (2024) described the equation system in detail. APPENDIX B also presents it. Eqs. (4.1) and (4.2) determine the time evolution of the gas density and liquid slug velocity for each cell in the numerical domain. Table 4.1 shows the K and Q parameters used in those equations. Eq. (4.1) combines the gas and liquid mass balance. The LHS is the temporal variation of the gas density that is an unknown parameter. In the RHS, the first two parameters represent the gas crossing the boundaries, and the third one corresponds to the drift term. Eq. (4.2) defines the liquid momentum balance. The LHS is the time momentum ratio of the slug velocity that is also an unknown parameter. The RHS represents the momentum exchange, the pressure difference between two neighboring cells, the wall friction at the liquid slug, and the hydrostatic forces due to gravity.

Table 4.1. The K and Q parameters of Eqs. (4.1) and (4.2).

Parameters	Expressions
K_1	$\frac{1}{\rho_G^j}\left[L_B^j \alpha_f^j + L_S^j \alpha_s^j\right]$
K_2	$R_S^{j-1}\left[1 + \frac{c_b^{j-1}\alpha_S^{j-1}}{1 - c_b^{j-1}\alpha_S^{j-1}}\right]$
K_3	$R_S^j\left[1 + \frac{c_b^j \alpha_S^j}{1 - c_b^j \alpha_S^j}\right]$
K_4	$u_D^{j-1}\left[\frac{\alpha_S^{j-1}}{1 - c_b^{j-1}\alpha_S^{j-1}}\right] - u_D^j\left[\frac{\alpha_S^j}{1 - c_b^j \alpha_S^j}\right]$
Q_1	$\frac{1}{L_S^j}\left\{\left(\frac{R_S^j}{R_f^{j+1}} - 1\right)\left(1 - \frac{dx^j/dt}{U_S^j}\right)^2\right\}$
Q_2	$2C_f^j \frac{\rho_M^j}{\rho_L}\frac{\left\|U_M^j\right\|}{D.R_S^j}\left(\frac{1}{1 - c_b^j\left(1 - R_S^j\right)}\right)\left(R_S^j + \frac{u_D^j\left(1 - R_S^j\right)}{U_S^j}\right)$

Q_3	$\frac{1}{\rho_L^j R_S^j L_S^j}$
Q_4	$g\sin(\theta)$

4.1.1 Closure laws

To complete the equation system, the numerical model requires closure equations to determine the fluids and mixture properties, elongated and dispersed bubble velocities, the liquid slug and bubble front positions and the relation of density and pressure. Both parameters are correlated assuming an ideal gas for an isothermal process:

$$\frac{1}{\rho_G}\frac{d\rho_G}{dt} = \frac{1}{P_G}\frac{dP_G}{dt} \ . \tag{4.3}$$

The liquid slug wall shear stress is calculated by:

$$\tau_S^j = \frac{1}{2} C_f \rho_M U_M \left|U_M\right| \ , \tag{4.4}$$

where C_f is the Fanning factor. It could be defined using Blasius or Colebrook White correlation based on the mixture Reynolds number.

The liquid slug is similar to a dispersed bubble flow. Furthermore, the homogenous model is employed in this region to define the mixture properties:

$$\chi_M = \chi_G\left(1-R_S\right) + \chi_L R_S \, , \tag{4.5}$$

where χ represents the density or the dynamic viscosity and the subscripts G and L refer to the gas and liquid phases. The mixture velocity (U_M) is:

$$U_M = U_S R_S + U_b\left(1-R_S\right) \ . \tag{4.6}$$

The dispersed bubble velocity (U_b) is:

$$U_b = c_b U_M + u_D \ . \tag{4.7}$$

The distribution parameter (c_b) represents the nonuniformity of dispersed bubble concentration within the liquid slug (Zuber and Findlay, 1965). In vertical pipelines,

Wallis (1969) pointed out that c_b varies between 1.0 to 1.5. Taitel and Barnea (1990) recommended c_b equal to 1.0 for the horizontal lines. In this orientation, the dispersed bubble is concentrated in the top of the pipe due to the buoyancy effects. However, the author considered it as a unit because the dispersed bubble and liquid have the same average velocities. This work follows the Taitel and Barnea (1990) recommendation.

According to Harmathy (1960) and Ishii and Zuber (1979), the drift velocity for relatively large and deformable bubbles is:

$$u_D = 1.54\left(\frac{\sigma \times g\left(\rho_L - \rho_G\right)}{\rho_L^2}\right)^{0.25} \left(R_S\right)^{1.75} \operatorname{Sin}\theta \ . \tag{4.8}$$

Regarding the translational bubble velocity, Taitel and Barnea (1990) explained this parameter is a superposition of the elongated bubble velocity in a stagnant liquid and the contribution of the mixture velocity. Later, the wake effect is added as part of this superposition (Rodrigues, 2009):

$$U_T = \left(C_0 U_M + \nu_D\right)\left(1 + h\left(L_S\right)\right) \ . \tag{4.9}$$

The C_0 and ν_D are respectively the distribution parameter and drift velocity for the elongated bubble. Several authors have been developing correlations to define those parameters (Bendiksen, 1984; Bhagwat and Ghajar, 2014, 2012; Choi et al., 2012; Woldesemayat and Ghajar, 2007). The simulations conducted in this work employ two different correlations: Choi et al. (2012) and Bendiksen (1984) plus Viana et al. (2003). The first one is given by:

$$C_0 = \frac{2}{1 + \left(\mathrm{Re}_L/1000\right)^2} + \frac{1.2 - 0.2\sqrt{\rho_G/\rho_L}\left(1 - \exp\left(-18\alpha_U\right)\right)}{1 + \left(1000/\mathrm{Re}_L\right)^2} \ , \tag{4.10}$$

$$\nu_D = 0.0246 \cdot \cos\theta + 1.606\left(\frac{g\sigma\Delta\rho}{\rho_L^2}\right)^{1/4} \sin\theta \ . \tag{4.11}$$

Table 4.2 shows the drift parameters proposed by the second correlation. Regarding the wake effect, the bubble velocity accelerates as a function of the liquid slug length in front of it (Nydal and Banerjee, 1996). Barnea and Taitel (1993) pointed out the bubble velocity reduces exponentially when the distance between the leading and trailing bubbles increases.

Several authors (Moissis and Griffith, 1962; Grenier, 1997; Cook and Behnia, 2000; van Hout et al., 2003) have studied this phenomenon and proposed a wake function:

$$h\left(L_S\right) = a_w \exp^{\left(b_w \cdot L_S/D\right)} + c_w \,. \tag{4.12}$$

This work uses Grenier's (1997) constants values, with a_w, b_w and c_w equal to 0.4, 0.5 and null, respectively.

Table 4.2. Drift parameters proposed by Bendiksen (1984) plus Viana et al. (2003) correlation.

Re_M	Fr_M	C_0	v_D
≥ 2000	≥ 3.5	1.2	$A \cdot \left(C_\infty^V \operatorname{Sin}\theta\right)$
	< 3.5	$1.0 + 0.2\operatorname{Sin}^2\theta$	$A \cdot \left(C_\infty^H \operatorname{Cos}\theta + C_\infty^V \operatorname{Sin}\theta\right)$
< 2000	-	2.0	$A \cdot \left(C_\infty^H \operatorname{Cos}\theta + C_\infty^V \operatorname{Sin}\theta\right)$
where, $Re_M = \frac{\rho_M U_M D}{\mu_M}$, $Re_L = \frac{\rho_L U_L D}{\mu_L}$, $Fr = \frac{U_M}{\sqrt{gD}}$, $Eo = \frac{\left(\rho_L - \rho_G\right) g D^2}{\sigma}$, $C_\infty^H = \left(0.542 - \frac{1.76}{Eo^{0.56}}\right)$, $C_\infty^V = \frac{0.34}{\left(1 + 3805/Eo^{3.06}\right)^{0.58}}$ and $A = \sqrt{\left(1 - \rho_G/\rho_L\right) gD}$			

The last two parameters are the positions of the bubble (y^j) and liquid slug (x^j) fronts. The bubble nose front travels with the translational bubble velocity. Thus, its position is determined as:

$$\frac{dy^j}{dt} = U_T^j \,. \tag{4.13}$$

The liquid slug front position is estimated by applying a mass balance in a control volume, which encompasses only the bubble region (x^{j-1} to y^j):

$$\frac{dx^{j-1}}{dt} = \frac{\left(1 - R_f^j\right) L_B^j \left[\frac{1}{P_G^j}\frac{dP_G^j}{dt}\right] + \frac{dy^j}{dt}\left(R_S^j - R_f^j\right) - \left(1 - R_S^{j-1}\right) U_b^{j-1} + \left(1 - R_S^j\right) U_b^j}{\left(R_S^j - R_f^j\right)} \,. \tag{4.14}$$

4.1.2 Numerical method

Rosa et al. (2015) discretized their equation system using Crank-Nicolson method and solved it through TDMA (TriDiagonal Matrix Algorithm). Other authors applied the same

methodology (Grigoleto et al., 2021; Rodrigues, 2009; Vásquez and Avila, 2021). However, the current slug tracking model employs a new approach, using the fourth-order Runge-Kutta method. It aims to improve the model's stability and speed.

As Eqs. (4.1) to (4.14) are solved for each cell in the numerical domain in each time step, the numerical method directly influences the run time. With this new approach, a higher time step was applied (5.0×10^{-3}). In addition, the number of cells inside the pipe increases significantly for actual oil and gas application. For example, the lazy wave experimental tests (Section 5.3) has a maximum of 75 cells in the numerical domain, while the field data simulation (Section 5.4) reaches around 1160 cells. Thus, the solution speed of the equation system is crucial to ensure the applicability of the software in real-world scenarios.

Figure 4.2 illustrates the sequential process to solve the system equation using Runge-Kutta method. The solution of Eqs. (4.1) to (4.14) occurs in four steps. The first step has inputs from the previous time simulation or from the start-up condition (see Section 4.3). The results of each step are the input data for the next one. In the fourth step, the updated variables are registered in the list of cells. The thermodynamic properties are also refreshed as a function of the new gas pressure.

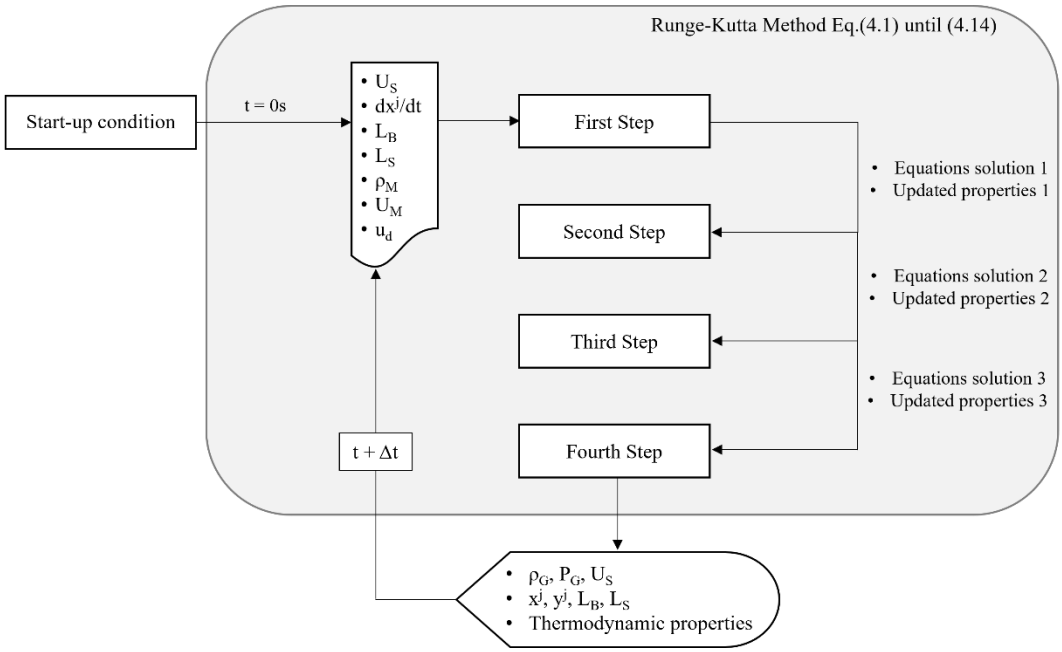

Figure 4.2. Flowchart of the solution steps for the equation system using Runge-Kutta.

4.2 Lazy wave singularities

As discussed in Section 2.1, the change of pipeline inclination and the flow direction affect the slug flow properties. In lazy wave risers, that influence is even more noticeable because there are higher upward and downward inclination changes than in previous studies (Al-safran et al., 2004; Taitel and Barnea, 2000; Zheng et al., 1994). Figure 4.3 shows six positions where those modifications occur. These points are named as *singularities* in this work.

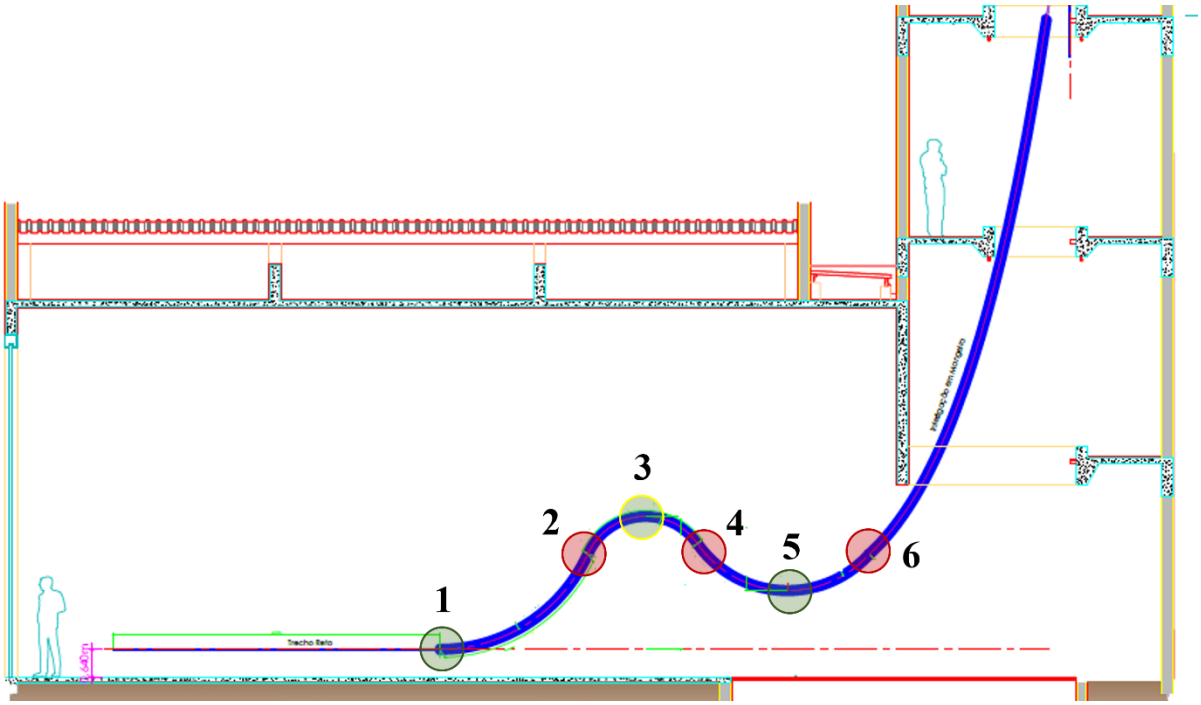

Figure 4.3. Schematic of the experimental lazy wave line with its marked singularities.

Based on the literature review, the influence of these singularities will be briefly described from left to right:

- Singularity 1 - V format (green circle): The liquid length increases and slug initiation can occur (Taitel and Barnea, 2000; Yin et al., 2018; Zhang et al., 2003a; Zheng et al., 1994).
- Singularity 2 - Bubble interface transition (red circle): The bubble region changes its interface from eccentric (plane) to concentric due to the pipeline inclination.
- Singularity 3 - A format (yellow and green circle): The bubble loses its liquid film to the upstream and downstream pipe sections by gravity due to the flow direction change. It can cause a dry zone; the gas phase occupies the entire cross-section area (Taitel and Barnea, 2000).

- Singularity 4 - Bubble interface transition (red circle): Similar to Singularity 2, but the bubble returns to eccentric (plane) interface due to the downhill section.
- Singularity 5 - V format (green circle): Similar to Singularity 1.
- Singularity 6 – Bubble interface transition: Similar to Singularity 2. The bubble reaches the second upward inclined section and migrates to the center of the pipe due to its inclination.

The submodels related to the singularities 1 and 5 are discussed in Section 4.2.1. Section 4.2.2 treats the singularities 2, 4 and 6. Regarding the Singularity 3, the recorded flow images show that dry zone does not occur for the tests conducted in this work. Figure 4.4 supports this statement.

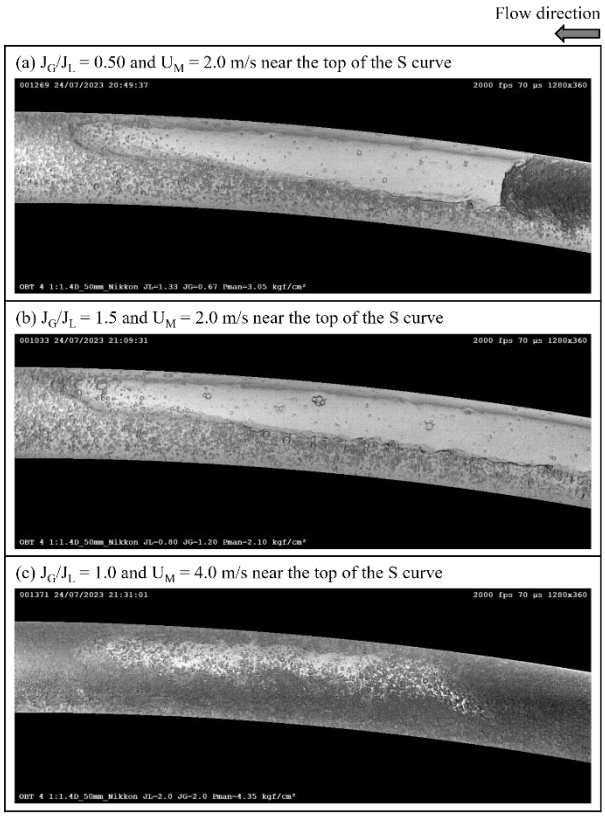

Figure 4.4. The flow images captured near the top of the S curve (Singularity 3) for an air-water experimental tests: (a) J_L = 1.33m/s and J_G=0.67 m/s, (b) J_L = 0.8m/s and J_G = 1.2 m/s and J_L = J_G = 2.0m/s.

Figure 4.4 demonstrates the bubble passage near the top of the top curve and provides a good idea about the flow behavior. Figure 4.4 (a) and (b) demonstrates the bubble has a well-defined profile and has a plane interface. In Figure 4.4 (c), the bubble also has a plane interface, but its profile is not clear due to the high aeration of the liquid film. The

recorded flow movies also show the losing liquid film depends on the superficial liquid and gas velocities. The liquid film travels in the same direction of the bubble in tests (a) and (c). In test (b), the bubble loses some liquid to the upstream section, but it is not enough to create that dry zone. Section 5.1 describes and illustrates these phenomena in detail. For this section, Figure 4.4 only justifies the fact of this work does not propose any submodel for Singularity 3.

4.2.1 Hilly terrain: V format

The change of pipeline orientation from horizontal to the upward inclined or from downward to upward inclined causes the V format phenomena. Those geometry configurations intensify the liquid accumulation at the bottom elbow. Thus, it can lead to (i) the liquid slug length increase or (ii) the generation of a unit cell. The numerical occurrence of any of these mechanisms depends on the criterion of cell generation. Thus, it is a critical point of the V format submodel.

To calculate the liquid accumulation at the bottom elbow, this work employs a formulation similar to Zheng et al. (1995) and Conte et al. (2011) approaches. The submodel assumes the liquid accumulation occurs during the bubble passage over the elbow, as discussed by Taitel and Barnea (2000) (see Figure 4.5). In addition, another assumption is that the bubble length remains constant during this process. The accumulated liquid only affects the liquid film thickness. Figure 4.5 illustrates the control volume that encompasses the unit cell passing over the bottom elbow and the upstream liquid slug. The figure also shows the liquid film velocity crossing the boundaries.

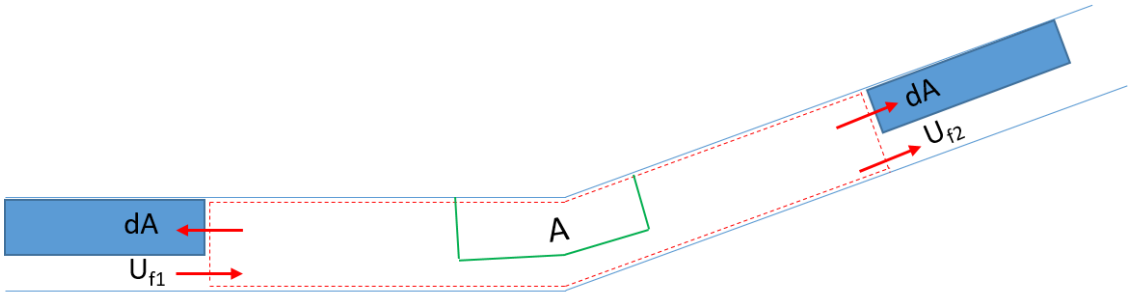

Figure 4.5. Control volume applied between x^j and y^{j-1} to predict the liquid accumulation at the bottom elbow (V format).

By applying the liquid mass balance in the control volume shown in Figure 4.5, the equation becomes:

$$\rho_L \frac{d\forall}{dt} + \left[\rho_L U_f A_L\right]_2 - \left[\rho_L U_f A_L\right]_1 = 0 \ . \qquad (4.15)$$

Eq. (4.15) is different from Zheng et al. (1995) and Conte et al. (2011) formulations because of the control volume. It results in the usage of the liquid film velocities from bubbles (j-1) and (j+1). The liquid accumulation is calculated in each time step as:

$$\Delta\forall = \forall_{LIQ}^{NEW} - \forall_{LIQ}^{OLD} = A\left(U_{f_1}R_{f_1} - U_{f_2}R_{f_2}\right)\Delta t\,. \tag{4.16}$$

The liquid film velocity is defined through a mass balance applied to a control volume that encompasses half of the film and liquid slug (Rodrigues, 2009):

$$U_f = U_T + \frac{R_S}{R_f}\left(U_S - U_T\right)\,. \tag{4.17}$$

The translational bubble velocity is calculated by correlation. Roumazeilles et al. (1996) pointed out that U_T is insensitive to the downward inclination angle. Based on Figure 4.6, the authors also affirmed that the drift correlation for horizontal and almost horizontal pipeline predicts the distribution parameter (C_0) in downward flow. Figure 4.6 (a) presents the U_T data for a horizontal line. The authors concluded that the experimental C_0 has a good agreement with Bendiksen's (1984) correlation. In Figure 4.6 (b), they demonstrate the similarity between the U_T obtained in horizontal and downward inclined pipelines.

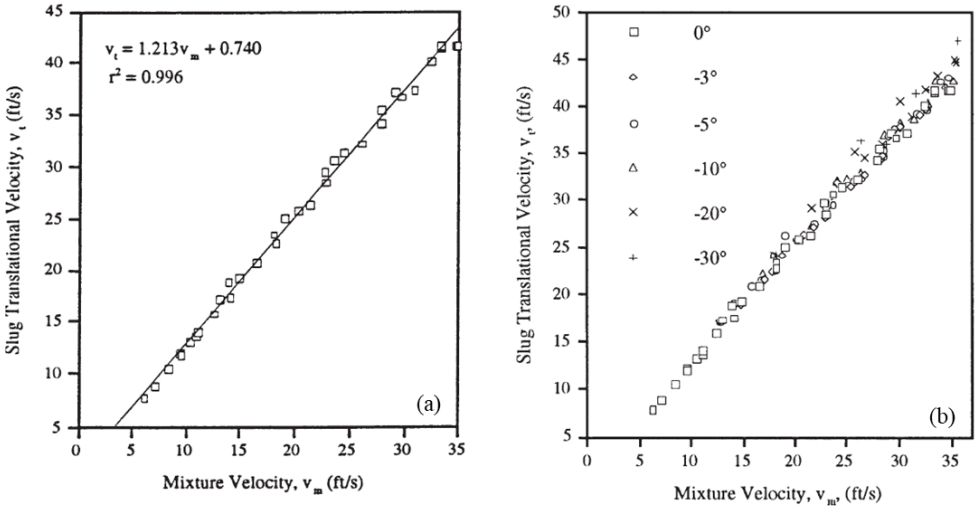

Figure 4.6. Experimental translational bubble velocity obtained by Roumazeilles et al. (1996) in (a) horizontal pipeline and (b) with inclination angles from 0° to -30°.

Since the bubble length remains constant during the accumulation, Eq. (4.18) determines the area occupied by the liquid phase in this region:

$$A_{LIQ}^{NEW} = \frac{\forall_{LIQ}^{NEW}}{L_B^j} \ . \tag{4.18}$$

Regarding the criterion for cell generation, this work combines two approaches. The first one applies the stability criterion from Taitel and Dukler (1976). The authors proposed an equation to determine the critical gas velocity:

$$V_G \geq C_2 \left(\frac{(\rho_L - \rho_G) g \cos(\theta_1) A_G}{\rho_G \, dA_L / dh_f} \right) , \tag{4.19}$$

where C_2 is:

$$C_2 = \left(2 \frac{\left(A_G^{'} / A_G \right)^2}{1 + A_G^{'} / A_G} \right)^{0.5} \text{ or } C_2 = 1 - \frac{h_f}{D} \ . \tag{4.20}$$

Eqs. (4.19) and (4.20) show that criterion is a function of the gas and liquid density, the inclination angle of the first pipeline section, the old gas area $\left(A_G = (1 - R_f) A \right)$ and the new one after the liquid accumulation $\left(A_G^{'} \right)$ as well as the variation of the cross-section area occupied by the liquid over the thickness film.

Since the elongated bubble has similar features to stratified pattern, Taitel and Dukler (1976) calculated the geometric parameters by:

$$\tilde{A}_L = \frac{A_L}{D^2} = 0,25 \left[\pi - \cos^{-1} \left(2 \frac{h_f}{D} - 1 \right) + \left(2 \frac{h_f}{D} - 1 \right) \sqrt{1 - \left(2 \frac{h_f}{D} - 1 \right)^2} \right] , \tag{4.21}$$

$$\frac{dA_L}{dh_f} = D \sqrt{1 - \left(2 \frac{h_f}{D} - 1 \right)^2} \ . \tag{4.22}$$

Eq. (4.18) and (4.21) should provide the same value, thus the liquid film thickness is updated. By combining Eq. (4.19), (4.20) and (4.22), the critical gas velocity is defined. The first criterion considers that the generation of a unit cell occurs when the gas velocity is greater than or equal to the stability criterion. However, the simulations conducted in this research highlight the problem pointed out by Zheng et al. (1994), the pseudo-slugs.

If only Eq. (4.19) is used, it can result in the creation of a new cell that has a small liquid slug. It quickly causes the bubble coalescence and introduces instabilities to the numerical model. Thus, the second approach defines a minimum liquid slug length, which should be greater than or equal to 70% of the mean liquid slug length at the inlet. If the length is not long enough, the upstream slug traps the liquid amount. The two phenomena lead to different updates to the cell properties, so the submodels address them separately. The following subsections will describe them.

4.2.1.1 Sudden liquid slug length increase

In some cases, the level of liquid accumulation is not enough to meet the criterion. It physically means the instabilities on the gas-liquid interface were not able to reach the top of the pipe and the generation of a unit cell does not happen (Taitel and Dukler, 1976). When it occurs, the upstream slug captures the accumulated liquid, and its length suddenly increases. Figure 4.7 [t+Δt] illustrates it.

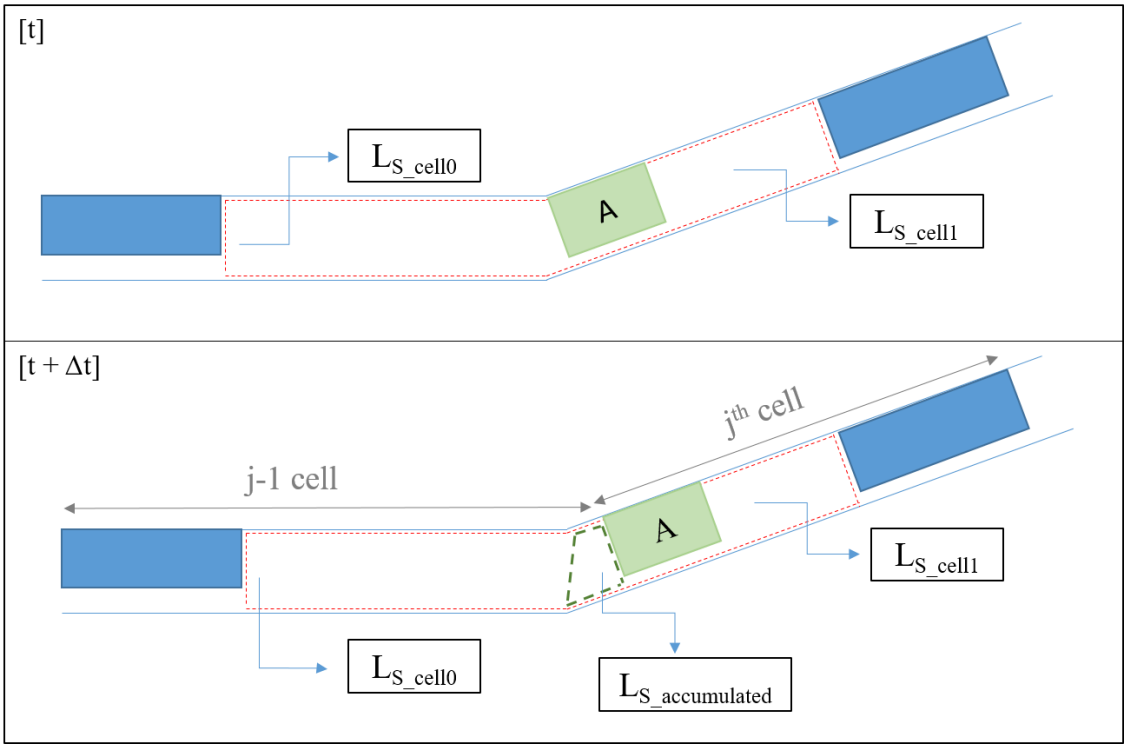

Figure 4.7. Schematic illustration of the unit cell configuration during the sudden liquid slug length increase: [t] the bubble passes the bottom elbow and [t+Δt] the previous liquid slug traps the accumulated liquid.

Figure 4.7 also shows the sequential step of the submodel. As previously discussed, the liquid accumulation occurs during the bubble passage over the bottom elbow. Thus, the process finishes when the bubble tail passes the elbow and reaches the new pipeline section.

Figure 4.7 [t] represents it. In sequence, Figure 4.7 [t+Δt] demonstrates the increase of L_{S_cell0} due to the accumulated liquid. This phenomenon affects the properties of the unit cell "A" and the upstream liquid slug.

The $L_{S\_accumulated}$ is a function of the liquid volume accumulated at the elbow. By considering that the equivalent length has the same liquid slug holdup of upstream slug, Zheng et al. (1993) proposed that the length is obtained by Eq. (4.23). The volume $\left(\forall\right)$ is the sum of the results obtained by Eq.(4.16) in each time step:

$$\forall = AL_{S\_accumulated}\left(R_S^{j-1} - R_f^{j}\right) . \tag{4.23}$$

As illustrated in Figure 4.7, the submodel should update the following cell properties: liquid slug length (j-1 cell), length and void fraction of the elongated bubble "A" (j cell). For this purpose, three hypotheses are assumed:

i. The liquid slug length (j-1 cell) is the sum of its length at time [t] and the equivalent length calculated by Eq. (4.23), resulting in:

$$L_{S\_Cell0} = \left[L_S^{j-1}\right]^{New} = \left[L_S^{j-1}\right]^{Old} + L_{S\_accumulated} . \tag{4.24}$$

ii. The liquid holdup of the slug (j-1 and j^{th} cells) and the bubble remain constant.

iii. The sum of the three structure lengths remains constant:

$$\left[L_S^{j-1} + L_B^{j} + L_S^{j}\right]^{OLD} = \left[L_S^{j-1} + L_{S\_accumulated} + L_B^{j} + L_S^{j}\right]^{NEW} . \tag{4.25}$$

Based on these assumptions, the new bubble and liquid slug lengths (j^{th} cell) are calculated to ensure the gas and liquid mass conservation inside the control volume:

$$\left[\forall_{G\_old}\right]^{CV} = \left[\forall_{G\_new}\right]^{CV} \quad \text{and} \quad \left[\forall_{L\_old}\right]^{CV} = \left[\forall_{L\_new}\right]^{CV} . \tag{4.26}$$

The new lengths modify the position of bubble (y^j) and liquid slug front (x^{j-1}):

$$x^{j-i} = y^{j-i} + L_{S\_Cell0}^{j-1} , \tag{4.27}$$

$$y^{j} = x^{j-1} + L_B^{j} . \tag{4.28}$$

4.2.1.2 Unit cell generation

In this case, the instability in the gas-liquid interface was enough to break the elongated bubble and the unit cell generation occurs. Physically, the gas velocity increases due to the larger film thickness and the wave reaches the top of the pipe. Similar to the transition from stratified to slug flow pattern (Taitel and Dukler, 1976). If the flow features meet both numerical criteria, the submodel adds a new unit cell to the numerical domain, as exemplified in Figure 4.8.

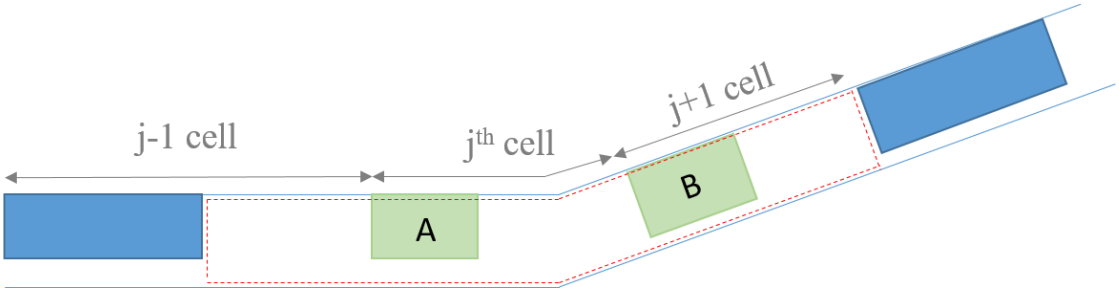

Figure 4.8. Schematic illustration of the moment when the unit cell generation occurs.

Figures 4.5, 4.7 and 4.8 have the same control volume, but the flow structures inside it are significantly different. Figure 4.8 shows that the instability breaks the bubble, resulting in structures "A" and "B". Both structures have different lengths and liquid holdups. As illustrated in Figure 4.8, the control volume contains the upstream liquid slug (j-1 cell), bubbles "A" (j^{th} cell) and "B" (j+1 cell).

By considering this new scenario, the submodel has five unknown variables: L_S^{j-1}, $\left[L_B^j \text{ and } R_f^j\right]^{\text{Bubble A}}$ and $\left[L_B^{j+1} \text{ and } R_f^{j+1}\right]^{\text{Bubble B}}$. The new liquid slug length generated between bubbles "A" and "B" is obtained from Eq. (4.23). To determine those parameters, the submodel considers:

i. The properties of liquid slug from (j+1) cell remain constant. It is not affected by the liquid accumulation.
ii. The liquid holdup of the slug from (j-1 and j^{th}) cells remains constant.
iii. The sum of the structure lengths is constant:

$$\left[L_S^{j-1} + L_B^j + L_S^j\right]^{OLD} = \left[L_S^{j-1} + \left(L_B^j\right)^A + L_{S\_accumulated}^j + \left(L_B^{j+1}\right)^B + L_S^{j+1}\right]^{NEW} . \qquad (4.29)$$

An iterative process is required to ensure the gas and liquid mass conservation inside the control volume. An initial guess is assumed for L_B^j, then its liquid holdup is

calculated by Taitel and Barnea's (1990) bubble model. A guess for L_B^{j+1} is obtained by Eq.(4.26) through a momentary assumption that both bubbles have the same liquid holdup $\left(R_f^A = R_f^B\right)$. Sequentially, R_f^B is updated by bubble model and Eq. (4.29) determines L_S^{j-1}. This process continues until both mass phases are conserved.

Based on those new parameters, the structure fronts are:

$$x^{j-i} = y^{j-i} + L_S^{j-1} \ , \tag{4.30}$$

$$y^j = x^{j-i} + \left(L_B^j\right)^A \ , \tag{4.31}$$

$$x^j = y^j + L_{S\_accumulated}^j \ . \tag{4.32}$$

Briefly, the Taitel and Dukler (1976) stability criterion and the minimum liquid slug length are checked in each time step during the bubble passage over the bottom elbow. If this combination is true, the submodel described in Section 4.2.1.2 is solved. It leads to the insertion of a new unit cell in the numerical domain and the update of the cell properties. On the other hand, if the flow features do not meet the criterion, the submodel from Section 4.2.1 is utilized.

4.2.2 Bubble interface transition

As illustrated in Figure 4.3, the lazy wave riser has three positions where the submodel predicts the modification of the bubble profile. It occurs because the pipeline geometry has different orientations (horizontal or near horizontal, upward and downward inclined) and reaches high inclination angles. The gas-liquid interface shape in the bubble region was extensively discussed for horizontal and vertical pipes. For horizontal or near horizontal, the bubble travels at the top of the pipe and the liquid film at the bottom, which is named eccentric or plane interface (Bueno, 2010; Dukler and Hubbard, 1975; Mazza et al., 2010; Shoham, 2005). On the other hand, the bubble flows in the center of the pipe with thin film around it in vertical lines, named as concentric interface (Fernandes et al., 1983; Taitel et al., 1980; Taitel and Barnea, 1990). However, the identification of bubble shape in a pipeline with gradual transition between horizontal and vertical orientations is still limited.

According to Mazza et al. (2010), the interface shape is a function of the pipeline inclination and flow velocity. They also pointed out that there is not a threshold characteristic,

which defines the transition between the plane and concentric interface. Based on this, the first step of this submodel was to define a criterion to change the gas-liquid interface along the pipe.

Bueno (2010) developed an air-water experimental campaign to determine the variation of slug flow parameters as a function of the pipeline inclination. Figure 4.9 presents one of his tests, in which the length of an isolated bubble is measured in different angles. The figure shows the length has a stronger reduction between 0° to 30°. Above this angle, the change is slight. This behavior supports the assumption of the pipe angle as the criterion to change the gas-liquid interface along the pipe.

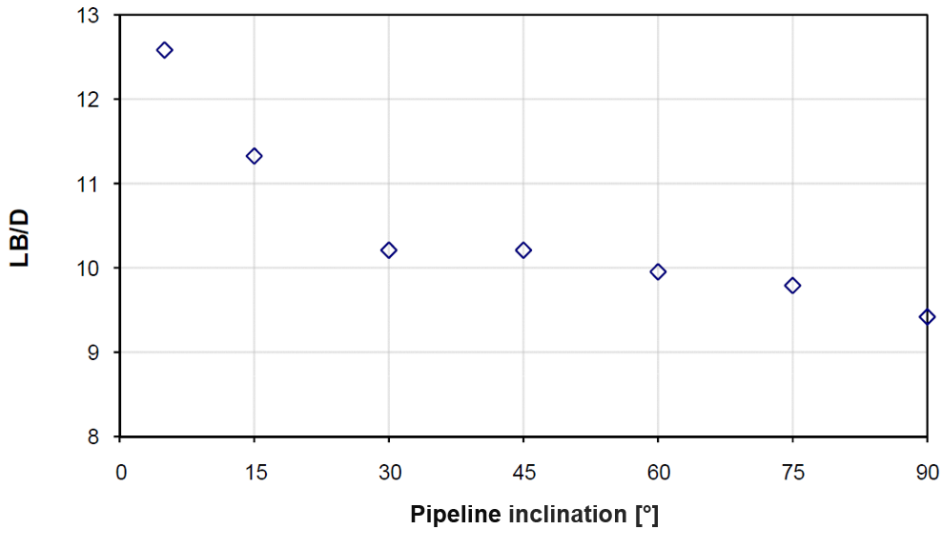

Figure 4.9. The length variation of an isolated bubble in different pipeline inclination – adapted from Bueno (2010)

It is important to check the performance of the numerical method to predict the bubble properties. Since the current slug tracking model defines the bubble profile through Taitel and Barnea (1990) model (Eq. (4.40)), an approach similar to Bueno (2010) was done to validate the numerical profile. The experimental loop test has an inner diameter equal to 0.026 m, and the superficial air and water velocities are equal to 0.60 m/s. The numerical tests use the same properties. Bueno (2010) also provided the unit cell frequency. The liquid slug holdup was defined by Malnes's (1982) correlation (see Table 4.3).

Figure 4.10 shows the bubble length comparison between experimental and numerical data. Taitel and Barnea's (1990) model provides a good agreement until 30°. Above this angle, the numerical data remains almost constant and greater than the experimental. Since the liquid slug holdup correlation is not sensitive to the pipe inclination, it can affect the cell

properties. However, based on Figure 4.9 and on the fact that the numerical bubble length does not significantly change above 30°, this angle is assumed as the criterion for air and water flow.

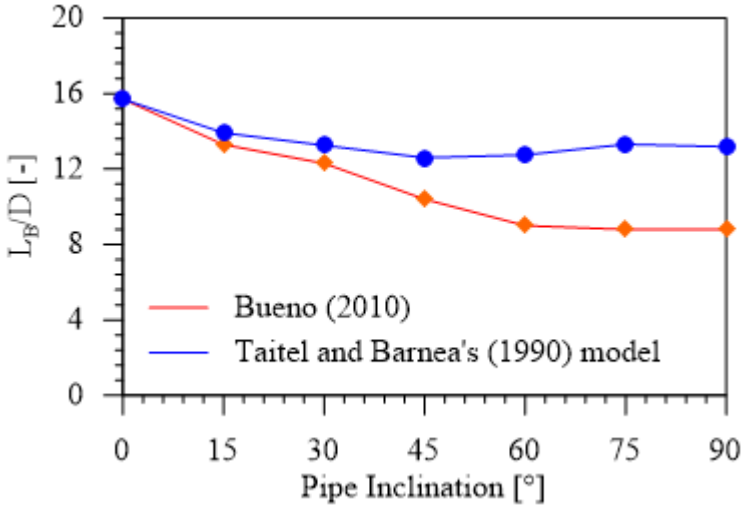

Figure 4.10. Comparison between the bubble length obtained by Bueno's (2010) experimental campaign and from Taitel and Barnea's (1990) bubble model.

The oil and gas production lines have different fluid properties and larger diameter. Thus, Taitel and Barnea's (1990) model was tested to verify the influence of these features on the bubble profile, and consequently in the angle criterion. The pipeline has an inner diameter equal to 0.1524 m (6 inches), and the mixture velocity is 2.0 m/s. The simulation considers an oil and gas mixture with 32° API. The gas density, GOR, BSW and temperature are respectively 1.1, 400 sm^3/sm^3, 0.5 and 50 °C (Gaspari and Santim, 2017). Section 4.3 presents the Black-Oil model used to calculate the thermodynamic properties. Figure 4.11 presents the numerical bubble and void fraction in different inclination angles.

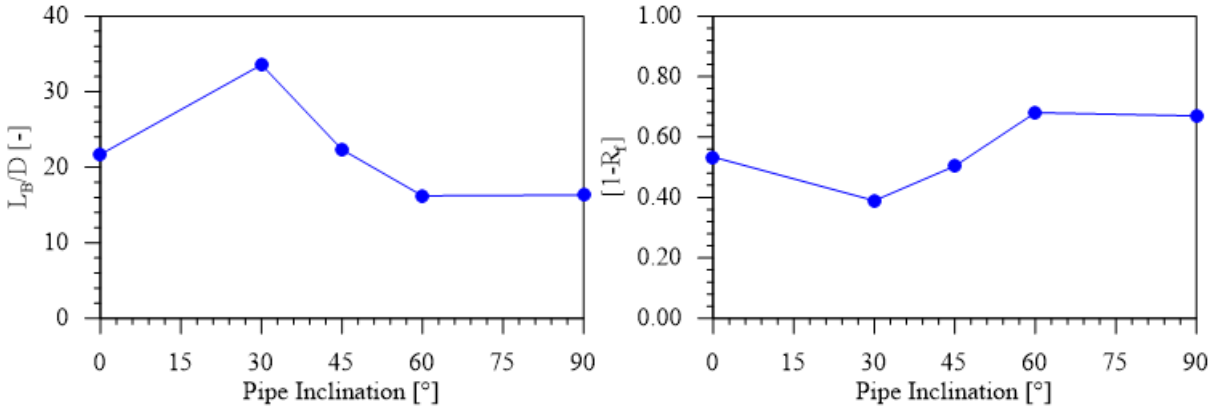

Figure 4.11. The bubble length and void fraction obtained by Taitel and Barnea (1990) in different pipeline inclinations with mixture velocity equal to 2.0m/s.

The transition from plane to concentric interfaces leads to the bubble length reduction and its void fraction increase, since the bubble diameter is almost equal to the pipe

diameter. For oil and gas flow, the angle 30° does not reproduce this behavior. Figure 4.11 shows that the angles 0° and 45° result in a similar data for L_B and [1-R_f], but there is a punctual variation at 30°. Thus, the angle criterion should be different. Based on Figure 4.11, the angle 60° presents the properties expected for concentric shape. In addition, it remains constant until the vertical orientation. Therefore, 60° is adopted as the angle criterion for oil and gas flow.

The submodel modifies the cell properties when the structure reaches a pipeline section with inclination greater than the angle criterion. The bubble tail is the position where the unit cell is transferred between different pipeline sections. Figure 4.12 illustrates the transition from plane to concentric shape. At time [t], the j^{th} cell is inside the pipeline section 1 so it still has a plane interface. Then, at time [t+Δt], the bubble tail reaches the beginning of section 2 and changes to concentric interface characteristics.

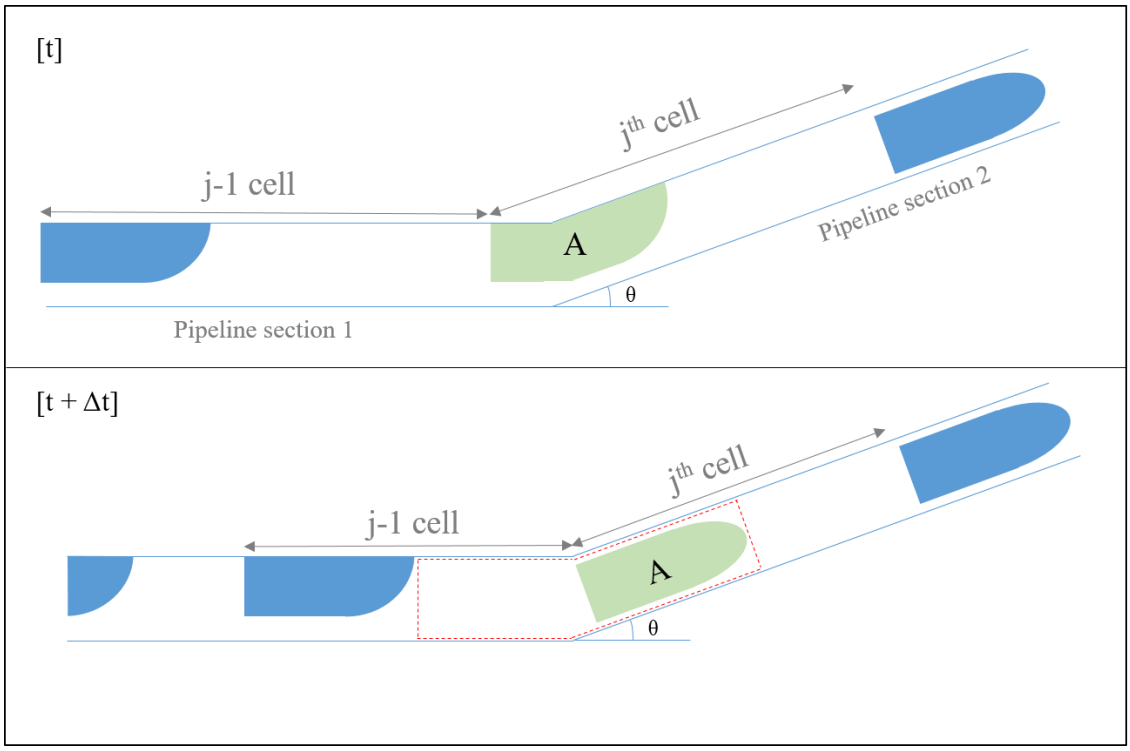

Figure 4.12. Schematic illustration of the interface transition: plane to concentric.

The liquid film volume reduces due to the new bubble shape. The current submodel assumes the liquid slug from (j-1) cell captures that amount to ensure the liquid mass balance. It also considers the liquid holdup has a new value calculated by correlation. Table 4.3 presents some options. The new position leads to a different holdup due to the flow scenario (mixture velocity, liquid and gas properties, surface tension and pipe inclination).

Table 4.3. Liquid slug holdup correlations.

Correlations	R_S
Malnes (1982)	$R_S = 1 - \dfrac{1}{1 + \left(\dfrac{A}{Fr_j \, Bo_L^B} \right)}$ where $\begin{cases} Bo_L = \dfrac{gD^2 \rho_L}{\sigma} \\ Fr_j = \dfrac{J_L + J_G}{\sqrt{gD}} \\ A = 83 \text{ and } B = 0.25 \end{cases}$
Ferschneider (1983)	$R_S = \dfrac{1}{\left[1 + \left(\dfrac{Fr_j^2 Bo_L^B}{A} \right) \right]^2}$ where $\begin{cases} Bo_L = \dfrac{gD^2 \left(\rho_L - \rho_G \right)}{\sigma} \\ Fr_j = \dfrac{\left(J_L + J_G \right) \sqrt{\rho_L}}{\sqrt{gD \left(\rho_L - \rho_G \right)}} \\ A = 625 \text{ and } B = 0.2 \end{cases}$
Andreussi and Bendiksen (1989)	$R_S = \dfrac{(F_0 + F_1)}{\left(Fr_J + F_1 \right)}$ where $\begin{cases} F0 = \max\left(0; A \left[1 - 2 \left(\dfrac{2.5}{D} \right)^2 \right] \right) \\ F1 = B \left(1 - \dfrac{\text{sen}(\alpha)}{3} \right) Bo^{-3/4} \\ A = 2.6,\ B = 2400 \text{ and } C = 3 \end{cases}$
Gomez et al. (2000)	$R_S = \exp\left[A\alpha + B \, Re_J \right] -,$ where $A = -0.45$ and $B = -2.48 \cdot 10^{-6}$
Pereyra et al. (2012)	New constants Malnes (1982): A = 81.526 and B = 0.294 Ferschneider (1983): A = 10211.22 and B = 0.592 Andreussi and Bendiksen (1989): A = 0.84, B = 1226.904 and C = 1.091 Gomez et al. (2000): $A = -0.344$ and $B = -7.23 \cdot 10^{-6}$

The transition process affects the parameters of bubble (j) and the liquid slug (j-1), which are highlighted in Figure 4.12 by a dashed red line. However, the gas volume inside this pseudo-cell should be the same before (VG_O) and after (VG_N) the transition because the pressure does not significantly modify between two time steps:

$$VG_N = VG_O = L_S^{j-1} \left(1 - R_S^{j-1} \right) + L_B^j \left(1 - R_f^j \right) . \qquad (4.33)$$

The parameters from old time are known, but the new ones should be updated. The submodel assumes the sum of bubble and liquid slug lengths remains constant, so the new slug length can be determined as:

$$\left[L_S^{j-1}\right]^N = L_U - \left[L_B{}^j\right]^N \ . \tag{4.34}$$

By combining Taitel and Barnea's (1990) model and a liquid holdup correlation, the new parameters are refreshed to guarantee that Eqs. (4.33) and (4.34) are true. The update of the liquid holdup occurs at the first bubble shape transition only. In the next singularities, it remains constant. The same process is employed for three bubble interface treatments (Figure 4.3, singularities 2, 4 and 6).

Figure 4.12 also evidences another mechanism. As mentioned above, the unit cell only changes its inclination when the bubble tail reaches the new pipeline section. However, the new pipe angle is already acting on the liquid slug. Therefore, the adjustment of this angle can directly affect the pressure gradient, especially when the flow has large unit cells. As shown in Eq. (4.2) and Table 4.1, the gravitational term is influenced by the liquid slug holdup and length. The liquid slug holdup does not change in this process, so the liquid slug length is the unique required parameter.

Table 4.4 shows the definition of liquid slug length for three scenarios, which depend on the bubble and liquid slug front. In the first one, the entire cell is in the same pipeline section. The second one, the liquid slug is totally in the new section, since the bubble nose is at pipe transition. In the third scenario, the liquid slug occupies both pipeline sections. Based on this new calculation, the adjusted gravitational term is:

$$\Delta P_{GRAVITATIONAL} = \vec{g} \times R_S^j \times \left[L_{S\_1}^j \times \text{sen}\left(\theta_1\right) + L_{S\_2}^j \times \text{sen}\left(\theta_2\right)\right] \ . \tag{4.35}$$

Table 4.4. Liquid slug length definition during the transition of a unit cell between two pipeline sections.

	$L_{S\_1}^j$	$L_{S\_2}^j$
1. $y^j < L_{Section1}$ and $x^j < L_{Section1}$	$L_{S\_1}^j = x^j - y^j$	$L_{S\_2}^j = 0$
2. $y^j = L_{Section1}$	$L_{S\_1}^j = 0$	$L_{S\_2}^j = x^j - y^j$
3. $y^j < L_{Section1}$ and $x^j > L_{Section1}$	$L_{S\_1}^j = L_{Section1} - y^j$	$L_{S\_2}^j = x^j - L_{Section1}$

*$L_{Section1}$ is the end of a pipeline section.

4.3 Initial and boundary conditions

The initial and boundary conditions are important to the numerical model convergence. Rodrigues (2009), Rosa et al. (2015), Grigoleto et al. (2021) and Vásquez and Avila (2021) utilized the same approach to describe the flow near the outlet. They considered the unit cell exits the numerical domain when the bubble nose touches the end of the pipe. At this moment, the bubble assumes the outlet pressure. Unlike the previous authors, Padrino et al. (2023) considered the unit cell exits the pipe when its liquid slug length is shorter than 2.5D. The current outlet approach is discussed in Section 4.3.1.

Regarding the inlet condition, the slug tracking model is not able to reproduce the slug formation process. Therefore, the cell properties must be provided at the inlet. The required parameters are superficial gas and liquid velocities (J_L and J_G), the lengths (L_B and L_S) and holdups (R_f and R_S) of the bubble and slug. Rosa et al. (2015) highlighted that the inlet condition affects the results representativeness. The authors also defined the list of cells in two manners: periodic and random. The first option is the simplest one, which considers that all cells have the same properties. In the latter one, the parameters assume a random distribution. Section 4.3.2 describes the submodel proposed to predict both types of inlet condition.

In addition, the solution of Eq. (4.1) and (4.2) is a time-marching procedure. Thus, it is necessary to provide the properties of the cells inside the numerical domain at time t = 0 s. The previous models assumed that the pipeline is full of liquid (as a long liquid slug) and there is a bubble positioned at the inlet (Grigoleto et al., 2021; Meléndez Vásquez, 2020; Padrino et al., 2023; Rodrigues, 2009; Rosa et al., 2015). The current updated model employs a different methodology, as presented in Section 4.3.3.

4.3.1 Outlet boundary condition

Rosa et al.'s (2015) model considers the unit cell exits the numerical domain when the bubble nose touches the pipe outlet, as presented in Figure 4.13 [t+Δt]. Therefore, the model neglected the contribution of liquid film volume in the pressure gradient during the exit process. It was not a problem because the model application had resulted in small cells, and the liquid fraction had been minor. However, in oil and gas production lines, long elongated bubbles are expected due to the pressure gradient. Thus, the liquid film contribution becomes significant.

Since the momentum equation is not applied to the last cell (n), the current slug tracking proposes a new approach to treat that contribution. This treatment assumes that the

bubble (n) is no longer moving (U_T = 0.0m/s). Thus, the liquid film is drained to the previous slug by gravity. As shown in Figure 4.13 [t+2Δt], it causes a sudden increase of liquid slug length (n-1), and the bubble (n) becomes a gas plug.

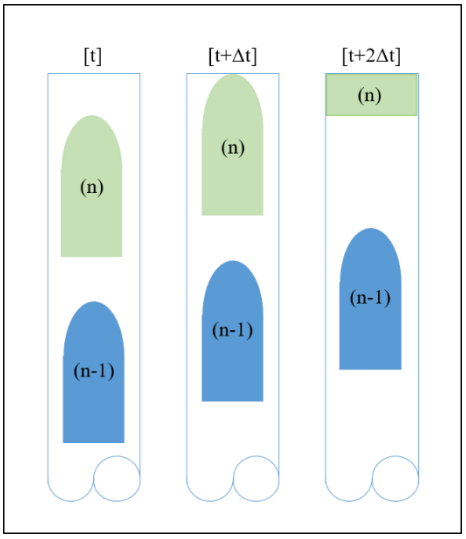

Figure 4.13. Schematic illustration of the outlet treatment.

The submodel employs a liquid mass balance between time [t+Δt] and [t+2Δt] to determine the new liquid slug length. Eq. (4.36) reveals the new liquid volume (VL) in the slug (n-1) should be equal to the sum of the liquid volume of slug (n-1) and bubble (n) at the previous time. In this process, the liquid slug holdup does not change.

$$\left[\mathrm{VL}_{\mathrm{Slug}}^{\mathrm{n-1}}\right]^{\mathrm{N}} = \left[\mathrm{VL}_{\mathrm{Slug}}^{\mathrm{n-1}} + \mathrm{VL}_{\mathrm{Bubble}}^{\mathrm{n}}\right]^{\mathrm{O}} . \tag{4.36}$$

Based on Eq.(4.36), the new liquid length is:

$$\left[\mathrm{L}_{\mathrm{S}}^{\mathrm{n-1}}\right]^{\mathrm{N}} = \left[\mathrm{L}_{\mathrm{S}}^{\mathrm{n-1}}\right]^{\mathrm{O}} + \left[\frac{\mathrm{R}_{\mathrm{f}}^{\mathrm{n}} \times \mathrm{L}_{\mathrm{Bubble}}^{\mathrm{n}}}{\mathrm{L}_{\mathrm{S}}^{\mathrm{n-1}}}\right]^{\mathrm{O}} . \tag{4.37}$$

In accordance with Rodrigues (2009) and Rosa et al. (2015), $\mathrm{L}_{\mathrm{S}}^{\mathrm{n-1}}$ remains constant during the bubble exiting. The position x^{n-1} is a function of the bubble nose movement.

4.3.2 Inlet boundary condition

The literature shows that the definition of the cell properties at the inlet is strongly dependent on the experimental data (Conte et al., 2011; Rodrigues, 2009; Rosa et al., 2015) or hypotheses to simplify the flow features. The most common assumptions are: (i) the film thickness is constant and equal to the equilibrium thickness and (ii) the liquid slug is non-

aerated (Barnea and Taitel, 1993; Cook and Behnia, 2000; Nydal and Banerjee, 1996; Padrino et al., 2023; Taitel and Barnea, 1998; Vásquez and Avila, 2021). For oil and gas production lines, the above hypotheses are too conservative. As discussed in Section 4.2.2, the change of bubble profile directly affects its length and void fraction, as well as the liquid slug properties. In addition, the presence of dispersed bubbles in the liquid slug is essential to predict a realistic pressure gradient, especially when the flow structures are long.

The flow properties are organized as a list, which is used by the numerical model to define the cell parameters at the pipe inlet. This database can be constant or random. The following subsections describe each one.

4.3.2.1 Periodic inlet condition

This approach considers that the cells have the same properties (J_G, J_L, L_B, L_S, R_f e R_S) at the inlet. The flow consequently varies along the pipeline, but it is almost constant over time. It limits the performance, since the slug flow parameters actually change in time. On the other hand, the periodic condition provides a good idea about mean parameters and flow behavior along the pipe. In addition, its definition is easier and simpler than the random condition.

To determine the cell list, the current methodology requires the gas and liquid flow rates and correlations to unit cell frequency, bubble translational velocity and liquid slug holdup. Several authors proposed correlation to cell frequency, but their performance highly depends on the fit between their database and desired case (Al-Safran, 2009; Gregory and Scott, 1969; Heywood and Richardson, 1979; Jepson and Taylor, 1993; Schulkes, 2011; Zabaras, 2000). It is also possible to employ the experimental frequency when it is available. The bubble velocity is determined by Eq. (4.9), using the drift parameters proposed by Bendiksen (1984) plus Viana et al. (2003) and a null wake constant. For the liquid slug holdup, there are many correlations available, as shown in Table 5.1.

The superficial gas and liquid velocities are defined by:

$$J_k = \frac{Q_k}{A}, \tag{4.38}$$

where k is either the gas or liquid phase.

By applying the mass balance to a unit cell, the superficial gas velocity is:

$$J_G = U_b\left(1-R_S\right)+L_B f\left(R_S-R_f\right)\ . \tag{4.39}$$

Eqs. (4.7) and (4.38) provide the dispersed bubble and superficial gas velocities, respectively. Since R_S and f are known by correlation or experimental data, L_B and R_f are the unknown parameters. Taitel and Barnea's (1990) bubble model correlates both parameters by:

$$\frac{dh_f}{dx_f}=\frac{\frac{\tau_{wf}S_f}{A_f}-\frac{\tau_{wG}S_G}{A_G}-\tau_i S_i\left(\frac{1}{A_f}+\frac{1}{A_G}\right)+\left(\rho_L-\rho_G\right)g\sin\theta}{\left(\rho_L-\rho_G\right)g\cos\theta-\rho_L v_f\frac{\left(U_T-U_{LS}\right)R_S}{{R_f}^2}\frac{dR_f}{dh_f}-\rho_G v_G\frac{\left(U_T-U_{GS}\right)\left(1-R_S\right)}{\left(1-R_f\right)^2}\frac{dR_f}{dh_f}}\ . \tag{4.40}$$

Eq. (4.40) has been employed to determine the film profile, and consequently the liquid holdup in this region. However, its solution demands a complex numerical integration. Mazza et al. (2010) discussed that procedure. Eqs. (4.39) and (4.40) are solved in an iterative process. By considering an appropriate error criterion, the process finishes when Eq. (4.39) becomes true. Therefore, the periodic condition is defined.

The mean data of U_T, L_B and L_S are employed as input data for the random condition. For this reason, Bueno's (2010) test (presented in Section 4.2.2 and Figure 4.10) is utilized to assess the performance of the current methodology in different pipe inclinations. For this study, it was used the experimental frequency and Malnes's (1982) slug holdup correlation. The superficial gas and liquid velocities are equal to 0.6m/s. Table 4.5 shows the experimental data obtained by Bueno (2010), the data obtained by the current methodology and their relative errors (RE).

Table 4.5 reveals that three mean parameters have relative errors lower than 8.5% until 30°. Above this angle, the relative error for L_B increases significantly. It can be justified by the liquid slug holdup and the bubble shape hypotheses. Mazza et al. (2010) pointed out the assumption of plane or concentric interface affects how the geometrical properties are defined. For inclined angles, it is not known exactly which formulation is valid. It can consequently induce a poor prediction of the bubble profile, holdup and length. The liquid slug length has relative errors lower than 9.0% for all inclinations. Unlike the experimental U_T, the numerical velocity increases with the angle. Therefore, the correlation was not able to capture the experimental variation.

Table 4.5. Mean value of U_T, L_B/D and L_S/D for Bueno's (2010) experimental campaign with mixture velocity equal to 1.2 m/s.

	Bueno (2010)			Slug tracking					
Angle	L_B/D [-]	L_S/D [-]	U_T [m/s]	L_B/D [-]	RE L_B [%]	L_S/D [-]	RE L_S [%]	U_T [m/s]	RE U_T [%]
0	15.70	12.00	1.36	15.71	0.05	11.26	6.16	1.40	3.23
15	13.30	13.40	1.39	13.91	4.60	14.10	5.19	1.46	4.90
30	12.30	12.90	1.41	13.26	7.79	13.97	8.30	1.52	8.05
45	10.40	13.70	1.45	12.59	21.07	13.79	0.64	1.59	9.45
60	9.00	14.20	1.39	12.75	41.66	14.50	2.09	1.63	17.44
75	8.80	16.90	1.47	13.32	51.37	15.43	8.69	1.64	11.87
90	8.80	15.60	1.37	13.18	49.82	15.56	0.27	1.61	17.79

4.3.2.2 Random inlet condition

The usage of random inlet condition is not a recent approach, Barnea and Taitel's (1993) slug tracking model employed an uniform or normal distribution for the liquid slug length. Cook and Behnia (2000) and Wang et al. (2006) assumed a normal distribution for L_S based on arbitrary span (2-8D or 3-5D), but they did not account for the liquid and gas mass balance inside the cell. More recently, some authors used the unit cell frequency to create the flow intermittence (Grigoleto et al., 2021; Padrino et al., 2023; Vásquez and Avila, 2021). Vásquez and Avila (2021) chose two different correlations to calculate the mean inlet parameters, resulting in cells with different properties. Grigoleto et al. (2021) employed a lognormal distribution for cell frequency, and the other parameters were determined based on it. Padrino et al. (2023) used the cell frequency to estimate the liquid slug length, and then created a lognormal distribution for this parameter only. Nonetheless, these latest authors do not consider the typical distribution of slug flow parameters. Most of them has a normal distribution, except for the slug length that has it close to the lognormal (Al-Safran et al., 2005; Bernicot and Drouffe, 1991; Nieckele et al., 2013; Nydal et al., 1992).

The random approach provides an inlet condition closer to the slug flow features. It directly affects the data representativeness, resulting in a better prediction of the temporal and spatial variation. The current methodology determines the cell list based on the mean value of U_T, L_B and L_S (Section 4.3.2.1) and their typical distributions, which are also a function of the standard deviation data. These parameters are not easily encountered in the literature, especially for conditions similar to oil and gas production systems. Padrino et al. (2023) combined the studies proposed by Fabre and Line, (1992), Al-Safran et al. (2005) and

Klinkenberg and Tijsseling (2021) to determine the standard deviation of L_S. Grigoleto et al. (2021) assumed that the cell frequency deviation is 50% based on Vicencio's (2013) experimental campaign. The current methodology uses the coefficient of variation (the ratio of the standard deviation and mean data) obtained by Dalla Maria's (2016) experimental campaign. These values were 0.0468, 0.3354, and 0.3498 for U_T, L_B and L_S, respectively.

The creation of the list has two steps. In the first one, a random list (N_i) with average (μ) and standard deviation (s) equal to 0.0 and 1.0 is created by:

$$N_i = \cos\left(2\pi U_2\right)\sqrt{-2\mathrm{Ln}\left(U_1\right)} \ , \tag{4.41}$$

where U_1 and U_2 are random lists with uniform distribution.

In a sequence, the list of U_T and L_B are adjusted to the correct average (μ) and standard deviation (s) data:

$$\varphi_i = \mu + s \times N_i \ . \tag{4.42}$$

The liquid slug length requires a different adjustment due to its typical lognormal distribution:

$$\psi_i = \mathrm{Exp}\left[N_i \sigma_0 + \mathrm{Ln}\left(\mu_{50\%}\right)\right] , \tag{4.43}$$

where σ_0 and $\mu_{50\%}$ are:

$$\sigma_0 = \sqrt{\mathrm{Ln}\left[\left(\frac{s}{\mu}\right)^2 + 1\right]} \text{ and } \mu_{50\%} = \mu \cdot \mathrm{Exp}\left(-\frac{\sigma_0^2}{2}\right) . \tag{4.44}$$

Based on those three random lists, the other required parameters are calculated. For each set of U_T, L_B and L_S, Eqs. (4.39) and (4.40) are solved considering a correlation for liquid slug holdup (Table 4.3). Eq. (4.7) is used to calculate the dispersed bubble. The cell frequency is determined by:

$$f = \frac{1}{\Delta t_U} \equiv \frac{U_T}{L_B + L_S} \ . \tag{4.45}$$

In addition, it is assumed that the mixture velocity is equal to the sum of superficial gas and liquid velocity. Thus, Eq. (4.9) is rearranged to calculate the superficial liquid velocity:

$$J_L = \frac{U_T - C_\infty \sqrt{gD}}{C_0} - J_G \ , \tag{4.46}$$

where the drift parameters come from Table 4.2.

Gonçalves and Mazza (2024) presented the validation of the random inlet condition methodology, as demonstrated in Figure 4.14. The mean and distribution data were calculated and compared to Dalla Maria's (2016) test. It was a water and air experimental campaign in a horizontal pipe with 0.026 m ID. The superficial gas and liquid velocities were equal to 0.54 and 0.6 m/s. The author pointed out the liquid slug was non-aerated, and the cell frequency was equal to 2.49.

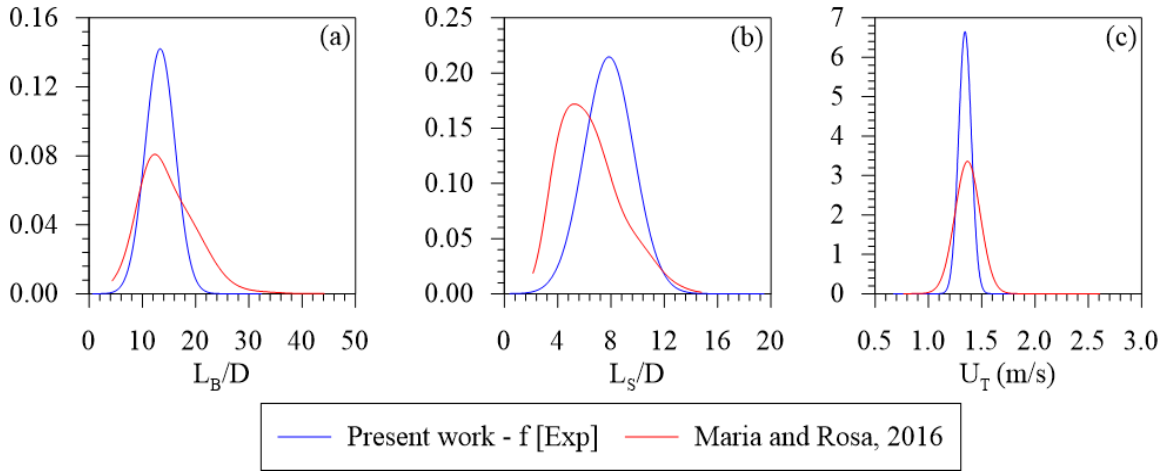

Figure 4.14. Comparison between the experimental and numerical statistical distribution of U_T, L_B/D and L_S/D at inlet for Dalla Maria's (2016) test with mixture velocity equal to 1.2 m/s – Gonçalves and Mazza (2024).

Based on this setup, the periodic methodology leads to relative errors equal to 1.6% (U_T), 11.5% (L_B) and 21.4% (L_S). As shown in Figure 4.14, the numerical distribution has a good agreement with the experimental one, but the spread out is lower. The creation of random list requires some criteria to avoid major properties changes between sequential cells, since it can cause model divergence. It consequently affects their spread out and average.

4.3.3 Start-up procedure

Similar to the previous paper, Rosa et al. (2015) assumed that the simulation starts with a pipeline full of liquid. However, this assumption becomes a challenge for long pipelines like oil and production systems. For example, Andreolli (2018) presented the geometry of an

actual lazy wave riser, which is approximately 9,081 m long and 2,159 m high. If this pipe is filled with liquid only, its length and inclination result in a high gravitational load at the inlet. It consequently causes instabilities during the cell insertion process. For this reason, the current slug tracking model initiates the simulation from a guess condition. Figure 4.15 exemplifies the initial condition utilized to simulate the lazy wave riser presented by Andreolli (2018). Section 5.4 presents the numerical results obtained for this test.

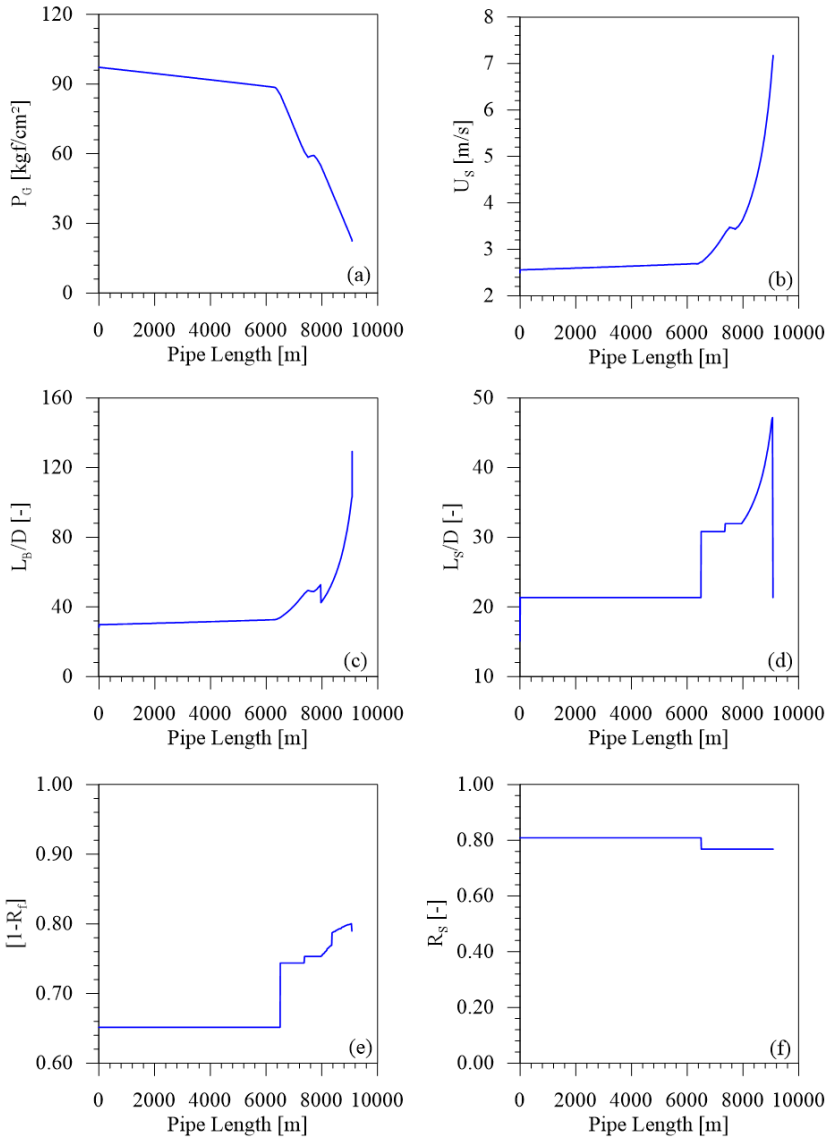

Figure 4.15. Initial condition for an actual lazy wave riser.

This initial condition is determined based on the boundary conditions and the pipeline geometry. The parameters shown in Figure 4.15 are estimated using a cell-based model proposed by Taitel and Barnea (1990). This is an iterative process, in which the cell properties are calculated from the outlet to inlet. It stops when the superficial gas velocity at inlet matches the desired condition.

Since the Taitel and Barnea's (1990) bubble model is employed to define the bubble profile, Figure 4.15 (e) shows that the void fraction varies above the angle criterion. As discussed in Section 4.2.2, the first bubble interface transition also changes the liquid slug holdup and length. Figure 4.15 (d) and (f) illustrate them. The expansion of the gas due to the pressure gradient is also accounted for, as shown in Figure 4.15 (b) and (c).

4.4 Fluid characterization

The characterization of oil and gas mixture is conducted using a Black-Oil model. It uses empirical correlation to determine the fluid properties. The current slug tracking employs a similar approach to Santim et al. (2020). The required thermodynamic data is the densities and viscosities of the liquid and gas as well as the superficial tension. All of them in International System of Units (SI). As cited in Section 4.1, Rosa et al.'s (2015) model is isothermal. Therefore, the temperature remains constant, and those properties are a function of the gas pressure only.

As input data, the Black-Oil model requires the following information: °API, GOR, relative gas and water densities, BSW, CO_2 molar fraction, the presence or not of emulsion, and the maximum and minimum values for kinematic viscosity and temperature utilized within the ASTM chart. This research assumes the simulation does not have oil-water emulsions. The following subsections present each required parameter.

4.4.1 Gas density

The gas density is calculated in kg/m³ by:

$$\rho_G = \frac{M_G P_G}{R Z_G T} = \frac{\left(d_G \times 28.9625\right) \times \left(P_G \times 98066.5\right)}{8.0465 \times 1000 \times Z_G \times \left(T + 273\right)} \ , \tag{4.47}$$

where the pressure and temperature are given in kgf/cm² and °C. The relative gas density and temperature are constant. The gas pressure [Pascal] is one of the results obtained by Eqs. (4.1) to (4.14). The gas compressibility is a function of the pseudocritical temperature and pressure, which are calculated by Piper et al.'s (1993) correlation.

When the program is used for air and water simulation, the gas density is the only parameter updated in each time step. It also employs Eq. (4.47), but the gas compressibility factor is equal to a unit. The other required thermodynamic properties are constant. The water

density and viscosity, the air viscosity and surface tension are respectively 999 kg/m³, 8.55×10^{-4} Pa.s, 1.7×10^{-5} Pa.s, and 0.07 N/m.

4.4.2 Liquid density

The liquid density is a function of the live oil, the gas dissolved in the oil and the water fraction:

$$\rho_L = \frac{\text{Mass}_{\text{Oil}} + \text{Mass}_{\text{Water}}}{\left[(1-\text{BSW}) \times B_O + \text{BSW}\right]} \ . \tag{4.48}$$

The oil and water mass are calculated by:

$$\text{Mass}_{\text{Oil}} = (1-\text{BSW}) \times \rho_O + \frac{\rho_G \times 1.225 \times \text{RS} \times 6.29}{35.31467} \ , \tag{4.49}$$

$$\text{Mass}_{\text{Water}} = \text{BSW} \times 1000 \times \rho_w \ . \tag{4.50}$$

where B_O is the volume factor formation and RS is the solution gas-oil ratio. They are calculated by Vasquez and Beggs (1980) and Standing (1947), respectively. The oil density is obtained by °API formulation:

$$\rho_O = \rho_W \left[\frac{141.5}{°\text{API} + 131.5}\right] . \tag{4.51}$$

4.4.3 Gas viscosity

The gas viscosity is determined by Lee et al.'s (1966) correlation:

$$\mu_G = A \cdot \text{Exp}\left[B(\rho_G)^C\right] . \tag{4.52}$$

The A, B and C terms are:

$$\begin{aligned} A &= \frac{(9.4 + 0.02M_G)T^{1.5}}{209 + 19M_G + T} \\ B &= 3.5 + \frac{986}{T} + 0.01M_G \\ C &= 2.4 - 0.2X \end{aligned} \ , \tag{4.53}$$

where T is given in °R and the viscosity is provided in cP.

4.4.4 Liquid viscosity

There are three types of viscosity formulations according to the oil thermodynamic condition. The first one is named as dead oil viscosity (μ_{OD}), in which the fluid is in stock-tank oil condition. For its determination, it is used ASTM relations. This method is a chart that correlates the kinematic viscosity and temperature. The lowest and highest values are provided as input data. The viscosity within this range is calculated by linearization.

The second formulation determines the live oil viscosity, which is the required parameter to the slug tracking system. Unlike the previous one, this fluid is in [P, T] condition. If the oil pressure is below to the bubble point, the viscosity is calculated by Beggs and Robinson's (1975) correlation:

$$\mu_O = A \cdot \mu_{OD}^B \ , \tag{4.54}$$

where the A and B are:

$$\begin{aligned} A &= 10.715\left(RS+100\right)^{-0.515} \\ B &= 5.44\left(RS+150\right)^{-0.338} \end{aligned} \ . \tag{4.55}$$

Eqs. (4.54) and (4.55) are a function of the solution gas-oil ratio (RS) in scf/stb and the dead oil viscosity. If the oil pressure is above the bubble point, the undersaturated oil viscosity is determined by Vasquez and Beggs (1980):

$$\mu_O = \mu_{OB}\left(\frac{P}{P_b}\right)^m \ , \tag{4.56}$$

where the exponent m is:

$$m = 2.6 \cdot P^{1.187} Exp\left(-11.513 - 8.98 \cdot 10^{-5} P\right) \ . \tag{4.57}$$

Eqs. (4.56) and (4.57) are a function of the pressure at the bubble point in psia, and μ_{OB} given by Eq. (4.54). The authors named the oil viscosity below the bubble point as μ_{OB}. The ASTM relations, Eqs. (4.54) and (4.56) provide the viscosity in cP.

4.4.5 Surface tension

The liquid surface tension is calculated by a weighted average between the tension of oil and water and their fractions in the fluid:

$$\sigma_L = \sigma_O \times F_O + \sigma_W \times F_W \ , \tag{4.58}$$

where the tension of each phase is obtained from predefined tables [T *versus* σ].

4.5 Program logic: modeling improvement

Rosa et al.'s (2015) model was implemented using an Object Oriented Programming in FORTRAN language. Therefore, the program organizes the pipeline and cell properties using a list of objects (pipeline sections, bubble and liquid slug variables, thermodynamic properties, etc.). For example, each cell inside the numerical domain has its own information that describes its position, flow and fluid properties. This feature facilitates the tracking and the recording of the cell parameters.

The program main logic remains the same in this updated version. However, the methodologies presented in Sections 4.2, 4.3 and 4.4 added some steps to the original solver. These submodels work as a function or subroutine of the main program, which are called in function of the cell positions and specific criteria. Section 4.2 presents the treatment of singularities in some specific positions of a lazy wave riser, but the same methodology can be used for different unit cells. For example, the riser has two V formats (Section 4.2.1), so two cells can pass through them at the same time, and they should be treated simultaneously. Since that treatment occurred during a period of time (liquid accumulation), the involved variables must be registered as properties of the cell object. The Object Oriented Programming was essential to manage the submodels calling.

Figure 4.16 presents a flowchart that depicts the program implementation logic, showing all added methodologies. The gray elements highlight the updated points developed in this work. The simulation starts with the determination of pipeline sections and their respective inclinations, diameters and roughness. In a sequence, the initial and boundary conditions are determined, and the solution of the equation system initiates. This iterative process continues until it reaches a reference number of cells that exit the pipe. For short pipes (experimental campaigns), this number is 600 cells. In long pipes (oil and gas systems), it is 3 times the number of cells inside the pipe at the start-up procedure. In each time step, Eqs. (4.1) to (4.14) provide

the liquid slug velocity, gas pressure, the bubble and liquid slug parameters. Based on the updated pressure, the thermodynamic properties are refreshed. In oil and gas simulations, the Black-Oil model is invoked. The criteria from singularities submodels are also checked.

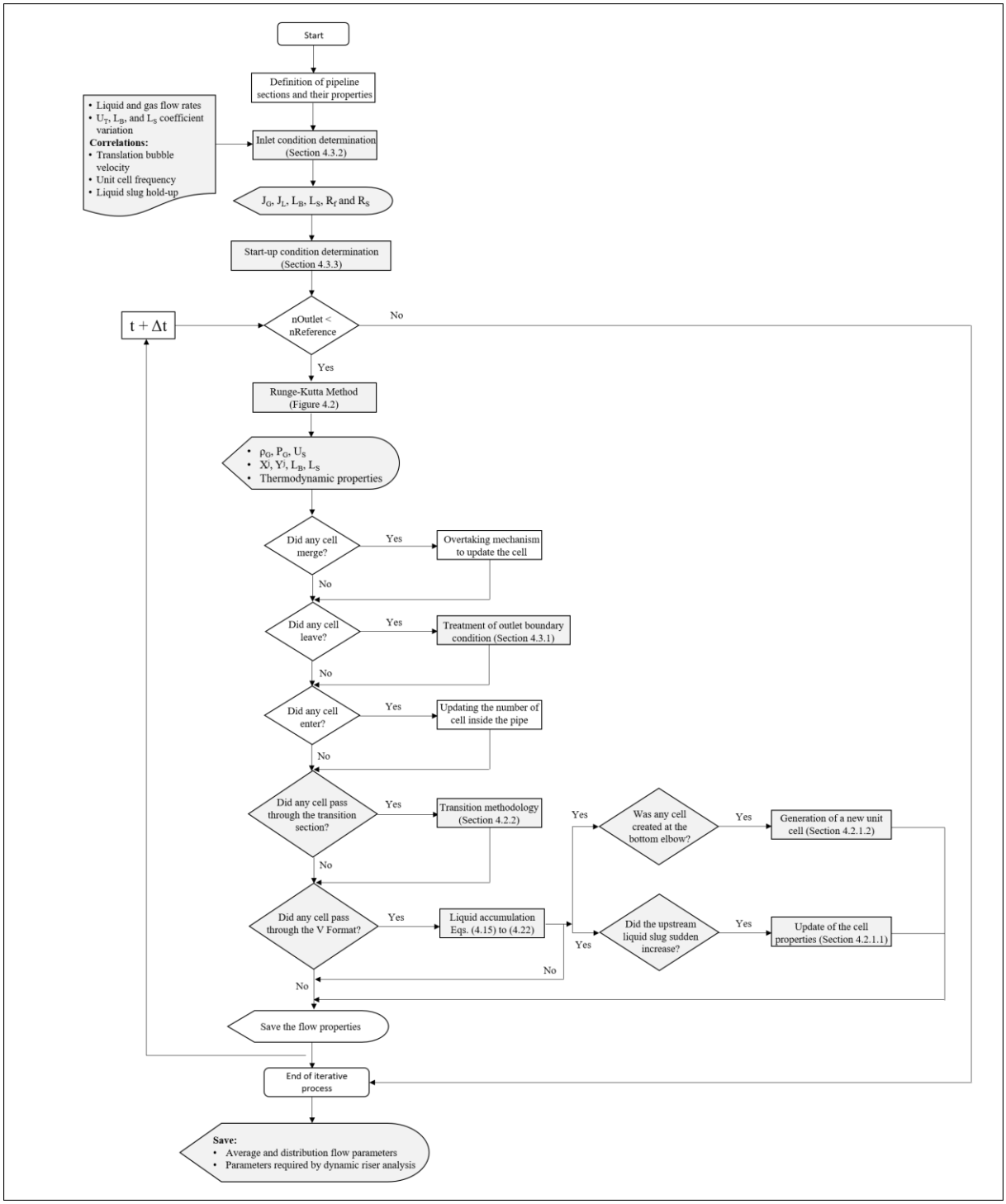

Figure 4.16. Slug tracking flowchart: program logic.

5 RESULTS AND DISCUSSIONS

This chapter presents the results of experimental and numerical analysis. As shown in Table 3.7, the test grid has six operation points, which cover two mixture velocities (2.0 and 4.0 m/s) and four superficial liquid and gas velocities ratios (0.5, 0.67, 1.0 and 1.5). The choice for those mixture velocities aims to represent oil and gas production conditions, and to encounter the slug flow pattern in the entire S curve. Different ratios are employed to assess the gas fraction influence on the flow behavior.

Section 5.1 uses the flow images to describe the phenomena, comparing the main characteristics reported in the literature review. Section 5.2 discusses the slug flow properties obtained by the post-processing program. The coupling of images and data analyses is extremely important due to the potential pattern transition in the downward inclined section. In addition, Section 5.3 compares the experimental data with the results obtained by the numerical model. This comparison validates the proposed models added to the slug tracking.

Section 5.4 highlights a practical application of the numerical model. The current slug tracking simulates the flow through an actual lazy wave riser, which is used in a petroleum field. Andreolli (2018) provided its geometry, production and pressure data. The comparison between the numerical and field data is not just a validation exercise, but also an evidence to the model capacity to simulate the oil and gas flow under high-pressure gradients over long distances and complex geometry pipelines. This analysis reinforces the research credibility and highlights the model relevance to the real-world scenarios.

5.1 Experimental images: phenomenon description

The previous studies highlighted the influence of small inclination changes on modifying the slug flow parameters, the slug formation or the transition to the stratified pattern (Al-safran et al., 2004; Alves et al., 2019; Barros et al., 2022; Taitel and Barnea, 2000; Yoshida et al., 2000; Zhang et al., 2003a; Zheng et al., 1994, 1993). When the slug flow is present, the most influenced parameters are the lengths and void fractions of liquid slug and elongated bubble, as well as the unit cell frequency (Al-Safran et al., 2005; Yin et al., 2018; Zheng et al., 1995). In addition, the operational condition influences the transition to stratified flow in the downward inclined section and the slug flow initiation at the low elbow. Yang et al. (2017) added that the pipe inclination is crucial to the occurrence of that phenomenon. As the lazy

wave riser configuration has more significant inclination changes, the flow parameters and their alteration along the pipe must be studied. This research aims to improve the knowledge about that topic.

The images recorded along the S curve will be qualitatively analyzed to describe the flow behavior. As explained in Section 3.5, the image acquisition is limited to Tests 1, 4 and 5 due to the complex pipeline geometry and the positions of interest. However, those operational conditions cover both mixture velocities and three different superficial gas and liquid velocities ratios (0.5, 1.0 and 1.5). Thus, it is possible to identify the impact of the liquid and gas fraction on the phenomena occurrence. The following analyses discuss the properties of the slug flow structures, the liquid-gas interface on the bubble region, the overtaking mechanism and the potential occurrence of initiation and dissipation mechanisms along the downhill section and low elbows (A and V formats).

Figure 5.1 shows Test 1 images at the first recorded section (riser basis), which demonstrates that the slug flow is not fully developed. The image uses two notations: letters and numbers. The letters (a) and (b) illustrate two different times that highlight the variability of the bubble and liquid regions features. The numbers 1 and 2 show sequential structures in each time. In Figure 5.1 (a.1) and (a.2), the bubble does not have a well-defined profile and the liquid film and slug are extremely aerated. In contrast, Figure 5.1 (b.1) and (b.2) shows that the bubble is longer, and its interface seems more stable, as well as the liquid slug is less aerated. Regarding Tests 4 and 5, those variabilities are not observed. Figure 5.2 presents their images.

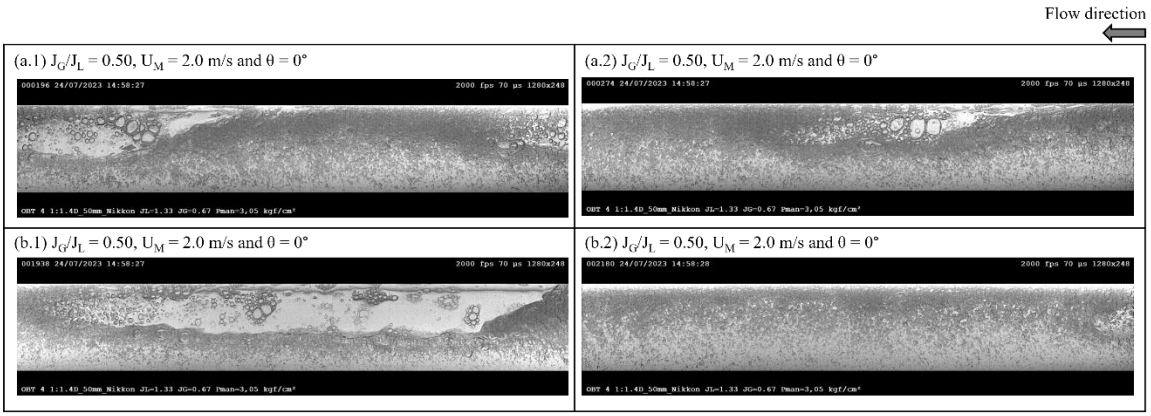

Figure 5.1. Entrance effect for Test 1 at S1 (θ = 0°): (a) and (b) illustrate pictures of different times, while the numbers 1 and 2 display both slug flow structures.

Figures 5.2, 5.3, 5.4, 5.5, 5.7 and 5.8 present the flow images obtained from the six positions of interest (see Section 3.5). All figures follow the same notation and setup. The notation a, b and c represent Test 1 (U_M = 2.0 m/s and J_G/J_L = 0.5), Test 4 (U_M = 2.0 m/s and

J_G/J_L = 1.5) and Test 5 (U_M = 4.0 m/s and J_G/J_L = 1.0), respectively. Each letter has the numbers 1 and 2, which display the flow structures.

Figure 5.2 (a.1), (b.1) and (c.1) shows that the bubble has a plane interface at S1, as described by Shoham (2005) for horizontal flow. Nevertheless, the bubble nose does not completely touch the upper pipe wall. The bubble region also contains a thick and aerated liquid film at the bottom of the pipe. There is also an aerated and thin liquid film around the bubble, which is drained on the pipe wall. As illustrated in Figure 5.1 and 5.2 (c.1), some bubbles have their nose quite aerated, which makes it harder to extract the bubble front from the impedance sensor signal. The sensor description is in Sections 3.1.1 and 3.2, and Section 5.2 discusses the results obtained from them. The liquid slug is aerated, and the dispersed bubbles are concentrated at the top of the pipe due to the buoyancy, as shown in Figure 5.2 (a.2) and (b.2).

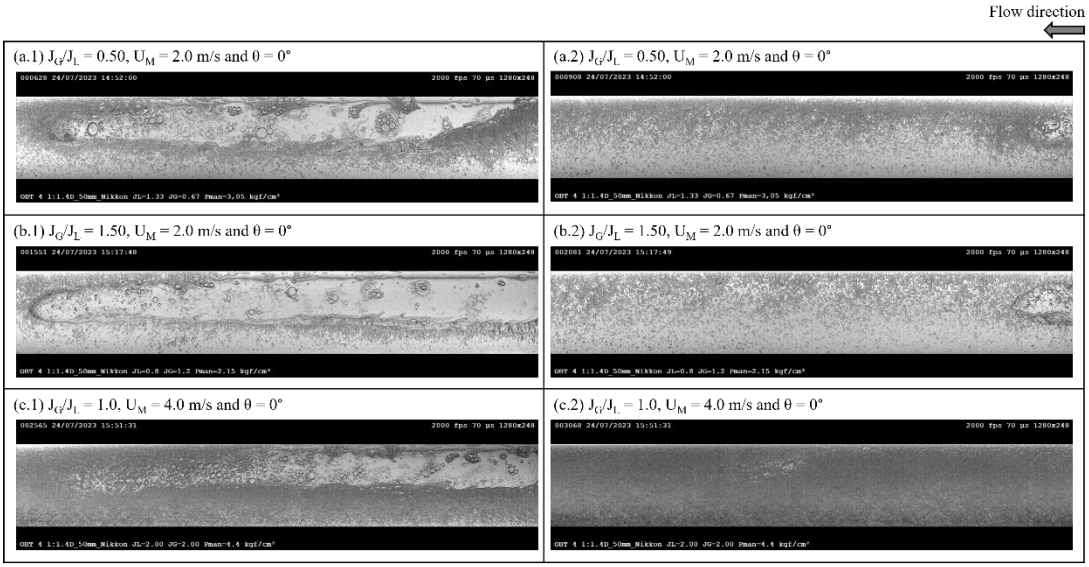

Figure 5.2. The flow images at S1 (θ = 0°) for Tests 1 (a), 4 (b) and 5 (c): the numbers 1 and 2 respectively display the bubble and liquid slug features.

Tests 1 and 4 have the same mixture velocity, but Test 4 has a higher superficial gas and liquid velocities ratio. As the gas fraction increases, the bubble and liquid slug lengths seem longer than observed in Test 1. The elongated bubble transports the higher amount of gas in this region, and the liquid slug is less aerated as presented in Figure 5.2 (b.1) and (b.2). The thin liquid film on the pipe wall is also noted, as shown in Figure 5.2 (b.1). The images from Test 5 are presented in Figure 5.2 (c.1) and (c.2). The superficial gas and liquid velocities are the same (U_M = 4.0 m/s) in that test. The liquid film and slug are extremely aerated. It complicates the interpretation of the bubble profile. Figure 5.2 (c.1) shows that the bubble also has a thin and aerated liquid film around it. As shown in the center of Figure 5.2 (c.2), there is

the coalescence of the dispersed bubble in the liquid slug. This process can further result in a new unit cell.

Figure 5.3 reproduces the flow structures that have just traveled across a pipe orientation change (horizontal to upward inclined pipe). According to other studies, this change also works as a V format of the hilly terrain. Due to the new inclination (approximately 43°), the elongated bubble starts to move to the center of the pipe and reduces its liquid film thickness. Figure 5.3 (a.1), (b.1) and (c.1) demonstrates that for Tests 1, 4 and 5. This movement (transition from plane to concentric) causes some instabilities in the air-liquid interface. Figure 5.3 (a.1) and (b.1) shows the film thickness has a wavy surface. In addition, that figure also reveals that the film is not symmetric due to the gravity effect; the upper film is thinner than the lower one. Due to the lower superficial liquid velocity, the gravity effect drains the liquid film in Test 4. The collision between that countercurrent flow and the flowing mixture generates a recirculation area in the bubble tail[1]. This phenomenon might increase the coalescence rate if the liquid slug is small. It can explain why the pseudo-slugs are not observed in those images. The countercurrent liquid film might enhance the liquid accumulation when this mechanism occurs near the low elbow. In addition, Yin et al. (2018) suggested that phenomenon might cause the generation of a new unit cell in that position.

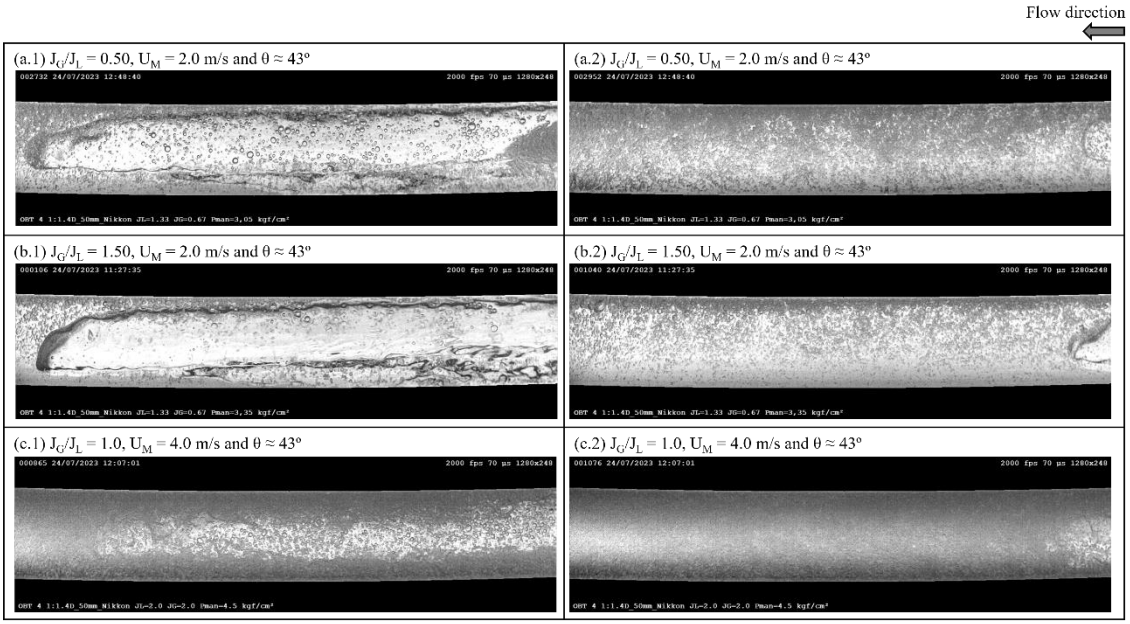

Figure 5.3. The flow images at S3 (approximately θ = 43º) for Tests 1 (a), 4 (b) and 5 (c): the numbers 1 and 2 respectively display the bubble and liquid slug features.

[1] See this phenomenon in YouTube link (Section 3.5), the movie is "JL_0.8_JG_1.2\E3\TestSession 001".

The liquid slug holdup at S3 seems lower than in S1 (see Figures 5.2 and 5.3). This behavior agrees with Zheng et al. (1995) since the authors explained that tiny bubbles are trapped in the liquid slug at the low elbow. Zheng et al. (1995) and Al-Safran et al. (2005) also comment on the increase of liquid slug length in the uphill section, but this behavior is not visualized in the movies.

Figure 5.4 illustrates the flow structures close to an important singularity discussed by Taitel and Barnea (2000), the A format. As shown in Figure 2.2, the authors suggested that the change from uphill to downhill inclined pipelines causes the formation of a dry zone at the elbow and a potential dissipation of the liquid slug at the upstream section. The first phenomenon will be discussed based on Figure 5.4. Due to experimental limitations, capturing the images at the top of the curve was impossible. However, the recorded section is close enough to describe the effect of the pipeline orientation change in the flow behavior.

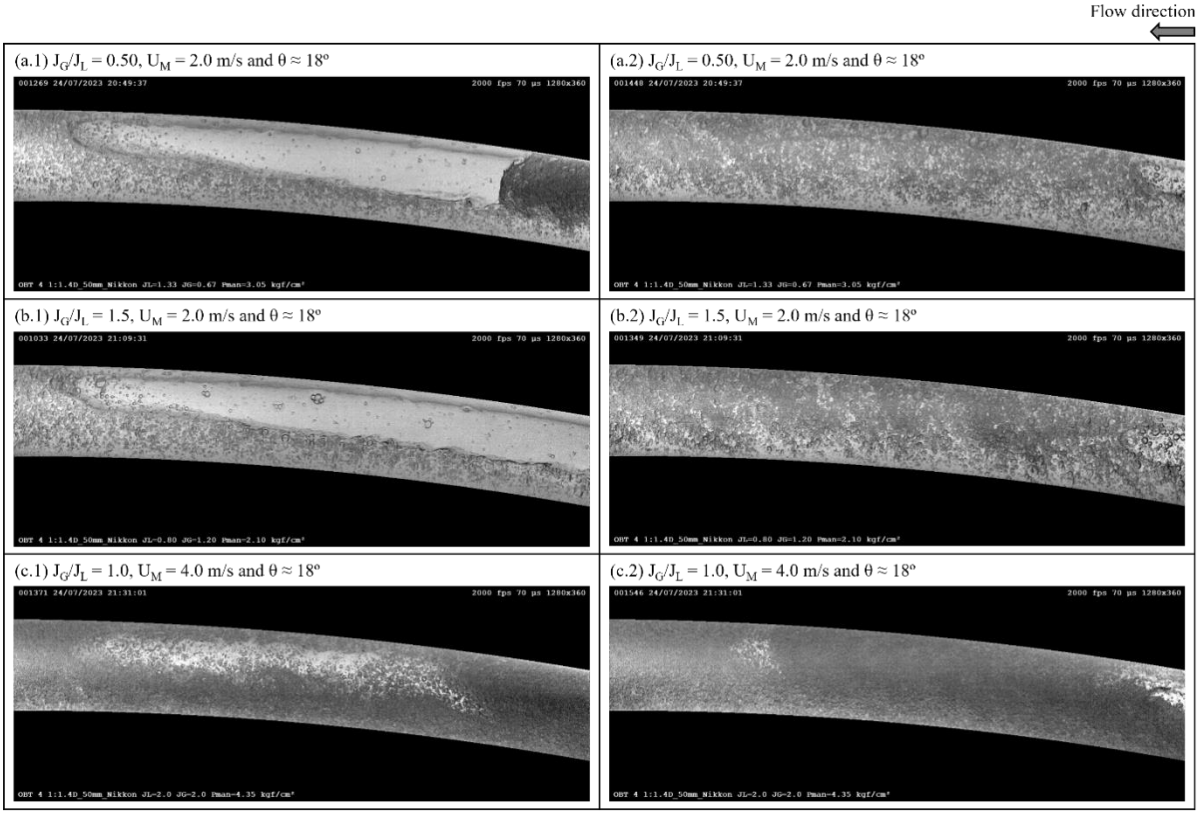

Figure 5.4. The flow images in the recorded section between S4 and S5 (approximately θ = 18°) for Tests 1 (a), 4 (b) and 5 (c): the numbers 1 and 2 respectively display the bubble and liquid slug features.

Unlike Figure 5.3, the elongated bubble returns to a plane interface in all tests. Figure 5.4 (a.1), (b.1) and (c.1) demonstrates that. For the mixture velocity equal to 2.0 m/s, Test 1 has the highest superficial liquid velocity. The presence of a higher amount of liquid in

the system leads to longer slugs. Test 1 images support this statement. The liquid film looks less aerated between S4-S5 compared to S3. The recorded movies[2] also demonstrate the bubble and liquid film travel in the same direction. Taitel and Barnea (2000) pointed out the liquid film drainage occurs during the bubble passage through the top. However, the unit cell quickly passes over this position, and there is not enough time for that phenomenon in Test 1. For Test 4, there is more gas in the system (higher superficial gas and liquid velocities ratio), thus the bubble is larger than in Test 1. As the bubble takes more time at the top of the curve, it is noted that part of its liquid film travels in the flow direction, and the other is drained to the upstream liquid slug. Nonetheless, this liquid loss is not enough to create a dry zone.

Test 5 represents the mixture velocity equal to 4.0 m/s, thus the structures travel quickly across this section. The liquid film and the elongated bubble travel in the same direction. Al-Safran et al. (2005) pointed out the hilly terrain does not affect the flow structures for high liquid and gas velocities. Lastly, Figure 5.4 (c.2) shows that the high aeration within the liquid slug results in the coalescence of the dispersed bubble (Taitel et al., 1980).

Figure 5.5 reproduces the phenomena that occur in the downward inclined section. According to Taitel and Barnea (2000), the losing liquid film at the top elbow results in the liquid slug dissipation at the downhill and the bubble void fraction (or film thickness) change. Taitel et al. (2000) and Zhang et al. (2003) suggested that the superficial velocities influence the liquid slug dissipation. Al-Safran et al. (2005) created five categories to describe it. They also pointed out that the gravity force (pipe inclination) also influences that dissipation. This section geometry has a high gravity influence since the minimum pipe angle is approximately - 45°. Al-Safran et al. (2005) extended Zhang et al.'s (2003) statement and explained that the increase of the gas velocity minimizes the gravity effect. In addition, the increase of superficial liquid velocity results in the quick passage of structure across this section. Both consequences reduce the hilly terrain effects. However, the authors alerted that reduction is not expected if the gas velocity is high enough to create quite aerated and foamy slugs.

[2] See this phenomenon in YouTube link (Section 3.5), the movie is “JL_1.33_JG_0.67\E4-5\TestSession 000”.

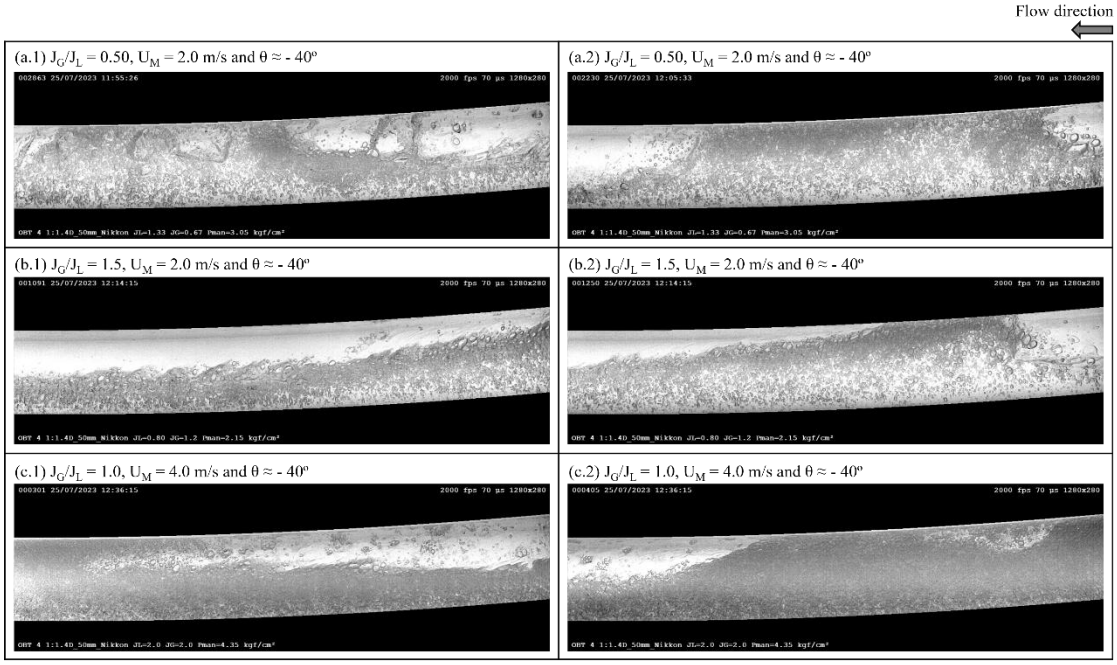

Figure 5.5. The flow images in the recorded section between S6 and S7 (approximately θ = 40°) for Tests 1 (a), 4 (b) and 5 (c): the numbers 1 and 2 display the flow structures.

As demonstrated in Figure 5.5 (a.2) and (b.2), there are some liquid slugs on the downhill section in Tests 1 and 4. Thus, the transition to stratified flow did not occur until this position. Nonetheless, the inclination pipe strongly influences the flow structures in both tests. Test 1 has the lowest superficial gas and liquid velocities ratio; thus, the system has a large liquid mass. On the other hand, Test 4 has the highest ratio and, consequently, the highest gas fraction. Due to the gravity effect, liquid film and slug are faster than the elongated bubble. This quick movement causes three phenomena:

i. The high bubble coalescence rate is due to liquid loss, which increases bubble length and dissipates some liquid slug. Figure 5.6 (a) exemplifies this for Test 4.
ii. The liquid film is discharged on the downstream liquid slug as a jet, which can break the elongated bubble nose, as demonstrated in Figure 5.5 (a.1). Barros et al. (2022) observed the same behavior for tests with low gas-to-liquid ratio. In these cases, the gravity effect is more intense, resulting in a liquid film even faster and a recirculation area close to the bubble nose. Its discharge can justify the observed phenomenon.
iii. As the bubble is slower than the liquid film, it pushes the air-liquid interface and creates small waves, modifying the region's characteristics. The same

elongated bubble has different film thicknesses, as shown in Figure 2.2, proposed by Taitel and Barnea (2000). Figure 5.6 (b) shows both behaviors.

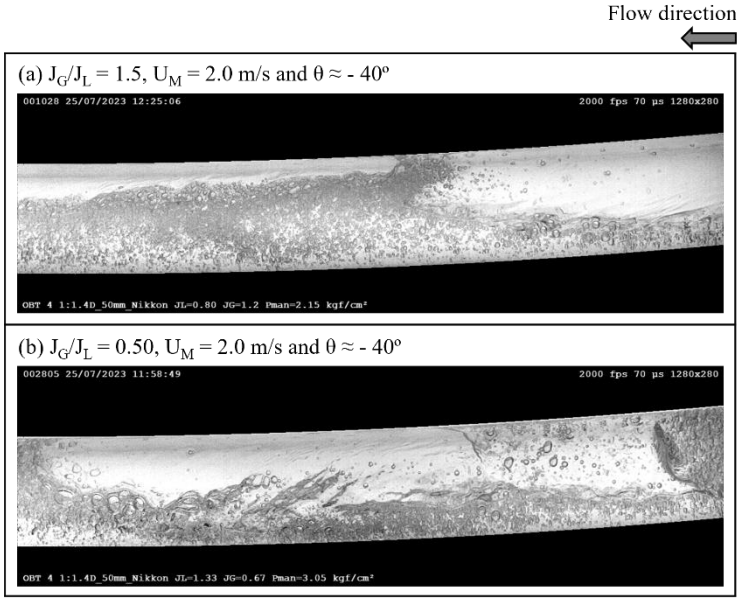

Figure 5.6. The effects of downward inclined pipe on the flow structures: (a) bubble coalescence and (b) instabilities on the air-liquid interface.

Taitel et al. (2000) pointed out that the transition from slug to stratified pattern occurs after some distance in the downhill section. In addition, this distance depends on the superficial liquid and gas velocities. Thus, the operational condition of Tests 1 and 4 will affect the dissipation distance and the flow behavior. Their flow images support that, as shown in Figure 5.5 (a) and (b). Since there is more liquid in the pipe and its velocity is higher in Test 1, the hilly terrain influence is slightly less than in Test 4. The (i), (ii) and (iii) mechanisms are observed in Test 1. However, the liquid slug is longer in the downhill section compared to Test 4, as illustrated in Figure 5.5 (a.2) and (b.2). Since there is more gas in Test 4, the liquid slug is small, and it facilitates the bubble coalescence. The (i) and (iii) mechanisms are noted in this test. The images show that the liquid slug dissipation is almost complete in Test 4. Thus, the transition to stratified flow occurs close to this section.

Based on the recorded images from Test 4, the slug flow structures are poorly defined due to the intense and quick interaction in the downward inclined section. This flow behavior can affect the representativeness of the experimental data at the S6 and S7 since the impedance sensors identify the passage of the structure fronts.

Test 5 has the highest mixture velocity, and both phases have the same superficial velocity. The increase of these velocities reduces the hilly terrain effect, as reported by Al-

Safran et al. (2005). Figure 5.5 (c.1) and (c.2) show that the alternate passage of bubble and liquid slug occurs, even though the flow is quite aerated. Figure 5.5 (c.2) illustrates a small bubble within the liquid slug, which can be correlated with the bubbles previously demonstrated in Figure 5.2 (c.2) and Figure 5.4 (c.2). Nonetheless, the leading bubble traps these short bubbles in the downhill section.

Alves et al. (2019) and Barros et al. (2022) analyzed the flow along the downward inclined section through an experimental campaign. Both have operational points similar to the current test grid (see Table 3.7). Their inner diameter and working fluids coincide with this research, but their inclination is lower. Figure 5.5 (a.2) shows that the bubble tail is thin and long. Alves et al. (2019) and Barros et al. (2022) claimed that is a result of the liquid film acceleration. The higher superficial liquid velocity (Test 1) intensify this acceleration (Barros et al., 2022). In addition, that higher acceleration retards the bubble coalescence. It can justify the fact of the transition to stratified pattern occurred faster in Test 4. Similar to the current recorded images, both authors observed in their tests that the flow remains in the slug flow pattern in an operational point similar to Test 5.

Figure 5.7 demonstrates the influence of the V format on the flow behavior. As the upstream section is a downward inclined pipe and the downstream is an upward inclined tube, the hilly terrain effects are expected to be more pronounced than at S1 (riser basis). Zheng et al. (1995) and Taitel and Barnea (2000) commented about the unit cell generation and the sudden increase of liquid slugs in this region. Al-Safran et al. (2005) and Yin et al. (2018) deepened their studies to describe the slug initiation across this section. According to the authors, there are three types of slug formation: (a) Kelvin-Helmholtz instability, (b) wave coalescence and (c) collision between the flowing liquid in the flow direction and the falling liquid from the upward line. Those mechanisms will be analyzed in the following figures. However, Yin et al. (2018) attested that the last two methods were observed for low superficial liquid velocities experiments.

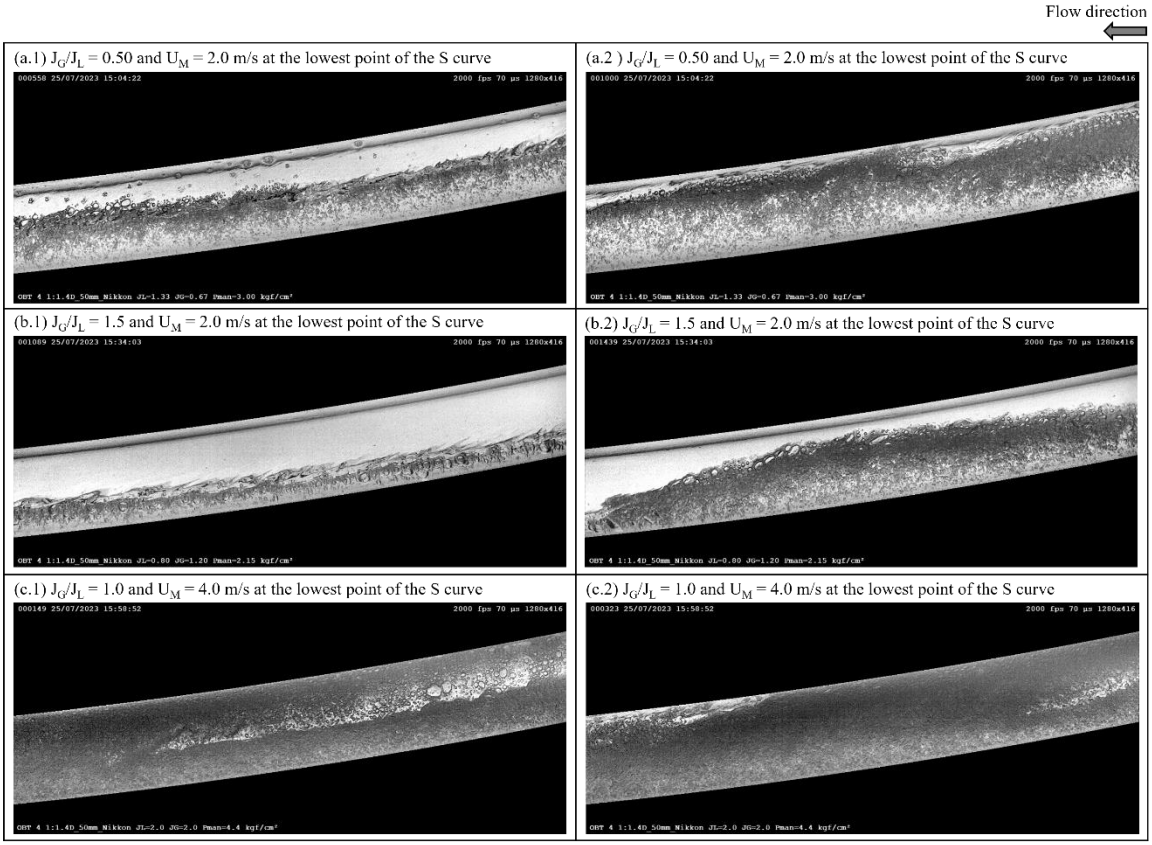

Figure 5.7. The flow images at S8 (the lowest point of the S curve) for Tests 1 (a), 4 (b) and 5 (c): the numbers 1 and 2 respectively display the flow structures.

Based on Test 1 and 4 images at S8, it is noted that the transition to stratified flow occurred after the last recorded section (S6-S7). As demonstrated in Figure 5.7 (a.1) and (b.1), the gas phase flows at the top of the pipe and the liquid at the bottom. This figure also shows that the film thickness varies significantly, representing the generated instabilities (waves) in the air-liquid interface. For Test 1, the liquid film occupies an important part of the cross-sectional area, which can correlate with the high amount of the liquid accumulated at S8. Figure 5.7 (a.2) exemplifies when this wave grows and blocks the pipe, generating a new liquid slug at the elbow. Al-Safran et al. (2005) correlated the slug initiation at the elbow with the Kelvin-Helmholtz instability. As the slug formation due to the wave coalescence occurs downstream of the elbow (Al-Safran et al., 2005; Yin et al., 2018), it will be discussed in the following S9 images. In this test, the last formation type (liquid collision) is not observed since there is no backflow from the downstream pipe.

Test 4 has two different behaviors in relation to Test 1. Due to the higher gas fraction, the gas phase occupies a significant part of the cross-sectional area, as shown in Figure 5.7 (b.1). In addition, Figure 5.7 (b.2) demonstrates that the instabilities are insufficient to block the pipe. Thus, the transition to slug flow does not occur at S8 in Test 4.

The alternate passage of bubble and liquid slug is kept at the S8 in Test 5. Most structures are long, and there is no strong interaction between them. Nonetheless, there are isolated cases in which small liquid slugs are present, as shown in Figure 5.7 (c.2). Due to the high aeration, it is complicated to assess if it is a new slug generation (pseudo-slugs) or a small liquid slug from the downhill pipe.

The last recorded position (S9) demonstrates the flow behavior in the upward-inclined section. The S9 is close to S8, so the hilly terrain influences are still observed. It shows the flow behavior after the singularities of the S curve. According to Zheng et al. (1995), Taitel and Barnea (2000) and Zhang et al. (2003), there is an increase in the liquid slug length and the unit frequency in this section. However, Al-Safran et al. (2005) and Yin et al. (2018) commented that the last parameter depends on the slug initiation type at S8 and the position of interest. If the slug initiation occurs through the wave coalescence mechanism, it will generate small slugs (pseudo-slugs) that are quickly dissipated. In this case, the unit cell frequency changes along the first meters of the uphill section. As Tests 1 and 4 are not in the slug flow pattern at S8 (bottom elbow), the potential transition might occur close to S9, and then the flow is not fully developed. Moreover, the air-liquid interface at the bubble region might also change due to the pipe inclination.

Figure 5.8 (a.1) and (a.2) shows the presence of slug flow in the upward inclined section in Test 1. The images demonstrate that the flow is not steady; there is an intense interaction between the structures. Figure 5.9 (a) illustrates the coalescence mechanism. The recirculation zone accelerates the upstream bubble (which is close to the leading bubble tail). This process frequently occurs in Test 1 due to the liquid slug size. Al-Safran et al. (2005) and Yin et al., (2018) correlated the slug initiation downstream the low elbow to the wave coalescence. The high cell frequency and the formation of pseudo-slugs are characteristics of this method. Figure 5.9 (b) illustrates both features. Regarding the elongated bubble, Figure 5.8 (a.1) shows that it migrates to the center of the pipe due to its inclination. In addition, the longer bubbles still have instabilities in the air-liquid interface. Figure 5.9 (c) demonstrates a moment when the wave could block the pipe and break the elongated bubble. Thus, the slug initiation was happening.

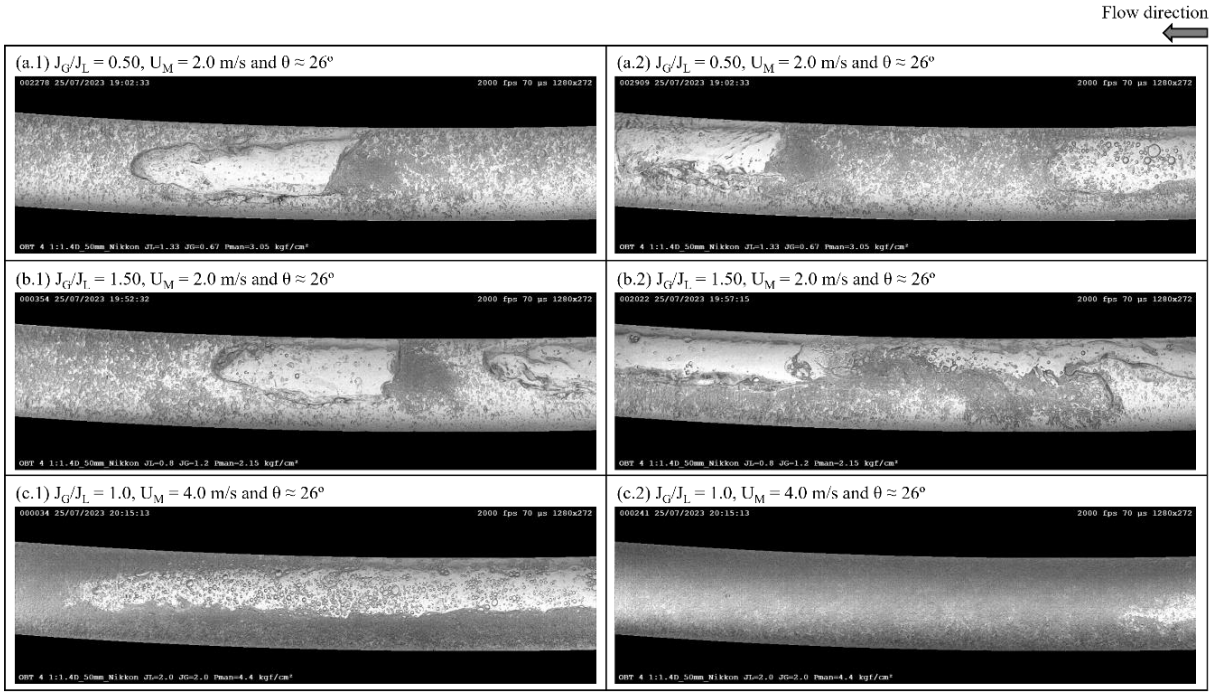

Figure 5.8. The flow images at S9 (θ = 26°) for Tests 1 (a), 4 (b) and 5 (c): the numbers 1 and 2 respectively display the flow structures.

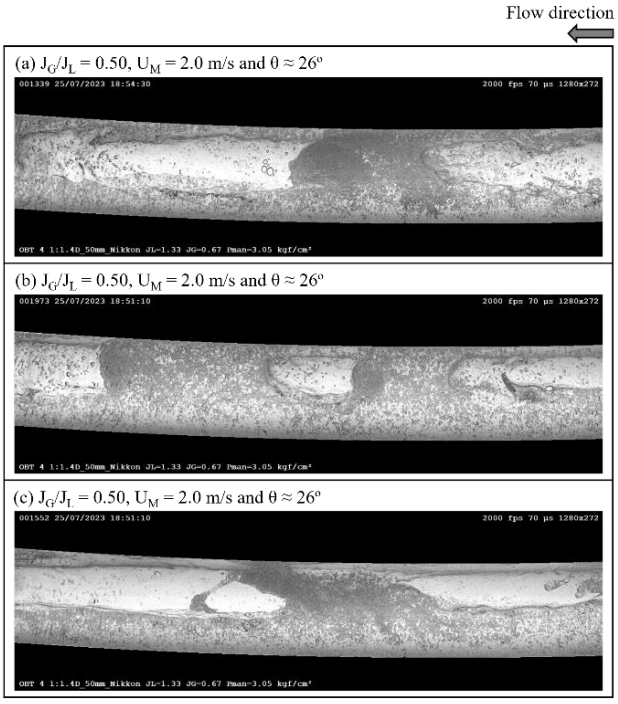

Figure 5.9. The effects of upward inclined pipe on the flow structures for Test 1: (a) bubble coalescence, (b) high cell frequency and (c) generation of a new slug.

Figure 5.8 (b.1) and (b.2) demonstrates the transition to slug flow in Test 4. The alternate passage of bubble and liquid slugs has already occurred, as shown in Figure 5.8 (b.1). However, the slug initiation process is ongoing. This test has bubbles longer than Test 1, and these structures are broken by the interface instabilities, as shown in Figure 5.8 (b.2). The number of new cells and the coalescence between them will influence the unit cell frequency

downstream of this section. In Test 5, the flow is similar to that observed in S8. Figure 5.8 (c.1) and (c.2) illustrates the bubble and liquid slugs. Both structures are longer than the other tests. The unit cells do not present high interaction. The small liquid slug observed at S8 probably disappeared due to the bubble's coalescence. The unit cell frequency slightly reduces compared to S8.

In summary, the transition to a stratified pattern occurs in the downward inclined section in Tests 1 and 4, according to the flow regime map presented by Santim et al. (2020). The flow behavior in both tests aligns with the description of Category 1 from Al-Safran et al. (2005). In the downward pipe (S6-S7 section), the liquid slug is not totally dissipated. However, it occurred in the vicinity, as observed at S8 (low elbow). It is also noted that the slug initiation process is complex. Modeling the phenomena involved in this process is complicated for a slug tracking model since it cannot predict the slug formation. In Test 5, the slug flow is observed along the entire S curve. The increase of the mixture velocity reduces the influence of the hilly terrain, as pointed out by Zheng et al. (1995), Yoshida et al. (2000), Zhang et al. (2003) and Al-Safran et al. (2005).

5.2 Experimental data: slug flow parameters

This section presents the experimental data of the pressure transducers and impedance sensors obtained for the six tests (Table 3.7). As explained in Section 3.2, the raw data post-processing results in the mean and distribution parameters of the slug flow. The impedance sensors identify the bubble and liquid slug passage across the first and second probes, and then the flow parameters are calculated. Thus, the presence of well-defined structures is essential to ensure data quality. For example, Figures 5.5 and 5.6 show different phenomena in the downhill section that can complicate that identification. Figure 5.7 (a) and (b) demonstrates that the transition to slug flow at S8 is ongoing, so the impedance sensors cannot correctly identify it. Thus, the representativeness of the data from each station will be analyzed based on previous discussions.

The post-processing program consists of individually treating each acquisition (120 seconds) and coupling the datasets (2, 4 and 6 repetitions). Those three samples lead to similar distributions for the parameters: translation bubble velocities, dimensionless bubble and slug lengths. Therefore, the data collection is enough to characterize the flow randomness.

Figures 5.10 to 5.15 show the following average data for Tests 1 to 6: (a) P_G - Gas pressure at bubble, (b) U_T -Translation bubble velocity, (c) V_S - Liquid slug front velocity, (d) Unit cell frequency, (e) L_B/D - Dimensionless bubble and (f) L_S/D - liquid slug lengths. These parameters are calculated by Eqs. (3.8), (3.3), (3.4), (3.7), (3.5) and (3.6), respectively. Those data are presented along the S curve, which contains 10 measuring stations named as S1 to S10. The relationship between pipeline height and length is depicted in each figure to facilitate the interpretation of the results. The distance from the air-water mixer to those stations are 6.44 m (275D), 7.56 m (323D), 9.25 m (395D), 10.94 m (467D), 11.81 m (505D), 12.69 m (542D), 13.79 m (589D), 14.90 m (637D), 16.00 m (684D), e 17.11 m (731D). For the following analyses are important to highlight that the stations S1-S2 and S7-S8-S9 represent the V format of the hilly terrain and the S4-S5-S6 the A format. The mean values obtained by the datasets with four and six repetitions are similar or coincident. The gas pressure profile is comparable in all tests, regardless of the number of repetitions.

Figure 5.10 demonstrates the Test 1 (J_G/J_L = 0.50 and U_M = 2.0 m/s) data. The bubble translation velocity (U_T) slightly increases between S1 and S3 (6.4%) due to gas expansion, and the V_S has a minor reduction (2.4%), as shown in Figure 5.10 (b) and (c). The first V format (S1-S2) does not influence the flow properties. U_T, L_B, V_S and L_S reduce by 18.7%, 7.8%, 16.2% and 25.8% at the beginning of the A format (S4). As discussed in Figures 5.5 (a) and 5.6, the high coalescence rate leads to the increase of the bubble (37.4%) and liquid slug (3.3%) lengths and the reduction of unit cell frequency (32.4%) between S5 to S7. Figure 5.10 (d), (e) and (f) shows that. The liquid film velocity tends to increase due to the gravity forces acting in the liquid. In addition, Barros et al. (2022) observed in their experimental campaign that U_T reduces in the downward section, and they addressed this phenomenon to the gravity acting in the liquid and the buoyancy effect in the gas phase. The authors also pointed out that in operational conditions with higher liquid fraction (as Test 1), the bubble velocity is also reduced due to the recirculation area generated by the discharge of liquid film in the downstream slug. Figure 5.5 (a) demonstrates the liquid film behavior. This process delays the bubble passage between the impedance sensors, so the time passage (Δt_B) increases and U_T reduces (see Eq.(3.3)). As also observed by Barros et al. (2022), the bubble tail velocity (V_S) is higher than U_T along the downhill section (S5 to S7) due to the gravity effects. As the inclination increases, the V_S becomes even higher than U_T at S5 (4.6%), S6 (8.0%) and S7 (15.5%).

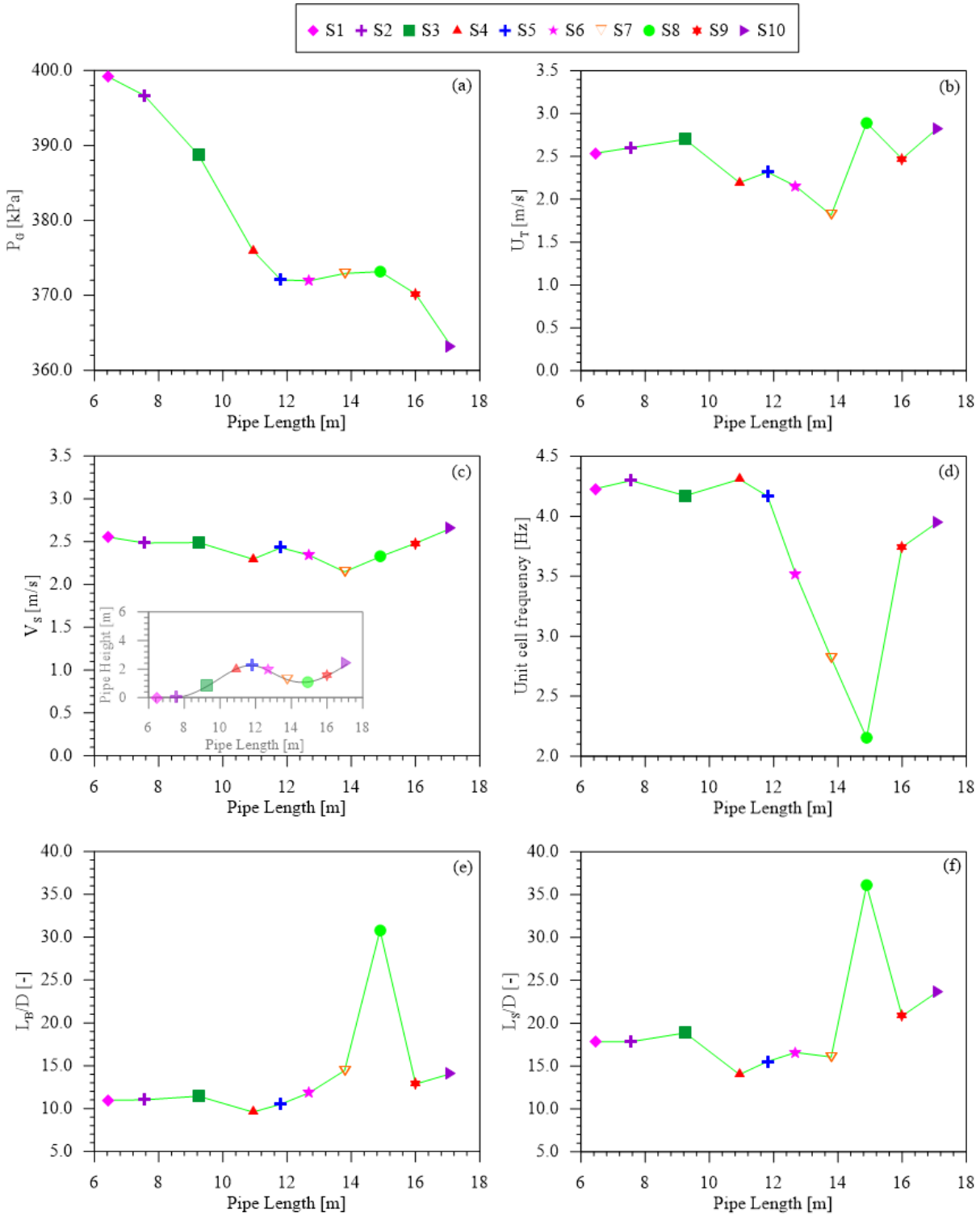

Figure 5.10. Averaged experimental data for Test 1 (J_G/J_L = 0.50 and U_M = 2.0 m/s): (a) gas pressure, (b) translation bubble and (c) liquid slug front velocities, (d) unit cell frequency and dimensionless (e) bubble and (f) liquid slug lengths.

The impact of the second V format (S7-S8-S9) is more notable, especially at S8. As discussed in Figure 5.7 (a), the process of slug formation has just restarted at S8. Thus, the data obtained by the impedance sensor is unrealistic and must be disregarded. Figure 5.10 (d) and (f)

presents an increase in liquid slug length (13.6%) and frequency (5.6%) between S9 and S10. The first parameter increases due to the liquid accumulation and flow development. The frequency is higher at S9 due to the slug formation, as shown in Figure 5.9. Since the generation of unit cells is still occurring, an increase in this parameter is expected at S10.

Figure 5.10 (a) shows the pressure evolution along the S curve. It is evident in the graphic that the pressure varies in three manners. Between S1 to S5 (horizontal to the top of the curve), the pressure gradient is - 5.04 kPa/m. From S5 to S8 (downward section), the pressure has a slight increase of 1.10 kPa due to the pipe inclination. In a sequence, between S8 to S10 (low elbow to upward section) the pressure gradient is - 4.5 kPa/m. The pressure gradient for the entire pipe is equal to - 3.37 kPa/m.

Figure 5.11 presents the Test 2 (J_G/J_L = 0.67 and U_M = 2.0 m/s) data. Tests 1 and 2 have the same mixture velocity and similar superficial liquid and gas velocities, but Test 2 has a higher gas fraction. The images from Tests 1 and 4 depict that the increase of the gas-to-liquid ratio induces a quicker transition to stratified flow. The liquid slug dissipates faster in the downward inclined section due to the coupling of the longer bubble lengths and the gravity effects. Nonetheless, the properties from Tests 1 and 2 present a similar behavior as demonstrated in Figures 5.10 and 5.11. Thus, the increase of the gas velocity in this test is not enough to change the flow behavior significantly. Thus, S8 data is disregarded by Test 1 images.

Figure 5.11 (b) shows that the bubble nose velocity (U_T) has lower reduction (10.0%) in the downhill section (S5 to S7) compared to measure in Test 1 (21.7%). The superficial liquid velocity in Test 2 is lower than in the previous test, so the liquid film also slows down. Figure 5.11 (e) shows the bubble length suddenly increases between S6-S7 (59%) and S7-S8 (83.4%). There is a higher coalescence rate because of the higher amount of gas in the system, which results in longer bubbles and a frequency reduction. The unit frequency slightly reduces between S9-S10 (0.8%), as illustrated in Figure 5.11 (d). According to Zheng et al. (1995), Taitel and Barnea (2000), Al-Safran et al. (2005) and Yin et al. (2018), it could occur due to the dissipation of pseudo-slugs.

Regarded to the gas pressure, Figure 5.11 (a) is similar to Test 1. The pressure evolution has three different behaviors. Between S1 to S5 (horizontal to the top of the curve), the pressure gradient is - 4.64 kPa/m. From S5 to S8 (downward section), the pressure is almost constant (increase of 0.29 kPa). Since the gas flow ratio is higher than in Test 1, the gravitational

impact in the downhill section is lower. In a sequence, between S8 to S10 (low elbow to upward section) the pressure gradient is - 4.1 kPa/m. The pressure gradient for the entire pipe is equal to - 3.15kPa/m.

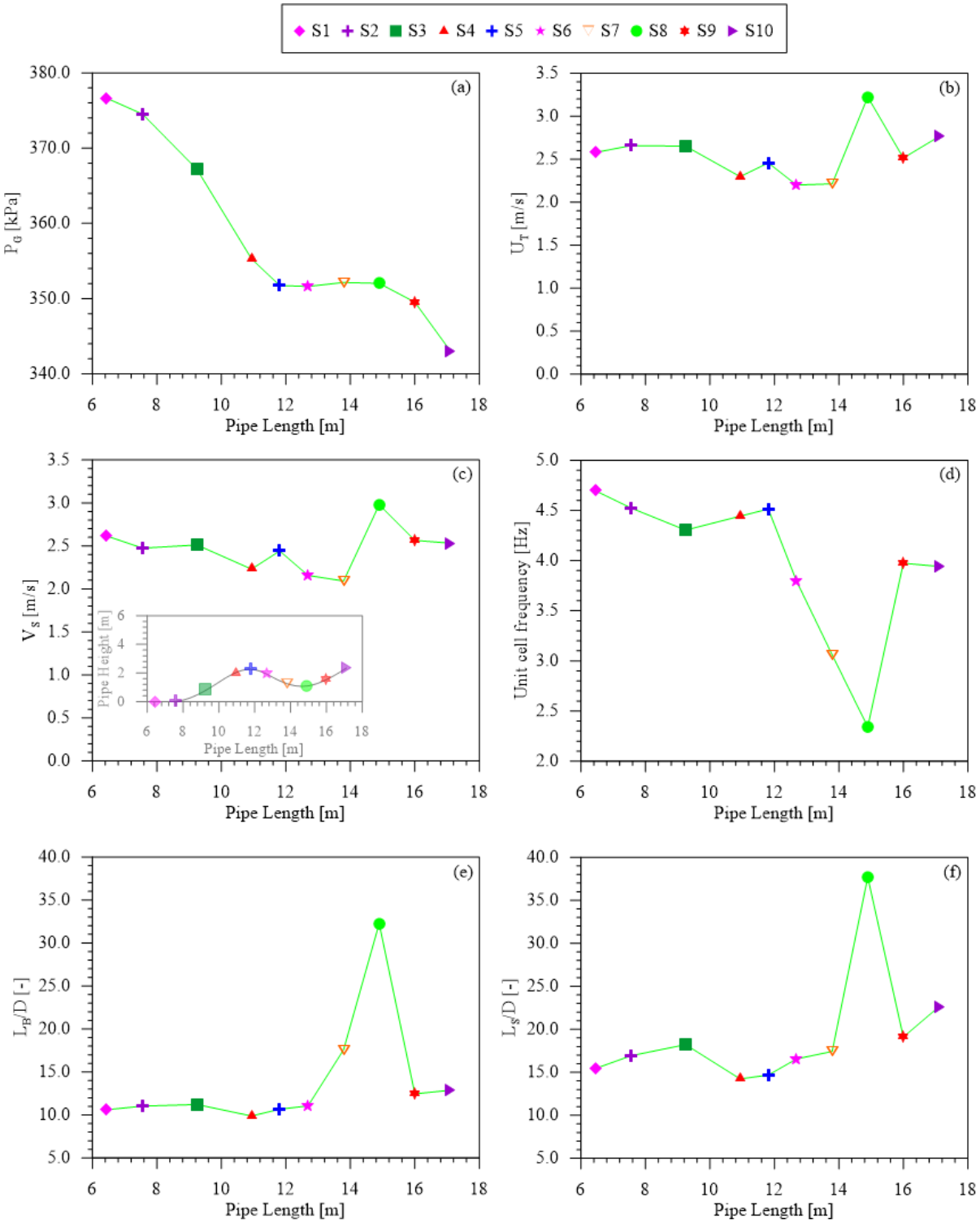

Figure 5.11. Averaged experimental data for Test 2 (J_G/J_L = 0.67 and U_M = 2.0 m/s): (a) gas pressure, (b) translation bubble and (c) liquid slug front velocities, (d) unit cell frequency and dimensionless (e) bubble and (f) liquid slug lengths.

Figure 5.12 shows the data from Test 3 (J_G/J_L = 1.0 and U_M = 2.0 m/s). In this case, both phases have the same superficial velocities. Tests 1 to 4 have the same mixture velocity, but the gas-liquid ratio gradually increases. Since the images of the lowest (Test 1 with J_G/J_L = 0.5) and highest (Test 4 with J_G/J_L = 1.5) superficial gas and liquid velocities ratio were recorded only, these tests support the analysis of the current data. Figures 5.12 and 5.13 show that Tests 3 and 4 share some similarities along the A and V formats. Figure 5.12 (e) and (f) illustrates that the bubble and liquid slug lengths vary between S1-S2 (L_B and L_S has an increase by 16.0% and 19.8%) and S2-S3 (L_B reduces by 6.7% and L_S increases by 8.0%). As the cell frequency gradually decreases (11.0%) between S1 and S3, there is no slug initiation in the first V format. Therefore, the presence of longer liquid slugs at S2 occurs due to the upstream liquid slug picks up the accumulated liquid on the riser basis (S1). In addition, the cells interact, and the number of unit cells decreases. Tests 1 and 4 images (Figure 5.3) demonstrate that the bubble starts to change its interface to concentric near to S3. It can justify the bubble length reduction and liquid slug increase.

Similar to Test 4, Figure 5.12 (b) shows an abrupt change in U_T across the A (S4-S5-S6) and V (S7-S8-S9) formats. The other parameters also suffer this alteration, as shown in Figure 5.12 (c), (d), (e) and (f). Based on the images from Test 4, it occurs due to the transition to the stratified pattern. According to Taitel and Barnea (2000) and the captured images, the reduction of bubble length is not expected in the downward section. The gravity effect induces a strong interaction between the slug flow structures, which can result in the gradual transition to stratified flow. As observed in Figures 5.5 and 5.7 (c), the higher gas-to-liquid ratio intensifies this process. Thus, the data obtained for S6 and S7 could show a physical inconsistency. As analyzed from the images of Test 4, the impedance sensors could not correctly identify the structures due to the transition process. Figure 5.7 (a) and (b) shows that the flow is still returning to the slug regime at S8, indicating that this data is not representative either.

Figure 5.12 (b) also shows the bubble translation velocity has a higher increase between S4-S5 in Test 3 (17.6%) compared to Test 1 (5.7) and 2 (7.0%). It demonstrated that the geometric effects are higher in the system with more gas. The bubble acceleration at S5 influences the quicker transition to stratified flow. Figure 5.12 (d) demonstrates a sudden increase (60.5%) in the unit cell frequency between S8-S9, which indicates the slug formation.

After this station, this parameter goes down (8.4%). By comparing this data with Tests 1 and 2, it is noted that the frequency between S9-S10 decreases with the gas-to-liquid ratio increase.

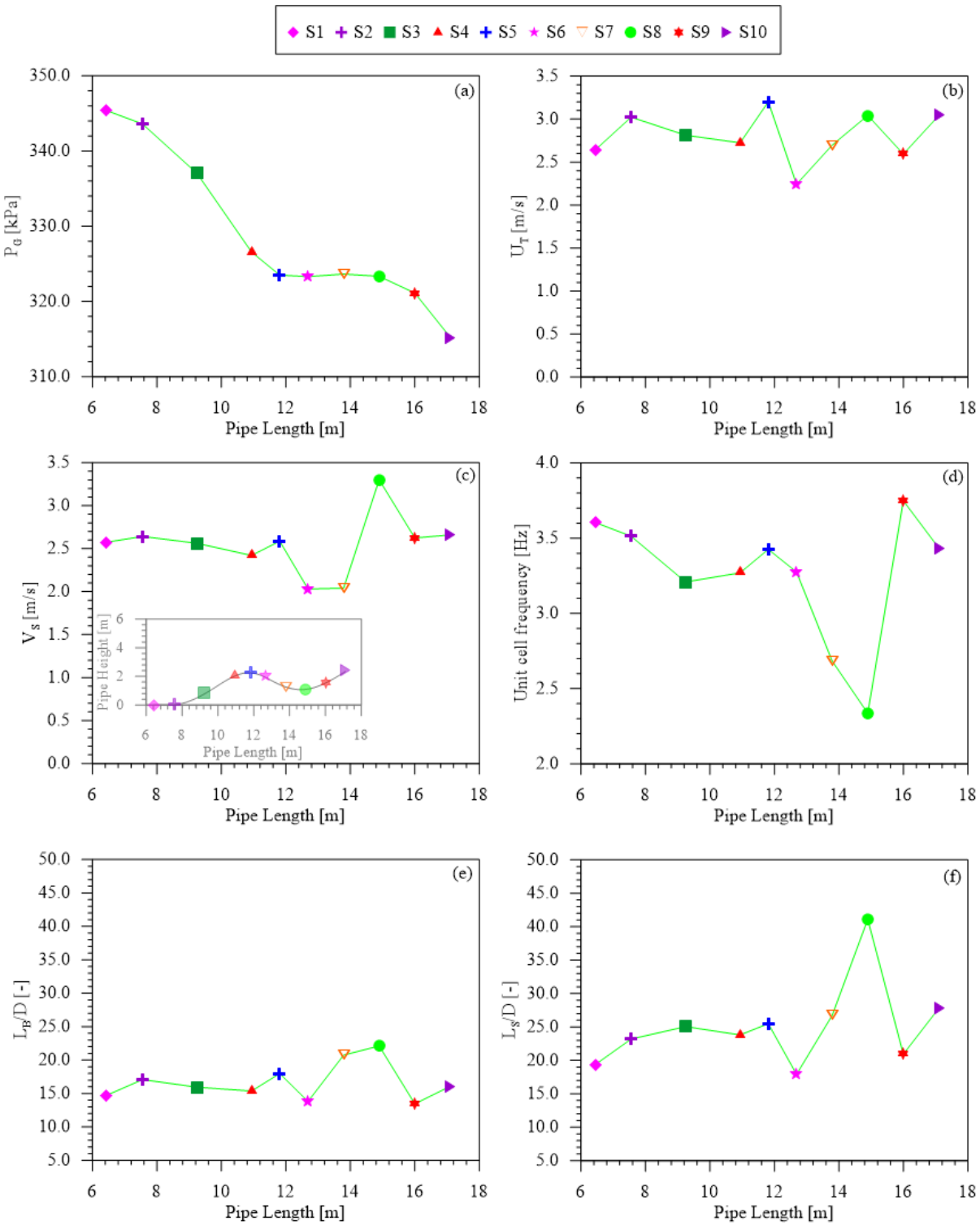

Figure 5.12. Averaged experimental data for Test 3 (J_G/J_L = 1.0 and U_M = 2.0 m/s): (a) gas pressure, (b) translation bubble and (c) liquid slug front velocities, (d) unit cell frequency and dimensionless (e) bubble and (f) liquid slug lengths.

Figure 5.12 (a) presents the pressure evolution, which the pressure gradient along the entire pipe is - 2.83 kPa/m. In addition, it also observed the presence of two different gradients and a pipeline section with pressure almost constant. The first pressure gradient (S1 - S5) is - 4.08 kPa/m. Unlike the previous tests, the downward inclined pipe leads to a small reduction (0.16 kPa/m) due to the higher gas-to-liquid fraction. The second upward inclined pipe results in a pressure gradient equal to - 3.69 kPa/m.

Figure 5.13 exhibits the data obtained from Test 4 (J_G/J_L = 1.5 and U_M = 2.0 m/s). This test represents the higher superficial gas and liquid velocities ratio. Figure 5.13 (b), (e) and (f) shows the bubble properties and the liquid slug length significantly vary along the S curve. Similar to Test 3, the liquid slug length increases by 62.9% over the first V format (S1 - S2), and the capture of the accumulated liquid can be the reason. Unlike the first two tests, there is a punctual increase of the bubble velocities between S1 and S2 in Tests 3 (14.5%) and 4 (50.5%). Figures 5.12 and 5.13 (b) demonstrated that. Figure 5.13 (c) reveals that the slug front velocity does not have the same behavior. It indicates a possible problem in the structure identification by the impedance sensors. According to Zheng et al. (1995), the V format (S1 - S2) can increase the liquid slug holdup. It might affect the identification of the bubble nose. Figure 5.3 (b.2) shows the holdup increases, but the bubble nose is already well-defined at S3.

Figures 5.12 and 5.13 (c) and (f) demonstrate the slug properties between S4 and S7 from Test 3 and 4 have a similar behavior, but Test 4 variation is more pronounced. Since the system has more gas and this phase is faster than the liquid, the bubble acceleration between S4-S5 increases (40.2%), as does the cell interaction along the downhill section. As discussed in Figures 5.5 and 5.7 (b), the S6, S7 and S8 are disregarded due to the pattern transition.

Figure 5.13 (d) shows the unit cell frequency increases by 45.7% between S8-S9 due to the slug initiation. However, this parameter also goes down across S9 and S10 (11.9%). Figures 5.10 to 5.13 (d) show that the increase in gas-to-liquid ratio affects the behavior of unit cell frequency between S9 and S10. For the lowest gas fraction, the increase in the frequency indicates that slug formation still occurs due to the wave coalescence. When the gas fraction gradually increases, the number of cells between those stations is reduced. Figure 5.8 (b.2) shows that the wave coalescence also occurs in Test 4, but the interaction of the structure can be more intense.

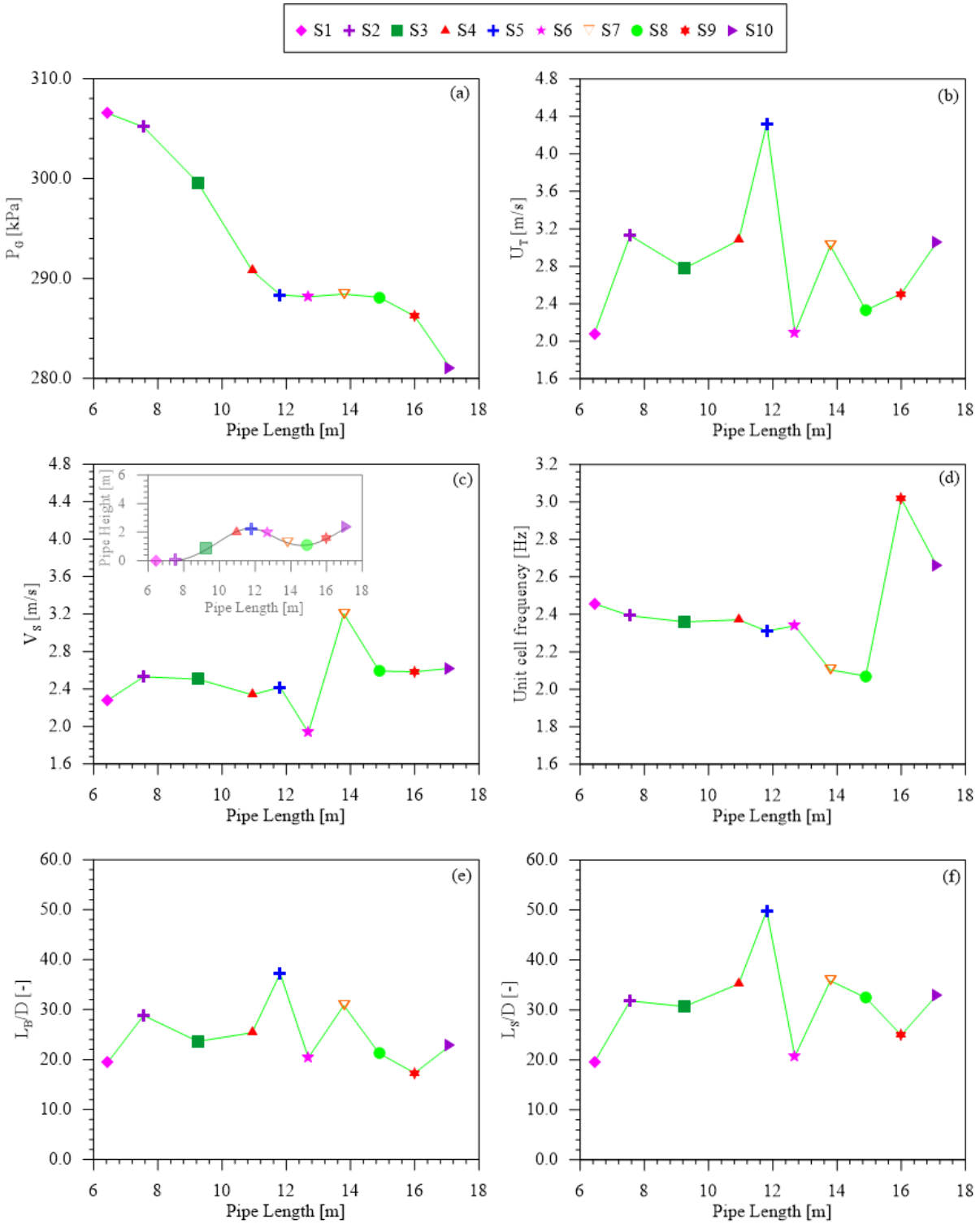

Figure 5.13. Averaged experimental data for Test 4 (J_G/J_L = 1.5 and U_M = 2.0 m/s): (a) gas pressure, (b) translation bubble and (c) liquid slug front velocities, (d) unit cell frequency and dimensionless (e) bubble and (f) liquid slug lengths.

Figure 5.13 (a) presents the pressure evolution. For this case, the pressure gradient in the entire pipe is - 2.39 kPa/m. The first and second pressure gradients are - 3.38 kPa/m and - 3.19 kPa/m. Between them, there is a downward inclined section, where the pressure has a

small reduction (0.23 kPa). By comparing the tests with mixture velocity equal to 2.0 m/s (Tests 1 to 4), the increase of the gas-to-liquid ratio influences the pressure profile. Firstly, both pressure gradients converge to a close value when the gas-to-liquid ratio increases (up to 1.0). For Tests 1 and 2, the difference between them is 0.55 kPa/m. This data gradually reduces in Tests 3 (0.38 kPa/m) and 4 (0.19 kPa/m). In addition, the gas fraction on the system also affects the behavior along the downhill section. In Test 1 (highest liquid fraction) is measured an increase of 1.1 kPa between S5 and S8. Since the system has more gas, that increase rate reduces (Test 2) or the pressure decreases (Tests 3 and 4).

Figure 5.14 shows the data from Test 5 (J_G/J_L = 1.0 and U_M = 4.0 m/s). It represents the first test with the highest mixture velocity. According to Zheng et al. (1995), Yoshida et al. (2000), Zhang et al. (2003) and Al-Safran et al. (2005), the high flow rate reduces the hilly terrain effects. It can be confirmed by comparing Figures 5.10 to 5.13 with Figure 5.14. However, unlike the experimental data of Zheng et al. (1995), the cell frequency is not kept constant. This difference might be correlated to the superficial velocities.

Figure 5.14 (d) exhibits the cell frequency decreases in the downhill section, around 12% between S6-S8. The coalescence between the unit cells occurs, but the liquid slug is not entirely dissipated, as observed in Figures 5.5 and 5.7 (c). Figure 5.14 (e) and (f) demonstrates the bubble and slug lengths remain almost constant from S5 to S7, the maximum variation was a L_S increase between S6-S7 (1.9%). Between S7 and S9, the bubble and liquid slug properties present a significant increase by a similar rate (around 43%). The increase of U_T and V_S is not observed in the previous tests. Regarding the bubble and liquid slug lengths, Figure 5.14 (e) and (f) show that both parameters have similar behavior along the S curve. If these data are combined with Al-Safran et al.'s (2005) categories, the flow could be fit in Category 4 since the slug growth and initiation are observed, as demonstrated in Figure 5.14 (d) and (f) between S8 and S9.

For Test 5 (see Figure 5.14 (a)), the pressure gradient along the entire pipe is - 5.7 kPa/m. The first and the second gradients are - 7.23 kPa and - 6.93 kPa/m. Similar to Test 2 (which has the same gas-to-liquid ratio), the difference between those gradients is 0.30 kPa/m. In addition, the increase of the superficial velocities minimizes the gravitational effect along the downhill section (S5-S8). The pressure gradient between S5 to S8 is - 2.1 kPa/m.

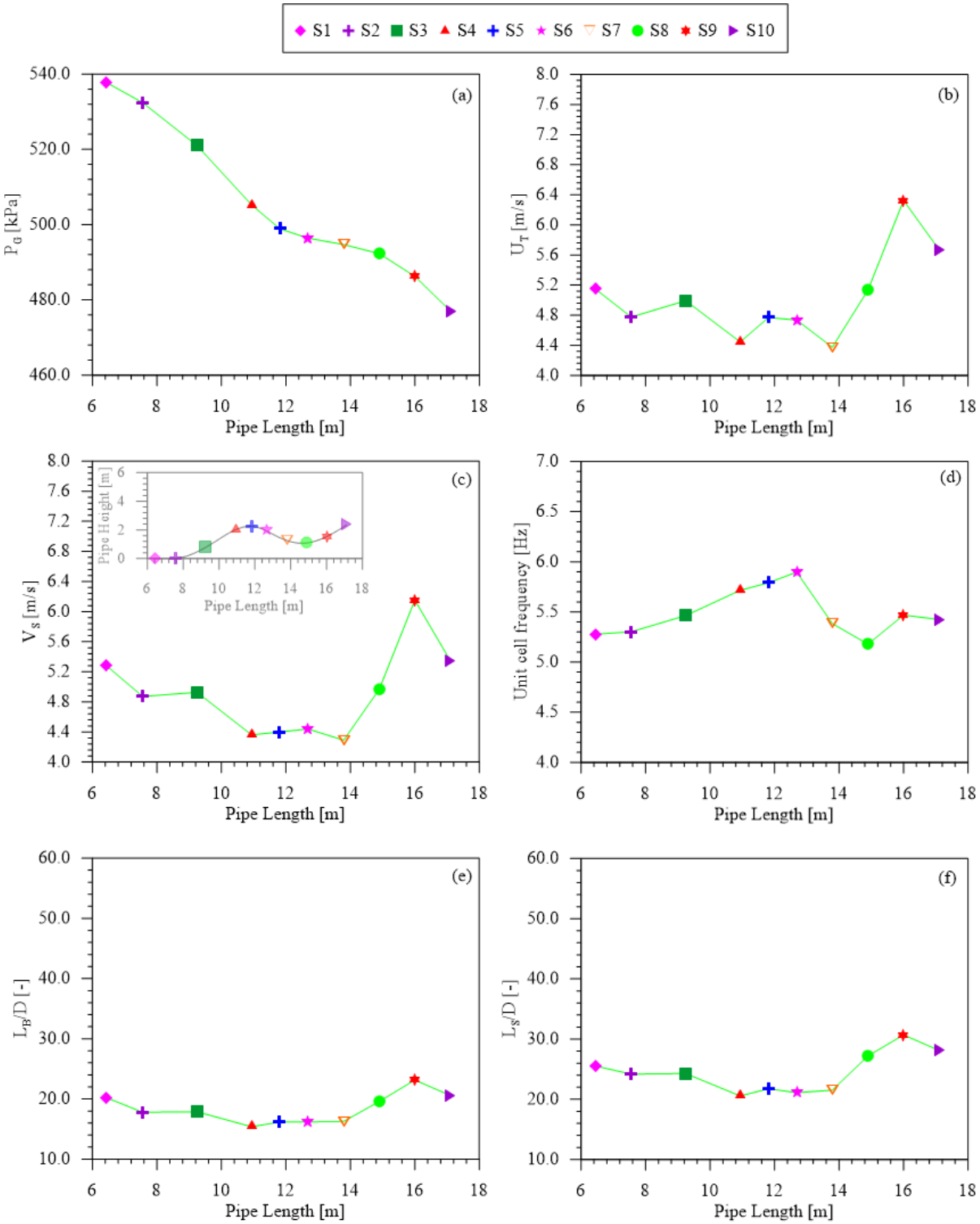

Figure 5.14. Averaged experimental data for Test 5 (J_G/J_L = 1.0 and U_M = 4.0 m/s): (a) gas pressure, (b) translation bubble and (c) liquid slug front velocities, (d) unit cell frequency and dimensionless (e) bubble and (f) liquid slug lengths.

Figure 5.15 presents the data obtained from Test 6 (J_G/J_L = 1.5 and U_M = 4.0 m/s). Tests 6 and 4 have the same superficial gas and liquid velocities ratio. The results obtained in Tests 5 and 6 are notably different, so the influence of the gas fraction on the hilly terrain effect

is evident. According to Al-Safran et al. (2005), if the gas velocity is high enough to create quite aerated and foamy slugs, the hilly terrain will affect the flow properties again. Figure 5.15 (d) shows the unit cell frequency is constant along the S curve in Test 6, following Zheng et al.'s (1995) experimental data.

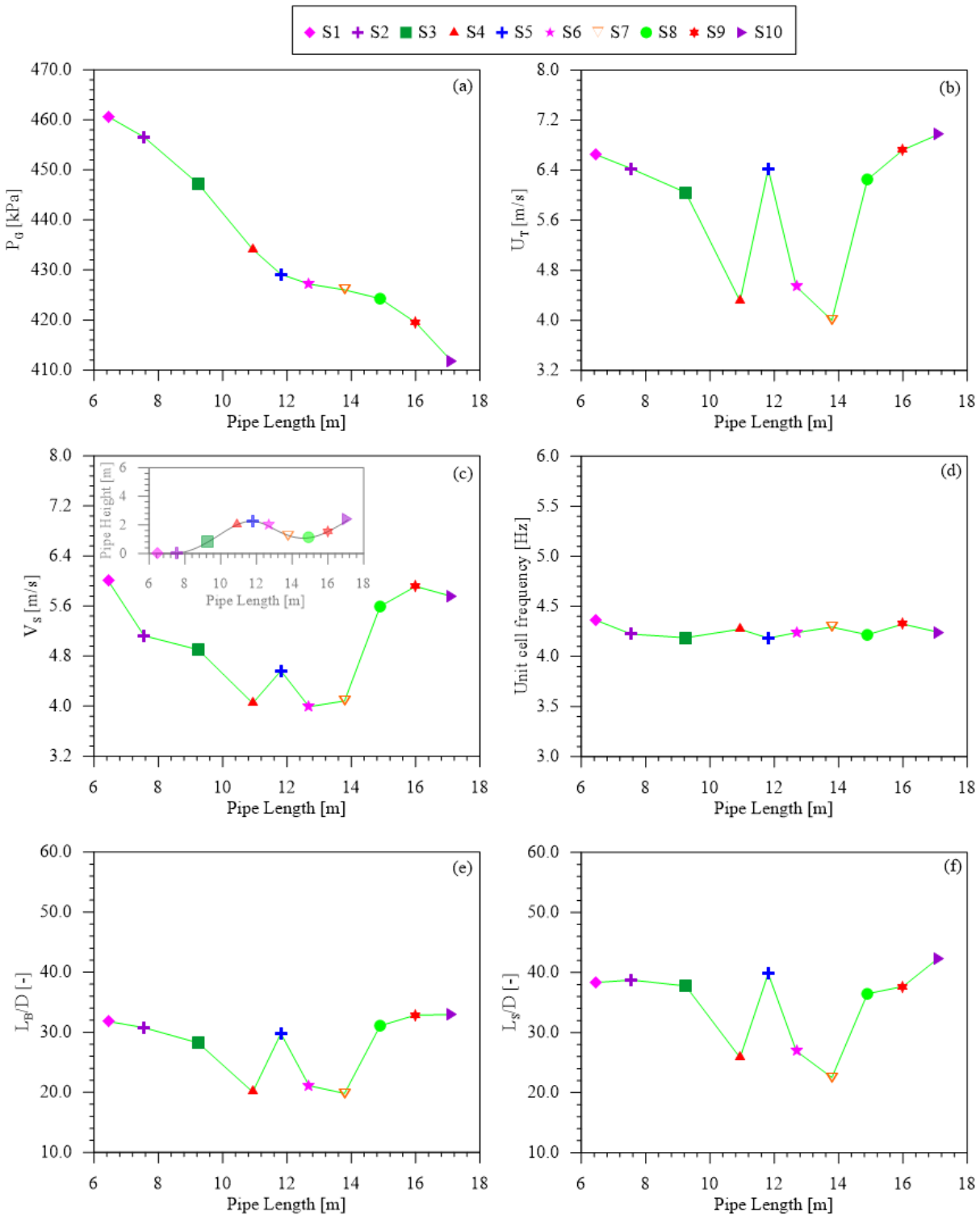

Figure 5.15. Averaged experimental data for Test 6 (J_G/J_L = 1.5 and U_M = 4.0 m/s): (a) gas pressure, (b) translation bubble and (c) liquid slug front velocities, (d) unit cell frequency and dimensionless (e) bubble and (f) liquid slug lengths.

Figure 5.15 (b) and (c) demonstrates that both velocities have a punctual increase at S4. This behavior is also observed in Tests 3 and 4. For Test 6, there is an increase by 48.8% (U_T) and 12.8% (V_S) between S4 and S5 and a decrease by 29.3% (U_T) and 12.6% (V_S) between S5 and S6. As previously discussed, gravity accelerates the structures at the top of the curve. The lengths of bubble and liquid slug are functions of their velocities, so Figure 5.15 (e) and (f) illustrates the same behavior. Figure 5.15 (f) shows a reduction of the bubble (33.4%) and liquid slug (43.5%) lengths in the downhill section (S5-S7), but it does not modify the unit cell frequency. In addition, L_S increases around 62% at S8, which can be justified by the capture of the accumulated liquid.

Figure 5.15 (a) presents the pressure evolution. Similar to the tests with mixture velocity equal to 2.0 m/s, the increase of the gas-to-liquid ratio reduces the difference between the two pressure gradients (before and after the downhill section). The first and second gradients are - 5.86 kPa/m and - 5.61 kPa/m. The difference is 0.25 kPa/m, which is close to the value of Test 4 (have the same gas fraction). In this case, it is also noted that another pressure gradient in the downhill section, which is equal to - 1.58 kPa/m. The pressure gradient in the entire pipe is - 4.58 kPa/m.

Figures 5.16, 5.17, 5.19, 5.20, 5.22 and 5.23 show the statistical distribution of the bubble translation velocity and dimensionless bubble and liquid slug lengths. The main characteristic of the slug flow pattern is the randomness, so the average data does not entirely describe the flow behavior. The following images will present how the parameters are distributed around their mean value at each station. Figure 5.16 also depicts the distribution obtained from the three datasets (2, 4 and 6 repetitions), which cover at least 455, 910 and 1330 cells. As demonstrated in that figure, the datasets with 4 and 6 repetitions result in close or equal distributions. For Tests 2 to 6, the distributions based on the dataset with 6 repetitions are presented. Each test contains at least 1200 cells. Lastly, the previous analyses concluded the data obtained for some stations must be disregarded, so the following figures will not present the distributions at these positions.

Figure 5.16 presents the distributions obtained from Test 1, excluding data from S8 due to the presence of the stratified pattern in this measuring station. For the translation bubble velocity (Figure 5.16), the lowest and highest coefficient of variation (the standard deviation to mean parameter ratio) are at S5 (0.1369) and S7 (0.3374), respectively. Station 3 (S3) also

shows an increase in the standard deviation in relation to the vicinity, indicating the influence of the low elbow on the flow properties. An increase of the U_T spread out is also noted in S9 and S10, where the second low elbow still affects the flow. In accordance with Figures 5.5 and 5.8 (a), the flow presents a strong cell interaction at S7, S9 and S10. This can also justify the dispersion of the data in these positions.

For L_B/D and L_S/D, the highest coefficient of variation occurs at S10. Figure 5.16 highlights that the maximum dimensionless bubble length spans from 26D to 87D at S4 and S7, respectively. The liquid slug length spans from 53D to 150D at S4 and S10, respectively. This variability shows how the distribution of the flow structures modifies along the curve during the flow, resulting in strong temporal variation of internal flow weight.

Figure 5.17 exhibits the distribution obtained in Test 2, excluding data from S8 due to the presence of the stratified pattern in this measuring station. The statistical data of Tests 1 and 2 are similar. The coefficient of variation obtained for the three properties along the stations has similar behavior, as shown in Figure 5.18. The main difference between both tests occurs at S9 and 10 for bubble length. Test 1 shows an increase in the mean of the unit cell frequency through these stations (Figure 5.10), while Test 2 remains almost constant (Figure 5.11). The slug initiation process in Test 1 can justify the higher L_B spread out at S9 and S10. In addition, the maximum dimensionless bubble and liquid slug lengths in Test 2 are longer than in the previous one and respectively span between 29D (S5) to 131D (S7) and 56D (S4) to 186D (S10). Figures 5.16 and 5.17 show the geometric parameter distributions have a minimal variation between S1 and S5. Beyond this point, the data has a more extensive spread out, and there are longer structures.

Figure 5.18 also reveals an increase in the coefficient of variation for U_T (S5 to S7) and L_B/D (S7) for both tests. The movie[3] recorded from Test 1 in section S6-S7 showed the flow structures present a strong interaction in the downhill section. The overtaking rate is high and the discharge of the liquid film in the downstream slug affects the bubble velocity (Barros et al., 2022). Tests 1 and 2 have similar superficial velocities, so it probably occurs in Test 2. This test has an additional influence due to the increase of the amount of gas in the system,

[3] See this phenomenon in YouTube link (Section 3.5), the movie is “JL_1.33_JG_0.67\E6-7\TestSession 002”.

which can facilitate the bubble coalescence. This fact can justify the higher increase in Test 2 compared to Test 1.

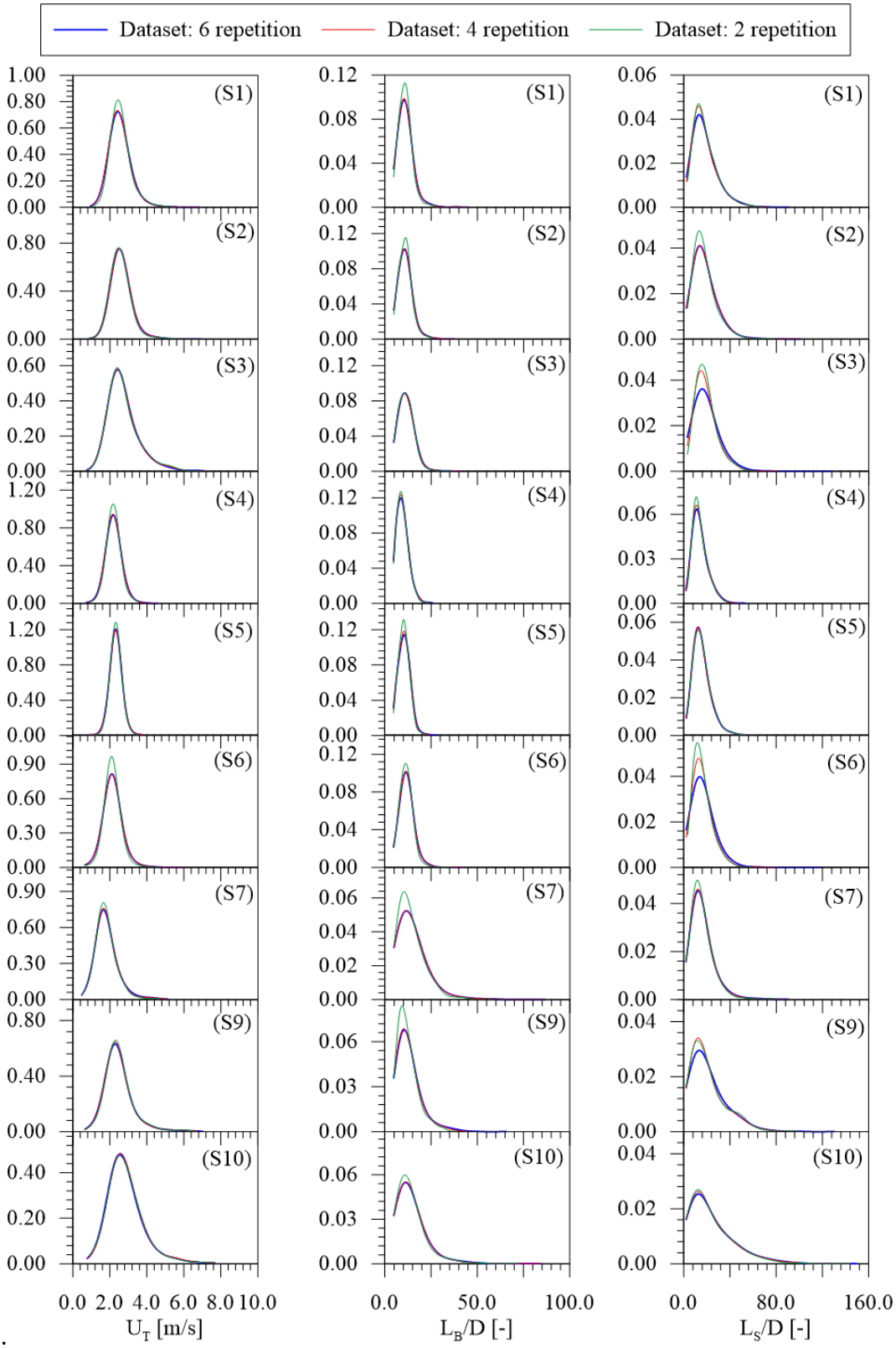

Figure 5.16. Statistical distribution of translational bubble velocity and dimensionless bubble and liquid slug length for Test 1 (J_G/J_L = 0.50 and U_M = 2.0 m/s).

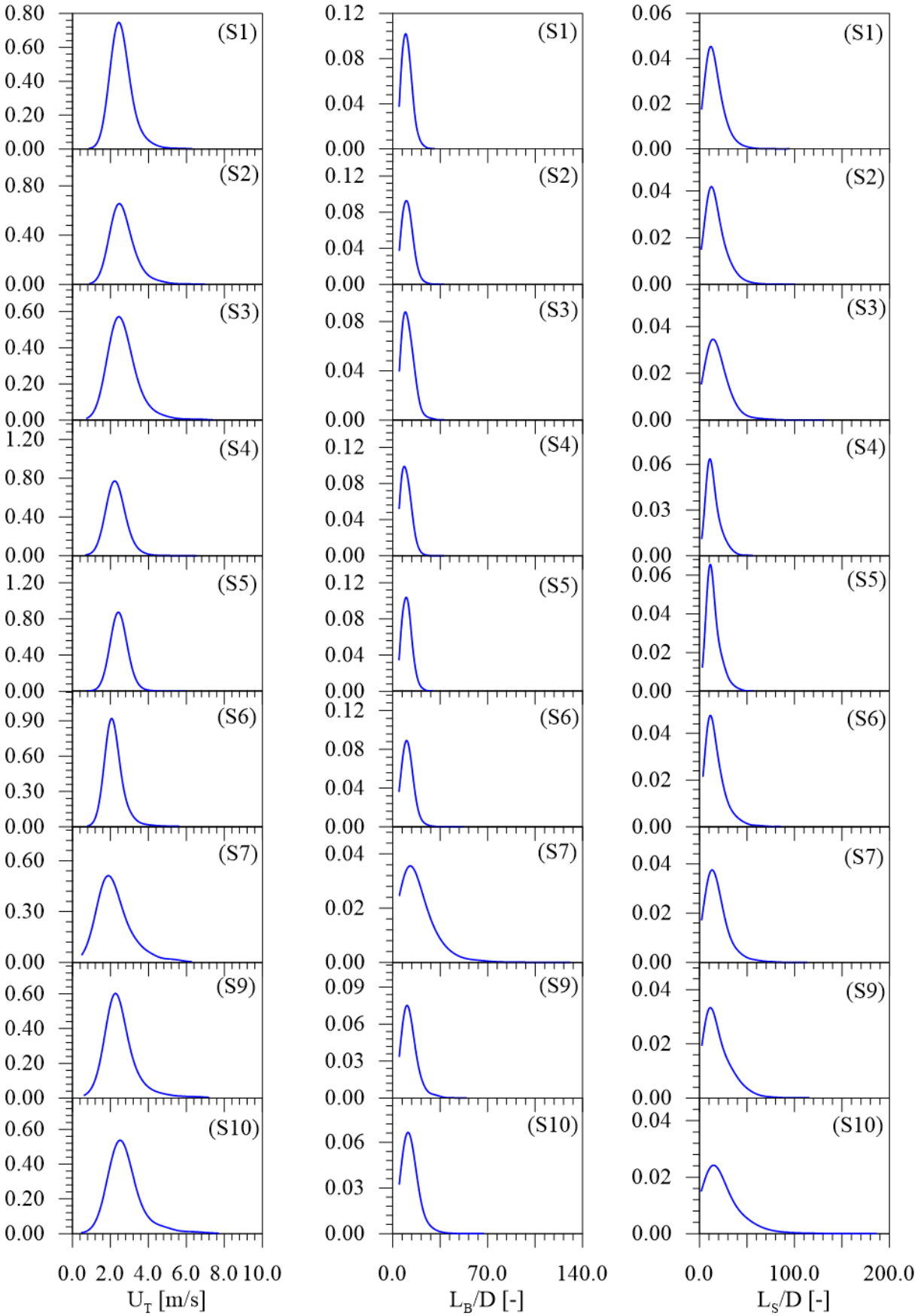

Figure 5.17. Statistical distribution of translational bubble velocity and dimensionless bubble and liquid slug length for Test 2 (J_G/J_L = 0.67 and U_M = 2.0 m/s).

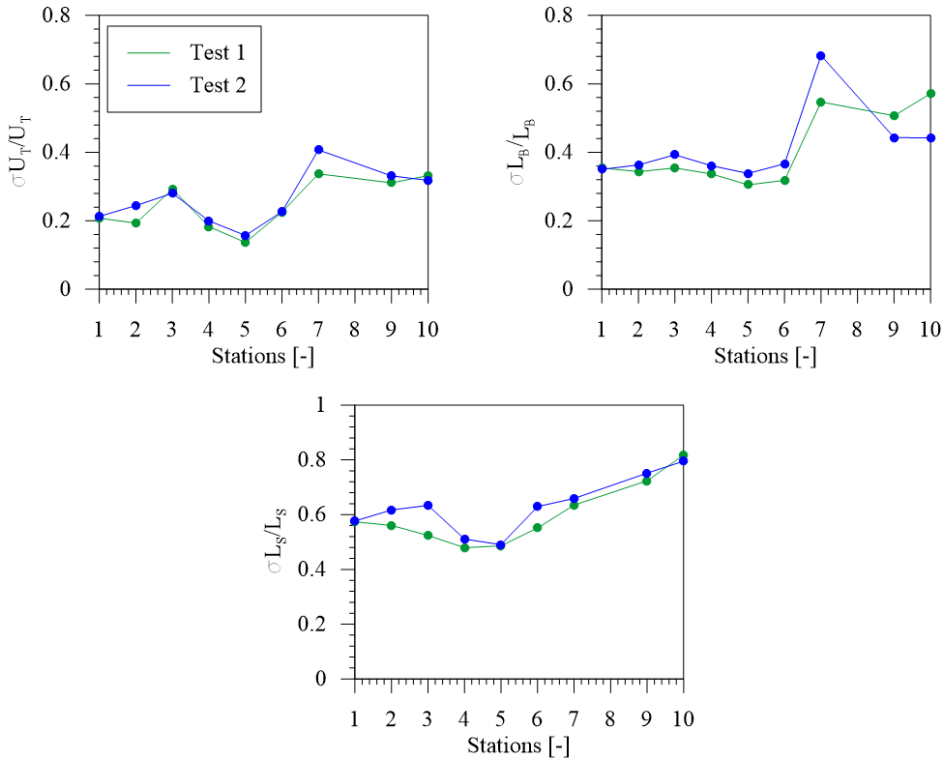

Figure 5.18. Coefficient of variation to translation bubble velocity, bubble and liquid slug lengths in Tests 1 (J_G/J_L = 0.50 and U_M = 2.0 m/s) and 2 (J_G/J_L = 0.67 and U_M = 2.0 m/s).

Figures 5.19 and 5.20 illustrate the distribution for Tests 3 and 4, excluding the data from S6, S7 and S8. These stations are disregarded due to the transition to stratified flow (Figures 5.5 and 5.7) and the impact of this process in the acquisition and processing of those data. As shown in Figures 5.12 and 5.13, these tests have some similarities, but the parameters from Test 4 present a more substantial variability along the entire S curve (S1-S10). Figure 5.21 shows that this intense variability and the unit cell interactions result in a more extensive spread in the translation bubble velocity and bubble length compared to Test 3. However, both cases behave similarly along the stations, except for S9 and S10.

By comparing Figures 5.18 and 5.21, the higher superficial gas and liquid velocities ratio (see Table 3.7) increases the coefficient of variation in U_T and L_B and reduces L_S. This behavior supports the discussions in Section 5.1, which associates the increase of the cell interaction with the larger amount of gas in the system. Since the interaction increases, the spread out of the flow parameters follows it.

Regarding the maximum dimensionless bubble and liquid slug lengths, the flow structures in Test 4 are longer than in Test 3. Figure 5.19 (Test 3) highlights that the maximum L_B/D spans from 48D (S1) to 78D (S5). For L_S/D, the maximum spans from 93D (S5) to

198D (S10). In Test 4 (Figure 5.20), the maximum bubble and liquid lengths span from 97D (S9) to 149D (S5) and 113D (S1) to 294D (S5), respectively.

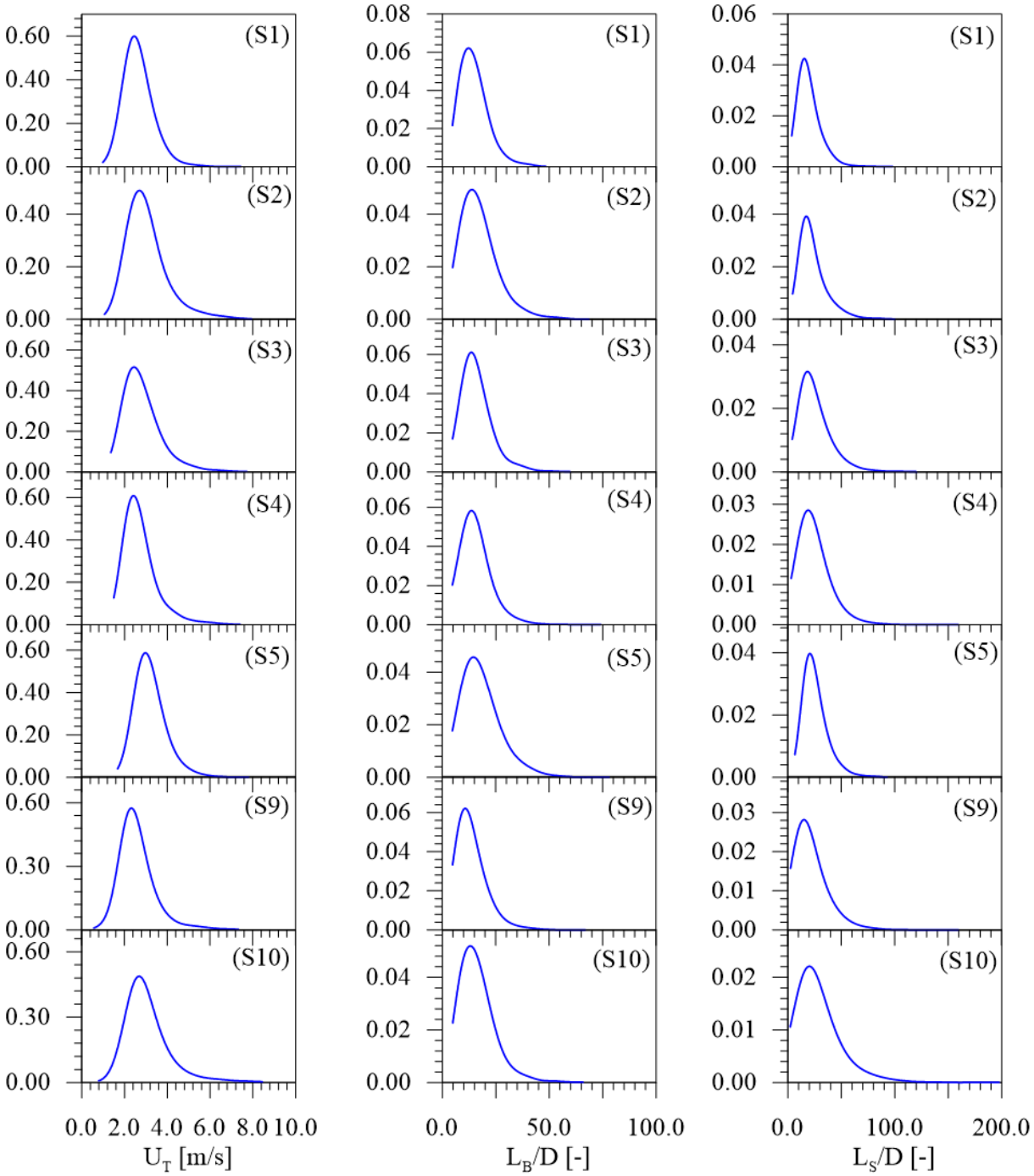

Figure 5.19. Statistical distribution of translational bubble velocity and dimensionless bubble and liquid slug length for Test 3 (J_G/J_L = 1.0 and U_M = 2.0 m/s).

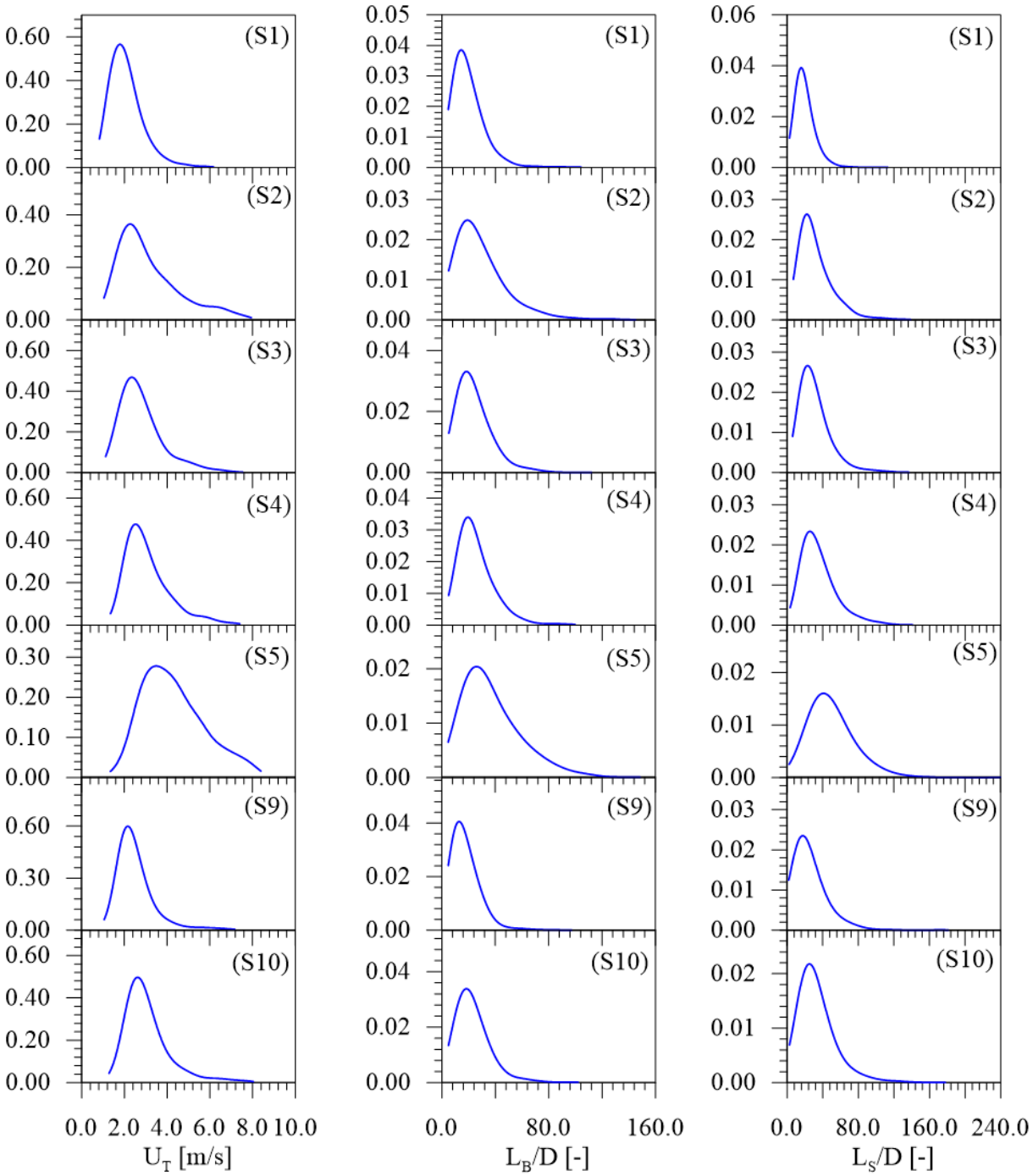

Figure 5.20. Statistical distribution of translational bubble velocity and dimensionless bubble and liquid slug length for Test 4 (J_G/J_L = 1.5 and U_M = 2.0 m/s).

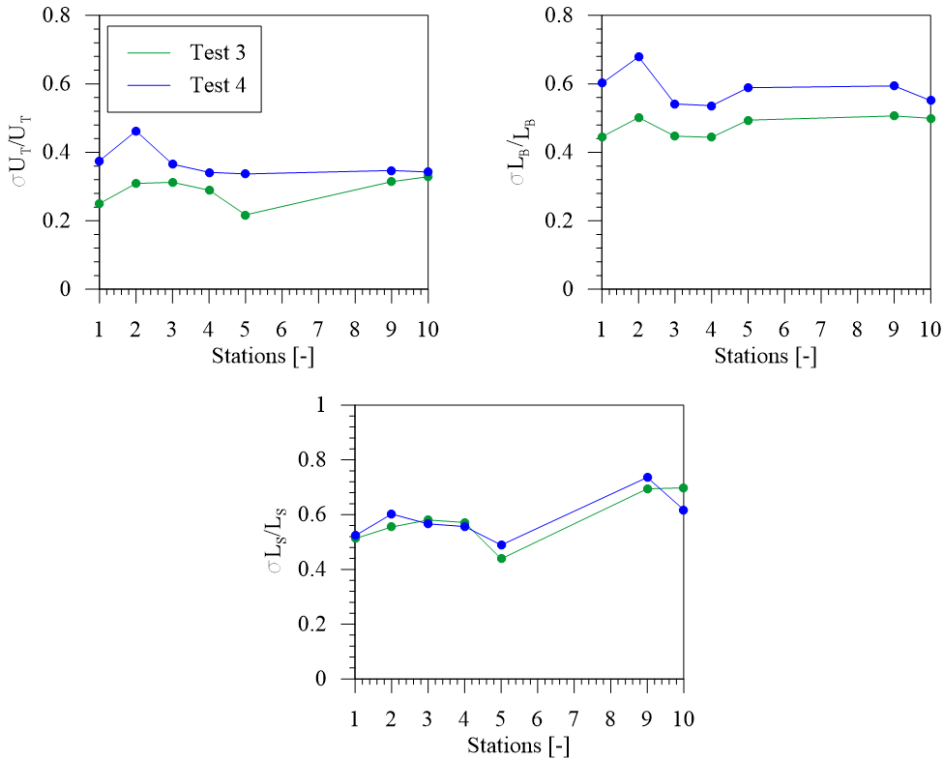

Figure 5.21. Coefficient of variation to translation bubble velocity, bubble and liquid slug lengths in Tests 3 (J_G/J_L = 1.0 and U_M = 2.0 m/s) and 4 (J_G/J_L = 1.5 and U_M = 2.0 m/s).

Figures 5.22 and 5.23 present the distribution obtained from Tests 5 and 6. Unlike previous cases, the ten stations are considered. As these tests have higher mixture velocities, those figures show higher maximum values for the translation bubble velocity. Figure 5.22 demonstrates that some stations have longer bubble and liquid slugs, but the parameter dispersion does not change significantly along S1 to S10. It supports the statement about the less influence of the hilly terrain. On the other hand, Figure 5.23 shows the increase in the gas fraction modifies the spread out in some stations.

Figure 5.22 (Test 5) shows that the maximum L_B/D spans from 62D (S2) to 144D (S9). For L_S/D, the maximum spans from 126D (S4) to 258D (S9). In Test 6 (Figure 5.23), the maximum bubble and liquid lengths span from 72D (S6) to 157D (S8) and 108D (S7) to 277D (S10), respectively. It is possible to note that those maximum values are close for both tests. Lastly, Figure 5.24 illustrates the coefficient of variation for these tests. Both tests do not present a similar behavior as observed in Figures 5.18 and 5.21. However, they have close absolute values.

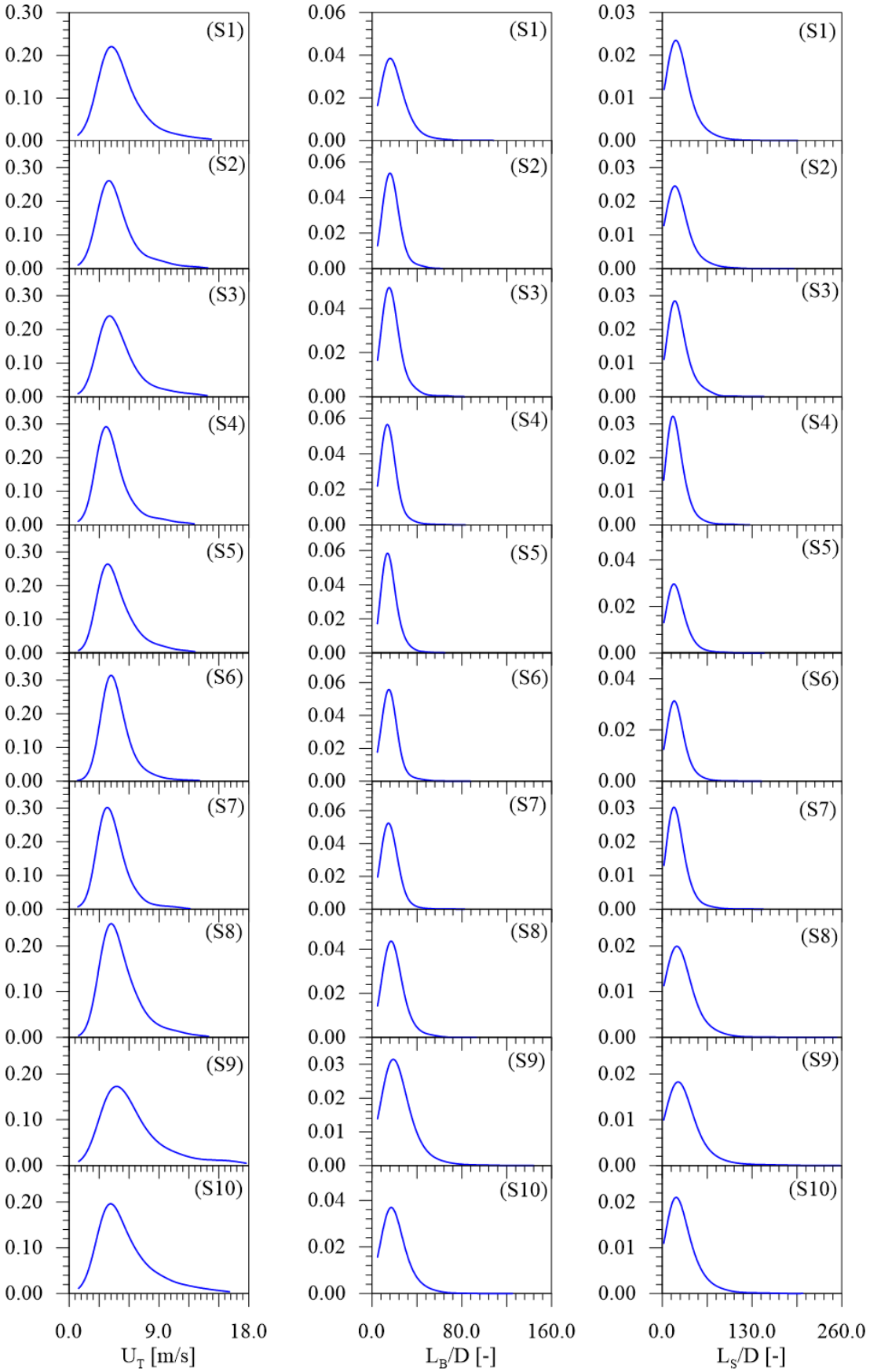

Figure 5.22. Statistical distribution of translational bubble velocity and dimensionless bubble and liquid slug length for Test 5 (J_G/J_L = 1.0 and U_M = 4.0 m/s).

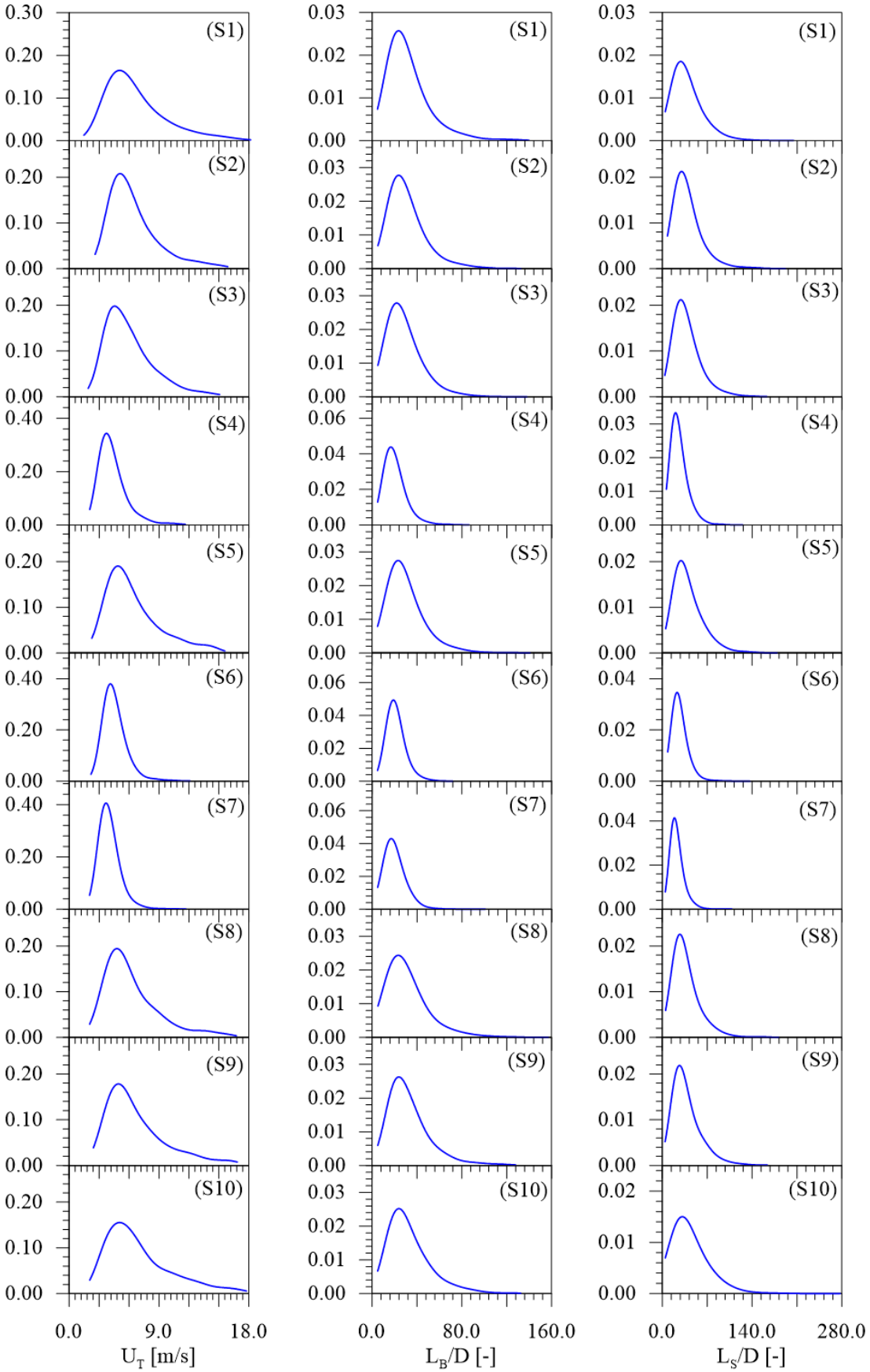

Figure 5.23. Statistical distribution of translational bubble velocity and dimensionless bubble and liquid slug length for Test 6 (J_G/J_L = 1.5 and U_M = 4.0 m/s).

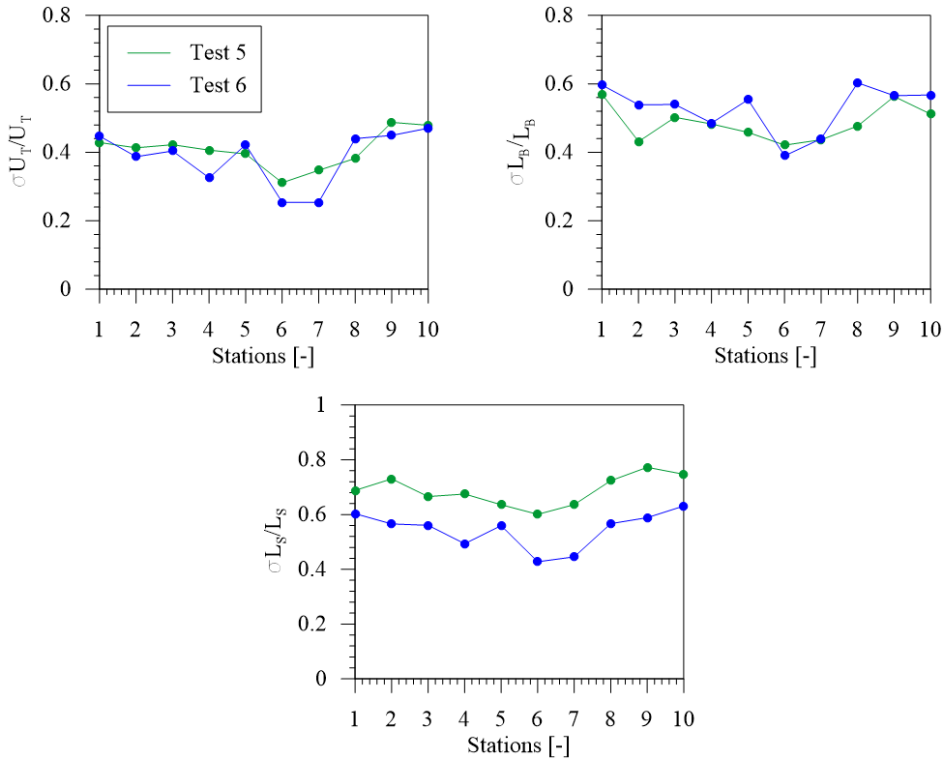

Figure 5.24. Coefficient of variation to translation bubble velocity, bubble and liquid slug lengths in Tests 5 (J_G/J_L = 1.0 and U_M = 4.0 m/s) and 6 (J_G/J_L = 1.5 and U_M = 4.0 m/s).

5.3 Slug tracking validation: experimental data

This section compares the numerical results obtained by the slug tracking model against the experimental data presented in Section 5.2. It aims to validate the improved slug tracking, which contains all submodels described in Section 4.2.1.

The procedure starts by specifying the experimental setup geometry through a list of straight pipeline sections that represents the lazy wave particular silhouette. Each section has its diameter, inclination and roughness. The pipeline extends from the water-air mixer to the separator facility, which is at atmospheric pressure. That line is 50 m long and 36 m high, maintaining a constant diameter (0.0234 m) and roughness (0.00021m). However, the focus of this analysis is the flow parameters along the S curve, where the experimental measuring stations (S1 to 10) are located. This region is approximately 10.665 m long and exhibits a significant inclination change; therefore, the straight inclined sections in this region should be small enough for a proper lazy wave representation. The numerical model employs 30 virtual probes along the S curve, and some of them coincide with the experimental measuring stations. These probes register the flow properties.

Figure 5.25 (a) visually represents the numerical line, the experimental S curve, and its projection to the separator. The choice of employing the entire line in the numerical model is based on the outlet boundary condition. The usage of the last pressure transducer could induce errors in the numerical data along the curve due to the outlet boundary treatment (Section 4.3.1). The experimental S curve has a small inclined section until it connects to the vertical tower, and then it remains vertical until the separator. On the other hand, the numerical line projection was proposed with a smoother inclination change after the curve, as shown in Figure 5.25 (a) and (b). The difference against the experimental line aims to avoid potential numerical divergences. It is not a problem because the slug flow parameters do not strongly affect their upstream structures behavior. Figure 5.25 (b) also highlights the inclination change along the S curve. The line has a short horizontal section followed by three sections with gradual inclination change: (i) an upward inclined that reaches approximately 55°, (ii) downward inclined that reaches approximately - 43° and (iii) upward inclined that reaches more than 80°. Figure 5.25 (b) has a similar shape observed in an actual riser, as illustrated in Figure 5.34 (b).

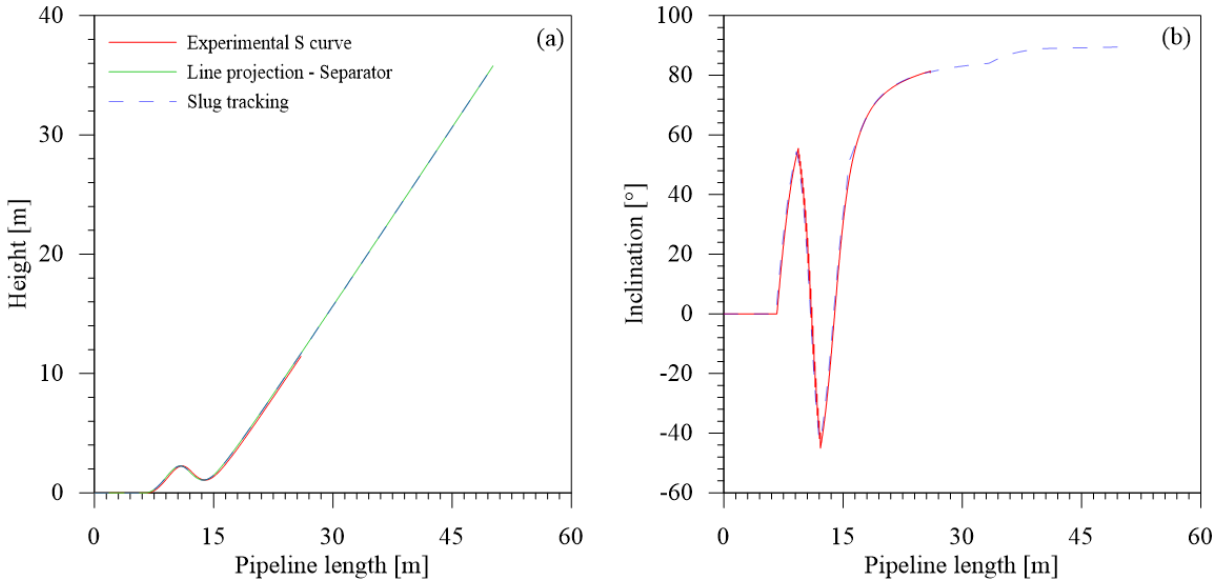

Figure 5.25. Comparison between the experimental S curve (red solid line), its projection to the separator (green solid line) and the line used in the numerical analysis (blue dashed line).

The methodology described in Section 4.3.2.2 is employed to determine the random inlet condition. It uses the experimental frequency and superficial liquid and gas velocities. Blasius and Choi et al. (2012) correlations and Grenier (1997) parameters were used for friction factor, drift parameters and wake coefficients, respectively. The liquid slug holdup correlation is still an open discussion; many correlations are available in the literature. Pereyra et al. (2012) reviewed this topic and proposed tuned constants for some previous correlations. Table 5.1 presents these original correlations (Andreussi and Bendiksen, 1989; Ferschneider, 1983;

Gomez et al., 2000; Malnes, 1982) and Pereyra et al.'s (2012) adjustments. As these equations are a function of the mixture velocity, the table presents the results obtained from Tests 1 and 5.

The original and adjusted correlations do not present significant changes, except for Gomez et al. (2000). Ferschneider (1983) and Andreussi and Bendiksen (1989) correlations provide high liquid slug holdup or low void fraction. However, Figures 5.2 to 5.8 show the liquid slug is highly aerated along the entire S curve, and neither correlation could describe such high void fraction. Pereyra et al.'s (2012) adjustments to Malnes (1982) and the original version led to similar results for both tests; the highest relative deviation is 3.6% in Test 5. This alignment supports the representativeness of Malnes (1982), since Pereyra et al. (2012) tested it against a vast database. Thus, the simulations conducted in this work employ the original version of Malnes (1982).

Table 5.1. Liquid slug holdup (R_S) by different correlations.

Correlations	Test 1		Test 5	
	Original	Pereyra et al. (2012)	Original	Pereyra et al. (2012)
Malnes (1982)	0.871	0.853	0.774	0.746
Ferschneider, (1983)	0.940	0.997	0.808	0.992
Andreussi and Bendiksen (1989)	0.923	0.899	0.886	0.836
Gomez et al. (2000)	0.874	0.717	0.766	0.520

The slug tracking model predicts the evolution and interaction over time and space, but it cannot reproduce the slug flow initiation. Furthermore, the model assumes the presence of slug flow in the entire numerical domain. Sections 5.1 and 5.2 pointed out that the transition to stratified flow occurs in the downhill inclined section in Tests 1 to 4 (U_M = 2.0 m/s), but the slug flow returns in the upward one. However, the numerical simulation neglects this phenomenon. The modeling of slug generation at the bottom elbows considers a punctual flow modification as a function of the flow parameters in its vicinity, as reported in Section 4.2.1.2.

The numerical analysis considers the six tests described in Table 3.7. Figures 5.26 to 5.31 present the following parameters along the S curve (S1 to S10): a) P_G - Gas pressure at bubble, (b) U_T - Translation bubble velocity, (c) V_S - Liquid slug front velocity, (d) Unit cell frequency, (e) L_B/D - Dimensionless bubble and (f) L_S/D - liquid slug lengths. The relationship

between pipeline height and length is depicted in each figure to facilitate the interpretation of the results. In addition, Table 5.2 shows the pressure gradients obtained by the slug tracking for each test and their relative errors against the experimental data. As observed in the experimental data (Figures 5.10 to 5.15), the pressure evolution has two different gradients in the upward inclined sections (S1 to S5 and S8 to S10) and another different behavior in the downhill section (S5 to S8). Table 5.2 presents the partial gradient in the upward sections and the total gradient along the S curve.

Table 5.2. Comparison of numerical pressure gradient against the experimental data.

		Pressure gradient [kPa]		
	Data	Gradient 1 (S1-S5)	Gradient 2 (S8-S10)	Total gradient (S1-S10)
Test 1	Experimental	-5.04	-4.50	-3.37
	Slug tracking	-3.28	-4.93	-2.68
	Relative error	35.0%	9.6%	20.5%
Test 2	Experimental	-4.64	-4.09	-3.15
	Slug tracking	-2.98	-4.45	-2.41
	Relative error	35.8%	9.0%	23.6%
Test 3	Experimental	-4.08	-3.69	-2.83
	Slug tracking	-2.63	-3.69	-2.06
	Relative error	35.4%	0.1%	27.1%
Test 4	Experimental	-3.38	-3.19	-2.39
	Slug tracking	-2.26	-2.77	-1.65
	Relative error	33.2%	13.3%	30.8%
Test 5	Experimental	-7.23	-6.93	-5.70
	Slug tracking	-4.84	-6.13	-4.27
	Relative error	33.1%	11.6%	25.0%
Test 6	Experimental	-5.87	-5.63	-4.58
	Slug tracking	-3.99	-4.83	-3.45
	Relative error	32.0%	14.2%	24.6%

Regarding the Gradient 1, the slug tracking underestimates the pressure gradient for all tests. The higher relative deviation is 35.8% for Test 2. For Gradient 2, the relative error is lower than Gradient 1. It is noted an impact of the gas-to-liquid ratio in the second gradient. For tests with mixture velocity equal to 2.0 m/s (Test 1 to 4), a different behavior is noted. The

numerical model overestimates the Gradient 2 in Test 1 (J_G/J_L = 0.67) and 2 (J_G/J_L = 0.5), but in Test 3 (J_G/J_L = 1.0) it is almost equal to the experimental data. In Test 4 (J_G/J_L = 1.5), the gradient is underestimated and has the second highest relative error (13.3%). The tests with mixture velocity equal to 4.0 m/s, the pressure gradient is underestimated in Test 5 (J_G/J_L = 1.0) and Test 6 (J_G/J_L = 1.5).

In the downward section (S5-S8), the experimental data shows different gradients as a function of the gas-to-liquid ratio. The gradient in Tests 1, 2, 3, 4, 5 and 6 are 0.6 kPa/m, 0.10 kPa/m, - 0.05 kPa/m, - 0.08 kPa/m, - 2.14 kPa/m and - 1.59 kPa/m, respectively. These gradients are strongly affected by the flow features (flow pattern and air-water velocities and fractions), which will define the dominant force (gravitational or shear stress). On the other hand, the numerical data shows a section with almost constant pressure for all tests.

In addition, Table 5.2 shows the numerical model underestimates the total pressure gradient in all tests. The numerical error can be justified by the liquid and gas fractions along the pipe, and by the friction factor correlation. This work employed Blasius correlation that neglects the pipe roughness. Those gradients are also influenced by the three different pressure behaviors along the S curve (S1-S5, S5-S8 and S8-10). The highest relative deviation was 30.8% and 27.1% for Tests 3 and 4.

Figure 5.26 compares Test 1 experimental to numerical data for all stations, except for S8. Figure 5.26 (a) shows the pressure profile; the highest relative deviation is 6.1% at S1. The numerical bubble translation and liquid slug front velocities have a similar behavior, as shown in Figure 5.26 (b) and (c). Both increase slightly until S3, then decrease until S5. After S5, they increase again.

The experimental U_T is calculated by the ratio of station distances and the traveling time of the bubble between the impedance sensors (Section 3.2). In the downhill section, the gravity forces and the liquid film acceleration influence that parameter (Barros et al., 2022). On the other hand, the numerical U_T is calculated by Eq.(4.9) with the drift parameter determined by correlation. This formulation does not capture the gravity forces acting in the liquid film and the buoyancy affecting the gas due to the pipe orientation change. The highest relative deviation is 30.5% at S7. The liquid slug front velocity (V_S or dx^j/dt, presented in Figure 5.26 (c)) is estimated with Eq. (4.14), which is a gas mass balance on the elongated bubble region and considered the pressure variation, dispersed bubble velocity, liquid slug and bubble lengths and

their holdups. Figure 5.26 (c) shows a good agreement with the experimental data, and the highest relative deviation is 15.6% (S7).

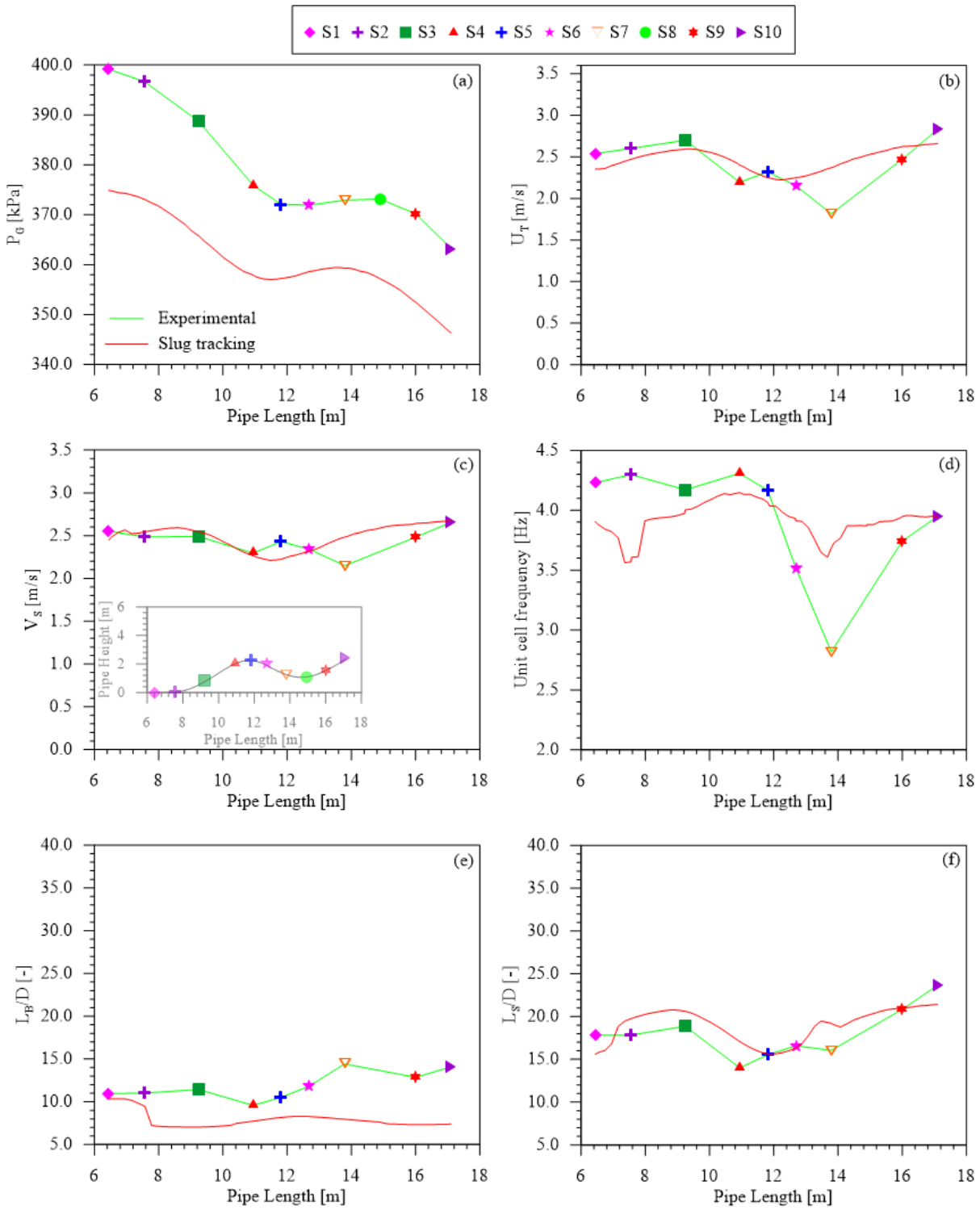

Figure 5.26. Comparison between slug tracking data and the experimental campaign for Test 1 (J_G/J_L = 0.50; U_M = 2.0 m/s): (a) gas pressure, (b) translation bubble and (c) liquid slug front velocities, (d) unit cell frequency and dimensionless (e) bubble and (f) liquid slug lengths.

Figure 5.26 (d) exhibits the cell frequency profile. The numerical data shows the effects of the hilly terrain submodels. After S1, the pipeline has the first singularity where the

V format phenomena are treated. It leads to a decrease of the cell frequency and a gradual increase in the liquid slug length, as illustrated in Figure 5.26 (f). These parameters suddenly increase near S2, which represents the second singularity effect. In this position, the cell reaches a pipeline inclination equal to or higher than 30° (in water-air simulations), and the transition from plane to concentric interface in the bubble region occurs, as discussed in Section 4.2.2. It causes a bubble length reduction and an increase in unit cell frequency and liquid slug length. Figures 5.3 and 5.8 demonstrate that transition occurs, but the first upward-inclined section is short. Due to the A format effects, the unit cell does not have time to complete the transition and quickly assumes the plane interface again. In the downhill section (S6 and S7), the frequency slightly reduces while the experimental data has a significant one. The highest relative deviation of the frequency is 30.7% at S7.

Figure 5.26 (e) and (f) shows that the liquid slug length agrees better than the bubble. The bubble remains almost constant after the punctual reduction due to the second singularity. The experimental data shows a gradual increment along the downhill section. Their highest relative deviations for bubble and liquid slug are 47.5% (S10) and 22.1% (S4), respectively.

As discussed in Section 5.2, Test 2 behaves similarly to Test 1. The numerical models also present this similarity, as shown in Figures 5.26 and 5.27. Figure 5.27 (a) shows the pressure profile; its highest relative deviation is 7.06% (S1). Figure 5.27 (b) and (c) demonstrates once again that the numerical model is not able to capture the punctual structures acceleration at the top of the curve (S5). However, both velocities agree well with their experimental data along the curve. The highest relative deviations for U_T and V_S are 9.5% (S1) and 17.6% (S7), respectively. Figure 5.27 (d) shows a numerical cell frequency profile similar to Test 1 but with a higher deviation. The highest relative deviation is 23.3% (S2).

Figure 5.27 (e) and (f) shows the bubble and liquid slug lengths. The numerical results also demonstrate a similar profile compared to Test 1. However, the current test presents a better concordance with the experimental data. The experimental bubble length has a sudden increase between stations S6 and S7, as exhibited in Figure 5.27 (e); the increase of superficial gas and liquid velocities ratio intensifies the coalescence in this region. Nevertheless, the numerical model is not able to predict it. The relative deviation is 40.4%, the highest one for L_B (S7). The liquid slug length demonstrates that the numerical and experimental data have

a similar evolution along the S curve, as shown in Figure 5.27 (f). The main difference between these profiles occurs near stations S5 and S6 since the slug tracking postpones the liquid slug increase. The highest relative deviation for L_S is 14.8% (S1).

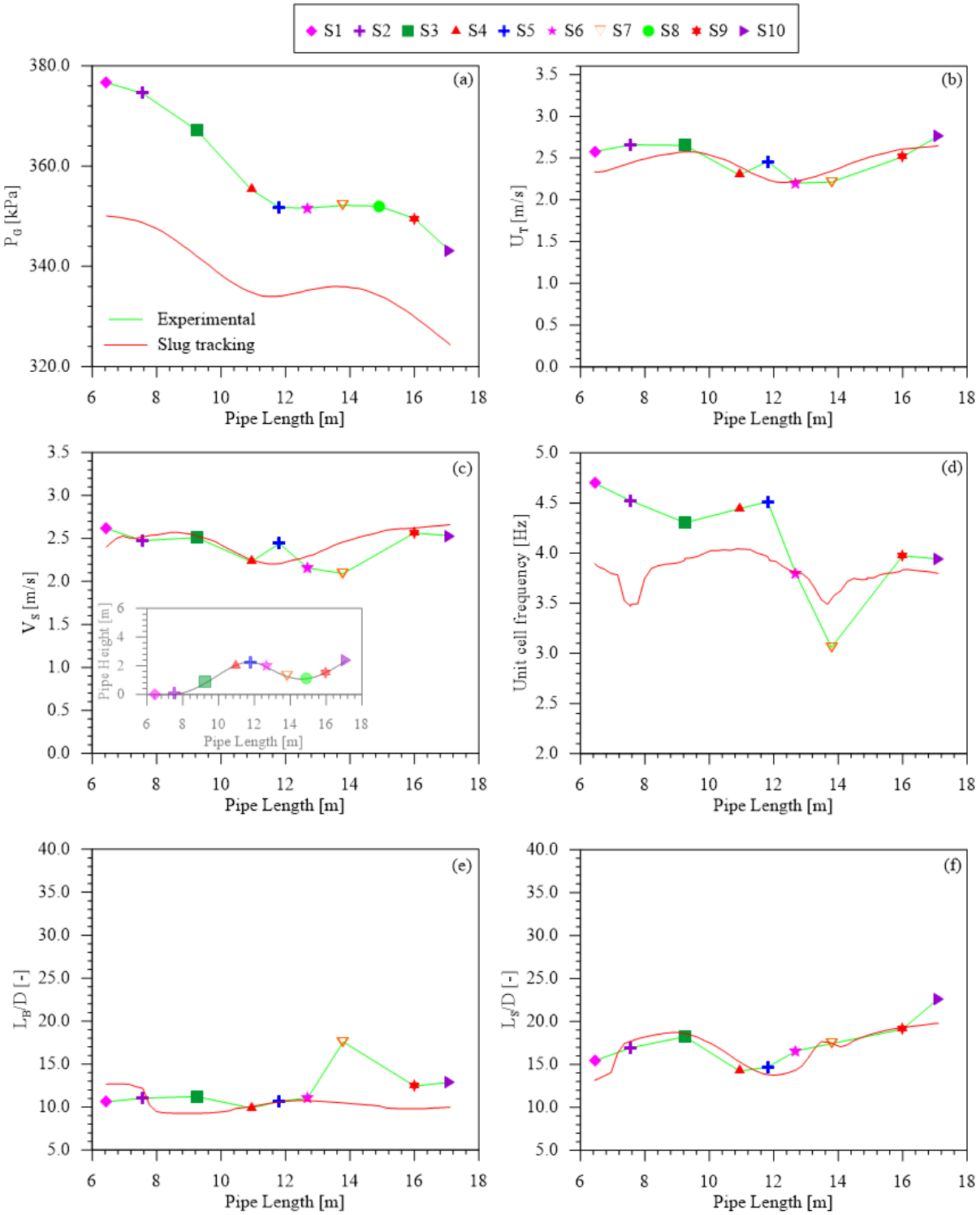

Figure 5.27. Comparison between slug tracking data and the experimental campaign for Test 2 (J_G/J_L = 0.67; U_M = 2.0 m/s): (a) gas pressure, (b) translation bubble and (c) liquid slug front velocities, (d) unit cell frequency and dimensionless (e) bubble and (f) liquid slug lengths.

Figure 5.28 presents the numerical and experimental data obtained from Test 3, which has the superficial gas and liquid velocities ratio equal to 1.0 m/s. As discussed in Section 5.2, the higher gas fraction increases the cell interaction along the downhill section (S5 to S8), resulting in a considerable variation in the slug parameters. The slug tracking is not able to predict it. Barros et al.'s (2022) experimental campaign showed the transition from slug to stratified pattern is caused by the liquid acceleration by gravity, which changes the hydrodynamics around the bubble, and causes the liquid dissipation and bubble coalescence. Figure 5.5 also supports their statement. The slug tracking considers the cell interaction and the overtaking mechanism, but the slug flow features are maintained along the pipeline. Furthermore, the impact of the transition to the stratified regime is not accounted for. It justifies the lower concordance between the experimental and numerical data in the current and subsequent test.

Figure 5.28 (a) shows the pressure profile; the highest relative deviation is 6.4% (S1). Similar to the previous cases, Figure 5.28 (b) and (c) demonstrate that the numerical model does not predict the bubble and liquid slug acceleration at S5, resulting in the highest relative deviations, respectively 26.1% and 10.9%. Figure 5.28 (d) also shows the difficulty of the numerical model in capturing the cell frequency variation over the S curve. Its highest relative deviation is 21.2% (S2).

Figure 5.28 (d) and (e) demonstrates that the increase in gas-to-liquid ratio (higher amount of gas in the system) makes the definition of the inlet condition more difficult. As discussed in Section 4.3, the gas balance should be guaranteed inside the unit cell. If the liquid slug holdup is overestimated, the bubble should be longer to contain the remaining gas mass. It consequently affects the determination of the structures size. The list of cells used as inlet boundary condition is a function of the liquid slug holdup correlation, bubble profile defined by Taitel and Barnea's (1990) model and cell frequency. As the experimental data provides the latter parameter, the lack of representativeness in the cell characteristics could be attributed to the other ones. For the bubble length, the highest relative deviation is 37.7% (S1). Figure 5.28 (e) shows a good qualitative agreement until S4. The highest relative deviation for L_S is 45.3% (S5).

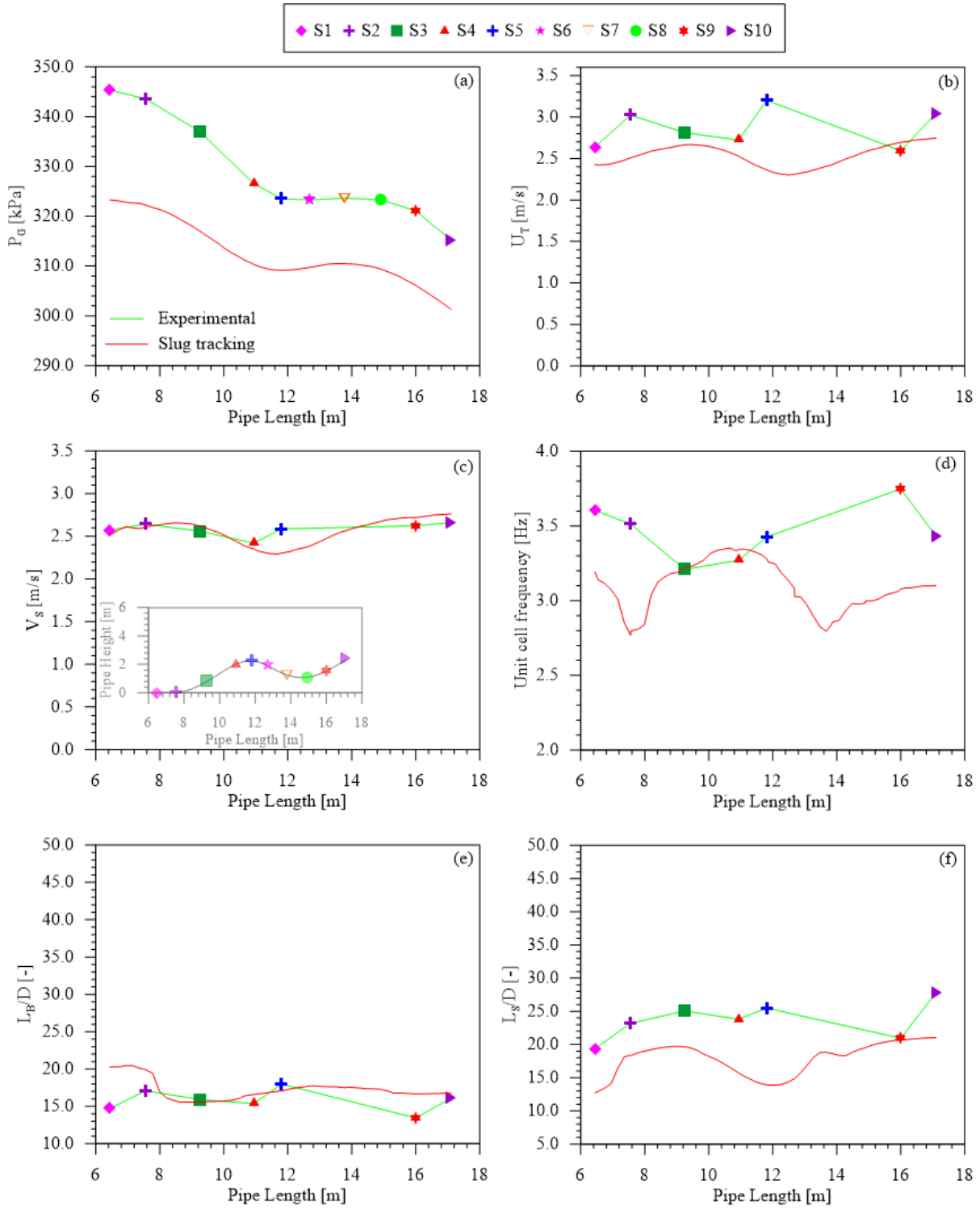

Figure 5.28. Comparison between slug tracking data and the experimental campaign for Test 3 (J_G/J_L = 1.0; U_M = 2.0 m/s): (a) gas pressure, (b) translation bubble and (c) liquid slug front velocities, (d) unit cell frequency and dimensionless (e) bubble and (f) liquid slug lengths.

Figure 5.29 exhibits the comparison of the results from Test 4. Figure 5.29 (a) demonstrates the pressure profile, and it is noted that the pressure after the top of the S curve is closer to the experimental data. The highest relative deviation for the pressure is 3.68% (S1). The numerical translational bubble velocity is not similar to the experimental, as shown in

Figure 5.29 (b). The highest relative deviation reaches 46.5% (S5). On the other hand, Figure 5.29 (c) demonstrated a good agreement, its highest relative deviation is at S5 (8.7%).

The numerical cell frequency from Tests 3 and 4 have similar profiles, but they do not accurately represent the experimental data, as shown in Figures 5.28 and 5.29 (d). In Test 4, the highest relative deviation is 26.9% (S9). The slug tracking neglects the transition process (from slug flow to stratified pattern and vice versa), so the model could neither predict the sudden increase of cell frequency after the bottom elbow (S8) nor the influence of the velocity ratio on the behavior of the cell frequency between the stations S9 and S10.

Test 4 exhibits the most distinct profile between the numerical and experimental lengths of bubble and liquid slug so far. However, the numerical data maintains a similar behavior to the previous tests, as shown in Figure 5.29 (e) and (f). As discussed in Test 3 data, the increase of amount of gas in the system affects the numerical definition of the inlet boundary condition. It consequently influences the geometric properties at S1, but it is more evident in the bubble region. Its higher relative deviation is 57.8% at S1. Gonçalves and Mazza (2022) and Toledo (2023) employed Rosa et al.'s (2015) slug tracking model, but their inlet condition is based on experimental data. They adopted the first experimental measuring station as the inlet. In this current research, the numerical determination of the flow parameters at the riser basis (first stations) is also a goal of this research. Furthermore, the numerical inlet coincides with the experimental air-water mixer and those data are not available. Test 4 is the only case in which the experimental and numerical L_B have a decrease between stations S2 and S3. The relative deviation for the liquid slug length is higher than 24.1% along the S curve, except for S9, which has an error equal to 5.8%.

Figure 5.30 presents the results from Test 5, the first one with a mixture velocity equal to 4.0 m/s. Figure 5.30 (a) shows the pressure between the stations S1 to S10. Its highest relative deviation is 4.2% (S1). The numerical and experimental bubble translation velocities have a good concordance, as shown in Figure 5.30 (b). However, the numerical model cannot capture its reduction at S4 and S7 or its acceleration after the bottom elbow (S8). The highest relative deviation for U_T is 19.7% (S9). The liquid slug front velocity also has a higher discrepancy with the experimental data at S7 and S9, with the highest relative deviation (16.8%).

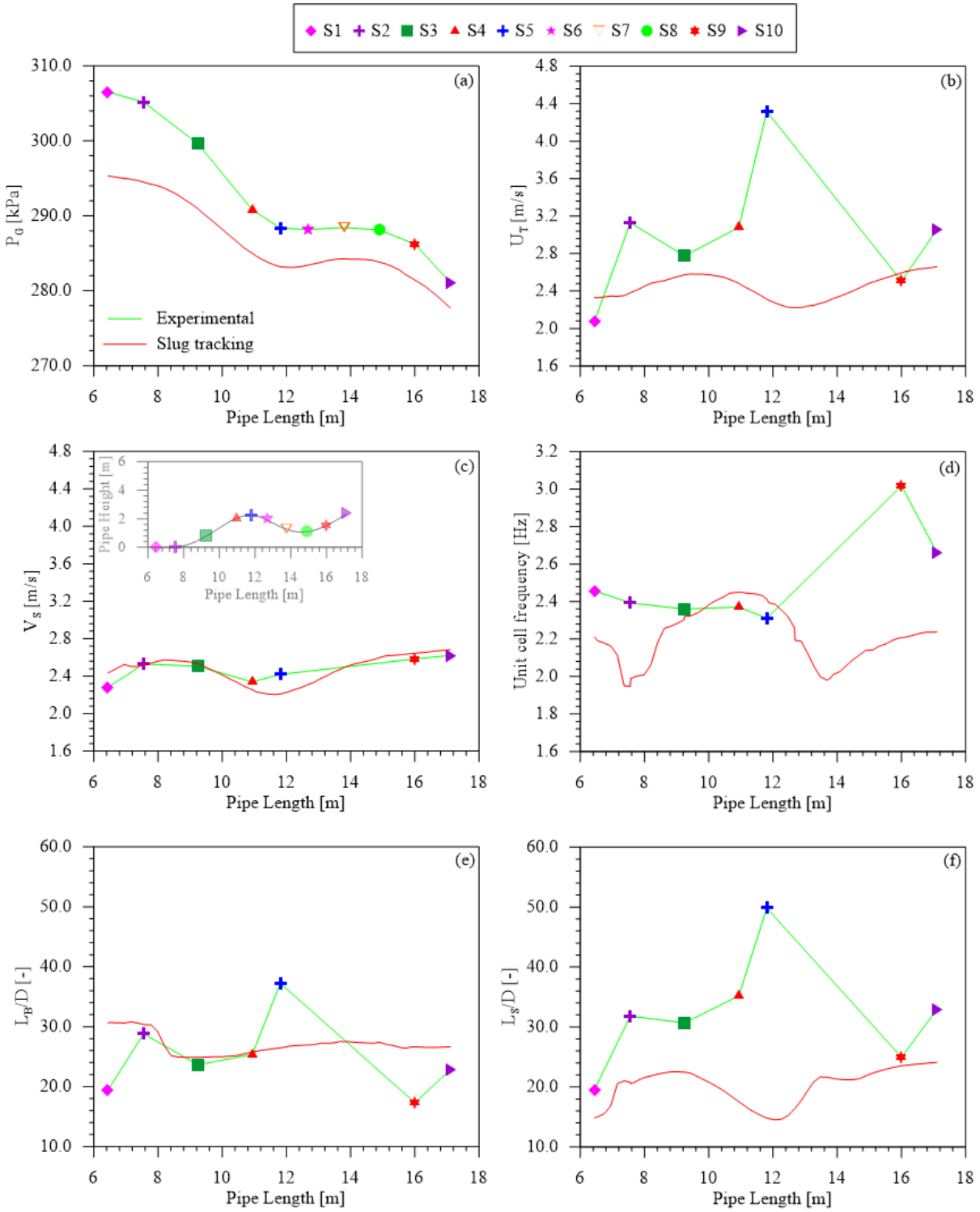

Figure 5.29. Comparison between slug tracking data and the experimental campaign for Test 4 (J_G/J_L = 1.5; U_M = 2.0 m/s): (a) gas pressure, (b) translation bubble and (c) liquid slug front velocities, (d) unit cell frequency and dimensionless (e) bubble and (f) liquid slug lengths.

Figure 5.30 (d) shows that the numerical cell frequency differs from the previous tests. The increase of the mixture velocity intensifies the impact of hilly terrain submodels. The first (6.8 m) and second (7.9 m) singularities are discussed in the Test 1 analysis, and the same effects are evident in the following tests. The current analysis (Test 5) noted a modification in

the frequency and the bubble and liquid slug lengths in some other curve positions: 10.5, 13.8 and 15.1 m. They represent the positions of the other singularities.

The third singularity treats the transition from concentric to plane interface in the film region because of the pipe orientation change (A format). As presented in Section 4.2.2, it increases the bubble length and decreases the liquid slug size. Figure 5.30 (e) and (f) show both phenomena. When the cell reaches the S8, the bottom elbow can cause an increase in the liquid slug length and the generation of a new cell (higher frequency). Figure 5.30 (d) and (f) also show them. The film region returns to the concentric interface at the last singularity, which is before S9 (15.1 m). Thus, the bubble length reduction and the increase of liquid slug length are expected. The impact on the bubble size is noticeable in the numerical data from Figure 5.30 (e). The experimental and numerical data agree on increasing cell frequency between stations S8 and S9.

Comparing the numerical and experimental data, some discrepancies in the numerical cell frequency are observed. The numerical frequency decreases at S4 and it only occurs at S6 in the experimental data. In addition, the first and second singularities also affect it. The highest relative deviation is 15.7% (S2). The comparison leads to a good agreement regarding the bubble and liquid slug lengths. Their highest relative deviations are 36.5% (S9) and 20.0% (S1) respectively.

Figure 5.31 presents the comparison of the results from Test 6. The figure (a) presents the pressure profile. This is the only case in which the numerical data overestimates the pressure in a part of the pipe. The highest relative deviation is 1.6% (S1). The other parameters do not present a good concordance between experimental and numerical data. As discussed in Test 4, the higher superficial gas and velocities ratio intensifies the parameter variability along the singularities. Similar to the data obtained from Tests 1 to 4, the slug tracking cannot capture the punctual acceleration of the structures at S5.

In addition, Figure 5.31 (b) demonstrates the numerical bubble translation velocity does not represent the actual velocity at S1. It consequently affects the representativeness of the other parameters. Figure 5.31 (f) also exhibits this difficulty; the numerical liquid slug length is much shorter than the experimental one at S1. The images from Test 5 show the liquid slug is highly aerated, which affected the determination of its inlet boundary condition, as shown in Figure 5.30 (f). If the gas fraction is higher, this process is even more complicated.

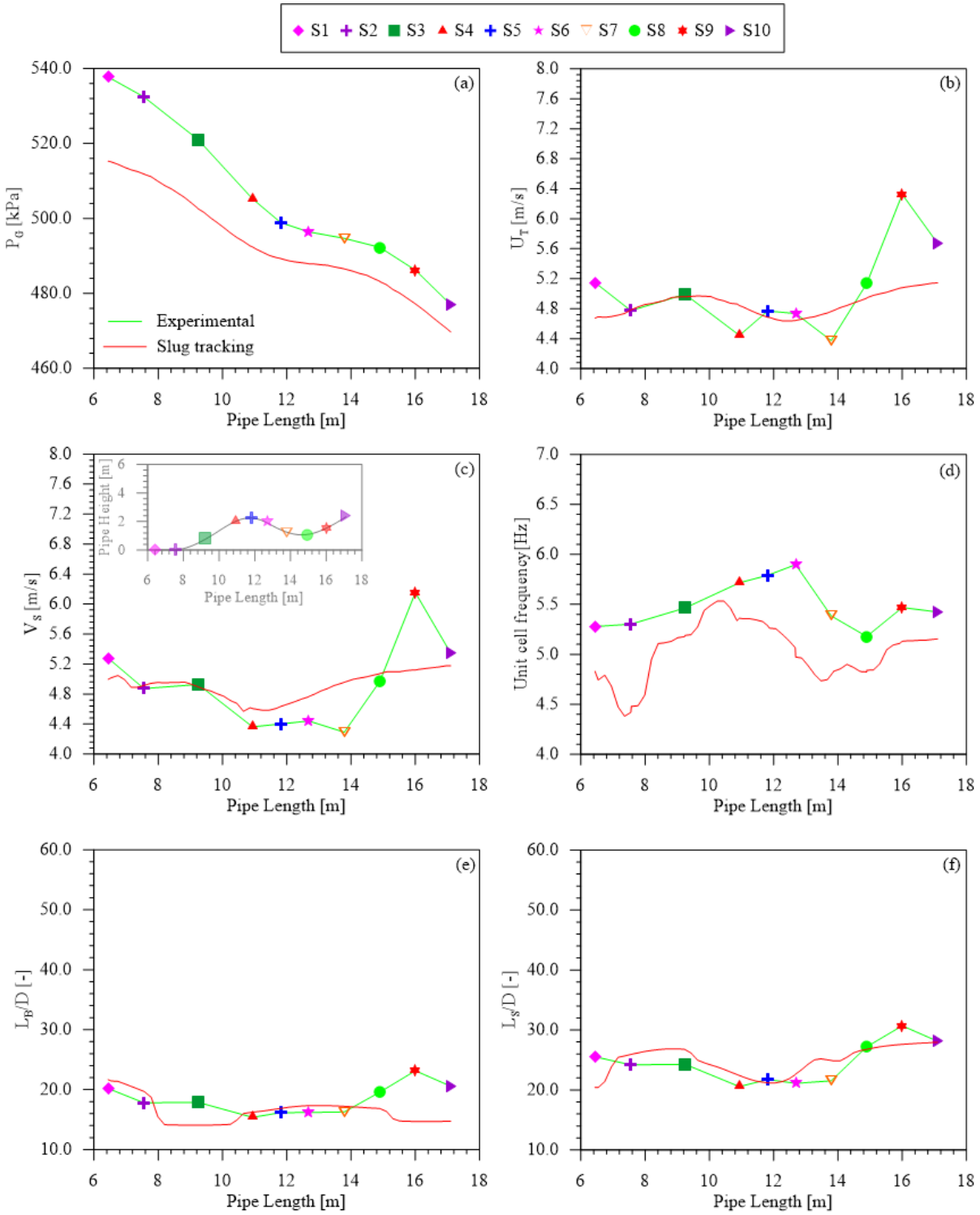

Figure 5.30. Comparison between slug tracking data and the experimental campaign for Test 5 (J_G/J_L = 1.0; U_M = 4.0 m/s): (a) gas pressure, (b) translation bubble and (c) liquid slug front velocities, (d) unit cell frequency and dimensionless (e) bubble and (f) liquid slug lengths.

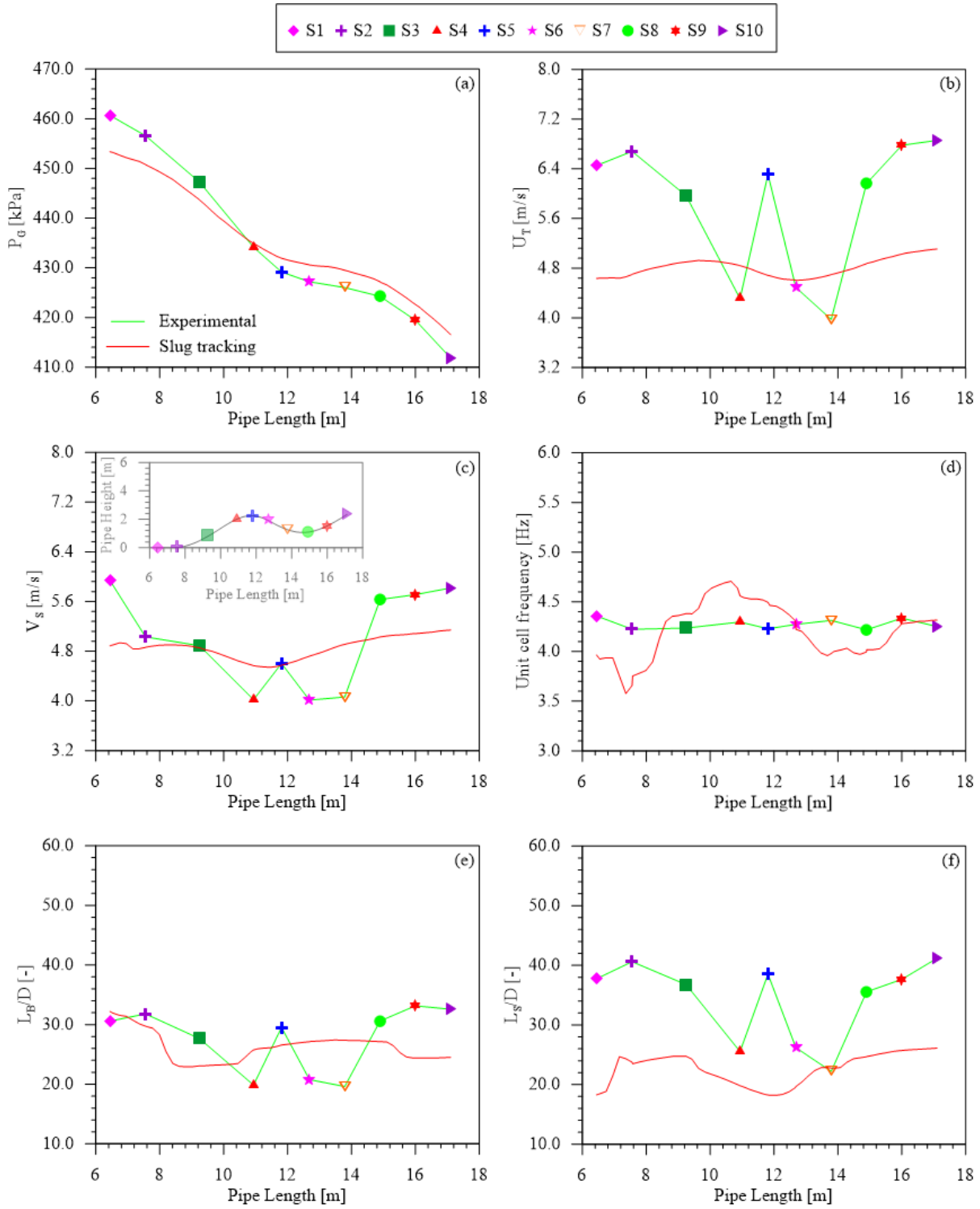

Figure 5.31. Comparison between slug tracking data and the experimental campaign for Test 6 (J_G/J_L = 1.5; U_M = 4.0 m/s): (a) gas pressure, (b) translation bubble and (c) liquid slug front velocities, (d) unit cell frequency and dimensionless (e) bubble and (f) liquid slug lengths.

Test 6 has the most discrepant comparison between experimental and numerical profiles. On the other hand, it is the better agreement regarding the pressure profile. The numerical pressure profile strongly depends on the bubble and liquid slug distribution along the pipe and their properties. Thus, the velocities and length discrepancies between the numerical

and experimental data may highlight a potential problem in this test's experimental data obtained by the impedance sensors. The high aeration of the flow could have affected the correct identification of the bubble nose or liquid slug front, influencing the results of the post-processing program.

Figures 5.32 and 5.33 present the last step of the validation process. The statistical distribution is essential for describing the randomness inherent to slug flow patterns. Thus, the following figures compare the numerical distribution obtained for U_T, L_B/D and L_S/D with the experimental one (dataset with six repetitions). Tests 2 and 5 were chosen to demonstrate the slug tracking performance along the S curve. These tests illustrate the results for mixture velocities (2.0 and 4.0 m/s) and two superficial gas and liquid velocities ratios (0.67 and 1.0).

Figure 5.32 shows Test 2 distributions. The numerical translation bubble velocity cannot represent the variation observed in the experimental campaign. The parameter is concentrated around the mean value (small spread out). These parameters are calculated by Choi et al.'s (2012) correlation, so this behavior is expected. Between stations S1 to S10, numerical U_T varies from 2.0 to 3.0 m/s. Thus, the numerical data does not capture the maximum experimental values. Regarding the bubble lengths, the numerical data agrees with the experimental data at stations S1, S2, S4 and S5. The numerical model could not capture the maximum values observed in the other stations in the experimental data. The numerical model leads to values concentrated around the mean value for the liquid slug length. Stations S2, S3, S7, S9 and S10 demonstrate the difficulty of capturing the smallest and longest lengths.

Figure 5.33 exhibits the Test 5 distributions. The numerical translational bubble velocity presents the same behavior discussed in Figure 5.32. The numerical parameter has a smaller spread out than the experimental. Between stations S1 and S10, numerical U_T varies from 2.8 to 5.7 m/s, much smaller than the maximum experimental value at S9 (17.7 m/s). The figure also shows the slug tracking could not predict the smallest and longest bubble and liquid slug lengths. The latter parameter has a lower variance, and it is clustered closely around the mean value.

Figures 5.32 and 5.33 demonstrate that the higher mixture velocity and the amount of gas in the line influence the numerical model performance. Unlike Test 5, slug tracking predicts the smallest bubble lengths for all stations in Test 2. Furthermore, the maximum bubble and liquid slug lengths are longer in Test 5, and the numerical model cannot capture it.

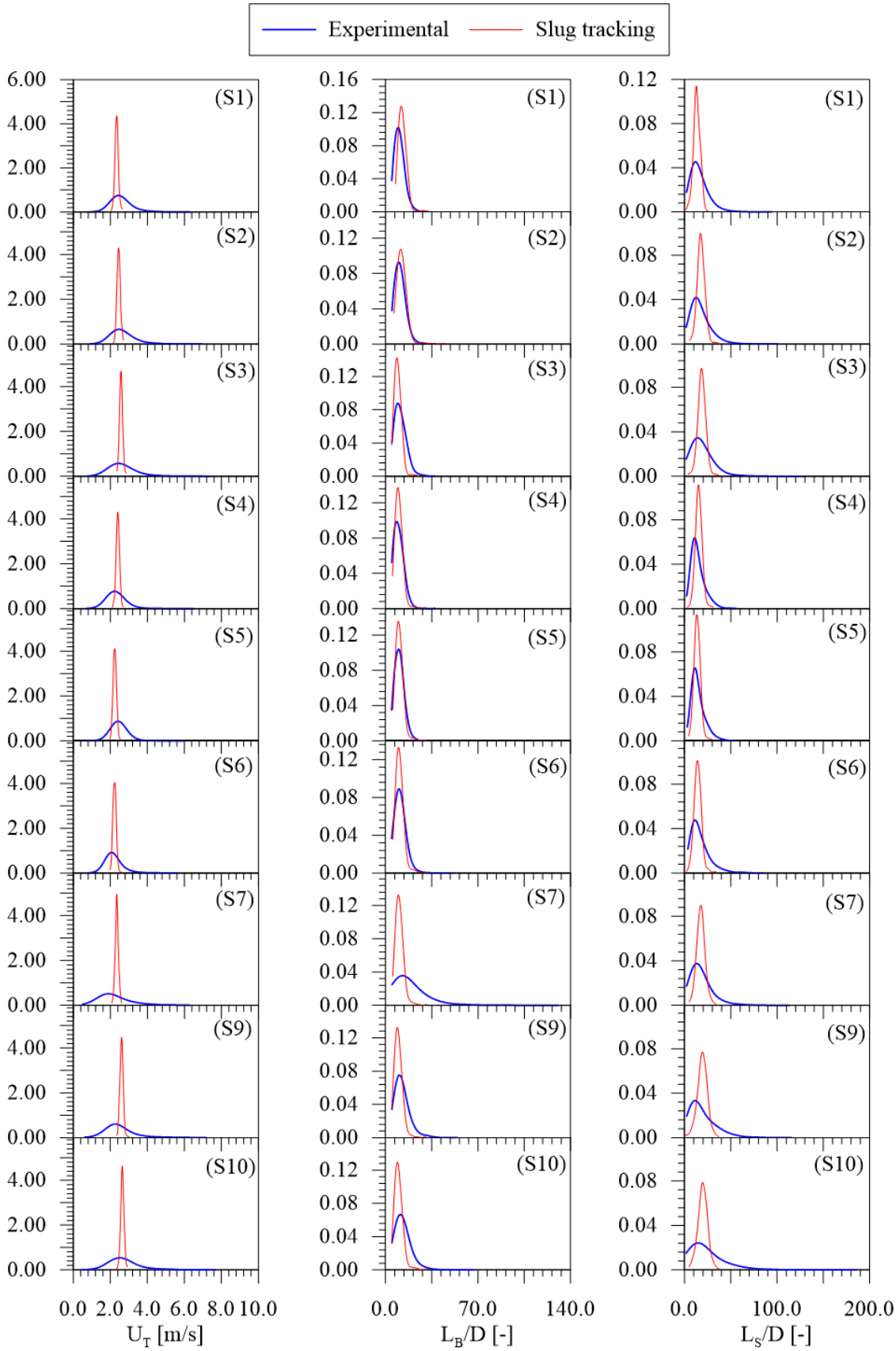

Figure 5.32. Distributions of the experimental (blue line) and numerical (red line) data of U_T, L_B and L_S in each station for Test 2 (J_G/J_L = 0.67 and U_M = 2.0 m/s).

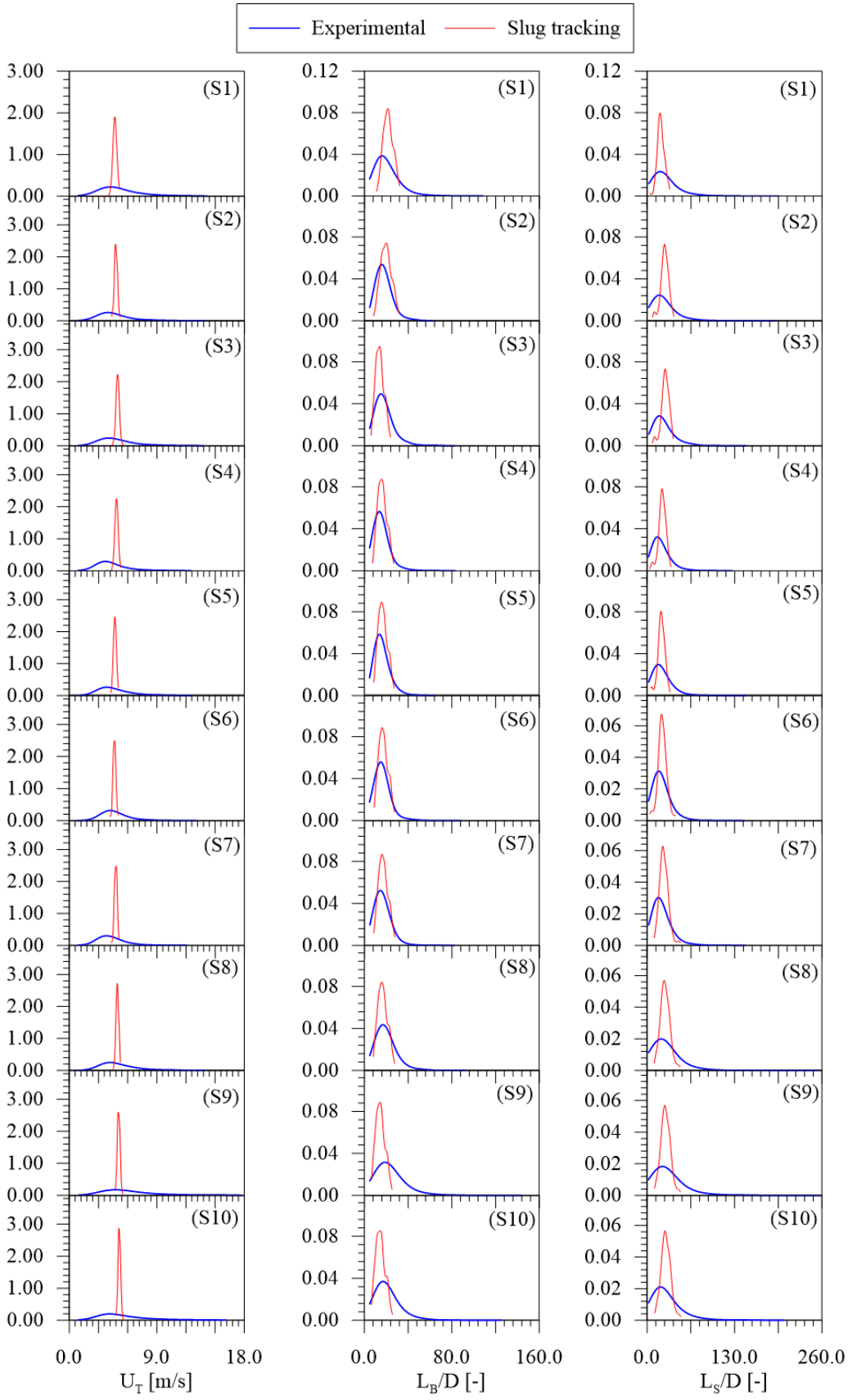

Figure 5.33. Distributions of the experimental (blue line) and numerical (red line) data of U_T, L_B and L_S in each station for Test 5 (J_G/J_L = 1.0 and U_M = 4.0 m/s).

5.4 Slug tracking validation: field data for actual lazy wave riser

This section presents a practical application in which the current slug tracking model is employed to simulate the flow through an actual lazy wave riser used in the petroleum field. Andreolli (2018) provided the pipeline geometry and operational conditions. According to the author, the model validation with actual field data is essential due to the complex features of the oil and gas production system. In this scenario, the pipeline is very long, resulting in a high-pressure gradient between the seafloor and the separator facilities and a high expansion of the natural gas. In addition, the complexity of the oil and gas mixture introduces a new challenge to the numerical model.

Andreolli (2018) proposed a linear stability analysis to identify the stable and unstable regions in multiphase flow. The author employed his model for different offshore oil production systems (steel catenary riser and lazy wave). One part of his research introduces steady-state flow modeling, which is validated against field data obtained in an actual lazy wave riser. This section employs the same data to demonstrate the slug tracking performance in this kind of application.

Andreolli (2018) provides a test grid with 16 operational points, with the flow rate and WOR (water-oil-rate) varying from 1,200 to 3,000 sm^3/d and from 0 to 22%, respectively. Six tests include gas lift. In addition, three tests are unstable (severe slugging). These tests are disregarded because the slug tracking has no submodel to consider the gas lift, and the severe slugging is out of this research scope. Among the available cases, the slug tracking simulates four points with different mixture velocities and superficial gas and liquid velocities ratios. Table 5.3 presents the following data for each case: superficial gas and liquid velocities and their ratio, mixture velocity, Gas-oil-ratio (GOR), Basic Sediment and Water (BSW), the pressure at the pipeline inlet (subsea wellhead) and outlet (SEP), and the mean temperature between the seabed and the separator facilities.

The oil and gas mixture has 29.05° API gravity, and the gas density is 0.83. As discussed in Section 4.4, a Black Oil model is employed to define the fluid properties. In addition to the parameters presented in Table 5.3, the fluid characterization requires the CO_2 fraction in the mixture and the input data for ASTM relations (minimum and maximum pairs of temperature and crude oil dynamic viscosity). The current simulations consider that the mixture does not contain CO_2.

Table 5.3. Test grid for the field data provided by Andreolli (2018).

	J_L [m/s]	J_G [m/s]	U_M [m/s]	J_G/J_O	GOR [sm³/sm³]	BSW [%]	$P_{wellhead}$ [kgf/cm²]	P_{SEP} [kgf/cm²]	T_{mean} [°C]
Case 1	1.175	1.363	2.538	1.160	214.310	12.0	124.774	22.382	33.263
Case 2	1.215	1.363	2.578	1.122	214.760	12.0	128.348	22.572	33.396
Case 3	1.251	1.394	2.645	1.114	218.077	10.0	130.624	22.725	33.468
Case 4	1.322	1.441	2.763	1.090	221.862	9.0	134.515	22.989	33.412

Figure 5.34 shows the geometry of the flowline-riser system by plotting the relation between the pipeline length versus its inclination and height. The pipeline is 9,081 m long, has a 6,313.01 m flowline and reaches 2,159 m height, as shown in Figure 5.34 (b). The numerical model divides it into 18 sections with different inclinations and employs 29 virtual probes along the pipe. These probes register the flow properties. The inner diameter and roughness are constant and equal to 6 inches (0.1524 m) and 0.00021 m, respectively. Figure 5.34 (a) illustrates that the pipe inclination varies significantly. Similar to experimental line, this section has a flowline followed by three sections with gradual inclination change: (i) an upward inclined pipe (943 m) that reaches approximately 79°, (ii) downward inclined (443 m) that reaches approximately - 18° and (iii) upward inclined (1,382 m) that reaches 90°.

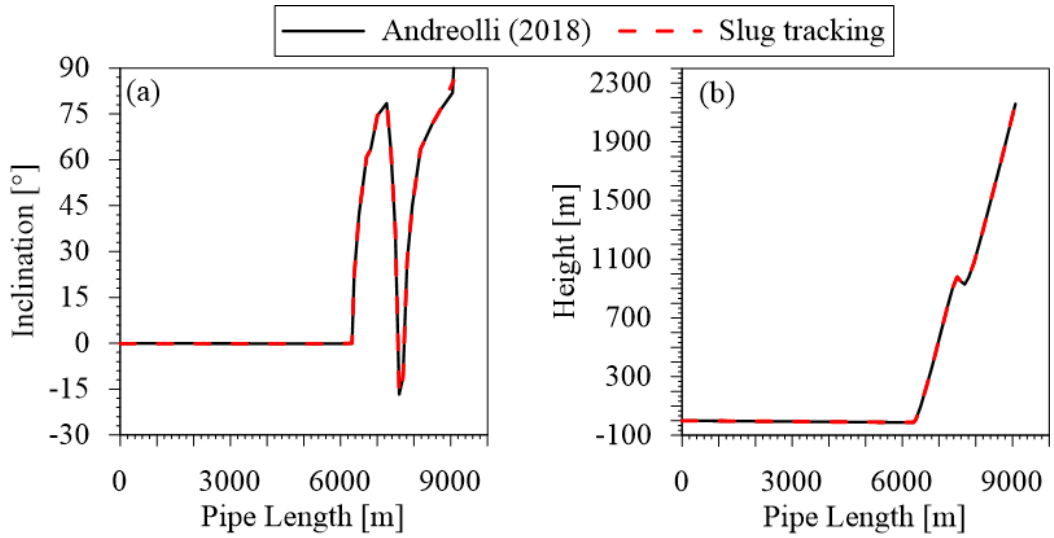

Figure 5.34. Comparison between the pipeline geometry provided by Andreolli (2018) and the numerical version applied in the slug tracking model.

As a boundary condition, the numerical model requires the pressure at the pipe outlet and a list of cell properties at the inlet. Table 5.3 provides the outlet pressure for all tests. As presented in Section 4.3, the simulation can employ a periodic or random inlet condition. This section employs both types. The periodic is the simplest one and it is used to validate the pressure at the subsea wellhead through field data from Andreolli (2018). The random condition

is applied to demonstrate the statistical distributions and the temporal and spatial variability of the internal flow parameters. The latter can be used in dynamic riser analysis. The analysis of average parameters presents both inlet condition types to assess their influences.

The liquid slug holdup, unit cell frequency, drift parameters and wake coefficients were determined by Malnes (1982), Schulkes (2011), Choi et al. (2012) and Grenier (1997) for all tests shown in Table 5.3. Table 5.4 presents the pressure gradients for each test. This table also shows the field pressure at the subsea wellhead and the relative errors.

In the current analysis, Choi et al. (2012) were adopted due to the good results obtained in the first validation (Section 5.3). The simulations were conducted using Colebrook White and Blasius correlations to assess their influences on the determination of the inlet pressure. As shown in Table 5.4, the slug tracking model agrees well with the field data for all tests.

Table 5.4. Comparison of inlet pressure (subsea wellhead) between the data obtained by the slug tracking model and the field data.

		$P_{wellhead}$ - Numerical data [kgf/cm²]			
	Field data - $P_{wellhead}$ [kgf/cm²]	Choi et al. (2012)			
		Blasius	Relative error [%]	Colebrook White	Relative error [%]
Case 1	**124.774**	127.791	2.42	132.380	6.1
Case 2	**128.348**	130.556	1.72	135.394	5.5
Case 3	**130.624**	132.100	1.13	137.239	5.1
Case 4	**134.515**	135.601	0.81	141.196	5.0

Andreolli (2018) conducted a similar approach in his stationary analysis using three correlations for drift parameters (Bendiksen, 1984; Bhagwat and Ghajar, 2012; Woldesemayat and Ghajar, 2007) and three approaches to calculate the two-phase frictional multiplier (two based on the Vieira and Garcia (2014) correlation and the third one based on Müller-Steinhagen and Heck (1986) correlation). According to the author, the relative errors varied between 11-40%, 10-38%, 8-36% and 7-35% for Cases 1, 2, 3 and 4, respectively. Bhagwat and Ghajar (2012) and Vieira and Garcia (2014) correlations provided the lowest relative errors for his cases.

The following analyses aim to demonstrate some additional results obtained by the slug tracking model, such as the mean and statistical distributions data as well as the temporal and spatial variability of the internal flow parameters. For this purpose, it was chosen only Case 1. The other tests would present similar behavior due to their similar mixture velocities and gas-to-liquid ratio. As reported in Table 5.4, Blasius correlation leads to the better results and is employed in the following discussions. The other closure equations are not changed. Figure 5.35 shows the numerical average parameters along the pipeline, obtained using periodic (blue line) and random (red line) inlet conditions. The field pressure and mixture velocity are available and presented in Figure 5.35 (a) and (b). Figure 5.35 (a) shows that the random condition provides an inlet pressure closer to the Andreolli's (2018) field data (see Table 5.4). Its relative error is 0.9%. The numerical mixture velocity at the inlet agrees well with the field data regardless of the inlet condition, as presented in Figure 5.35 (b). Both figures also demonstrate that the inlet boundary condition has a minor influence on the pressure and mixture velocity spatial evolutions.

Figure 5.35 (c) and (d) presents the bubble and liquid slug lengths. These graphics show additional data (gray bullet points) that represents the size of each structure inside the numerical domain at a specific time using the random inlet condition. Since the slug tracking is a Lagrangian approach, it is possible to identify the properties of each cell in the numerical domain for all time steps. It seems like a snapshot of the flow distribution along the pipe in an arbitrary time [t]. The acquisition of those data is obtained in several positions of the pipe that coincides with the cell locations.

The figure shows that the random condition results in longer bubbles and slugs. It occurs because the structures have different properties, intensifying the interaction between neighboring cells. In addition, the effects of the hilly terrain submodels are also noted. The five singularities are employed in this simulation (see Section 4.2), and they are positioned approximately at 6,337 m (V format), 6,707 m (plane to concentric bubble interface), 7,493 m (concentric to plane bubble interface), 7,699 m (V format) and 8,176 m (plane to concentric bubble interface).

The effects of the bubble interface transition are more noticeable in the mean parameters. Compared to the previous validation (Figures 5.26, 5.27, 5.28, 5.29, 5.30 and 5.31), their influences are even more evident in larger pipeline diameters. At the first interface transition (6,707 m), the bubble length significantly reduces due to the migration to the center

of the pipe, occupying most of this large cross-section area. Consequently, the part of the liquid film moves to the upstream liquid slug and its length increases. After this point, the interface transition occurs twice (at 7,493 m and 8,176 m), but the length changes are smaller.

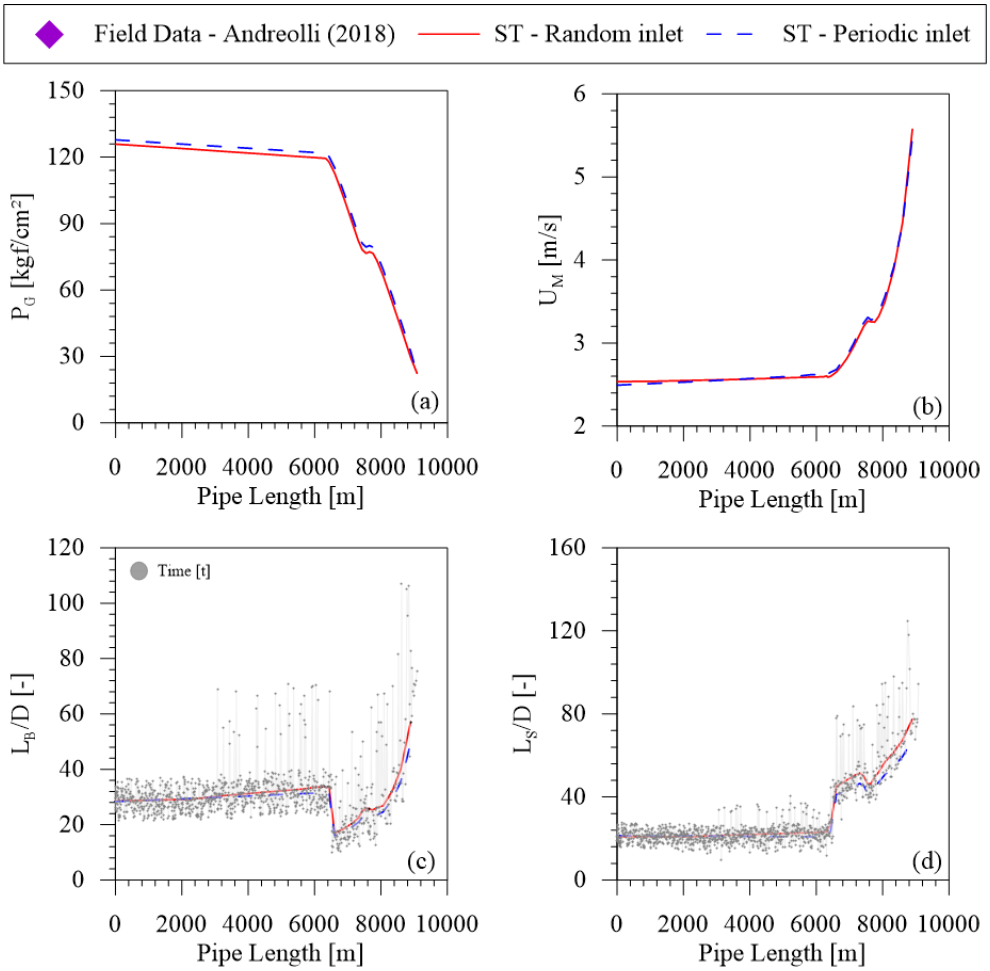

Figure 5.35. The slug flow parameters along the pipeline: (a) Gas pressure, (b) Mixture velocity, dimensionless (c) bubble and (d) liquid slug lengths. Numerical data using a random (red line) and periodic (blue line) inlet condition.

Figure 5.35 (c) and (d) demonstrates the slug flow variability regarding the bubble and liquid slug evolution at a specific time [t]. These properties change in time and space. Thus, the gas and liquid distribution along the pipe and the internal fluid weight vary significantly during oil and gas production. According to Ortega Malca (2015) and Zhu et al. (2021), this randomness is essential to measure the slug flow influence on the dynamic structural analysis of risers. Thus, the following analysis will only present the random inlet condition.

Figure 5.36 also demonstrates this variability through the statistical distributions. The numerical simulation considers 29 virtual probes along the pipe, but the following analysis focuses on five. Probes 13, 19, 23, 24 and 29 are at 6,309 m (flowline), 7,131 m (after the first

V format), 7,648 m (after the third singularity), 7,755 m (after the second V format) and 8,890 m (near the pipe outlet). Figure 5.36 (a) shows the translational bubble velocity, for which the greater spread out occurs at Probe 29. The five stations present a gradual increase in that parameter due to the gas expansion along the pipe.

Figure 5.36 (b) presents the bubble length reduction between Probes 13 and 19 due to the interface transition—the bubbles at Probes 23 and 24 slightly increase compared to the previous station. In addition, their means and distributions are almost the same. It occurs because the third and fourth singularities have a minor influence on the bubble size. The last virtual probe has the most extended bubbles due to the gas expansion (pipe reaches vertical orientation). In this position, the bubble sizes vary between 13D to 164D.

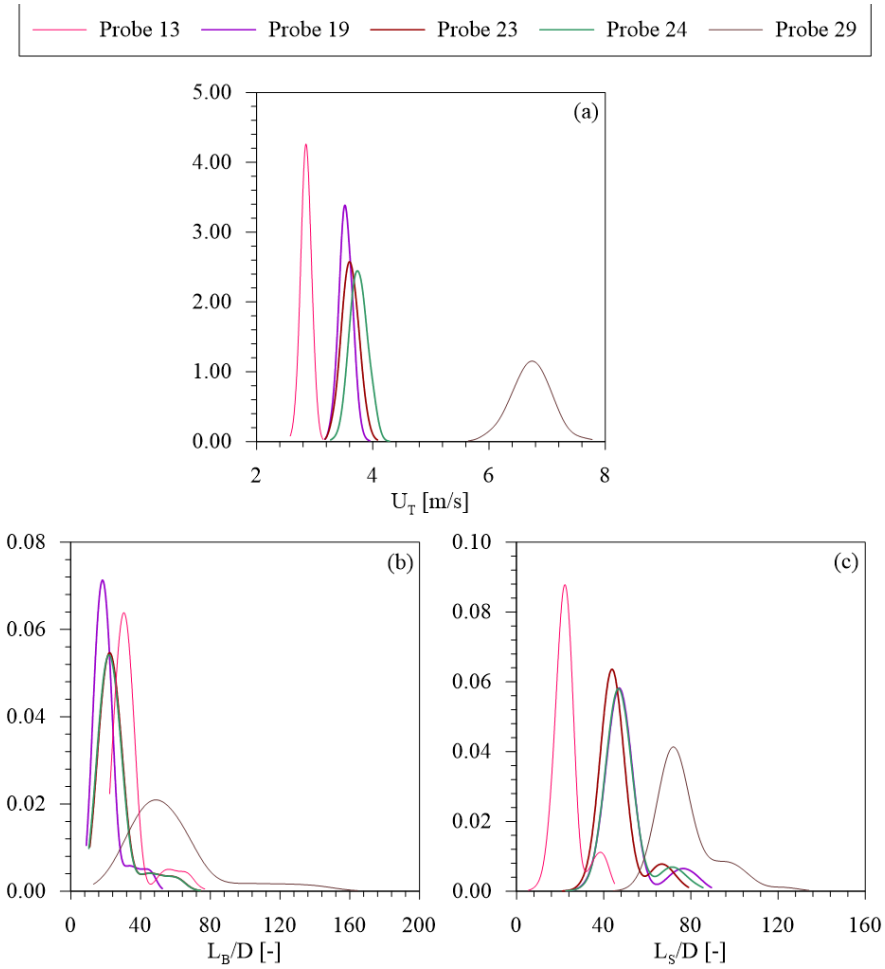

Figure 5.36. Distribution of the bubble translational velocity (a), dimensionless (b) bubble and (c) liquid slug lengths at virtual probes 14, 19, 23, 24 and 29.

Figure 5.36 (c) shows the effects of the singularities in the liquid slug length. The statistical distribution format is similar in all probes, except for the last one. As shown in Figure 5.35, the flowline section has the smallest liquid slug. Probes 19 and 24 are positioned after the

V format submodels. As discussed in Section 4.2.1, the criterion for creating a new unit cell or increasing the slug length is the coupling of the Kelvin-Helmholtz stability criterion and the minimum liquid slug length. This assumption can explain why both probes have similar means and distributions for L_S/D. The length reduction at Probe 23 occurs due to the transition from concentric to plane interface. Like L_B/D, the latter probe presents a greater spread out, and the lengths vary between 44D and 134D.

Finally, Figures 5.37 to 5.39 present the slug flow parameters for the dynamic riser analysis. The number of studies considering its influence has been increasing lately, but most of them use simplified models, as discussed in Section 2.2 (Table 2.3). The current slug tracking model includes all terms from previous ones and incorporates new approaches, such as flow randomness, oil and gas properties, and the effects of complex geometry on the flow parameters. Thus, the results of this model provide more realistic data.

Patel and Seyed (1989) and Vásquez and Avila (2021) pointed out the forces exerted by the internal flow is a function of the spatial and temporal variation of the pressure, mixture velocity and specific weight. The current slug tracking provides these data, and the acquisition needs to be long enough to describe all flow variabilities. It starts when there is no effect of the flow start-up process (Section 4.3.3). In addition, the frequency of parameters registration is a requirement of the structural software. The current model is able to register them in more than one frequency simultaneously. For this case, the frequency is 10 Hz, and the acquisition period is the time necessary for a cell travel twice the entire pipe. Figures 5.37 and 5.38 show the evolution of gas pressure and mixture velocity in two arbitrary moments of the simulations: [t] and [t+Δt]. Figure 5.39 presents the fluid weight along three pipeline sections in an arbitrary simulation time.

Figures 5.37 presents the pressure profile along the pipe, which is qualitatively similar in both moments. Since the numerical method assumes the outlet pressure as a constant, the inlet parameter can vary to accommodate the flow intermittence.

In Figure 5.38, the variability of the mixture velocity is more noticeable between both times. The first reason is the random inlet condition, which provides cells with different mixture velocities. The figure shows the difference in the entrance of the pipe. In addition, the outlet velocity differs for both times. The velocities at time [t] and [t+Δt] are 6.0 and 7.0 m/s, respectively. The increase and reduction of this parameter are cyclically observed during the

simulation. As discussed in Section 4.3.1, the bubble pressure is constant while it exits the numerical domain. This assumption increases the liquid slug velocity to conserve mass and momentum. When the exit process finishes, the previous cells damp the velocity wave, and the outlet velocity decreases again.

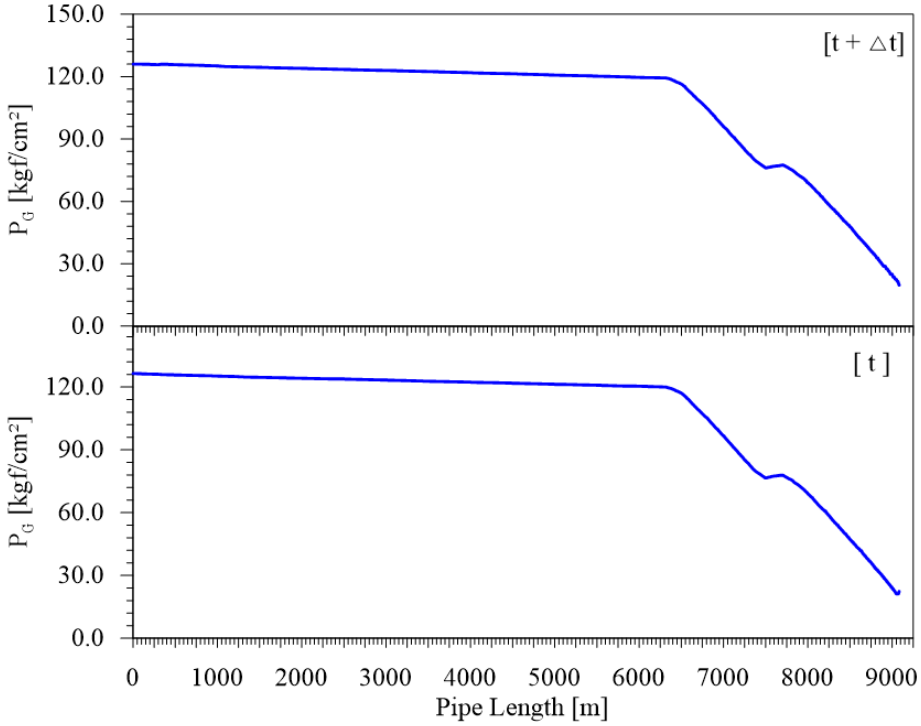

Figure 5.37. Spatial evolution of the pressure in two different time steps of the simulations.

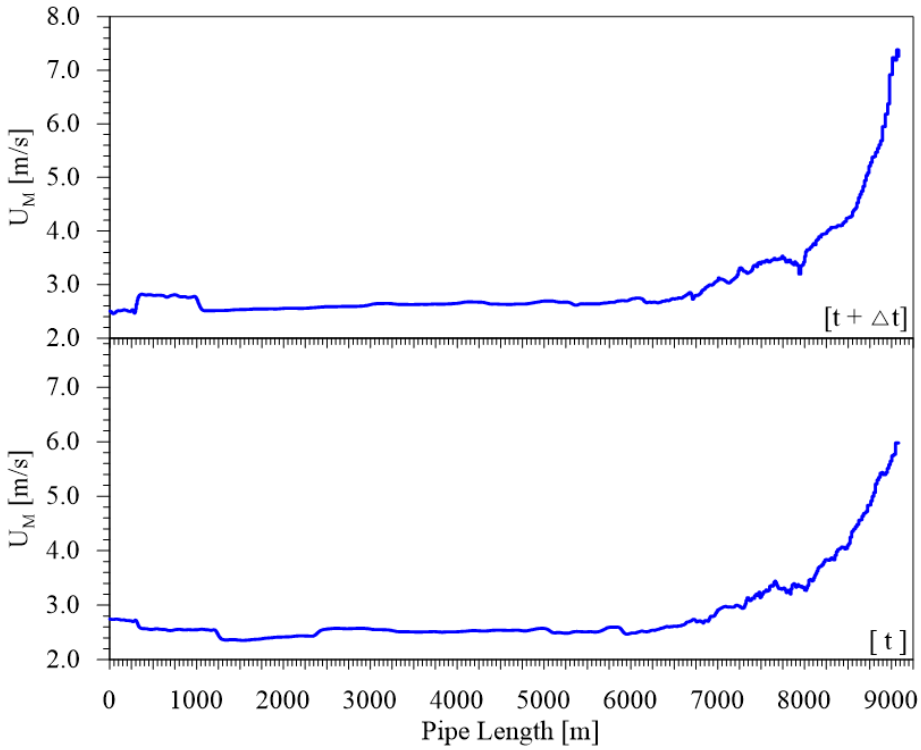

Figure 5.38. Spatial evolution of the mixture velocity in two different time steps of the simulations.

Figure 5.39 exemplifies the evolution of the specific weight of the bubbles and liquid slugs in a small section of the pipe (7,100 to 8,000 m). Figure 5.39 (a) to (c) represents the flow structures between the end of the first upward-inclined section (7,100 m) to the beginning of the second one (8,000 m). Furthermore, it covers the bubble interface transition and the second V format. The specific weight is determined for each bubble $\left(\gamma_B^j\right)$ and liquid slug $\left(\gamma_S^j\right)$ as a function of the gas and liquid densities and their holdups:

$$\gamma_B^j = \left[\rho_G\left(1-R_f\right)+\rho_L R_f\right]\times g \ , \tag{5.1}$$

$$\gamma_S^j = \left[\rho_G\left(1-R_S\right)+\rho_L R_S\right]\times g \ . \tag{5.2}$$

The highest specific weight (approximately 6.6 kN/m³) describes the liquid slugs. The lowest ones, spanning from 1.8 to 2.0 kN/m³, define the elongated bubble. Figure 5.39 (a) to (c) shows that both structures have different lengths along the sections. Nonetheless, the maximum level does not vary as the minimum does. It occurs because the liquid slug holdup only changes at the first singularity (6,707 m). On the other hand, each bubble has a different void fraction. It results in a more significant variability of the lower level.

The four sections presented in this chapter highlight the slug flow variability. The experimental images and data (Sections 5.1 and 5.2) show that the complex lazy wave geometry changes the flow structures (flow pattern, pressure gradients, velocities, lengths and frequency). That influence is a function of the mixture velocities and superficial gas and liquid ratio. In addition, it is also evident that the properties significantly vary along the time and space through the statistical distributions. These facts show the importance of slug flow models that take account of the randomness and the hilly terrain effects.

Sections 5.3 and 5.4 presents the validation of the slug tracking against the experimental campaign and a practical application of the model in a real-word scenario. Both tests show the model performance to predict the randomness inherent to the slug flow. The statistical distributions (Figures 5.32, 5.33 and 5.36) and the slug flow parameters for the dynamic riser analysis (Figures 5.37 to 5.39) show that. These results show the influence of the transition of the bubble interface (plane and concentric), hilly terrain submodels, liquid slug aeration, flow randomness and oil and gas properties. The improved slug tracking model can

provide more realistic slug flow parameters for dynamic riser analysis based on these new features.

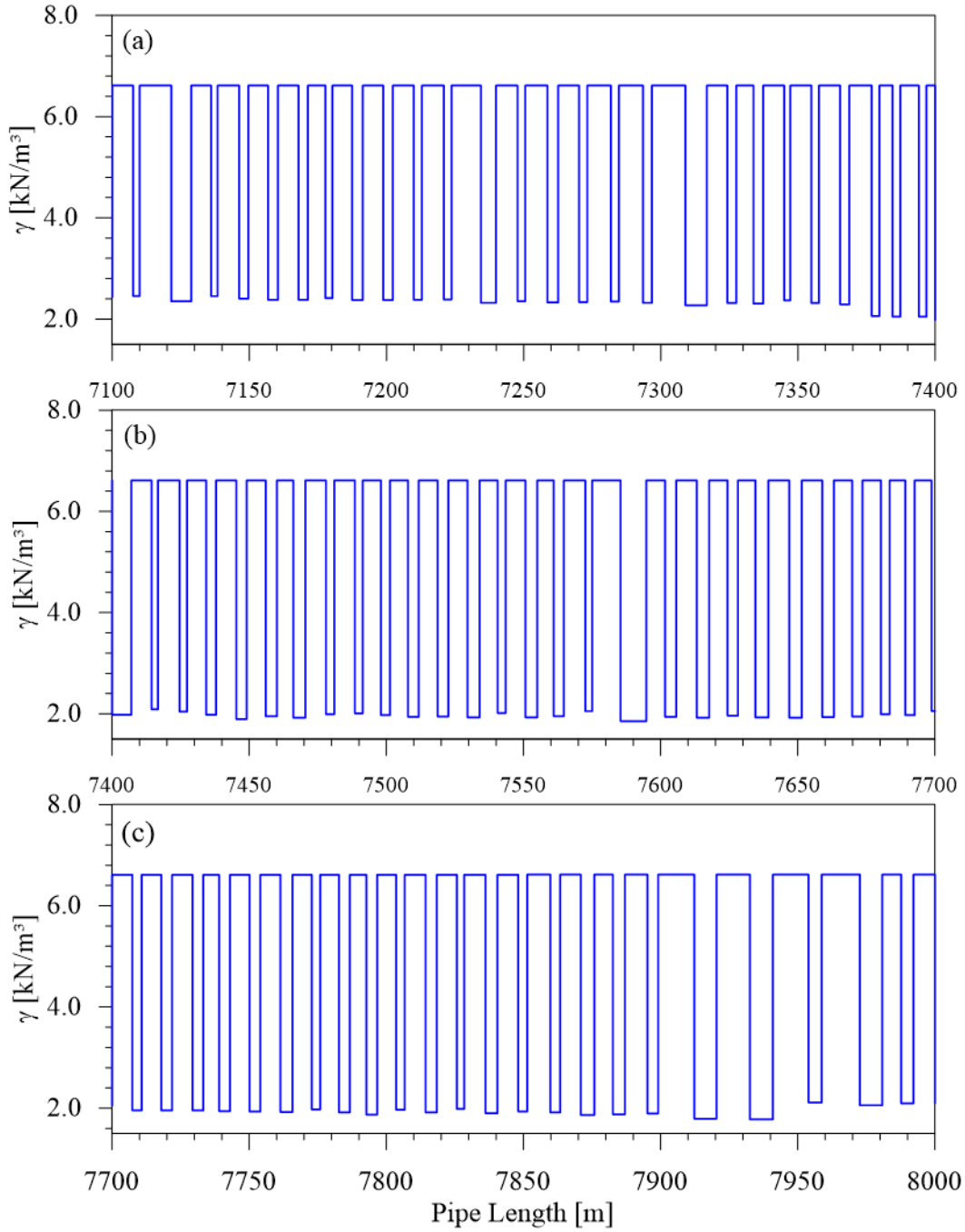

Figure 5.39. Bubble and liquid slug specific weight over three sections of the pipe: (a) 7,100 to 7,400 m, (b) 7,400 to 7,700 m and (c) 7,700 to 8,000 m.

6 CONCLUSIONS

The offshore oil and gas field has been encountered in increasingly deeper water. In this scenario, the flowline-riser configuration is crucial to ensure the security and to enhance its useful life. The forces exerted on the riser by the environment (wave, sea current, motion produced by offset vessels) and production (pressure, momentum and weight of the internal fluid) conditions become even stronger, which can lead to accidents with high environmental, economic and human impacts. One solution to reduce those risks is the usage of systems with different geometric configurations, such as Steel Lazy Wave Riser (SLWR). The SLWR has a buoyancy module that reduces the stress caused by those efforts and minimizes fatigue damage.

As reported in the literature review, the prediction of the slug flow properties is essential to guarantee a realistic dynamic structural analysis. The impact of that flow pattern is more noticeable due to its random feature. In addition, the SLWR geometry also intensifies the variation of flow properties due to the changes of pipeline inclination and orientation. Previous papers named those geometric changes as hilly terrain. Several authors discussed its influence on the flow, but most of them considered a simpler setup. Therefore, the current research aimed to visualize, understand, measure and model the impact of a complex geometry on the flow parameters.

This research is structured in two main areas: experimental and numerical. The experimental campaign was carried out in Flow&Rs Laboratory at Universidade de Campinas. The test loop is a laboratory-scale lazy wave riser, where the data acquisition and the flow visualization are conducted. The line has 10 measuring stations, and each of them contains a pressure transducer and two impedance sensors. The high-speed filming was recorded in six positions along the curve. The test grid contains six operation points that cover two mixture velocities and four superficial air and water velocities ratio. By applying a post-processing procedure, the experimental campaign provides the mean data of pressure, cell frequency, bubble and liquid slug lengths and velocities as well as the statistical distribution of some of those parameters.

The numerical study proposed some improvements to Rosa et al.'s (2015) slug tracking model such as: the treatment of initial and boundary conditions, the determination of oil and gas thermodynamic properties as well as the modeling of the phenomena caused by the

gradual pipeline inclination change and the hilly terrain setup. The improved model is validated against the data obtained by the experimental campaign. In addition, the slug tracking also simulates the flow through an actual lazy wave riser, presented in Andreolli (2018). The mean data and statistical distributions as well as the parameters required by dynamic riser analysis are also presented.

The acquisition of the flow images was limited to three operational conditions: Test 1 (J_L = 1.33 m/s and J_G = 0.67 m/s), Test 4 (J_L = 0.8 m/s and J_G = 1.2 m/s), and Test 5 ($J_L = J_G$ = 2.0 m/s). The images show the mixture velocities and the gas-to-liquid ratios strongly influences the flow behavior along the S curve. The slug flow is observed at the riser basis (S1) for all tests. As a function of the pipeline inclination, the bubble region interchanges between the concentric and plane interface at the upwards sections (close to S3 and S9) and at top of the curve (S5). At the A format (S4-S5-S6), the formation of a dry zone reported by Taitel and Barnea (2000) does not occur. It is also reported by Alves et al. (2019). The flow behavior along the downward inclined section varies for each test. The increase of the gas amount inside the pipe (Test 4) intensifies the bubble coalescence, and the total liquid slug dissipation occurs faster. When the liquid amount is higher (Test 1), the transition is postponed due to the intense liquid film acceleration. This liquid is discharged in the downstream slug, which retards the overtaking mechanism. It is also reported by Barros et al. (2022). In accordance with Al-Safran et al. (2005) and Yin et al. (2018) the slug formation mechanisms occurred due to Kelvin-Helmholtz instabilities at the low elbow (S8) and by wave coalescences in the downstream pipe (S9). Similar to observed by Zheng et al. (1995), Yoshida et al. (2000) and Al-Safran et al. (2005), the influence of hilly terrain is lower on high gas and superficial velocities (Test 5).

The experimental data reveals that the pressure profile has three different gradients along S1 to S10 due to the upward and downhill inclined sections. The pressure behavior in the downward pipe is influenced by the gas-to-liquid ratio. In addition, the bubble and liquid slug lengths and velocities, as well as the frequency, are affected by that. Tests 4 and 5 have the highest gas-to-liquid ratio (1.5). Their flow parameters present the greatest variability between S1 to S10, regardless of the mixture velocity. It reveals that the hilly terrain influence is more dependent on the phase fractions than the mixture velocity. For the tests with lower gas-to-liquid ratio ($\leq$ 1.0), the greatest variation of bubble and liquid lengths and frequency is along the downhill section and V format (S7 to S9). The intense bubble coalescence (or transition to

stratified pattern), liquid accumulation at the bottom elbow (S8) and slug formation can justify that.

The slug tracking validation against the experimental data shows the capacity of the model to predict the pressure profile accurately. The numerical model captures that the pressure presents three different behaviors caused by geometry. Regarding the bubble and liquid velocities and lengths, the model presents better results for the tests with lower gas-to-liquid ratio (≤ 1.0). The relative deviations depend on the tests, parameters and virtual stations. The experimental frequency along the S1-S10 is not captured in the numerical simulations. This difference is more noticeable in the downhill section. The slug tracking assumes slug flow presence along the entire pipe, is not able to predict the slug flow formation or the transition for another pattern. For these reasons, the intense cell interaction, it is difficult to capture the intense cell interaction and the variability of the flow behavior in the downward pipe, as well as the slug initiation process. The numerical statistical distributions of bubble and liquid slug lengths present a good agreement with the experimental data, but the maximum values are not captured.

The simulation of a real-word oil and gas scenario also demonstrated that the model is able to predict the pressure at the wellhead. Four cases with different mixture velocities, gas-to-liquid ratios, GOR and BSW were simulated. Two friction factor correlations are used and the highest relative deviation for the inlet pressure was 6.1%. The statistical distribution as well as the temporal and spatial evolution of mixture velocity, pressure and fluid weight highlight the flow variability once again. The experimental and numerical analyses show the importance of a slug flow model that considers the randomness inherent to this pattern, the hilly terrain submodels, the bubble profile and the correct prediction of the thermodynamic properties.

For future works, conducting an experimental campaign to obtain a flow pattern map along the S curve could provide a major contribution. For some tests, the recorded images show that the transition from slug to stratified pattern happens in the downward inclined section, and the flow returns to slug in the following upward pipe. However, the current research does not exactly predict where those processes occur. In the numerical field, the insertion of a submodel to predict the flow pattern transition in the downward section could enhance the numerical results in this region. In addition, the insertion of the influence of the riser movement on the flow parameters can improve the quality of the input data for dynamic riser applications.

REFERENCES

Al-Safran, E., 2009. Investigation and prediction of slug frequency in gas/liquid horizontal pipe flow. J. Pet. Sci. Eng. 69, 143–155. https://doi.org/10.1016/j.petrol.2009.08.009

Al-Safran, E., Sarica, C., Zhang, H.-Q., Brill, J., 2006. Mechanistic/Probabilistic Modeling of Slug Initiation in a Lower Elbow of a Hilly-Terrain Pipeline, in: Proceedings of SPE Annual Technical Conference and Exhibition. Society of Petroleum Engineers. https://doi.org/10.2523/102254-MS

Al-Safran, E., Sarica, C., Zhang, H.-Q., Brill, J., 2005. Investigation of slug flow characteristics in the valley of a hilly-terrain pipeline. Int. J. Multiph. Flow 31, 337–357. https://doi.org/10.1016/j.ijmultiphaseflow.2004.11.002

Al-safran, E.M., Taitel, Y., Brill, J.P., 2004. Prediction of Slug Length Distribution Along a Hilly Terrain Pipeline Using Slug Tracking Model. J. Energy Resour. Technol. 126, 54–62. https://doi.org/10.1115/1.1649971

Alves, R.F., Schneider, F.A., Barbuto, F.A., Santos, P.H.D., Morales, R.E.M., 2019. An experimental analysis on the influence of flow direction changes on the transitions in gas-liquid, slug-to-stratified downward flows. Int. J. Multiph. Flow 119, 155–165. https://doi.org/10.1016/j.ijmultiphaseflow.2019.07.008

Andreolli, I., 2018. Estabilidade linear aplicada ao escoamento multifásico de petróleo. Universidade de São Paulo, São Paulo. https://doi.org/10.11606/T.3.2018.tde-16072018-091052

Andreussi, P., Bendiksen, K., 1989. An investigation of void fraction in liquid slugs for horizontal and inclined gas-liquid pipe flow. Int. J. Multiph. Flow 15, 937–946. https://doi.org/10.1016/0301-9322(89)90022-0

Andreussi, P., Bendiksen, K.H., Nydal, O.J., 1993. Void distribution in slug flow. Int. J. Multiph. Flow 19, 817–828. https://doi.org/10.1016/0301-9322(93)90045-V

Bai, Y., Bai, Q., 2005. Subsea Pipelines and Risers (Ocean Engineering), Ocean Engineering Series. Elsevier B.V.

Barnea, D., Taitel, Y., 1993. A model for slug length distribution in gas-liquid slug flow. Int. J. Multiph. Flow 19, 829–838. https://doi.org/10.1016/0301-9322(93)90046-W

Barros, H.A.A., Rodrigues, R.L.P., Alves, R.F., Cozin, C., Rodrigues, H.T., Junior, R. da F., Silva, M.J. da, Neto, M.A.M., Morales, R.E.M., 2022. Experimental slug flow dissipation analysis in pipes with horizontal to inclined downward direction change. Exp. Therm. Fluid Sci. 139, 110740. https://doi.org/10.1016/j.expthermflusci.2022.110740

Beggs, H.D., Robinson, J.R., 1975. Estimating the Viscosity of Crude Oil Systems. J. Pet. Technol. 27, 1140–1141. https://doi.org/10.2118/5434-PA

Bendiksen, K.H., 1984. An experimental investigation of the motion of long bubbles in inclined tubes. Int. J. Multiph. Flow 10, 467–483. https://doi.org/10.1016/0301-9322(84)90057-0

Bendiksen, K.H., Malnes, D., Nydal, O.J., 1996. On the modeling of slug flow. Chem. Eng. Commun. 141–142, 71–102. https://doi.org/10.1080/00986449608936411

Bernicot, M.F., Drouffe, J.-M., 1991. A Slug-Length Distribution Law for Multiphase Transportation Systems. SPE Prod. Eng. 6, 166–170. https://doi.org/10.2118/17864-PA

Bhagwat, S.M., Ghajar, A.J., 2014. A flow pattern independent drift flux model based void fraction correlation for a wide range of gas–liquid two phase flow. Int. J. Multiph. Flow 59, 186–205. https://doi.org/10.1016/j.ijmultiphaseflow.2013.11.001

Bhagwat, S.M., Ghajar, A.J., 2012. Flow pattern and pipe orientation independent semi-empirical void fraction correlation for a gas-liquid two phase flow based on the concept of drift flux model. ASME 2012 Heat Transf. Summer Conf. Collocated with ASME 2012 Fluids Eng. Div. Summer Meet. ASME 2012 10th Int. Conf. Nanochannels, Microchannels Minichannels, HT 2012 2, 327–336. https://doi.org/10.1115/HT2012-58048

Bordalo, S.N., Morooka, C.K., 2018. Slug flow induced oscillations on subsea petroleum pipelines. J. Pet. Sci. Eng. 165, 535–549. https://doi.org/10.1016/j.petrol.2018.02.026

Bordalo, S.N., Morooka, C.K., Cavalcante, C.C.P., Matt, C.G.C., Franciss, R., 2008. Whipping Phenomenon Caused by the Internal Flow Momentum on the Catenary Risers of Offshore Petroleum Fields, in: Volume 1: Offshore Technology. ASMEDC, pp. 315–323. https://doi.org/10.1115/OMAE2008-57351

Bressani, M., 2016. Estudo experimental do escoamento bifásico padrão intermitente na transição vertical ascendente para horizontal. Universidade Estadual de Campinas, Campinas, SP. https://doi.org/10.47749/T/UNICAMP.2016.967424

Bueno, L.G.G., 2010. Estudo experimental de escoamentos líquido-gás intermitentes em tubulações inclinadas. Universidade Estadual de Campinas.

Chatjigeorgiou, I.K., 2017. Hydroelastic response of marine risers subjected to internal slug-flow. Appl. Ocean Res. 62, 1–17. https://doi.org/10.1016/j.apor.2016.11.008

Choi, J., Pereyra, E., Sarica, C., Park, C., Kang, J., 2012. An Efficient Drift-Flux Closure Relationship to Estimate Liquid Holdups of Gas-Liquid Two-Phase Flow in Pipes. Energies 5, 5294–5306. https://doi.org/10.3390/en5125294

Conte, M.G., Bassani, C.L., Cozin, C., Nakayama, A.E., Medina, C.D.P., Morales, R.E.M., 2011. Numerical analysis of slug flow in inclined ducts using slug tracking model. XXXII

CILAMCE - Congr. Ibero Lat. Am. Métodos Comput. em Eng.

Cook, M., Behnia, M., 2000. Slug length prediction in near horizontal gas–liquid intermittent flow. Chem. Eng. Sci. 55, 2009–2018. https://doi.org/10.1016/S0009-2509(99)00485-6

Dalla Maria, L., 2016. Estudo Experimental das Ondas de Fração de Vazio e Pressão em Escoamento Horizontal Transiente de Ar e Água no Padrão Intermitente. Universidade de Campinas.

Duan, J. long, Chen, K., You, Y. xiang, Gao, S., 2017. Experimental and computational investigations on severe slugging in a catenary riser. China Ocean Eng. 31, 653–664. https://doi.org/10.1007/s13344-017-0075-5

Duarte, M., 2007. Influencia da viscosidade sobre o escoamento gas-liquido horizontal intermitente. Universidade Estadual de Campinas, Campinas, SP. https://doi.org/10.47749/T/UNICAMP.2007.429277

Dukler, A.E., Hubbard, M.G., 1975. A Model for Gas-Liquid Slug Flow in Horizontal and Near Horizontal Tubes. Ind. Eng. Chem. Fundam. 14, 337–347. https://doi.org/10.1021/i160056a011

Ersoy, G., Sarica, C., Al-Safran, E.M., Zhang, H.Q., 2011. Experimental investigation of three-phase gas-oil-water slug flow evolution in hilly-terrain pipelines. Proc. - SPE Annu. Tech. Conf. Exhib. 3, 2069–2091.

Fabre, J., Line, A., 1992. Modeling of Two-Phase Slug Flow. Annu. Rev. Fluid Mech. 24, 21–46. https://doi.org/10.1146/annurev.fl.24.010192.000321

Fabre, J., Peresson, L.L., Corteville, J., Odello, R., Bourgeois, T., 1990. Severe slugging in pipeline/riser systems. Spe Prod. Eng. 5, 299–305. https://doi.org/10.2118/16846-pa

Fernandes, R.C., Semiat, R., Dukler, A.E., 1983. Hydrodynamic model for gas-liquid slug flow in vertical tubes. AIChE J. 29, 981–989. https://doi.org/10.1002/aic.690290617

Ferschneider, G., 1983. Ecoulements diphasiques gaz-liquide à poches et à bouchons en conduites. Rev. Inst. Fr. Pet. 38, 153–182. https://doi.org/https://doi.org/10.2516/ogst:1983010

Figueiredo, M. de M.F., 2020. Caracterização de escoamentos verticais bifásicos utilizando ultrassom. Tese doutorado, Univ. Estadual Campinas. Universidade Estadual de Campinas, Campinas, SP. https://doi.org/10.47749/T/UNICAMP.2020.1149399

Franklin, E.M., 2004. Modelagem numerica para seguimento dinamico de bolhas em escoamento intermitente horizontal gas liquido. UNICAMP.

Gaspari, E.F., Santim, C., 2017. Transient Analysis of a Gas-Lift Production System Using a Non-Isothermal Simplified Drift-Flux Model, in: IV Journeys in Multiphase Flows. São Paulo.

Gomez, L.E., Shoham, O., Taitel, Y., 2000. Prediction of slug liquid holdup: Horizontal to upward vertical flow. Int. J. Multiph. Flow 26, 517–521. https://doi.org/10.1016/S0301-9322(99)00025-7

Gonçalves, J.L., Mazza, R.A., 2024. Slug flow parameters applied to dynamic riser analysis. Int. J. Multiph. Flow 171, 104670. https://doi.org/10.1016/j.ijmultiphaseflow.2023.104670

Gonçalves, J.L., Mazza, R.A., 2022. A transient analysis of slug flow in a horizontal pipe using slug tracking model: Void and pressure wave. Int. J. Multiph. Flow 149, 103972. https://doi.org/10.1016/j.ijmultiphaseflow.2022.103972

Gregory, G.A., Nicholson, M.K., Aziz, K., 1978. Correlation of the liquid volume fraction in the slug for horizontal gas-liquid slug flow. Int. J. Multiph. Flow 4, 33–39. https://doi.org/10.1016/0301-9322(78)90023-X

Gregory, G.A., Scott, D.S., 1969. Correlation of liquid slug velocity and frequency in horizontal cocurrent gas-liquid slug flow. AIChE J. 15, 933–935. https://doi.org/10.1002/aic.690150623

Grenier, P., 1997. Evolution des longueurs de bouchons en écoulement intermittent horizontal. Institut de Mécanique des Fluides de Toulose, France.

Grigoleto, M.M., Bassani, C.L., Conte, M.G., Cozin, C., Barbuto, F.A., Morales, R.E.M., 2021. Heat transfer modeling of non-boiling gas-liquid slug flow using a slug tracking approach. Int. J. Heat Mass Transf. 165, 120664. https://doi.org/10.1016/j.ijheatmasstransfer.2020.120664

Hadi, D.-H., Jasim, H.H., 2018. Vibration effect on the corrosion rate of crude oil pipeline. Int. J. Eng. &Technology 7, 6447–6452. https://doi.org/10.14419/ijet.v7i4.23218

Haile, S.G., Woschke, E., Tibba, G.S., Pandey, V., 2022. Internal two-phase flow induced vibrations: A review. Cogent Eng. 9. https://doi.org/10.1080/23311916.2022.2083472

Harmathy, T.Z., 1960. Velocity of large drops and bubbles in media of infinite or restricted extent. AIChE J. 6, 281–288. https://doi.org/10.1002/aic.690060222

Heywood, N.I., Richardson, J.F., 1979. Slug flow of air—water mixtures in a horizontal pipe: Determination of liquid holdup by γ-ray absorption. Chem. Eng. Sci. 34, 17–30. https://doi.org/10.1016/0009-2509(79)85174-X

Hill, T.J., Fairhurst, C.P., Nelson, C.J., Beeerra, H., Bailey, R.S., 1996. Multiphase Production Through Hilly Terrain Pipelines in Cusiana Oilfield, Colombia, in: Society of Petroleum Engineers. Denver.

Hussein, A., 2023. Essentials of Flow Assurance Solids in Oil and Gas Operations, 1st Editio. ed. Elsevier. https://doi.org/10.1016/B978-0-323-99118-6.00015-0

Ishii, M., Zuber, N., 1979. Drag coefficient and relative velocity in bubbly, droplet or particulate flows. AIChE J. 25, 843–855. https://doi.org/10.1002/aic.690250513

Jepson, W.P., Taylor, R.E., 1993. Slug flow and its transitions in large-diameter horizontal pipes. Int. J. Multiph. Flow 19, 411–420. https://doi.org/10.1016/0301-9322(93)90057-2

Kim, S., Kim, M.H., 2015. Dynamic behaviors of conventional SCR and lazy-wave SCR for FPSOs in deepwater. Ocean Eng. 106, 396–414. https://doi.org/10.1016/j.oceaneng.2015.06.039

Kjeldby, T.K., Henkes, R., Nydal, O.J., 2011. Slug tracking simulation of severe slugging experiments. World Acad. Sci. Eng. Technol. 78, 928–933.

Kjølås, J., 2007. Plug propagation in multiphase pipelines: Modeling and small scale experiments. NTNU - Norwegian University of Science and Technology.

Klinkenberg, A.M., Tijsseling, A.S., 2021. Stochastic mechanistic modelling of two-phase slug flow forces on bends in horizontal piping. Int. J. Multiph. Flow 144, 103778. https://doi.org/10.1016/j.ijmultiphaseflow.2021.103778

Lee, A., Gonzalez, M.H., Eakin, B.E., 1966. The Viscosity of Natural Gases.

Ma, B., Srinil, N., 2020. Planar dynamics of inclined curved flexible riser carrying slug liquid–gas flows. J. Fluids Struct. 94, 102911. https://doi.org/10.1016/j.jfluidstructs.2020.102911

Madani, S., Caballina, O., Souhar, M., 2009. Unsteady dynamics of Taylor bubble rising in vertical oscillating tubes. Int. J. Multiph. Flow 35, 363–375. https://doi.org/10.1016/j.ijmultiphaseflow.2009.01.002

Maidana, N. da C., 2017. Perturbações induzidas por uma placa de orifício no escoamento horizontal de ar e água no padrão intermitente. Universidade Estadual de Campinas, Campinas, SP. https://doi.org/10.47749/T/UNICAMP.2017.984621

Makogon, T.Y., 2019. Handbook of Multiphase Flow Assurance. Elsevier. https://doi.org/10.1016/B978-0-12-813062-9.00001-4

Malnes, D., 1982. Slug flow in vertical, horizontal and inclined pipes. Kjeller, Norway.

Manfield, P.D., 2000. Analytical Studies of Slug Flow.

Mazza, R.A., Rosa, E.S., Yoshizawa, C.J., 2010. Analyses of liquid film models applied to horizontal and near horizontal gas-liquid slug flows. Chem. Eng. Sci. 65, 3876–3892. https://doi.org/10.1016/j.ces.2010.03.035

Meléndez Vásquez, J.A., 2020. Ferramenta computacional para análise de risers flexíveis dispostos em catenária com um escoamento interno bifásico gás- líquido em padrão golfadas.

Instituto Nacional de Pesquisas Espaciais.

Meneses, B.M., Ribeiro, L.G., Parente, E., Melo, A.M.C. de, Mineiro, F.P. da S., Carneseca, M.T.C.G., 2023. Post-failure behavior of lazy-wave risers. Ocean Eng. 280, 114777. https://doi.org/10.1016/j.oceaneng.2023.114777

Miwa, S., Mori, M., Hibiki, T., 2015. Two-phase flow induced vibration in piping systems. Prog. Nucl. Energy 78, 270–284. https://doi.org/10.1016/j.pnucene.2014.10.003

Moissis, R., Griffith, P., 1962. Entrance Effects in a Two-Phase Slug Flow. J. Heat Transfer 84, 29–38. https://doi.org/10.1115/1.3684284

Mokhatab, S., 2007. Severe Slugging In a Catenary-shaped Riser: Experimental and Simulation Studies. Pet. Sci. Technol. 25, 719–740. https://doi.org/10.1080/10916460601005695

Müller-Steinhagen, H., Heck, K., 1986. A simple friction pressure drop correlation for two-phase flow in pipes. Chem. Eng. Process. 20, 297–308. https://doi.org/10.1016/0255-2701(86)80008-3

Nieckele, A.O., Carneiro, J.N.E., Chucuya, R.C., Azevedo, J.H.P., 2013. Initiation and Statistical Evolution of Horizontal Slug Flow With a Two-Fluid Model. J. Fluids Eng. 135, 1–11. https://doi.org/10.1115/1.4025223

Nydal, O.J., Banerjee, S., 1996. Dynamic slug tracking simulations for gas-liquid flow in pipelines. Chem. Eng. Commun. 141–142, 13–39. https://doi.org/10.1080/00986449608936408

Nydal, O.J., Pintus, S., Andreussi, P., 1992. Statistical characterization of slug flow in horizontal pipes. Int. J. Multiph. Flow 18, 439–453. https://doi.org/10.1016/0301-9322(92)90027-E

Oliveira, J.V., Vaz, M.A., Jian, S., 2013. Severe slugging in catenary risers - Simplified modeling. Proc. Annu. Offshore Technol. Conf. 3, 1769–1784. https://doi.org/10.4043/24492-ms

Ortega Malca, A.J., 2015. Dynamic Response of Flexible Risers due to Unsteady Slug Flow. Norwegian University of Science and Technology.

Padrino, J.C., Srinil, N., Kurushina, V., Swailes, D., 2023. Prediction of unsteady slug flow in a long curved inclined riser with a slug tracking model. Int. J. Multiph. Flow 162, 104410. https://doi.org/10.1016/j.ijmultiphaseflow.2023.104410

Park, S., Nydal, O.J., 2014. Study on Severe Slugging in an S-Shaped Riser: Small-Scale Experiments Compared With Simulations. Oil Gas Facil. 3, 72–80. https://doi.org/10.2118/171559-PA

Patel, M.H., Seyed, F.B., 1989. Internal flow-induced behaviour of flexible risers. Eng. Struct. 11, 266–280. https://doi.org/10.1016/0141-0296(89)90046-1

Pereyra, E., Arismendi, R., Gomez, L.E., Mohan, R.S., Shoham, O., Kouba, G.E., 2012. State of the Art of Experimental Studies and Predictive Methods for Slug Liquid Holdup. J. Energy Resour. Technol. 134, 1–10. https://doi.org/10.1115/1.4005658

Piper, L.D., W.D., M., Corredor, J.H., 1993. Compressibility Factors for Naturally Occurring Petroleum Gases, in: Proceedings of SPE Annual Technical Conference and Exhibition. Society of Petroleum Engineers, Houston, Texas, pp. 23–33. https://doi.org/10.2523/26668-MS

Pollio, A., Mossa, M., 2009. A Comparison between Two Simple Models of a Slug Flow in a Long Flexible Marine Riser 1–33. https://doi.org/https://doi.org/10.48550/arXiv.0911.1873

Porter, K., Pereyra, E., Mesa, J., Sarica, C., 2023. Experimental investigation of induced vibrations in horizontal Gas-Liquid flow. Exp. Therm. Fluid Sci. 149, 111015. https://doi.org/10.1016/j.expthermflusci.2023.111015

Pots, B.F.M., Bromilow, I.G., Konijn, M.J.W.F., 1987. Severe Slug Flow in Offshore Flowline/Riser Systems. SPE Prod. Eng. 2, 319–324. https://doi.org/10.2118/13723-PA

Ragab, A., Brandstaetter, W., Ruthammer, G., Shalaby, S., 2008. Analysis of Multiphase Production through Hilly Terrian Pipelines in Matzen Field—Austria by CFD, in: SPE Annual Technical Conference and Exhibition. Denver. https://doi.org/https://doi.org/10.2118/115355-MS

Rodrigues, H.T., 2009. Simulação Numérica do Escoamento Bifásico Gás-Líquido no Padrão de Golfadas Utilizando um Modelo Lagrangeano de Seguimento de Pistões. Universidade Tecnológica Federal do Paraná.

Rosa, E.S., Mazza, R.A., Morales, R.E., Rodrigues, H.T., Cozin, C., 2015. Analysis of slug tracking model for gas–liquid flows in a pipe. J. Brazilian Soc. Mech. Sci. Eng. 37, 1665–1686. https://doi.org/10.1007/s40430-015-0331-7

Rosa, E.S., Salgado, R.M., Ohishi, T., Mastelari, N., 2010. Performance comparison of artificial neural networks and expert systems applied to flow pattern identification in vertical ascendant gas-liquid flows. Int. J. Multiph. Flow 36, 738–754. https://doi.org/10.1016/j.ijmultiphaseflow.2010.05.001

Roumazeilles, P.M., Yang, J., Sarica, C., Chen, X.T., Wilson, J.F., Brill, J.P., 1996. An experimental study on downward slug flow in inclined pipes. SPE Prod. Facil. 11, 173–178. https://doi.org/10.2118/28546-PA

Ruan, W., Chen, M., Nie, Q., Xu, P., Li, J., Wang, X., 2024. Dynamic response of steel lazy wave riser considering the excitation of internal solitary wave and ocean currents. Ocean Eng. 294. https://doi.org/10.1016/j.oceaneng.2024.116708

Santim, C.G.S., Fulchignoni, L.P., Rosa, E.S., Gaspari, E.F., 2020. Transient multiphase flow modeling and validation in a real production system with high CO2 content using the drift-flux model. J. Pet. Sci. Eng. 188, 106903. https://doi.org/10.1016/j.petrol.2020.106903

Schmidt, Z., Brill, J.P., Beggs, H.D., 1980. Experimental Study of Severe Slugging in a Two-Phase-Flow Pipeline-Riser Pipe System. Soc. Pet. Eng. J. 407–414. https://doi.org/10.2118/8306-pa

Schulkes, R., 2011. Slug Frequencies Revisited, in: 15th International Conference on Multiphase Production Technology. Cannes, France, pp. 311–325.

Scott, S.L., Kouba, G.E., 2004. Advances in slug flow characterization for horizontal and slightly inclined pipelines. SPE Repr. Ser. 78–93. https://doi.org/10.2523/20628-ms

Sharma, Y., Ihara, M., Manabe, R., 2002. Simulating Slug Flow in Hilly-Terrain Pipelines. Proc. SPE Int. Pet. Conf. Exhib. Mex. 149–156. https://doi.org/10.2523/74359-ms

Shoham, O., 2005. Mechanistic Modeling of Gas-Liquid Two-phase Flow in Pipes. Society of Petroelum Engineers, Tulsa.

Standing, M.B., 1947. A Pressure-Volume-Temperature Correlation For Mixtures Of California Oils And Gases, in: Drilling and Production Practice. p. API 275-286.

Swamee, P.K., Jain, A.K., 1976. Explicit equations for pipe-flow problems. J. Hydraul. Div. 102, 657–664.

Taitel, 1986. Stability of severe slugging. Int. J. Multiph. Flow 12, 203–217. https://doi.org/10.1016/0301-9322(86)90026-1

Taitel, Y., Barnea, D., 2000. Slug-Tracking Model for Hilly Terrain Pipelines. SPE J. 5, 102–109. https://doi.org/10.2118/61445-PA

Taitel, Y., Barnea, D., 1998. Effect of gas compressibility on a slug tracking model. Chem. Eng. Sci. 53, 2089–2097. https://doi.org/10.1016/S0009-2509(98)00007-4

Taitel, Y., Barnea, D., 1990. Two-Phase Slug Flow, in: Advances in Heat Transfer. pp. 83–132. https://doi.org/10.1016/S0065-2717(08)70026-1

Taitel, Y., Bornea, D., Dukler, A.E., 1980. Modelling flow pattern transitions for steady upward gas-liquid flow in vertical tubes. Aiche. J. 26, 345–354.

Taitel, Y., Dukler, A.E., 1976. A model for predicting flow regime transitions in horizontal and near horizontal gas-liquid flow. AIChE J. 22, 47–55. https://doi.org/10.1002/aic.690220105

Taitel, Y., Sarica, C., Brill, J.P., 2000. Slug flow modeling for downward inclined pipe flow:

theoretical considerations. Int. J. Multiph. Flow 26, 833–844. https://doi.org/10.1016/S0301-9322(99)00053-1

Taitel, Y., Vierkandt, S., Shoham, O., Brill, J.P., 1990. Severe slugging in a riser system: experiments and modeling. Int. J. Multiph. Flow 16, 57–68. https://doi.org/10.1016/0301-9322(90)90037-J

Talvy, C.A., Shemer, L., Barnea, D., 2000. On the interaction between two consecutive elongated bubbles in a vertical pipe. Int. J. Multiph. Flow 26, 1905–1923. https://doi.org/10.1016/S0301-9322(00)00004-5

Toledo, G.P., 2023. Modeling for Pressure Waves Propagation Velocity in Slug Flow. Universidade Estadual de Campinas.

van Hout, R., Shemer, L., Barnea, D., 2003. Evolution of hydrodynamic and statistical parameters of gas–liquid slug flow along inclined pipes. Chem. Eng. Sci. 58, 115–133. https://doi.org/10.1016/S0009-2509(02)00441-4

Vásquez, J.A.M., Avila, J.P.J., 2021. Three-dimensional dynamic behaviour of flexible catenary risers with an internal slug flow. J. Fluids Struct. 107, 103409. https://doi.org/10.1016/j.jfluidstructs.2021.103409

Vásquez, J.A.M., Avila, J.P.J., 2019. A parametric analysis of the influence of the internal slug flow on the dynamic response of flexible marine risers. Ocean Eng. 174, 169–185. https://doi.org/10.1016/j.oceaneng.2019.01.031

Vasquez, M., Beggs, H.D., 1980. Correlations for Fluid Physical Property Prediction. J. Pet. Technol. 32, 968–970. https://doi.org/10.2118/6719-PA

Viana, F., Pardo, R., Yánez, R., Trallero, J.L., Joseph, D.D., 2003. Universal correlation for the rise velocity of long gas bubbles in round pipes. J. Fluid Mech. 494, S0022112003006165. https://doi.org/10.1017/S0022112003006165

Vicencio, F.E.C., 2013. Caracterização experimental do escoamento intermitente líquido-gás em tubulações horizontais. Universidade Tecnológica Federal do Paraná.

Vieira, R.A. de M., Garcia, A.P., 2014. Combination of Petroleum Correlations and Drift-Flux Approaches: A New Model for Two-Phase Flow Pressure Gradient Calculation for Horizontal and Slightly Inclined Upward Flowlines, in: Volume 5: Materials Technology; Petroleum Technology. American Society of Mechanical Engineers, pp. 1–10. https://doi.org/10.1115/OMAE2014-24313

Vieiro, J.J., Akhiiartdinov, A., Sævik, S., Larsen, C.M., Nydal, O.J., 2019. Two-way coupled fluid-structure interaction of gas-liquid slug flow in a flexible riser: Small-scale experiments and simulations. Multiph. Sci. Technol. 31, 27–43. https://doi.org/10.1615/MultScienTechn.2019029489

Wallis, G.B., 1969. One Dimensional Two-Phase flow, McGraw-Hil. ed. New York.

Wang, L., Yang, Y., Li, Y., Wang, Y., 2018. Dynamic behaviours of horizontal gas-liquid pipes subjected to hydrodynamic slug flow: Modelling and experiments. Int. J. Press. Vessel. Pip. 161, 50–57. https://doi.org/10.1016/j.ijpvp.2018.02.005

Wang, X., Guo, L., Zhang, X., 2006. Development of Liquid Slug Length in Gas-Liquid Slug Flow along Horizontal Pipeline: Experiment and Simulation. Chinese J. Chem. Eng. 14, 626–633. https://doi.org/10.1016/S1004-9541(06)60125-0

Wen, Z., Wang, J., Wang, Z., He, Z., Song, C., Liu, X., Zhang, N., Ji, T., 2023. Analysis of the world deepwater oil and gas exploration situation. Pet. Explor. Dev. 50, 1060–1076. https://doi.org/10.1016/S1876-3804(23)60449-5

Woldesemayat, M.A., Ghajar, A.J., 2007. Comparison of void fraction correlations for different flow patterns in horizontal and upward inclined pipes. Int. J. Multiph. Flow 33, 347–370. https://doi.org/10.1016/j.ijmultiphaseflow.2006.09.004

Yakupov, N.M., Yakupov, S.N., 2018. Corrosion Wear under Vibrations. Dokl. Phys. 63, 147–149. https://doi.org/10.1134/S1028335818040109

Yang, Y., Li, J., Wang, S., Wen, C., 2017. Understanding the formation process of the liquid slug in a hilly-terrain wet natural gas pipeline. J. Environ. Chem. Eng. 5, 4220–4228. https://doi.org/10.1016/j.jece.2017.08.010

Yin, P., Cao, X., Li, Y., Yang, W., Bian, J., 2018. Experimental and numerical investigation on slug initiation and initial development behavior in hilly-terrain pipeline at a low superficial liquid velocity. Int. J. Multiph. Flow 101, 85–96. https://doi.org/10.1016/j.ijmultiphaseflow.2018.01.004

Yoshida, Y., Sharma, Y., Miyata, K., Manabe, R., Ikeda, K., Takahashi, S., Ihara, M., 2000. Slug tracking in pipelines: Part I - Experiments and analysis. Proc. SPE Asia Pacific Conf. Integr. Model. Asset Manag. 153–165. https://doi.org/10.2523/59414-ms

Yu, H., Xu, Q., Cao, Y., Huang, B., Guo, L., 2024. Effects of riser height and pipeline length on the transition boundary and frequency of severe slugging in offshore pipelines. Ocean Eng. 298, 117253. https://doi.org/10.1016/j.oceaneng.2024.117253

Zabaras, G.J., 2000. Prediction of Slug Frequency for Gas/Liquid Flows. SPE J. 5, 252–258. https://doi.org/10.2118/65093-PA

Zhang, D., Zhao, B., Zhu, K., Jiang, H., 2023. Dynamic analysis of the subsea production system with lazy-wave risers attached to FPSO. PLoS One 1–26. https://doi.org/https://doi.org/10.1371/journal.pone.0291603

Zhang, H.-Q., Al-Safran, E.M., Jayawardena, S.S., Redus, C.L., Sarica, C., Brill, J.P., 2003a.

Modeling of slug dissipation and generation in gas-liquid hilly-terrain pipe flow. J. Energy Resour. Technol. Trans. ASME 125, 161–168. https://doi.org/10.1115/1.1580847

Zhang, H.-Q., Jayawardena, S.S., Redus, C.L., Brill, J.P., 2000. Slug Dynamics in Gas-Liquid Pipe Flow. J. Energy Resour. Technol. 122, 14–21. https://doi.org/10.1115/1.483156

Zhang, H.-Q., Wang, Q., Sarica, C., Brill, J.P., 2003b. Unified Model for Gas-Liquid Pipe Flow via Slug Dynamics—Part 1: Model Development. J. Energy Resour. Technol. 125, 266–273. https://doi.org/10.1115/1.1615246

Zheng, G., 1991. Two-Phase Slug Flow in Hilly Terrain Pipelines. University of Tulsa, OK.

Zheng, G., Brill, J.P., Shoham, O., 1995. An Experimental Study of Two-Phase Slug Flow in Hilly Terrain Pipelines. SPE Prod. Facil. 10, 233–240. https://doi.org/10.2118/24788-PA

Zheng, G., Brill, J.P., Shoham, O., 1993. Hilly Terrain Effects on Slug Flow Characteristics, in: Proceedings of SPE Annual Technical Conference and Exhibition. Society of Petroleum Engineers, pp. 529–541. https://doi.org/10.2523/26566-MS

Zheng, G., Brill, J.P., Taitel, Y., 1994. Slug flow behavior in a hilly terrain pipeline. Int. J. Multiph. Flow 20, 63–79. https://doi.org/10.1016/0301-9322(94)90006-X

Zhu, H., Gao, Y., Zhao, H., 2019. Coupling vibration response of a curved flexible riser under the combination of internal slug flow and external shear current. J. Fluids Struct. 91, 102724. https://doi.org/10.1016/j.jfluidstructs.2019.102724

Zhu, H., Hu, J., Gao, Y., 2021. Severe slug flow-induced nonlinear dynamic behavior of a flexible catenary riser. Phys. Fluids 33, 071705. https://doi.org/10.1063/5.0054160

Zuber, N., Findlay, J.A., 1965. Average Volumetric Concentration in Two-Phase Flow Systems. J. Heat Transfer 87, 453–468. https://doi.org/10.1115/1.3689137

APPENDIX A – UNCERTAINTY ANALYSIS

This appendix presents in detail the uncertainty determination of each variable shows in Table 3.5. The uncertainty of bubble and liquid slug velocities and lengths, unit cell frequency, superficial liquid and gas velocities and pressure combines the uncertainties from all variables used for their calculations. Besides these parameters, Chapter 3 also describes about the uncertainties of the experimental friction factor and differential pressure resulted by the height difference between the stations. The following bullet points introduces each parameter:

- **Translation bubble (U_T) e liquid slug front (V_S) velocities**

As described in Eqs. (3.3) and (3.4), both parameters are function of the bubble and liquid slug time passage through the two impedance sensors and the distance between them. The passage time might be correlated with the acquisition frequency. The error of the measuring of the sensors distance depends on the methodology used to obtain it. Thus, the uncertainty is:

$$\delta V_S = \delta U_T = \sqrt{\left(\frac{\delta f_{aquisition}}{f_{aquisition}}\right)^2 + \left(\frac{\delta \Delta S}{\Delta S}\right)^2} \quad . \tag{A.1}$$

- **Dimensionless bubble and liquid slug lengths**

Eqs. (3.5) and (3.6) shows these parameters depend on the flow structures velocities and their passage time across the second impedance sensor. Therefore, these uncertainties combine the uncertain of the velocity, acquisition frequency and diameter:

$$\delta L_B = \sqrt{\left(\frac{\delta f_{aquisition}}{f_{aquisition}}\right)^2 + \left(\frac{\delta U_T}{U_T}\right)^2 + \left(\frac{\delta D}{D}\right)^2} \quad , \tag{A.2}$$

$$\delta L_S = \sqrt{\left(\frac{\delta f_{aquisition}}{f_{aquisition}}\right)^2 + \left(\frac{\delta V_S}{V_S}\right)^2 + \left(\frac{\delta D}{D}\right)^2} \quad . \tag{A.3}$$

- **Unit cell frequency**

The unit cell frequency is the inverse of the sum of bubble and liquid slug passage times as written in Eq. (3.7). As the time is correlated with the acquisition frequency, the uncertainty is:

$$\delta f = \sqrt{2 \cdot \left(\frac{\delta f_{aquisition}}{f_{aquisition}} \right)^2} \quad . \tag{A.4}$$

- **Superficial liquid and gas velocities**

The superficial velocity is the ratio of the volumetric flow rate to the pipe cross-sectional area. For the liquid phase, its uncertainty combines the water flow meter and diameter uncertainties:

$$\delta J_L = \sqrt{\left(\delta Q_L\right)^2 + 2 \cdot \left(\frac{\delta D}{D} \right)^2} \quad . \tag{A.5}$$

For the gas phase, other variables should be regarded due to the pressure difference between each station. As described in Section 3.1.3, the air volumetric flow rate, measured by the Merian laminar flow element, must be convert from its pressure condition to a new one in each station. Thus, the gas velocity uncertainty also considers the pressure at the laminar flow element and station:

$$\delta J_G{}^{Station} = \sqrt{\left(\delta Q_G\right)^2 + 2 \cdot \left(\frac{\delta D}{D} \right)^2 + \left[\left(\delta P\right)^2 \right]^{Station} + \left[\left(\delta \Delta P_{lam}\right)^2 + \left(\delta P_{atm}\right)^2 \right]} \quad . \tag{A.6}$$

- **Pressure at each station (S1-10)**

The test loop contains absolute and differential pressure sensors, as described in Section 3.1.1. For absolute pressure sensors (P0 and P10), the pressure reconstitution is given by the sum of the value measured by the sensor, the atmospheric pressure and the pressure obtained from the height difference, see Eq. (3.8). Both instruments have the same model so as their uncertainty is:

$$\delta P_{absolute} = \sqrt{\left(\delta \Delta P_{sensor}\right)^2 + \left(\delta P_{atm}\right)^2 + \left(\delta \Delta P_H\right)^2} \ . \quad \text{(A.7)}$$

For differential pressure transducers, the pressure reconstitution depends on the pressure at the upstream sensor. For this reason, the uncertainty is growing between the stations 2 and 9, see Table 3.5. It is determined by:

$$\delta P_n = \sqrt{\left(\delta P_{sensor}^{n-1}\right)^2 + \left(\delta \Delta P_{sensor}^{n}\right)^2 + \left(\delta \Delta P_H\right)^2} \ . \quad \text{(A.8)}$$

where, n is the number of the sensor.

- **Hydrostatic column generated by the height difference between stations.**

This topic describes the uncertainties of Method 1 and 2 to determine the $\delta \Delta P_h$ term. As described in Section 3.1.1, two methodologies were proposed to determine the pressure generated by the hydrostatic column. Both methods have different uncertainties. For the first method, the uncertainty is the ratio of the instruments accuracy (Table 3.1) and the lowest pressure measured due to hydrostatic column:

$$\delta \Delta P_H^{sensor} = \sqrt{\left(\frac{\delta \Delta P_{sensor}}{P_{\min}}\right)^2} \ . \quad \text{(A.9)}$$

For Method 2, the uncertainty determination is more complex. Its uncertainty depends on the methodology employed to specify the height, since the hydrostatic pressure is calculated by:

$$\Delta P_H = \rho \cdot g \cdot H \ . \quad \text{(A.10)}$$

The determination of this height needed two steps. Firstly, it was determined each station height in relation to a reference point using the communicating vases concept. Then, a measuring tape was used to determine the difference between the previous markings. Each procedure results in additional uncertainty. The curvature radius generated due to the capillary effect on the U-shaped hose is the first uncertainty, Eq. (A.11). The smallest scale on a measuring tape is the second one. Thus, the uncertainty of the second method is:

$$\delta R_{curvature} = \sqrt{\left(\frac{\delta\sigma_S}{\sigma_S}\right) + \left(\frac{\delta\rho}{\rho}\right)^2 + \left(\frac{\delta g}{g}\right)^2 + \left(\frac{\delta L_{tape}}{h_{P_0}}\right)^2 + \left(\frac{\delta\theta}{\theta}\right)^2} \quad , \qquad \text{(A.11)}$$

$$\delta\Delta P_h^{sensor} = \sqrt{\left(\frac{\delta\rho}{\rho}\right)^2 + \left(\frac{\delta g}{g}\right)^2 + \left[4\cdot\left(\delta R_{curvature}\right)^2 + \left(\frac{\delta L_{tape}}{h_{10}}\right)^2\right]} \quad . \qquad \text{(A.12)}$$

- **Experimental friction factor**

The differential pressure measured by the sensors are the basis to calculate the experimental friction factor for liquid flow (presented in Section 3.3). Eq. (A.13) shows the variables used in this procedure. Thus, the uncertainty of this parameter combines the errors of all of them:

$$C_f = \frac{\Delta P}{\rho}\frac{D}{L}\frac{2}{V^2} \quad , \qquad \text{(A.13)}$$

$$\delta C_f = \sqrt{\left(\delta\Delta P_{sensor}\right)^2 + \left(\frac{\delta\rho}{\rho}\right)^2 + \left(\frac{\delta D}{D}\right)^2 + \left(\frac{\delta L}{L}\right)^2 + 2\cdot\left[\left(\delta Q_L\right)^2 + 2\cdot\left(\frac{\delta D}{D}\right)^2\right]} \quad . \qquad \text{(A.14)}$$

APPENDIX B – SLUG TRACKING EQUATION

This appendix presents the formulation proposed by Rosa et al.'s (2015) to obtain Eqs. (4.1) and (4.2). Section 4.1 highlights the hypotheses used for the model development. The model is based on the mass and momentum balances employing a one-dimensional transient control volume analysis. The control volume encompasses the entire unit cell (bubble plus liquid slug), as shown in Figure 4.1. This figure also reveals the main flow parameters that will be used in the following equations.

The control volume boundaries coincide with the pipe wall and the pipe cross sections at x^{j-1} and x^{j}. Both terms represent the liquid slug front of two sequential cells. The bubble nose (y^{j}) is another important coordinate. The relation between those coordinates and the bubble and liquid slug lengths:

$$L_S^j = x^j - y^j \text{ and } \frac{dL_S^j}{dt} = \frac{dx^j}{dt} - \frac{dy^j}{dt} \ , \tag{B.1}$$

$$L_B^j = y^j - x^{j-1} \text{ and } \frac{dL_B^j}{dt} = \frac{dy^j}{dt} - \frac{dx^{j-1}}{dt} \ . \tag{B.2}$$

In addition, the liquid and gas mass flow rate crossing the x^j and y^j coordinates must be defined. By assuming that R_S, U_S and U_b are uniform throughout the liquid slug region, those formulations are:

$$\dot{m}_{G,y^j} = \rho_{G,y^j}^j \left(U_b^j - \frac{dy^j}{dt} \right) \left(1 - R_S^j \right) A \ , \tag{B.3}$$

$$\dot{m}_{L,y^j} = \rho_L \left(U_S^j - \frac{dy^j}{dt} \right) R_S^j A \ , \tag{B.4}$$

$$\dot{m}_{G,x^j} = \rho_{G,x^j}^j \left(U_b^j - \frac{dx^j}{dt} \right) \left(1 - R_S^j \right) A \ , \tag{B.5}$$

$$\dot{m}_{L,x^j} = \rho_L \left(U_S^j - \frac{dx^j}{dt} \right) R_S^j A \ . \tag{B.6}$$

- **Liquid and gas phase mass balance at the unit cell**

Eq. (4.1) is written by combining the gas and liquid mass balances applied to a unit cell. Both equations are:

$$A\frac{d}{dt}\left[\rho_G^j\left(1-R_B^j\right)L_B^j+\rho_G^j\left(1-R_S^j\right)L_S^j\right]+\dot{m}_{G,x^j}-\dot{m}_{G,x^{j-1}}=0\ , \tag{B.7}$$

$$A\frac{d}{dt}\left(\rho_L R_f^j L_B^j+\rho_L R_S^j L_S^j\right)+\dot{m}_{L,x^j}-\dot{m}_{L,x^{j-1}}=0\ . \tag{B.8}$$

By substituting the definitions given by Eqs. (B.2) and (B.5) into Eq.(B.7), it leads to:

$$\begin{aligned}&-\left(R_f^j-R_S^j\right)\frac{dy^j}{dt}-\left[1-\frac{\rho_{G,x^{j-1}}^{j-1}}{\rho_{G,x^j}^j}-R_f^j+\frac{\rho_{G,x^{j-1}}^{j-1}}{\rho_{G,x^j}^j}R_S^{j-1}\right]\frac{dx^{j-1}}{dt}-L_B^j\frac{dR_f^j}{dt}-L_S^j\frac{dR_S^j}{dt}=\\&-U_b^j\left(1-R_S^j\right)+U_b^{j-1}\frac{\rho_{G,x^{j-1}}^{j-1}}{\rho_{G,x^j}^j}\left(1-R_S^{j-1}\right)-\left[\left(1-R_f^j\right)L_B^j+\left(1-R_S^j\right)L_S^j\right]\frac{1}{\rho_G^j}\frac{d\rho_G^j}{dt}\end{aligned}\ . \tag{B.9}$$

In addition, Eqs. (B.1) and (B.6) are combined with Eq. (B.8), resulting in:

$$\left(R_S^{j-1}-R_f^j\right)\frac{dx^{j-1}}{dt}+\left(R_f^j-R_S^j\right)\frac{dy^j}{dt}+L_B^j\frac{dR_f^j}{dt}+L_S^j\frac{dR_S^j}{dt}=U_S^{j-1}R_S^{j-1}-U_S^jR_S^j\ . \tag{B.10}$$

The sum of Eqs. (B.9) and (B.10) reveals:

$$\begin{aligned}&\left[\left(1-R_f^j\right)L_f^j+\left(1-R_S^j\right)L_S^j\right]\frac{1}{\rho_G^j}\frac{d\rho_G^j}{dt}=-\left[R_S^{j-1}\left(1-\frac{\rho_{G,x^{j-1}}^{j-1}}{\rho_{G,x^j}^j}\right)-1+\frac{\rho_{G,x^{j-1}}^{j-1}}{\rho_{G,x^j}^j}\right]\frac{dx^{j-1}}{dt}\\&+U_S^{j-1}R_S^{j-1}-U_S^jR_S^j-U_b^j\left(1-R_S^j\right)+U_b^{j-1}\frac{\rho_{G,x^{j-1}}^{j-1}}{\rho_{G,x^j}^j}\left(1-R_S^{j-1}\right)\end{aligned}\ . \tag{B.11}$$

Some simplifications must be applied in Eq. (B.11) to obtain Eq. (4.1). It is assumed the gas density between two consecutive cells has a smooth change $\left(\rho_{G,x^{j-1}}^{j-1}/\rho_{G,x^j}^j\approx 1.0\right)$. In addition, the closure equations presented in Eqs. (4.6), (4.7) and (4.8) are substituted in Eq. (B.11). It results in the final equation:

$$\left[\left(1-R_f^j\right)L_B^j+\left(1-R_S^j\right)L_S^j\right]\frac{1}{\rho_G^j}\frac{d\rho_G^j}{dt}=\frac{U_S^{j-1}R_S^{j-1}}{1-c_b^{j-1}\left(1-R_S^{j-1}\right)}$$
$$-\frac{U_S^jR_S^j}{1-c_b^j\left(1-R_S^j\right)}+\frac{u_d^{j-1}\left(1-R_S^{j-1}\right)}{1-c_b^{j-1}\left(1-R_S^{j-1}\right)}-\frac{u_d^j\left(1-R_S^j\right)}{1-c_b^j\left(1-R_S^j\right)} \quad , \quad \text{(B.12)}$$

which is also presented in Eq. (4.1) and Table 4.1.

- **Momentum equation**

The gas and liquid momentum balance is applied to the same control volume used in the mass analyses. Its surfaces coincide with the pipe wall and the slug front (x^j) and bubble tail (x^{j-1}), as shown in Figure 4.1. Rosa et al.'s (2015) momentum equation is:

$$\begin{aligned}
&\frac{d}{dt}\int_0^{L_B}\left(\rho_L R_f^j U_f^j+\rho_G^j\left(1-R_f^j\right)U_G^j\right)Adz_f+\frac{d}{dt}\int_0^{L_S}\left(\rho_L R_S^j U_S^j+\rho_G^j\left(1-R_S^j\right)U_b^j\right)Adz_S+\\
&\left(U_{L,x^j}\dot{m}_{L,x^j}+U_{G,x^j}\dot{m}_{G,x^j}\right)-\left(U_{L,x^{j-1}}\dot{m}_{L,x^{j-1}}+U_{G,x^{j-1}}\dot{m}_{G,x^{j-1}}\right)=\left(P_G^j-P_G^{j+1}\right)A\\
&-g\sin(\theta)\left\{\left[\rho_L R_f^j+\rho_G^j\left(1-R_f^j\right)\right]L_B^j+\left[\rho_L R_S^j+\rho_G^j\left(1-R_S^j\right)\right]L_S^j\right\}A\\
&-\tau_S^jS\cdot L_S^j-\left(\tau_f^jS_f^j+\tau_G^jS_G^j\right)\cdot L_B^j+g\cdot\cos(\theta)\cdot D\left[\rho_L\xi_{L,x^{j-1}}R_{f,x^{j-1}}-\rho_L\xi_{L,x^j}R_{f,x^j}\right]A\\
&+g\cdot\cos(\theta)\cdot D\left\{\rho_{G,x^{j-1}}\xi_{G,x^{j-1}}\left(1-R_{f,x^{j-1}}\right)-\rho_{G,x^j}\xi_{G,x^j}\left(1-R_{f,x^j}\right)\right\}A
\end{aligned} \quad , \quad \text{(B.13)}$$

where the terms on the LHS represent the momentum time rate and the momentum fluxes from the j^{th} cell at the x^{j-1} and x^j boundaries. The RHS terms show the external forces acting on the mixture momentum balance: (1°) the pressure difference between two neighboring gas bubbles. This result arises naturally due to the different pressure acting on the boundaries, which correspond to the pressure of the (j) and (j+1) cells. The remaining terms are: (2°) the mixture weight, (3°) and (4°) the wall friction at the liquid slug and the liquid film zone, (5°) the hydrostatic pressure forces, which depend on the centroid coordinates for the gas and liquid phases, ξ_G and ξ_L. However, the implementation of the momentum equation currently disregards the latter term, as shown in Table 4.1.

The rate of momentum inside the film region is cumbersome to evaluate. It has a constant pressure, and the bubble behaves as a free surface subject to interfacial waves, see Madani et al. (2009). Since the model is one-dimensional, it is not possible to capture that wave feature. However, the rate of momentum inside the film region can be estimated by performing

a momentum analysis in this region only. The cross-section boundaries coincide with the bubble (y^j) and bubble tail (x^{j-1}). The momentum balance is:

$$\begin{aligned}&\frac{d}{dt}\int_0^{L_B}\left(\rho_L R_f^j U_f^j+\rho_G^j\left(1-R_f^j\right)U_G^j\right)A dz_f+\left(U_{L,y^j}\dot{m}_{L,y^j}+U_{G,y^j}\dot{m}_{G,y^j}\right)\\&-\left(U_{L,x^{j-1}}\dot{m}_{L,x^{j-1}}+U_{G,x^{j-1}}\dot{m}_{G,x^{j-1}}\right)=-g\sin(\theta)\left\{\left[\rho_L R_f^j+\rho_G^j\left(1-R_f^j\right)\right]L_B^j\right\}A\\&-\left(\tau_f^j S_f^j+\tau_G^j S_G^j\right)\cdot L_B^j+g\cdot\cos(\theta)\cdot D\left[\rho_L\xi_{L,x^{j-1}}R_{f,x^{j-1}}-\rho_L\xi_{L,y^j}R_{f,y^j}\right]A\\&+g\cdot\cos(\theta)\cdot D\left\{\rho_{G,x^{j-1}}\xi_{G,x^{j-1}}\left(1-R_{f,x^{j-1}}\right)-\rho_{G,y^j}\xi_{G,y^j}\left(1-R_{f,y^j}\right)\right\}A\end{aligned} \quad . \quad \text{(B.14)}$$

By combining Eq. (B.14) with Eq. (B.13), the momentum equation turns to:

$$\begin{aligned}&A\frac{d}{dt}\left[\left(\rho_L R_S^j U_S^j+\rho_G^j\left(1-R_S^j\right)U_b^j\right)L_S^j\right]+\\&+\left(U_{L,x^j}\dot{m}_{L,x^j}-U_{L,y^j}\dot{m}_{L,y^j}\right)+\left(U_{G,x^j}\dot{m}_{G,x^j}-U_{G,y^j}\dot{m}_{G,y^j}\right)\\&=\left(P_G^j-P_G^{j+1}\right)A-g\sin(\theta)\left\{\left[\rho_L R_S^j+\rho_G^j\left(1-R_S^j\right)\right]L_S^j\right\}A-\tau_S^j S\cdot L_S^j\\&+g\cdot\cos(\theta)\cdot D\cdot\rho_L\left(\xi_{L,y^j}R_{f,y^j}-\xi_{L,x^j}R_{f,x^j}\right)A\\&+g\cdot\cos(\theta)\cdot D\left[\rho_{G,y^j}\xi_{G,y^j}\left(1-R_{f,y^j}\right)-\rho_{G,x^j}\xi_{G,x^j}\left(1-R_{f,x^j}\right)\right]A\end{aligned} \quad . \quad \text{(B.15)}$$

The following equations do include the hydrostatic term anymore. In addition, it is assumed that the gas density is much smaller than the liquid density $\left(\rho_G/\rho_L \ll 1.0\right)$. Thus, Eq. (B.15) is simplified to:

$$\begin{aligned}&A\frac{d}{dt}\left(\rho_L R_S^j U_S^j L_S^j\right)+\left(U_{L,x^j}\dot{m}_{L,x^j}-U_{L,y^j}\dot{m}_{L,y^j}\right)\\&=\left(P_G^j-P_G^{j+1}\right)A-\rho_L R_S^j L_S^j A g\sin(\theta)-\tau_S^j S\cdot L_S^j\end{aligned} \quad . \quad \text{(B.16)}$$

The term $\left(U_{L,x^j}\dot{m}_{L,x^j}-U_{L,y^j}\dot{m}_{L,y^j}\right)$ is rewritten based on the definitions of Eqs. (B.4) and (B.6):

$$\begin{aligned}&\left(U_{L,x^j}\dot{m}_{L,x^j}-U_{L,y^j}\dot{m}_{L,y^j}\right)=\left[U_S^j\left(\frac{R_S^j}{R_f^{j+1}}\right)-\frac{dx^j}{dt}\left(\frac{R_S^j}{R_f^{j+1}}-1\right)\right]\left\{\rho_L\left(U_S^j-\frac{dx^j}{dt}\right)R_S^j A\right\}\\&-\left\{U_S^j\rho_L R_S^j A\left(U_S^j-\frac{dy^j}{dt}\right)\right\}\end{aligned} \quad . \quad \text{(B.17)}$$

By substituting Eq. (B.17) into Eq. (B.16) as:

$$\rho_L R_S^j L_S^j \frac{dU_S^j}{dt} + \rho_L R_S^j U_S^j \left\{ \frac{dL_S^j}{dt} + U_S^j \left(\frac{R_S^j}{R_f^{j+1}} - 1 \right) \left(1 - \frac{dx^j/dt}{U_S^j} \right)^2 + \left(\frac{dy^j}{dt} - \frac{dx^j}{dt} \right) \right\} \quad \text{.(B.18)}$$
$$= \left(P_G^j - P_G^{j+1} \right) - \rho_L R_S^j L_S^j g \sin(\theta) - \tau_s^j \frac{S}{A} \cdot L_S^j$$

The wall shear stress term is defined through the closure laws given by Eqs. (4.4), (4.6) and (4.7). Thus, the momentum balance becomes:

$$\frac{dU_S^j}{dt} = -\left(U_S^j \right)^2 \left\{ \frac{1}{L_S^j} \left(\frac{R_S^j}{R_f^{j+1}} - 1 \right) \left(1 - \frac{dx^j/dt}{U_S^j} \right)^2 \right\}$$
$$-U_S^j \left[2C_f^j \frac{\rho_M^j}{\rho_L} \frac{\left| U_M^j \right|}{D} \frac{1}{R_S^j} \frac{R_S^j}{1 - c_b^j \left(1 - R_S^j \right)} + 2C_f^j \frac{\rho_M^j}{\rho_L} \frac{\left| U_M^j \right|}{D R_S^j} \frac{u_d^j}{U_S^j} \frac{\left(1 - R_S^j \right)}{1 - c_b^j \left(1 - R_S^j \right)} \right]. \quad \text{(B.19)}$$
$$+ \frac{\left(P_G^j - P_G^{j+1} \right)}{\rho_L R_S^j L_S^j} - g \sin(\theta)$$

Thus, Eq. (B.19) is the formulation presented by Eq. (4.2) and Table 4.1.